Hydrothermal/Solvothermal Synthesis of Hierarchical Titanium Dioxide Photocatalysts for Indoor Air Purification

Alireza Haghighatmamaghani

A Thesis

In the Department

of

Building, Civil and Environmental Engineering

Presented in Partial Fulfillment of the Requirements

For the Degree of

Doctor of Philosophy (Building Engineering) at

Concordia University

Montreal, Quebec, Canada

January 2019

CONCORDIA UNIVERSITY

SCHOOL OF GRADUATE STUDIES

This is to certify that the thesis prepared

By: Alireza Haghighatmamaghani

Entitled: Hydrothermal/Solvothermal Synthesis of Hierarchical Titanium Dioxide Photocatalysts for Indoor Air Purification

and submitted in partial fulfillment of the requirements for the degree of

Doctor Of Philosophy (Building Engineering)

complies with the regulations of the University and meets the accepted standards with respect to originality and quality.

Signed by the final examining committee:

_____ Chair
Dr. Ketra Schmitt

_____ External Examiner
Dr. Zaher Hashisho

_____ External to Program
Dr. Martin Pugh

_____ Examiner
Dr. Zhi Chen

_____ Examiner
Dr. Maria Elektorowicz

_____ Thesis Co-Supervisor
Dr. Fariborz Haghighat

_____ Thesis Co-Supervisor
Dr. Chang-Seo Lee

Approved by

Dr. Fariborz Haghighat, Graduate Program Director

February 18, 2019

_____
Dr. Amir Asif, Dean
Gina Cody School of Engineering & Computer Science

Abstract

Hydrothermal/Solvothermal Synthesis of Hierarchical Titanium Dioxide Photocatalysts for Indoor Air Purification

Alireza Haghighatmamaghani, Ph.D.

Concordia University, 2019

Energy saving policies applied to modern buildings, tighter building envelopes, and decline in outdoor air quality promote the escalation in levels of indoor air pollutants. In recent years, concerns regarding the impact of indoor air quality (IAQ) on human health especially in well-insulated buildings in metropolitans have created a pressing need for reliable air remediation technologies. Heterogeneous ultraviolet photocatalytic oxidation (UV-PCO) has been put forward as an efficient method to ameliorate IAQ via catalytic degradation of harmful organic compounds to benign final products.

In this context, developing highly photoactive and durable photocatalysts that can perform satisfactorily under realistic conditions is sought after to expedite UV-PCO systems commercialization. Photocatalyst's performance is a function of several interconnected features: crystallinity, crystal phase and size, surface area, porosity, surface chemistry, light-harvesting ability, exposed facet, and charge-separation efficiency. In this regard, thanks to their unique morphology and multimodal porosity, hierarchical photocatalysts can incorporate high molecular diffusion/transport, superior light harvesting, and large surface area. Template-free hydrothermal/solvothermal route is a green, versatile, and less costly strategy for fabricating hierarchical photocatalysts with controlled characteristics.

Taking into account the above-mentioned merits of hierarchical photocatalysts and hydrothermal synthesis method, the core objectives of this research are:

1) Synthesize hierarchically porous titanium dioxide materials with enhanced photoactivity with respect to commercially available photocatalysts (e.g. P25) via hydrothermal method.

2) Explore the complex preparation-property-performance relationships for titanium dioxide photocatalysts utilized in photocatalytic air purification.
3) Examine the role of photocatalyst's morphology in photocatalytic degradation by developing several potentially promising structures and assess their performance.
4) Investigate the improvement in photocatalytic filter activity and stability with combining hierarchical titanium dioxide with carbonaceous support.
5) Evaluate the activity of photocatalysts under realistic operating conditions to provide reliable information regarding the capability of UV-PCO air purifiers.

To accomplish these goals, a large number of TiO_2 photocatalysts are synthesized by systematically varying the hydrothermal preparation parameters (e.g. time, temperature, pressure, pH, solvent, titanium precursor, calcination temperature, etc.). Accordingly, by means of comprehensive characterization, the influence of synthetic methodology on textural, morphological, and crystallographic properties of photocatalysts is investigated. In the last stage, the performance of photocatalyst is evaluated by degradation of two prevalent indoor air pollutants (toluene and methyl ethyl ketone (MEK)) at wide ranges of operating conditions.

Acknowledgment

First, I would like to express my sincere gratitude to my supervisor, Professor Fariborz Haghighat, for his valuable guidance and continuous support throughout my PhD program. He kindly provided me the opportunity to work on this challenging area and always gave me intellectual freedom. I am very appreciative that the door of his office was always open and that he was willing to answer questions with cheerfulness and good humor. I also appreciated his encouragement during setbacks and his patience. From him, I have learned many lessons which will benefit me in professional and personal life.

I am also deeply grateful to Dr. Chang-Seo Lee, my co-supervisor, for her invaluable comments and suggestions. I benefited a great deal from her knowledge and experience in the field of indoor air purification. Her positive energy and lovely smile made our lab a pleasant environment to work in for long hours.

I am thankful to Mr. Luc Demers, Mr. Josef Hrib, and Ms. Hong Guan for their help with the construction of the experimental set-up and constant technical assistance.

I acknowledge the financial support from Concordia University, Concordia Collaborative Research and Training Experience (CREATE) program, l'Institut de recherche Robert-Sauvé en santé et en sécurité du travail (IRSST) and ASHRAE Grant-in-Aid Scholarship.

I would like to thank the members of my committee Dr. Maria Elektorowicz, Dr. Martin Pugh, Dr. Zhi Chen, and Dr. Zaher Hashisho for their time spent reading the proposal and dissertation, and providing comments and constructive criticism.

Finally, I would like to express my deepest gratitude to my mother and my sisters for their spiritual support throughout my life.

Dedication

To:

My Mother

Without you, I would not be who I am and where I am today

Table of Contents

List of Figures

List of Tables

List of Abbreviations and Symbols

AC	Activated carbon
ACF	Activated carbon filter
ASHRAE	American society of heating, refrigerating and air conditioning engineers
BDDT	Brunauer, Deming, Deming, and Teller
BET	Brunauer, Emmett, and Teller
BRI	Building related illness
CB	Conduction band
CO	Carbon monoxide
CO_2	Carbon dioxide
CVD	Chemical vapor deposition metal-organic
EDS	Energy dispersive spectroscopy
EPA	Environmental Protection Agency
ESR	Electron spin resonance
FTIR	Fourier transform infrared spectroscopy
GC-MS	Gas chromatograph-mass spectrometer
HPLC	High performance liquid chromatograph
HPCs	Hierarchical photocatalysts
HRI	Health-related index
HVAC	Heating, ventilating and air-conditioning
IAQ	Indoor air quality
MEK	Methyl ethyl ketone (2-butanone)
MOCVD	Metal-organic chemical vapor deposition
NFF	Nickel foam filter
NIOSH	National Institute for Occupational Safety and Health
NO_x	Nitrogen oxides
OH	Surface hydroxyl group

$^{\bullet}OH$	Hydroxyl radicals
$O_2^{\bullet-}$	Superoxide radical anions
O_3	Ozone
OSHA	Occupational Safety & Health Administration standards
PCO	Photocatalytic oxidation ppb
PID	Photoionization detector
PL	Photoluminescence
ppb	Parts per billion
ppm	Parts per million
PTR-MS	Proton transfer reaction-mass spectrometer
REL	Recommended exposure limit
RH	Relative humidity
SBS	Sick building syndrome
SEM	Scanning electron microscopy
TA	Terephthalic acid
TBOT	Tetrabutyl titanate or $Ti(OBu)_4$
TEM	Transmission electron microscopy
TGA	Thermo-gravimetrical analysis
THP	3-D hierarchically porous titania
THS	Titania hollow spheres
TiO_2	Titanium dioxide, titania
TMMS	Titania mesoporous microspheres
TNS	Titania nanosheets
TNT	Titania nanotubes
TPD-TPO	Temperature-programmed desorption and oxidation
TSMS	Titania solid microspheres
TSU	Titania 3-D sea urchin-like

TTIP	Titanium isopropoxide or $Ti(OPr)_4$
UVC	Ultraviolet C radiation
UV-PCO	Ultraviolet photocatalytic oxidation
UV-vis	UV/vis absorption spectroscopy
VB	Valence band
VOCs	Volatile organic compounds
XPS	X-ray photoelectron spectroscopy
XRD	X-ray diffraction
2,4-DNPH	2,4-dinitrophenylhydrazine
2-HTA	2-hydroxyterephthalic acid

English Symbols	**Description**
C	Concentration (ppb or ppm)
e^--h^+	Electron and hole pair
K	Langmuir absorption constant (1/ppm)
m	Photocatalyst mass on support (g)
M	Molar mass (g/mol)
Q	Volumetric airflow rate (m^3/min)
r	PCO reaction rate (mol/(min.g))
t	Time (s or min)
wt	Weight percent (wt%)

Greek symbol	Description
Å	Angstrom
n	Nano
μ	Micro
μ_{max}	Maximum amount adsorbed (g/g)
η	Single pass removal efficiency (%)
θ	Adsorption capacity (g/g)

Chapter 1

1. Introduction

1.1. Indoor air quality issue

Indoor air pollution is currently regarded as one of the main environmental risks to public health according to the environmental protection agency (EPA) [1]. Owing to the fact that nowadays people spend most of their time (more than 90% [2]) in an indoor environment, indoor air quality (IAQ) has a significant impact on human health, comfort and productivity [3]. Therefore, indoor air quality has been increasingly becoming a pressing concern to public health officials and a challenging research topic. It has been shown that a long-term exposure to indoor air pollutants can be detrimental to human health and lead to Sick Building Syndrome (SBS), Building Related Illnesses (BRI) and in extreme cases cancer [4]. In non-industrial buildings, pollutants mainly originate from outdoor polluted air (through infiltration or ventilation process) and emissions from indoor sources. Accordingly, levels of pollutants in indoor environment can be higher than those of outdoor air due to the contribution of indoor sources such as combustion by-products, building materials, occupant-related activities, office equipment (e.g. printers and computers), and consumer products [4, 5]. It is noteworthy that two of the central reasons for poor IAQ in modern buildings are the tight building envelopes and the reduced ventilation rate, which limit the air exchange. Volatile organic compounds, nitrogen oxides (NO_x), carbon monoxide (CO), and particulate matter are among the main indoor air pollutants. In most commercial and residential buildings, volatile organic compounds are the primary source of poor IAQ. VOCs encompass various chemical groups: alkanes, alcohols, aldehydes, ketones, esters, terpenes, aromatic hydrocarbons, etc. The potential harmful health effects of VOCs are irritations of upper respiratory system, sinus infection, allergic reaction, asthma, headache, fatigue, poor concentration, nausea, and dizziness [6]. Despite the fact that VOC concentrations are relatively low in non-industrial environments, the high potential for many VOCs' presence in indoor air to cause symptoms is a result of both additive and synergistic effects [7].

1.2. IAQ control methods in buildings

1.2.1. Dilution

The most conventional and utilized approach to lower the levels of air pollutants in buildings is dilution through ventilation. In this method, the outdoor air is introduced into the heating, ventilating, and air conditioning (HVAC) system and mixed with the recirculated indoor air. The design and operation of the HVAC system should guarantee a safe environment for the occupants and also minimize the energy consumption. A considerable portion of Canada primary energy consumption is associated with HVAC operation in buildings. In this regard, one must keep in mind that in countries with extreme climates (such as Canada), in many periods throughout the year, the outdoor air does not satisfy the comfort temperature and humidity levels required for residential/commercial buildings. Consequently, a huge amount of energy needs to be consumed to heat, cool, humidify, or dehumidify the outdoor air to reach the acceptable thermal comfort level. This can substantially elevate the energy cost associated with building operation and put a limit on the maximum allowed ventilation rate. On the other hand, it should be highlighted that the dilution method is only effective when the outdoor air is cleaner than the indoor air, which is not necessarily true in metropolitans considering the drastic climate changes in recent years.

1.2.2. Adsorption

Most air cleaners used in air handling units of buildings for removing gaseous contaminants such as VOCs are based on the adsorption phenomenon. During the adsorption process, the challenge compounds are transferred from the gas phase to the solid phase. Activated carbon (AC), zeolites, and clays are among the most investigated adsorbents for VOCs removal owed to their large surface area, porous structure, and high adsorption capacity. Despite the fact that adsorption, especially on activated carbon, is very effective for air cleaning, this method suffers from a number of shortcomings. The first issue is the deactivation or performance drop of the filter, which necessitates frequent replacement or regeneration of the adsorbent. This issue is exacerbated by the lack of experimental data on the breakthrough times of adsorbents for operation under actual conditions (i.e. low VOC concentration). Secondly, since pollutants are solely transferred from one medium to another, saturated or used adsorbent filter can be a source

of pollution and poses environmental concerns. Moreover, at high airflow rates, the pressure drop associated with the air filter can be significant and increase the energy demand.

1.2.3. Purification

In recent years, increased awareness regarding the impact of IAQ on human health and the growing need for energy efficient buildings have resulted in a great deal of research in the field of indoor air purification. Accordingly, numerous air purification technologies have been developed: UV-PCO, catalytic oxidation, thermal and non-thermal plasma, catalytic plasma, and ozonation. These technologies cannot only improve the air quality, but also by lowering the ventilation rate lead to a considerable decline in building energy consumption (i.e. energy cost) [8]. The main advantage of these strategies, with respect to adsorption, is that the pollutants are ideally decomposed to innocuous products; therefore, less maintenance is required. Furthermore, normally these oxidation-based remediation systems bring about a lower pressure drop, resulting in smaller fan sizes for the HVAC units and thereby a lower energy demand. An air purification system should be evaluated from different aspects: long-term performance, energy consumption, capital cost, effectiveness for wide range of indoor pollutants, and last but not least the amount and type of by-products produced during the process.

Among various methods developed so far to enhance IAQ, photocatalytic oxidation has gained considerable attention for removal of gaseous pollutants at low concentrations (i.e. part per billion (ppb) level). PCO technology is founded on the application of semiconductor catalysts, generally a metal oxide semiconductor with an appropriate band gap energy, and UV light to convert challenge compounds into less harmful products [9, 10]. Room temperature operation, low pressure drop, medium to high efficiency for many common air pollutants, destruction of airborne microbes, low energy consumption, and compatibility with HVAC are the most acknowledged benefits of PCO technology. Despite these upsides, deactivation of photocatalyst (i.e. gradual decline in pollutant removal efficiency), low efficiency under severe operating conditions, and generation of unwanted by-products are the main limitations of this method.

1.3. Research objectives

In photocatalytic oxidation, like any other catalytic reaction, photocatalyst plays a critical role. Therefore, designing and synthesizing highly photoactive and durable photocatalysts is of great importance to boost the efficiency and to prolong the lifetime of PCO systems. In this context,

optimization of photocatalyst's key characteristics including crystallinity, crystal phase, crystal size, specific surface area, porosity, surface chemistry, and exposed crystal facet is crucial and indeed a very challenging endeavor. The main reason is that these properties usually take conflicting pathways during preparation; therefore, it is difficult to optimize each characteristic without jeopardizing the others. A viable approach to tackle this issue is to find the optimal trade-off among the key parameters at which the maximum performance can be achieved. However, to do so, one needs deep understanding of the relationships between preparation-property and property-performance. Elucidating such connections for TiO_2-mediated photocatalytic oxidation of indoor air pollutants is one of the ultimate goals of the present research.

In the past 10 years, hierarchical materials have received tremendous academic interest in various fields including semiconductor-mediated environmental remediation. There are a limited number of works specifically designed to assess the efficacy of hierarchical titanium dioxide photocatalysts for air purification. However, in these works the performance of photocatalysts was determined at ideal operating conditions which cannot provide solid information about their actual performance. Motivated by this research gap and considering the unique properties of hierarchical TiO_2 materials for photocatalysis, fabrication of highly photoactive hierarchically porous titanium dioxides tailored for removal of pollutants at extremely low concentration is another major objective of this research.

1.4. Approach and methodology

To realize the above-mentioned objectives, the following stages were taken into consideration chronologically:

1. Design and implement of the test-rig
    - A small-scale photoreactor, resembling the air-handling units of buildings, was constructed and installed.
    - The calibration, validation, and operation of the set-up under wide ranges of operating conditions were performed.
2. Development of coating technique and selection of support material

- Among considered methods (dip-coating, spray-coating, film-coating, sol-gel, etc.), a facile and straightforward coating process, pipetting technique, was developed and employed.
- The homogeneity of coating was assessed by scanning electron microscopy (SEM) and energy dispersive spectroscopy (EDS) elemental mapping.
- Nickel (Ni) foam filter was chosen as titanium dioxide support due to its mechanical stability, inertness to light, low affinity and adsorption capacity for VOCs, and compatibility with the coating technique.

3. Adsorption of VOCs on various titanium dioxide photocatalysts
    - Comprehensive Fourier transform infrared spectroscopy was performed to investigate the nature and density of surface hydroxyl (OH) groups.
    - Adsorption isotherms and breakthrough behaviors were studied for toluene and methyl ethyl ketone at three humidity levels and six inlet concentrations.
    - The impact of relative humidity on adsorption process and the interaction between VOCs and titania photocatalysts were explored.
4. Photocatalytic degradation of various VOCs on titanium dioxide photocatalysts
    - Impact of operating conditions including relative humidity, airflow rate, light intensity, and VOC inlet concentration on removal efficiency and by-products generation were investigated.
5. Synthesis, characterization, and performance evaluation of hydrothermally-prepared titanium dioxide photocatalysts
    - Employing the hydrothermal/solvothermal preparation route, a huge number of titania photocatalysts were fabricated, characterized, and tested for removal of VOCs (toluene or MEK).
    - The impacts of hydrothermal preparation conditions including time, temperature, pressure, medium pH, type of acid/base, type of reaction solvent, type of titanium precursor, and calcination temperature on key properties of developed TiO_2 samples were studied.
    - Detailed characterization was conducted via X-ray diffraction (XRD), N_2 adsorption-desorption, field emission SEM (FE-SEM), transmission electron microscopy (TEM), FTIR, UV-vis spectroscopy, photoluminescence (PL), thermo gravimetric

analysis (TGA), hydroxyl radical analysis, and X-ray photoelectron spectroscopy (XPS).

- Variations in structure of TiO_2 with preparation parameters were discussed considering the physical and chemical phenomena (e.g. Ostwald ripening, hollowing effect, surface protonation, and crystallization) during hydrothermal treatment.
- Photocatalysts were tested under severe operating conditions to acquire reliable information for actual applications.
- Connections among the preparation conditions, photocatalyst's properties, and the performance were highlighted and explained.
- Considering the detected by-products in the gas phase, tentative detailed reaction pathways for VOC photodegradation were proposed.

6. Combination of hierarchical titanium dioxide and activated carbon
    - The adsorption capacity of "titanium dioxide/activated carbon" was evaluated and compared to that of hierarchical titanium dioxide for MEK.
    - The photocatalytic reaction rate and by-products generation for titanium dioxide/activated carbon were assessed and compared to those of activated carbon filter, commercial P25, and hierarchical titanium dioxide.
    - The concept of in-situ regeneration of activated carbon via photocatalysis was investigated.

1.5. Limitations of the research

- The performance of developed photocatalysts was assessed at realistic operating conditions; nonetheless, the experiments were carried out in a small-scale photoreactor.
- During photocatalysts design and fabrication, the following aspects were not of primary concern: (i) cost of titanium precursors, solvents, additives, and equipment; (ii) amount and nature of produced chemicals during catalyst preparation and waste management; and (iii) possible environmental impacts of the preparation route.
- Long-term activity of yielded photocatalysts under severe operating conditions was not evaluated.
- Energy consumption associated with the PCO air cleaning system was not determined.

1.6. Thesis outline

Chapter 1- Introduction

Chapter 2- Literature review – Chapter 2 offers an overview of the topics that have been studied in order to carry out this research project. Section 1 of Chapter 2 provides a brief introduction to the basics of photocatalysis in the gas-phase and band gap model. In sections 2 and 3, titanium dioxide and its main properties, and hierarchical photocatalysts are respectively reviewed. Principles of hydrothermal/solvothermal synthesis including the most influential preparation factors are introduced in section 4. Section 5 gives a quick summary of chemical/physical coating methods utilized for deposition of titanium dioxide on various support materials. Sections 6 and 7 present a brief literature review on the influence of operating conditions (e.g. relative humidity, residence time, etc.) on photocatalytic processes as well as the proposed reaction pathways and intermediates/by-products for common VOCs.

Chapter 3- Methodology – The 1st, 2nd, and 3rd sections of this chapter describe the design and implementation of the small-scale continuous flow photoreactor, the experimental procedures for adsorption and PCO tests, analytical methods, and details of the coating process. The last section of this chapter deals with a brief description of theory and application of adopted photocatalyst characterization techniques.

Chapter 4- Adsorption and photocatalytic oxidation performance of commercial titanium dioxide photocatalysts – The first section focuses on mere adsorption of toluene and MEK onto different titanium dioxide photocatalysts. In this section, a comprehensive FTIR study is carried out and toluene/MEK adsorption isotherms at different humidity levels are obtained. In the second part of this chapter, the photocatalytic activity of four photocatalysts towards toluene and MEK at wide ranges of operating conditions is evaluated.

Chapter 5- Photocatalytic activity of hydrothermally/solvothermally prepared titanium dioxide photocatalysts- This chapter is dedicated to investigation of various hydrothermal preparation parameters and their effects on photocatalysts' properties and performance. In sections 1 through 4, hydrothermal time, temperature, pressure, solution pH, type of acid/base, solvent, titanium precursor, morphology, and calcination temperature are meticulously studied. In section 5, combination of titanium dioxide and activated carbon filter for enhancing the

stability of photocatalytic system is examined. In addition, the concept of in-situ regeneration of activated carbon via photocatalysis is introduced and assessed.

Chapter 6- Conclusions and recommendations – This chapter presents a summary of the research outcomes and provides recommendations for future work on the topic.

Chapter 2

2. Literature review

2.1. Fundamentals of photocatalytic oxidation

Heterogeneous catalysis involves an interaction between solid and reactant molecules in the gas phase. There are two characteristics namely UV light participation in energy initiation and occurrence of photochemical reactions at photocatalyst surface which differentiate PCO from classic catalytic reactions. The overall UV-PCO process can be broken down into the sequence of individual steps depicted in Figure 2.1:

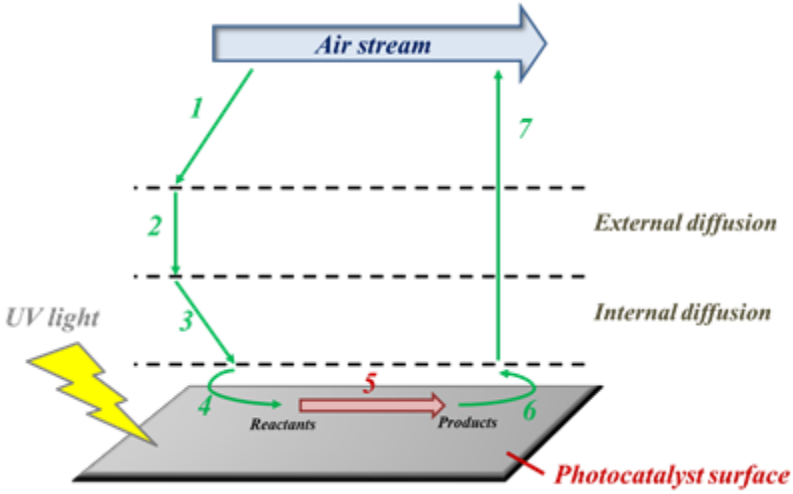

Figure 2.1 Steps in a heterogeneous photocatalysis

1) Advection

2) Mass transfer of the reactants from the main flow to the exterior surface of the catalyst

3) Molecular diffusion of the reactants from the exterior surface of the catalyst particle into the interior pore structure

4) Adsorption onto the catalyst surface

5) Photochemical reaction on the catalyst surface

6) Desorption of the reaction product(s) from the surface of catalyst

7) Mass transfer of products from the catalyst interior pores to the surface by molecular diffusion and/or Knudsen diffusion, followed by external diffusion to the main flow

In PCO, a crucial step is the formation of electron and hole (e^--h^+) pair, which requires the illumination of semiconductor, absorption of photons with sufficient energy, and promotion of electrons from the valence band (VB) to the conduction band (CB). According to the band gap model, VB electrons are transferred to the CB when semiconductor is illuminated with photons having energy content equal or higher than the band gap. From a thermodynamic point of view, VB holes can oxidize adsorbed compounds if the redox potential of the VB is more positive than that of the adsorbates. Similarly, CB electrons can reduce adsorbed species if they have a more negative redox potential than the adsorbates. The photogenerated charge carriers participate in a series of reactions with other molecules such as oxygen and water and produce highly reactive radicals (such as hydroxyl radicals ($^{\bullet}OH$)). After being adsorbed onto the surface, pollutant molecules come into contact with the produced reactive species and break down to lower molecular weight products and eventually to CO_2 and water (depicted in Figure 2.2).

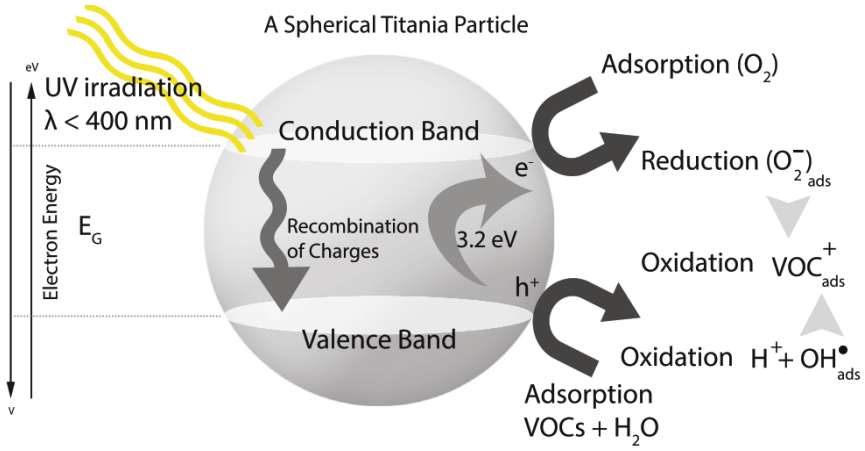

Figure 2.2 Reaction mechanisms of PCO on catalyst particle [11]

The basic PCO reaction mechanism using TiO_2 can be regarded as follows:

$$TiO_2 + hv \rightarrow TiO_2(e^-_{CB} + h^+_{VB}) \quad (2.1)$$

$$TiO_2(h^+_{VB}) + H_2O \rightarrow TiO_2 + H^+ + OH^{\bullet} \quad (2.2)$$

$$TiO_2(h^+_{VB}) + OH^- \rightarrow TiO_2 + OH^{\bullet} \quad (2.3)$$

$$TiO_2(e_{CB}^-) + O_2 \rightarrow TiO_2 + O_2^{\bullet -} \quad (2.4)$$

$$O_2^{\bullet -} + H^+ \rightarrow HO_2^{\bullet} \quad (2.5)$$

$$HO_2^{\bullet} + HO_2^{\bullet} \rightarrow H_2O_2 + O_2 \quad (2.6)$$

$$TiO_2(e_{CB}^-) + H_2O_2 \rightarrow OH^- + OH^{\bullet} \quad (2.7)$$

$$VOC + O_2 + OH^{\bullet} \rightarrow \ H_2O + CO_2 + other\ products \quad (2.8)$$

Apart from their beneficial participation in oxidation and reduction reactions, electrons and holes also go through recombination process where they neutralize one another. The recombination of charge carriers, whether in the bulk or on the surface, drastically decreases the quantum efficiency and PCO performance. The time scale for generation, trapping, recombination, and interfacial charge transfer reactions on the surface of TiO_2 photocatalyst is provided in Figure 2.3. As can be noted, recombination of electron and hole pairs happens in the order of a few nanoseconds, while interfacial charge transfer reactions may take hundreds of nanoseconds.

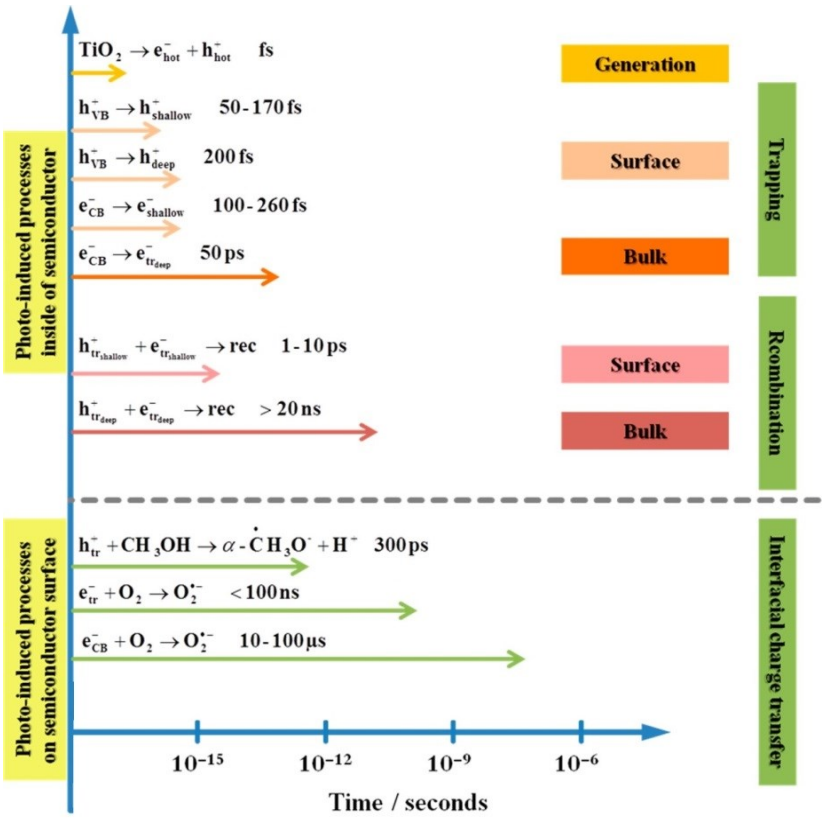

Figure 2.3 Photoinduced reactions in TiO_2 photocatalysis and the corresponding time scales [12]

2.2. Titanium dioxide photocatalyst

Among a wide spectrum of photocatalysts (e.g. TiO_2, ZnO, ZrO_2, SnO_2, WO_3, CeO_2, ZnS, and Fe_2O_3), TiO_2, as the most promising photocatalyst, has been the focus of majority of the works owing to its moderate performance as a photocatalyst under UV light irradiation, chemical stability, and suitable positions of valence and conduction bands [13]. Energy positions of VB and CB govern the ability of photocatalyst to engage in photoinduced electron/hole transfer with given adsorbed species. Band gaps, and VB and CB positions of some common semiconductors as well as the standard redox potentials of the ($O_2/O_2^{\bullet-}$) and ($^{\bullet}OH/^{-}OH$) redox couples are brought in Figure 2.4. Unlike most of the semiconductors, the VB redox potentials of both anatase and rutile TiO_2 are more positive than that of the ($^{\bullet}OH/^{-}OH$) redox couple. As a result, adsorbed water and hydroxyl groups can be oxidized to hydroxyl radicals on both excited rutile and anatase surfaces. On the other hand, the CB redox potential of anatase is more negative than that of ($O_2/O_2^{\bullet-}$), allowing formation of superoxide radical anions ($O_2^{\bullet-}$).

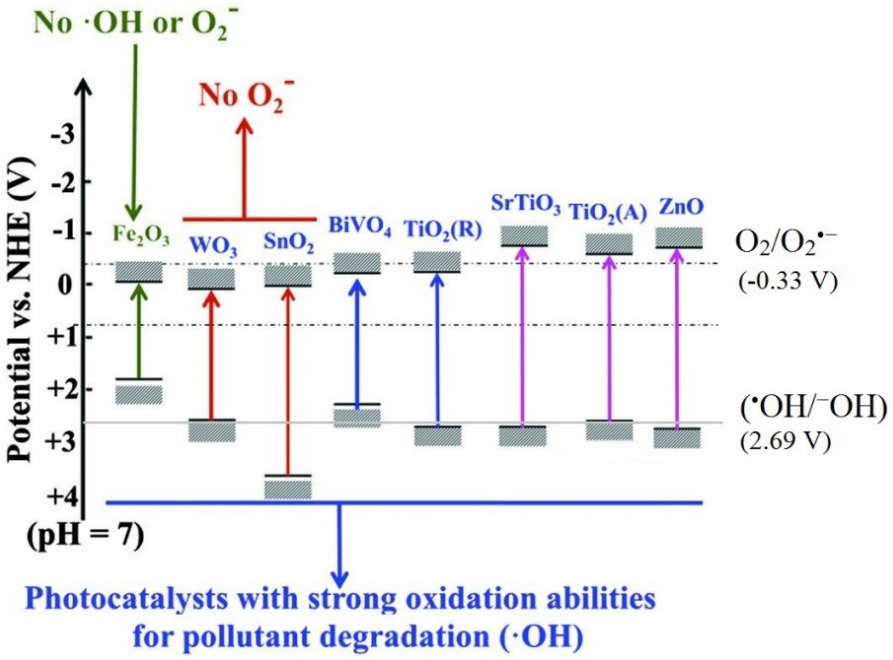

Figure 2.4 Band positions of some typical photocatalysts [14]

Titanium dioxide has three main crystalline states: anatase, rutile and brookite (shown in Figure 2.5). Rutile is a thermodynamic stable state, while anatase and brookite are metastable state. The building block of all three crystal forms of TiO_2 is TiO_6 octahedra but with a different spatial arrangement in each phase [15].

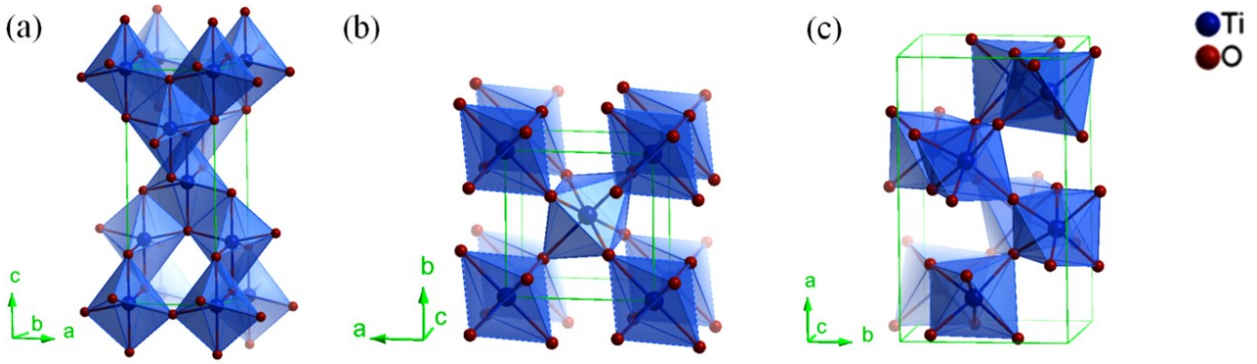

Figure 2.5 Crystalline structure of TiO_2 in different phases: (a) anatase, (b) rutile, and (c) brookite [16]

Titanium dioxide has a relatively large band gap: 3.23, 3.02, and 3.14 eV, for anatase, rutile and brookite phases, respectively [17]. The valence band of TiO_2 is composed of the 2p orbitals of oxygen hybridized with the 3d orbitals of titanium, while the conduction band is only the 3d orbitals of titanium [18].

The photocatalytic activity of TiO_2 depends on several factors including crystallinity, crystalline phase, crystal size, accessible surface area, pore structure, pore size, and surface chemistry. It is generally accepted that the differences in the photocatalytic activity result from joined effects of several electronic, textural and structural factors. As a result, an efficient TiO_2 photocatalyst should possess simultaneously an appropriate phase structure with textural and electronic properties since lack of one of these criteria leads to a sharp decline in photoactivity.

2.2.1. Effect of photocatalyst crystallinity and crystal size

Light harvesting, charge carrier generation (i.e. electron excitation) and separation, and charge migration to the surface exert significant influence on the quantum efficiency and photocatalytic activity of TiO_2. Due to the fact that recombination process is facilitated by the presence of lattice defects, crystal imperfections, and impurities, much attention has been paid to the achievement of high bulk crystallinity in order to enhance the photon utilization efficiency [14]. Anatase and rutile are the most common crystalline forms and the most investigated for photocatalytic applications. It is generally recognized that anatase is more active than rutile, which can be ascribed to several properties of anatase phase: (i) better generation of e^--h^+ pair; (ii) higher affinity towards O_2 due to the more negative redox potential of CB; (iii) higher amount of surface hydroxyl groups; and (iv) lower recombination rate than rutile [5, 19].

Hajaghazadeh et al. [20] ascribed the higher initial mineralization rate of methyl ethyl ketone over P25 and PC50 compared to that of PC500 to the slow decay of charge carriers in P25 and PC50, which was also reported by other researchers [21, 22]. Similar behavior has been found by Thevenet et al. [23] in acetylene degradation over P25 and PC500; however, the superior activity of P25 was rationalized differently. The authors speculated that since P25 particles are single crystallites, the electron migration to the surface is easier/faster than in PC500 where electrons have to cross crystallites interfaces. Taranto et al. [24] claimed that higher initial reaction rate of n-octane over P25 and PC105 compared to PC500, despite their lower surface areas, could arise from their preparation methods at high temperatures which led to lower structural defects. Besides crystallinity, several authors have stressed the critical role of crystal size in PCO reactions in the gas phase. It has been proposed that small particle size of UV100 (~10 nm) results in a better balance between surface and bulk recombination [25, 26]. Alonso-Tellez et al. [25] argued that this feature of UV100 is the key reason for its superior performance in comparison to P25 in photocatalytic oxidation of MEK. Furthermore, it was observed that nano-sized photocatalysts, P25 and PC105, exhibit higher performance in degradation of acetone, acetaldehyde, and toluene with respect to the micro-sized ones, Kronos 1077 and Cristal AT-1 [27].

2.2.2. Effect of catalyst surface area, porosity, and surface chemistry

The photocatalytic activity can be greatly influenced by the structural features such as surface area and porosity. Keeping the surface chemistry unchanged, as the surface area is increased, greater numbers of active sites and e^--h^+ pairs, and higher concentration of pollutants on the photocatalyst can be envisaged. In view of this, larger surface area can enhance the photocatalytic activity and mineralization of challenge compounds to CO_2 [25]. Hajaghazadeh et al. [20] reported that MEK conversion follows the order of PC500 > P25 > PC50 under steady state condition. It was suggested that PC50 and P25 activities drop over time because of their low surface areas while for PC500 the positive impact of high surface area outweighs the adverse effect of fast e^--h^+ recombination in the long-term. Similar trends have been observed by Taranto et al. [24] in PCO of methanol where initially P25 and PC105 outperform PC500 owing to their lower charge carriers decay; however after 45 minutes, PC500 performs better in terms of conversion and mineralization since high surface area of PC500 allows higher adsorption of methanol and formaldehyde (methanol PCO intermediate). Alonso-Tellez et al. [25] pointed out

that, apart from its higher surface area, one of the major reasons for superior photocatalytic activity of UV100 compared with P25 is its microporosity. Suligoj et al. [28] attributed the fast PCO reaction of formaldehyde over PC500 to the presence of mesopores (2.1 nm) which enable the access of small molecules like formaldehyde and improve the adsorption. It should be noted that besides surface area and porosity, surface chemistry can also play a critical role in gas phase PCO reactions [29, 30]. Verbruggen et al. [30] estimated that the effective surface area available for acetaldehyde adsorption on PC500 is 3.5 times higher than P25, while, interestingly, PC500 surface area is about six times than that of P25. They justified that the adsorbed amount of acetaldehyde agrees well with the total number of OH groups (obtained from TGA) on PC500 surface, which is nearly four times of that on P25. d'Hennezel et al. [31] found that water-impregnation and HCl-impregnation of P25 can improve the PCO of benzene and toluene owing to the higher amount of hydroxyl groups on TiO_2/H_2O and the chlorine radical chain transfer mechanism over TiO_2/HCl. In another study, in order to determine the presence of Lewis or Bronsted acid centres on P25, PC100, and UV100, Arana et al. [29] investigated the interaction of ammonia with the catalysts surface. The FTIR spectra of NH_3 interaction with these photocatalysts revealed the presence of both acid centres, Lewis and Bronsted, with the following intensity: P25>UV100>PC100.

2.2.3. Effect of photocatalyst adsorption properties

Adsorption of pollutant onto the surface of photocatalyst is a crucial step that greatly affects the reaction rate and removal efficiency. Adsorption of challenge compounds on photocatalyst brings about better contact between photocatalyst and reactant molecules, which in turn leads to higher oxidation rate. The role of adsorption step is more critical when dealing with gas streams with high humidity level (typical condition in the mechanical ventilation system of buildings) due to the competition between VOC and water molecules for adsorption sites. Depending on the type of active site available on the surface of photocatalyst and target VOC, different adsorption mechanisms may exist. Nimlos et al. [32] suggested that alcohols and organic acids can be adsorbed over the surface of TiO_2 via both dissociative adsorption at oxygen bridging sites and hydrogen bond to the OH groups while aldehydes can only be adsorbed via hydrogen bond to the surface OH groups. Based the obtained adsorption efficiencies for several linear and branched alkanes (pentane < hexane < i-pentane < i-hexane < heptane), Boulamanti and Philippopoulos [33] stated that branched molecules are more strongly adsorbed on P25. Given the similarities in

molecular structure, it was suggested that toluene, m-xylene, and p-xylene can be adsorbed on P25 via the OH…π electron-type interaction, and accordingly, adsorption competition among them is expected [34]. In a detailed study on PCO of aromatics [35], it was shown that the adsorption constants follow the sequence: ethylbenzene < benzene < o-xylene < p-xylene ~ m-xylene ~ toluene. The authors highlighted that the low adsorption of ethylbenzene and o-xylene could result from their molecular structures, which induce bigger stereochemical hindrance during adsorption on P25. Qijin et al. [36] examined the adsorption of methanol−benzene binary mixture over P25 in a fluidized bed reactor and argued that due to the presence of electron-donor functional group, hydroxy group, in methanol the adsorption affinity of methanol is stronger than that of benzene (resulting from van der Waals forces). Similarly, Alberici and Jardim [37] reported that the adsorption of VOCs on P25 follows the order: methanol > isopropanol > MEK > acetone > toluene > i-Octane, indicating higher adsorption of alcohols than aromatics over TiO_2. Based on the FTIR spectra of P25 and PC500 in contact with acetaldehyde, Verbruggen et al. [30] concluded that on P25 acetaldehyde adsorbs via H-bridge with a surface hydroxyl group ($CH_3CH{=}O\ldots HO{-}Ti$) and carbonyl bonding with a cation Ti^{4+} surface group ($CH_3CH{=}O\ldots Ti^{4+}$); while on PC500, acetaldehyde mainly binds with the surface hydroxyl groups. In a study on the competitive interaction between water and different VOCs, Yu et al. [38] noted a positive linear relationship between the reciprocal of Langmuir adsorption constant and the Henry's Law constant of aromatic compounds. Geng et al. [39] and Zhang et al. [40] noticed a significant decrease in cyclohexane and chlorobenzene adsorption with increasing the RH. They stated that hydrophobic nature of cyclohexane and chlorobenzene molecules hinder their adsorption onto the water layer as well as their penetration through the water film and contacting the TiO_2 surface. In another study [36], it was observed that unlike benzene (a hydrophobic molecule), methanol (a hydrophilic molecule) adsorption efficiency increased with increasing RH up to 35%. This behavior was explained by high water solubility of methanol, which allows its molecules to penetrate through layers of water and adsorb on the photocatalyst surface. In contrast, formaldehyde adsorption isotherms at low concentration ([HCHO]~120 ppbv) revealed that despite the fact that formaldehyde is a hydrophilic compound, at higher humidity level, P25 reaches its complete saturation faster (i.e. 0% HCHO adsorption efficiency): 200, 90 and 50 min for 0, 10, and 65% RH, respectively [41].

2.3. Hierarchical photocatalysts (HPCs)

Hierarchy is an ordering of individual elements relative to each other, often accompanied with a certain degree of branching (Figure 2.6). In order for a material to be called hierarchical, it has to have two basic criteria: (i) different length scales for the structural elements, and (ii) each structural element has to have a very specific but complementary function [42].

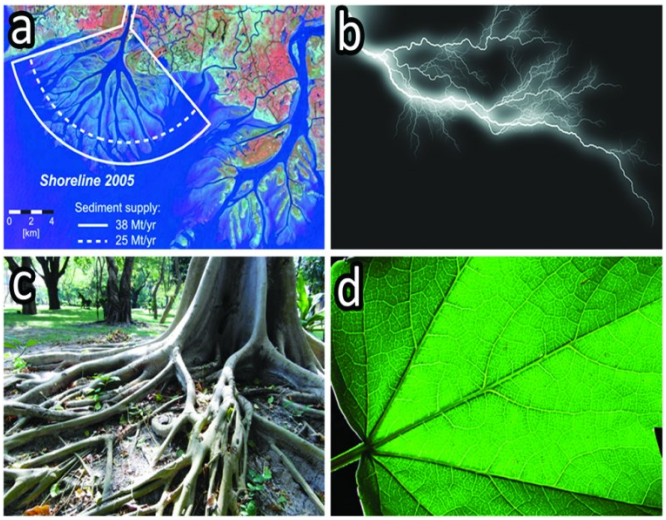

Figure 2.6 Examples for natural hierarchical systems: (a) river delta, (b) lightning, (c) roots of a tree, and (d) leaf [43]

For porous materials, the term hierarchy is mostly referred to materials which possess different pore types or, in other words, bi or multimodal pore size distributions. Depending on how these pores are connected to each other, two categories of hierarchically porous materials can be introduced (Figure 2.7):

Class 1: Larger/wider pores subdivide into several parts of smaller/narrower pores.

Class 2: Larger pores intersect the smaller pore system, i.e. small pores branch off from a continuous large pore.

As a result, any porous material with different pore sizes cannot be named hierarchical. The system of pores should provide the possibility to divide the flow into smaller parts [43]. In 1998, Yang et al. [44] reported the synthesis of porous silica, niobia, and titania with 3-D structures patterned over multiple length scales by combining micromolding, polystyrene sphere templating, and cooperative assembly of inorganic sol-gel species with amphiphilic triblock copolymers. Since then, HPCs came to be known as viable candidates for enhancing the performance of photocatalytic reactions and many researchers focused on fabrication of

inorganic semiconductors with hierarchical architecture via the oriented assembly of various building blocks [45-47].

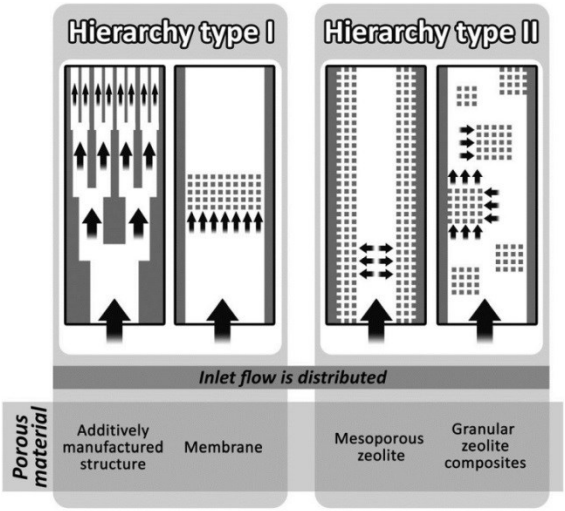

Figure 2.7 Schematic representation of the proposed classification for hierarchical pore systems [43]

2.3.1. Advantages of HPCs for environmental remediation

HPCs benefit from a number of advantages including: accessible and intertwined networks of pores, high specific surface area, improved light harvesting, and better adsorption performance for capturing pollutants from air stream. In addition, micro- and mesopores provide the size and shape selectivity for the guest molecules, enhancing the host–guest interactions, while macropores can considerably help the diffusion and access to the active sites by reactants [42].

2.3.1.1. Molecular diffusion and transport

Based on size, pores can be classified into: micropores (< 2 nm in diameter), mesopores (2-50 nm) and macropores (> 50 nm). Hierarchical morphology and interconnected pores provide more efficient pathways for the transport of molecules to active sites of the photocatalyst and facilitate mass transfer via diffusion. It is widely accepted that diffusion of organic molecules into micro pores is not efficient [48]. On the contrary, catalysts with ordered mesoporosity have the ability to boost reactants molecules diffusion into the catalysts and the removal of products. However, mesoporous catalysts suffer from small surface area and slow mass transfer, which are of great importance in heterogeneous catalysis. Hierarchical structures with pores of different sizes possess high accessible surface area and interconnected channels at different length scales, which significantly resolve the aforementioned issues.

2.3.1.2. Light harvesting

Light harvesting ability of a catalyst can greatly influence its photocatalytic performance. In this regard, hierarchical macroporous/mesoporous structures showed superior light absorption ability. This improvement originates from the larger number of light traveling paths in hierarchical catalysts, which increases the number of light reflection within the pore channels and interiors of cavities. Yu et al. [49] and Li et al. [50] suggested that the enhanced photoactivity on porous TiO_2 and WO_3 stems from better utilization of light due to multiple reflections in hollow structures.

2.3.1.3. Surface area

One of the most influential factors in heterogeneous catalysis is the specific surface area of the catalyst. Accordingly, fabrication of photocatalysts with high surface area for efficient diffusion and adsorption of pollutants and subsequent PCO reactions is highly favorable. Hierarchical macro/mesopores nanostructures have large accessible surface area and high surface to volume ratio, which provide abundant active sites for photocatalytic reactions. On the other hand, nanoparticles tend to agglomerate which not only decreases the surface area, but also adversely affect the reactants diffusion to the pores. These issues can be partly evaded by application of hierarchical photocatalysts formed by self-assembly of nano sized building blocks.

2.3.2. Strategies for fabrication of HPCs

Numerous studies have been dedicated to developing synthesis methods of hierarchical semiconductors such as titanium dioxide. The most common approach to prepare 3-D hierarchical structures is the self-assembly of smaller compartments or building blocks such as nanoparticles, nanowires and nanosheets. Despite its advantages, this approach is demanding, expensive, complicated and hard to scale-up. Consequently, there is an enormous need for new synthesis techniques, which not only are simple and low-cost but also produce hierarchical photocatalysts with controlled morphologies. Figure 2.8 depicts the main synthesis techniques utilized for preparation of hierarchical semiconductors. Even though hard templating and sacrificial-template dissolution techniques are well established and used by many researchers, it has a number of drawbacks: (i) need of templates which are often expensive, (ii) time-consuming procedure, (iii) unwanted structural variations during template removal, and (iv) high amount of

impurities in the final product [51]. The second group, template-free methods, are much cheaper, simpler, and more environmentally-friendly compared to templating strategies.

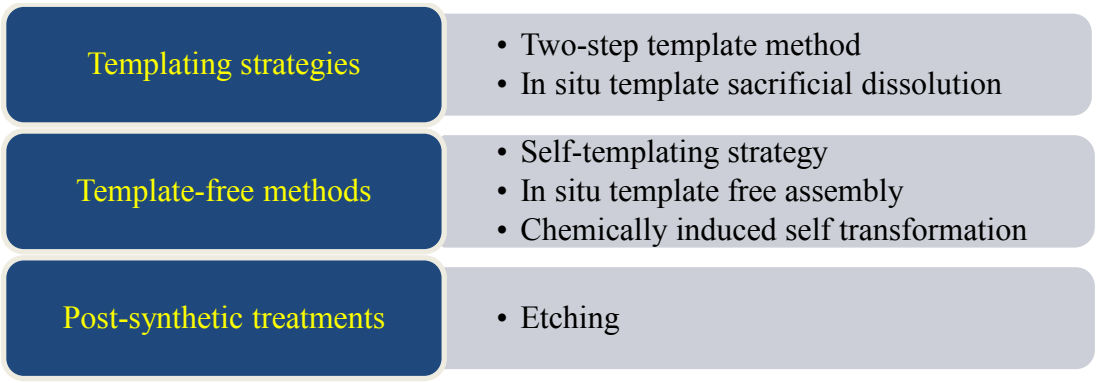

Figure 2.8 Synthetic methods of hierarchical catalysts [14]

2.3.2.1. Self-templating strategy

Many research groups have attempted to come up with simple, environmentally-friendly, and low-cost routes for preparation of hierarchical micro/nano structures without using templates [52, 53]. Among these methods, self-templating strategy is very promising and has been employed extensively for fabrication of hierarchical catalysts. For instance, Xiang et al. [54] could successfully prepare hierarchical CdS via hydrothermal treatment of $Cd(OH)_2$ precipitates following by an anion ion-exchange with solution containing Na_2S which replaces OH by S. In other studies BiO_X nanostructures were used as self-template to reach $BiWO_6$ hollow spheres, Bi_2S_3 nanocrystals/BiOCl, and Ag/AgBr/BiOBr hybrids [55, 56]. Troung et al. [57] synthesized TiO_2 hollow nanostructures based on Ostwald ripening mechanism. In the preparation of TiO_2 hollow structure, H_2O_2 served as coordination agent and interface stabilizer and was crucial to the self-assembly of microspheres and their transformation into hollow nanostructures.

2.3.2.2. In situ template-free assembly

It has been proposed that hierarchically macro/mesoporous TiO_2 can be synthesized by self-assembly of amorphous TiO_2 particles in alkoxide–water mixed solution [58]. In order to achieve the desired crystallinity, samples were subjected to calcination at 300-800 °C. It is noteworthy that calcination at temperatures higher than 500 °C destroyed the hierarchically macro/mesoporous structures [58]. In another study, Shi et al. [59] synthesized sea-urchin shaped Bi_2S_3/CdS hierarchical photocatalysts using a one-pot growth rate controlled route. They

suggested a growth mechanism initiates with fast formation of Bi_2S_3 nanoflowers, which act as support for the growth of CdS nanoparticles. Rutile TiO_2 photocatalyst was prepared under microwave-hydrothermal condition which promotes the self-assembly of 1-D nanowires resulting in a three dimensional hierarchical structure [60]. Jiao et al. [61] synthesized dendritic Fe_2O_3 hierarchical structures via hydrothermal route. This photocatalyst exhibited good performance in degradation of Congo red in liquid phase, which was attributed to its superior light harvesting and accessibility of active sites.

2.3.2.3. Chemically induced self-transformation

In order to obtain hierarchically hollow microspheres, several works have used chemically induced self-transformation method. Different from situ template-free assembly, in this method hierarchical nanostructures are produced through chemical etching of primary particles by etching agents such as HF and OH^-. In this regard, Yu et al. [62] could synthesize SnO_2 hollow microspheres by hydrolysis of SnF_2 at 180 °C. The authors postulated that the SnO_2 particles are transformed into hollow microspheres via F^- mediated self-transformation process. Similarly, hollow TiO_2 microspheres composed of anatase nanocrystals could be synthesized by using a modified F^- mediated self-transformation strategy [63].

2.3.3. Application of HPCs in air purification

Among various applications of HPCs, in this research, the focus will be on their potential for air purification. Despite the aforementioned advantages of hierarchical materials for gas phase heterogeneous catalysis and photocatalysis, there are a handful of works which explored the potentials of hierarchical photocatalysts for indoor air purification. In this regard, several studies have been devoted to fabrication and performance evaluation of TiO_2 HPCs for photocatalytic degradation of prevalent VOCs (such as toluene, acetone, and formaldehyde) and NO_x in air [64-66]. Zhang and Yu used sonochemical synthesis method to fabricate hierarchically porous titania spheres which demonstrated good activity toward degradation of n-pentane in air [64]. In another study, a trimodally hierarchically macro-/mesoporous TiO_2 was prepared by hydrothermal method and its photocatalytic activity towards acetone was around three times higher than that of P25 [65]. In another study, Xiang and Yu [66] used a two-step hydrothermal synthesis to fabricate hierarchical flower-like TiO_2 with dominant [001] facets. Three main pore sizes could be identified in the TiO_2 samples: fine mesopores (peak pore of 10 nm), large mesopores (peak

pore of 40 nm), and flower-like microspheres with a macroporous framework (100-500 nm). Even though P25 possesses larger surface area with respect to the prepared TiO_2 (55.1 vs. 38.9 m^2/g), the hierarchical flower-like TiO_2 shows higher acetone removal efficiency after 60 minutes of reaction (25.9% vs. 16.4%). As mentioned earlier, templating strategy is one of the most common methods for preparation of hierarchical nanostructured materials. For instance, self-assembly of surfactant under hydrothermal conditions was used to direct the formation of inorganic phases for synthesizing macro/mesoporous metal oxides. Wang et al. [67] used a nonionic poly(alkylene oxide)-based surfactant as the structural-directing agent for preparing hierarchically macro/mesoporous titania. A short calcination step (at 350-800 °C) was considered after the hydrothermal treatment at 80 °C in order to remove the surfactant and improve the crystallization. Chen et al. [68] used ZrO_2 and SiO_2 as structural stabilizers to fabricate macro/mesoporous TiO_2/SiO_2 and TiO_2/ZrO_2 nanocomposites. Introduction of ZrO_2/SiO_2 into TiO_2 not only brought about superior thermo–mechanical strength, but also improved surface acidity due to the presence of surface hydroxyl groups, which capture h^+, thereafter initiating the generation of strong active species capable of oxidizing adsorbed organics.

2.4. Hydrothermal method

Hydrothermal synthesis is defined as any heterogeneous chemical reaction in the presence of a solvent (aqueous or non-aqueous) above ambient temperature and pressure in a closed system. These operating conditions facilitate the dissolution and recrystallization of materials that are relatively insoluble under ambient conditions. The precursors go into solution as complexes with the help of mineralizers or solvents. Solvent can exert great influence on the properties of final product. Water is regarded as the most prevalent solvent and it is extensively employed as a hydrothermal mineralizer. Water is environmentally-safe, cheap and can act as a mineralizer/catalyst under high pressure and temperature. However, there are materials which have low solubility in water and necessitate applying other solvents. One of the key advantages of hydrothermal route is that crystallinity, crystal size, and textural properties can be controlled via proper selection of concentration of precursor and solvent/mineralizer, pH, hydrothermal time, pH, hydrothermal temperature, etc. [69]. A variety of metals oxides have been prepared through hydrothermal method which are most importantly characterized by high surface area in comparison to their counterparts by other methods such as sol-gel followed by calcination. The term solvothermal is used when water or other solvents (e.g. organic solvents) are used, while

hydrothermal refers specifically to those processes conducted in water as reaction medium. The following advantages can be attributed to hydrothermal method: 1) mild temperature: for the same degree of crystallinity, much lower temperature is needed in hydrothermal process compared to temperature during post-treatment (i.e. calcination) of photocatalysts prepared via sol-gel; 2) high purity of products and reproducibility; 3) environmentally-friendly and green; 4) high anatase content; 5) simultaneous achievement of high crystallinity and large surface area.

2.4.1. Effect of precursor

Titanium dioxide photocatalysts can be prepared from various titanium sources such as inorganic (e.g., $TiCl_4$) and organometallic (e.g., titanium alkoxide) precursors. The most employed titanium precursors for fabrication of titania photocatalysts are tetrabutyl titanate $Ti(OBu)_4$ or TBOT and titanium isopropoxide $Ti(OPr)_4$ or TTIP. Many researchers used anatase or rutile powders (such as P25) as titanium source in the hydrothermal preparation of photocatalysts. For the hydrothermal synthesis, usage of the amorphous TiO_2 resulting from sol-gel process is very common. Consequently, the preparation and properties of the amorphous TiO_2 can be very important and influential on the final product. In this regard, Yanagisawa and Ovenstone [70] investigated the impact of using different titanium precursors ($TiCl_4$ and $Ti(OC_2H_5)_4$) during the sol-gel step on the crystallinity of titania after hydrothermal treatment. They showed that when $TiCl_4$ was used as precursor due to the chloride contamination nucleation occurs earlier. Kolen'ko et al. [71] chose $TiOSO_4$ and $TiCl_4$ as titanium precursors for hydrothermal synthesis. In the case of $TiCl_4$ regardless of the hydrothermal time (10 min or 6 h), according to the XRD results only anatase phase exists in the nanocrystals while for $TiOSO_4$ co-presence of anatase and rutile was observed after 6 h hydrothermal treatment at 523 K.

2.4.2. Effect of temperature

Increasing the temperature in the autoclave during hydrothermal synthesis brings about a number of well-known outcomes: (i) crystal growth, (ii) higher degree of crystallinity, and (iii) decrement in surface area. Kim et al. [72] investigated the influence of reaction temperature (100, 150, 200 °C) on key properties of TiO_2 after 48 h hydrothermal treatment. They found that in the absence of nitric acid, at all hydrothermal temperatures, only titanate can be reached while by increasing the concentration of acid in the reaction vessel first anatase appears and by further increase in acidity rutile phase could be produced as well. In another study [73], it was witnessed

that with decreasing the temperature, grains become smaller and the agglomeration among them becomes more vivid. Yanagisawa and Ovenstone [70] observed that raising the temperature up to 250 ˚C has no significant impact on the crystal size while further increment in temperature to 400 ˚C resulted in remarkable crystal growth. This was attributed to a change in the crystal growth mechanisms from solid-state epitaxy to dissolution/precipitation.

2.4.3. Effect of holding time

Prolonging the hydrothermal reactions leads to an increase in crystallinity and crystal size of TiO_2 nanoparticles and naturally decline in surface area. In this regard, Yu et al. [65] studied the effect of hydrothermal duration on the properties of titanium dioxide photocatalysts prepared at 180 ˚C. At t=0, the samples is completely amorphous (i.e. no photocatalytic activity); however, as the reaction time is increased, anatase phase content gradually goes up and after only 3h of treatment brookite (15%) is also observed in the crystalline structure. It should be highlighted that after the initial sharp decline in surface area with hydrothermal time, after 10h treatment, the surface area shows no significant drop. In another work, in order to obtain mesoporous TiO_2 nanofibers, titanate nanotubes were treated hydrothermally at 200 ˚C and varying hydrothermal durations (1-24 h) [74]. XRD results showed that after only 1 h hydrothermal treatment, transformation of titanate nanotubes to anatase phase has initiated. The authors suggested that anatase phase is formed due to the dehydration among titanate layers and the rearrangement of TiO_6 octahedron cells. After 3h, no titanate diffraction peaks was observed which confirms the total destruction of nanotubes and formation of anatase crystals. Also, with increasing the hydrothermal time, the length of titania and their diameter nanofibers declined, indicating the gradual trend toward formation of TiO_2 nanoparticles. Zhou et al. [75] prepared titania microspheres by hydrothermal treatment of a solution containing titanium sulfate and urea for different reaction times. Even though longer reaction time led to larger crystal sizes, the average diameter of the microspheres did not show any considerable change. They attributed the material mesoporosity to inter-aggregated mesopores formed from accumulation of primary particles.

2.4.4. Effect of reaction media

Reaction media properties such as viscosity and dielectric constant can strongly influence the mobility, reactivity and solubility of species in solution. Therefore, the composition of the solution media affects the produced titania characteristics. Yanagisawa and Ovenstone [70]

postulated that water has an important role in the formation of anatase crystals from amorphous sols. They suggested that water facilitates the rearrangement of TiO_6 octahedra and coordinates the amorphous titania surface. A combination of water and an alcohol can be employed as the reaction medium to adjust the crystal size and degree of crystallinity by varying the ratio between water and alcohol. In this regard, Wang and Tang [76] reported that as the alcohol/water ratio is increased, the particle size decreases while the surface area and porosity of the final product increase. In another study, Lei and Duan [77] attempted to control the phase composition of titania by changing the water to ethanol ratio during solvothermal synthesis at very low temperature (353 K). They could successfully tune the anatase content from 0 to 100% by increasing the amount of ethanol in the mixture. Besides the reaction medium, adding mineralizers can affect the resulting titania phase. Cheng et al. [73] used four mineralizers (NH_4Cl, NH_4F, NaCl, and $SnCl_4$) and investigated their impact on crystalline phase during hydrothermal synthesis. Applying mineralizers was in favor of the formation of rutile; therefore, only rutile was achieved in the presence of any of four mineralizers.

2.4.5. Effect of pH

pH can play a significant role in the preparation process since it affects the rate of hydrolysis and condensation reactions. Accordingly, one efficient and facile way to control the properties of titania photocatalyst is changing the pH. In this regard, Chen et al. [78] synthesized a three-phase (i.e. anatase, rutile, and brookite) titania at low hydrothermal temperature in the presence of nitric acid. Similar behavior was noticed by other researchers [72, 79] in hydrothermal preparation of titania with HNO_3 as peptizing agent. Mesoporous TiO_2-graphene nano-composites were prepared by UV-assisted hydrothermal hydrolysis of $Ti(SO_4)_2$ in aqueous solution of sulfuric acid and graphene oxide [80]. Akple et al. [81] could achieve nitrogen-doped anatase titania microsheets with 65% [001] facet and 35% of [101] facet by using hydrothermal synthesis method in the presence of HF and HCl. Cheng et al. [73] attempted to explain the impact of acidity on crystal structure of titanium by synthesizing titania from $TiCl_4$ precursor at a wide pH range (0-14). They postulated that the type of titanium (IV) complexes is dependent on the acidity and ligand in solution. Based on this, they suggested that at high pH the probability of edge-shared bonding (i.e. anatase) between two Ti complexes is higher, while at low pH due to smaller number of OH ligands in Ti complexes, the corner-shared bonding is easier (i.e. rutile). In another study, Chen et al. [82] hydrothermally prepared titania nanocrystals from 1-D titanate

nanotubes and investigated the impact of using different acids (CH_3COOH, HNO_3, HCl, HF, and H_2SO_4). With HF, H_2SO_4, or CH_3COOH, regardless of the concentration (i.e. pH), only anatase phase was achieved; while with HNO_3 and HCl, depending on the concentration, anatase and rutile contents could be adjusted.

2.4.6. Effect of calcination temperature

One of the well-established techniques to alter photocatalyst crystallinity and structural properties is heat treatment. Heat treatment of catalyst at high temperatures on the one hand improves the crystallinity (i.e. less bulk defects), whereas on the other hand it adversely affects the surface area and porous structure. Amorphous TiO_2 particles can be transformed to anatase at temperature above 400 ˚C. However, such high calcination temperatures result in the increase in nanoparticle size and the decrease in specific surface area. To achieve small nanocrystalline TiO_2 powders with high photocatalytic activity and large specific surface area, a reasonable method would be to lower the temperature of the phase transition and crystallization, so that using methods such as hydrothermal. To alleviate the negative effect of calcination and minimize sintering, Chen et al. [68] used ZrO_2 and SiO_2 as structural stabilizers to prepare hierarchical macro/mesoporous TiO_2/SiO_2 and TiO_2/ZrO_2 nanocomposites. Nguyen and Bai [83] prepared titania nanotubes from P25 in autoclave at 135 ˚C and subsequently calcined the samples at 400-600 ˚C. As the calcination temperature exceeded 300 ˚C, the tubular structure started to transform to rodlike (at 400 ˚C) and particle-like (at 600 ˚C) structures, accompanied by substantial reduction in the surface area.

2.5. Photocatalyst coating technique and support materials

Photocatalyst coating has a significant influence on the performance of the PCO systems. A number of coating techniques have been employed so far including: dip-coating (sometimes called wash-coating), chemical vapor deposition (CVD), metal-organic CVD (MOCVD), sol–gel and spray coating. Dip-coating is the most popular method in the laboratory scale and has been applied for deposition of commercial photocatalysts on different substrate materials (e.g. glass plate, fiber glass, and activated carbon) [84]. In gas phase PCO, lowering the aggregation of photocatalyst nanoparticles and maximizing their exposure to light irradiance and air stream are highly sought in order to improve the quantum efficiency and adsorption capacity. This objective can be accomplished by immobilization of photocatalyst on support material. The ideal support

material should possess several properties including high surface area, high transparency, porous structure, high adsorptive affinity towards VOCs, and stability under UV irradiation. In addition, the supporting material should sufficiently bond either via physically or chemically to TiO_2 without reducing its reactivity. In this regard, due to the unique and controllable structural as well as electrical properties, porous carbonaceous materials such as activated carbon, carbon nanotubes and fullerene become great interest for the structural support and photocatalytic enhancement of TiO_2-based systems [85-87]. However, some problems still hinder further promotion of efficiency of the present TiO_2 composites, such as the weakening of light intensity arriving at catalysts' surface and the lack of reproducibility due to the preparation and treatment variation [88].

2.6. Influence of operating parameters on photocatalytic oxidation processes

2.6.1. Airflow rate and residence time

Mass transfer of pollutants from the gas phase to the surface of photocatalyst entails several processes and is a function of airflow conditions (humidity, temperature, speed, etc.), type of pollutant, and properties of photocatalyst [3]. Considering a fixed photocatalyst loading, there is general agreement that airflow rate has a dual antagonistic effect on photocatalytic reactions: (i) as the airflow rate increases, the residence time of VOC molecules inside the reactor decreases which leads to a reduction in the adsorption of the pollutant and lower conversion; (ii) higher airflow rate enhances the mass transfer coefficient between the air and photocatalyst surface, resulting in higher PCO reaction rate [89, 90]. Taking into consideration the airflow rates normally applied in air handling units, it seems reasonable to rule out the contribution of enhanced mass transfer rate and conclude that any increment in the airflow rate (i.e. shorter residence time) deteriorates the VOC removal efficiency. Several studies have pointed out that apart from the heterogeneous reactions, gas phase reactions can also contribute to the removal of VOCs [91-93], especially when ozone-generating lamps are utilized. Therefore, increasing the airflow rate reduces the contact time between the VOC molecules and reactive species and lowers the removal efficiency.

2.6.2. Type and concentration of pollutant

One of the major shortcomings of the previous studies conducted on photocatalytic degradation of VOCs is the evaluation of performance at high VOC concentrations (ppm range) rather those

associated with the indoor environment (ppb range). Nevertheless, for various classes of VOCs and broad ranges of concentration, there is general agreement that higher concentration of VOC results in an improved reaction kinetics (until rate reaches its plateau), lower removal efficiency, and poorer mineralization of pollutants to CO_2 [94-98]. The impact of higher VOC concentration on PCO reactions can be analyzed from different aspects: (i) the number of VOC molecules that can be adsorbed and oxidized on photocatalyst surface increases which boosts the reaction kinetics [99]; (ii) the ratio of reactive species plus active sites to pollutant molecules decreases and consequently, more VOCs can leave the reactor without undergoing degradation [98]; (iii) high amount of by-products/intermediates generated during PCO reactions can reduce the mineralization and/or occupy part of the active sites, impeding the oxidation progress.

2.6.3. Relative humidity

Water molecules can connect to different types of OH surface groups on TiO_2 via hydrogen bond. In addition, water molecules can attach to each other by hydrogen bond and generate well-organized network of adsorbed water layers. The attraction forces between the reactants and TiO_2 are adversely affected by the water layer and in order to be adsorbed on the surface, pollutants must break or disorganize the water network [100]. Still no general relationship can be put forward between the VOC removal efficiency, mineralization degree, or reaction rate with the humidity level. Several groups [90, 101-104] recognized a promoting effect of humidity whereas others found the presence of water vapor in PCO inhibiting [33, 90, 105-109]. On the other hand, some studies have demonstrated that depending on the experimental conditions (e.g. VOC type and concentration, RH range, catalyst loading, and catalyst/support adsorption capacity), a dual effect, positive and negative, of RH can be realized [34, 91, 99, 106, 110, 111]. In general, water vapor can have two sets of conflicting functions:

I: (a) adsorbed water molecule is oxidized to hydroxyl radicals which improves the PCO reactions; (b) RH maintains the oxidation rate by replenishing surface hydroxyl groups [91, 112]; and (c) surface hydroxyl groups can trap holes and hinder e^--h^+ recombination.

II: (a) water molecules adsorbed on the surface of TiO_2 via hydrogen bonding with hydroxyl groups form a multi-layer film which impedes pollutants from contacting TiO_2 surface or reactive species in the boundary layer [113]; and (b) water molecules compete with VOCs for adsorption on active sites of TiO_2 [91].

2.6.4. Light source and intensity

Light is one of the main pillars of photocatalysis; therefore, light source wavelength and light intensity can affect the reaction rate and removal efficiency. Considering the band gap energy of titania, theoretically, UV light with wavelength less than 380 nm can excite the electrons in the valence band [13, 112]. Germicidal lamp (UVC, 254 nm) and fluorescent black-light lamp (300-400 nm) are the most utilized light sources in PCO of indoor air pollutants. Some studies employed UV light emitting diode (wavelength usually centered at 365 nm) due to long lifetime and high efficiency [20, 114]. For the same photon energy distribution, i.e. light wavelength, increasing the light intensity leads to generation of a larger number of photons and consequently e^--h^+ pairs. It is proposed that the impact of UV intensity on the reaction rate can be divided into two regimes: i) a first-order regime at low light intensity and high VOC concentration where e^--h^+ pairs are consumed faster by chemical reactions than by recombination and ii) a half-order regime at high light intensity and low VOC concentration in which the rate of recombination exceeds the rate of oxidation reactions [115].

In order to improve the removal efficiency and mineralization, many studies [41, 116, 117] employed ozone-generating UV lights (254+185 nm), which may offer a combination of photolysis, ozonation, and PCO processes. Nonetheless, it is noteworthy that using ozone-generating lights can result in high concentrations of ozone at the outlet stream, which necessitates installation of ozone scrubber after PCO section. On the other hand, even though direct ozonation of VOCs in the gas phase has been reported in the literature [118], considering the slow rate of ozonation reactions and short residence time of VOCs in the reactor (<<1s), some researchers believe that ozonation may not have significant contribution [41, 116, 117].

2.7. Reaction pathways and main intermediates/by-products

Ideally, products of PCO of hydrocarbon VOCs are carbon dioxide and water. However, given the short residence time of reactants and adsorption competition, in reality, VOC mineralization can proceed up to a certain degree and many oxidation by-products/intermediates exist both in the gas phase and on photocatalyst. In fact, generation of by-products is one of the main concerns associated with the application of PCO technology in buildings since some of these by-products can be even more toxic than their parent compounds. Based on the type of challenge compound,

different reaction pathways have been proposed and various by-products/intermediates have been identified in photocatalytic degradation of VOCs.

2.7.1. Alcohols

Muggli et al. [119] employed isotope labeling and temperature-programmed desorption and oxidation (TPD-TPO) to identify the reaction pathways and intermediates for PCO of ethanol over P25. Based on the obtained results they suggested two reaction pathways: a) ethanol → acetaldehyde (widely accepted as the first step in PCO of ethanol) → acetic acid → CO_2 + formaldehyde → formic acid → CO_2 and b) ethanol → acetaldehyde → formic acid + formaldehyde → formic acid → CO_2. A similar mechanism was put forward by Nimlos et al. [32]: ethanol → acetaldehyde → acetic acid → formaldehyde → formic acid + CO_2 → CO_2. Benoit-Marquie´ et al. [120] proposed the following degradation mechanism during 1-butanol photocatalytic degradation: 1-butanol → butanal → butanoic acid → propionaldehyde and 1-propanol. In agreement with this study, it was found that butanal and 1-butene are the two major by-products of PCO of 1-butanol over P25 at low [121] and very high concentration [122].

2.7.2. Aromatics

Photocatalytic oxidation of toluene and benzene has been examined extensively and, accordingly, many studies have been focused on the identification/quantification of reaction intermediates. It is suggested by many researchers that PCO of benzene and toluene entails the generation of strongly adsorbed intermediates, which are less reactive than their parent compounds [13, 31]. In the case of toluene, benzaldehyde, benzoic acid, benzyl alcohol, phenol and benzene have been found to be the first reaction intermediates [13, 27, 31, 123]. d'Hennezel et al. [31] proposed a step-by-step reaction pathway for PCO of toluene over H_2O/HCL pretreated P25. It was suggested that the primary pathway involves hydrogen abstraction from methyl group and benzyl radical formation via hole transfer to toluene, hydrogen abstraction by an OH radical, and hydrogen abstraction by chlorine radical [31]. Sleiman et al. [107] stated that the humidity content influences the adsorption mode of toluene on PC500 and, therefore, brings about two competitive initial reaction pathways: i) at low RH, h^+-mediated reactions lead to the formation of an aromatic radical cation and a benzyl radical, followed by further oxidation and aromatic ring opening reactions; ii) at high RH, the first step is the addition of OH radical on the aromatic ring or the H-abstraction from the methyl group. Based on the detected by-products in

gas phase and on P25 surface using proton transfer reaction-mass spectrometer (PTR-MS) and gas chromatography–mass spectrometry (GC-MS), Mo et al. [13] put forward a reaction pathway for toluene PCO. They considered OH radical induced aromatic ring opening mechanism, previously suggested by Frankcombe and Smith [124], for toluene and its three initial by-products (benzaldehyde, benzoic acid, and benzyl alcohol) and proposed the following reaction mechanism: toluene → benzaldehyde → benzoic acids → ring broken → O=C–R–C=C–R'–C=O → shorter-carbon-chain aldehydes and alcohols. Using TPD-TPO, Larson and Falcon [123] identified benzaldehyde, benzyl alcohol and m-cresol as intermediates of degradation of toluene.

2.7.3. Aldehydes

Ao et al. [125] proposed a reaction pathway for formaldehyde photocatalytic degradation over P25 which starts with the generation of formic acid via direct photolysis and photocatalysis, followed by h^+-mediated conversion of formic acid into carbon dioxide. Ye et al. [126] examined PCO of butanal and proposed a reaction pathway as follows: aldehydes → acids → shorter carbon-chain aldehydes. In another study, Hauchecorne et al. [127] proposed a relatively complicated reaction pathway for PCO of acetaldehyde over TiO_2 using FTIR in-situ reactor. Acetaldehyde is adsorbed on TiO_2 surface where it undergoes aldol condensation (formation of 3-hydroxybutanal and crotonaldehyde) and oxidation reactions (formation of bidentate acetate bound on the surface). These initially formed species are converted into other intermediates such as acetic acid, formic acid and formaldehyde upon further illumination.

2.7.4. Alkanes, alkene and alkynes

It has been suggested that the photocatalytic degradation of alkanes entails less complexity in comparison to that of alcohols and aromatic hydrocarbons; therefore, the amount of generated intermediates/by-products is smaller for alkanes [38]. Degradation of alkane is initiated by the abstraction of proton to form alkyl radical, which then reacts with oxygen and produces alkyl proxy radical. This alkyl proxy radical can go through reactions with alkane itself or with $HO_2^{\cdot}$ and generate carboxylic acid [38]. In a research focused on the reaction mechanism and intermediates of decane PCO over P25, Debono et al. [128] monitored the formation and consumption of reactants and intermediates at each step of the reaction advancement. They reported that 18 reaction intermediates were identified in the gas phase, mainly from aldehyde, ketone and alcohol families. In another study, Einaga et al. [101] suggested that the addition of

OH radicals to unsaturated C=C bonds of cyclohexene and also the abstraction of H atoms from saturated C–H bonds of cyclohexane and cyclohexene result in a number of intermediate radicals which are subsequently oxidized by molecular O_2 and eventually converted into CO_2.

2.7.5. Ketones

Acetone and MEK are the most studied members of ketone family [129-132]. Vincent et al. [130] put forward three main reaction schemes for PCO of acetone over P25 (two of them chain reactions initiated by $OH^{\bullet}$ and aldol condensation as the third one) based on the identified reaction intermediates and their relative abundance which can be ranked in this order: diacetone alcohol > acetic acid > MEK > methyl alcohol > other by-products. Choi et al. [129] stated that at high concentrations, both hydroxyl radical attack and h^{+}-mediated oxidation pathways are important in PCO of acetone.

Chapter 3

3. Methodology

3.1. Experimental set-up

3.1.1. Adsorption experiments

Figure ***3.1*** depicts the experimental set-up employed to study the adsorption of toluene and MEK on TiO_2 coated nickel (Ni) foam filters at different humidity conditions and challenge compound concentrations. The main component of the system is a 0.1 m × 0.1 m × 1.3 m (width × height × length) single-pass continuous flow reactor made of aluminum. Compressed air (RH=0%) is utilized as the carrier gas and a mass flow controller (OMEGA, FMA5542A) adjusts its flow rate. It should be mentioned that the relative humidity of compressed air is 0% and its temperature is around 20 °C based on the readings of two sensors installed at the reactor inlet. On the other hand, high-performance liquid chromatography (HPLC) and GC-MS analyses confirmed that the compressed air contains no volatile organic compounds. The stainless steel straightener is employed to provide a more uniform distribution of airflow in the entrance. The relative humidity of the air stream to the reactor is controlled by passing a portion of it through a distilled water cylinder (i.e. humidifier). The relative humidity can be varied in a wide range (0-80%) to provide sufficient information regarding the impact of humidity content on adsorption. The airflow rate enters the photoreactor is controlled by a rotameter. The temperature and humidity inside the reactor are monitored using temperature and humidity sensors (DATAQ Instruments, Model EL-USB-2). The challenge compound is automatically injected by a syringe pump (KD Scientific, Model KDS-210) into the airflow and the injection rate is calculated based on the airflow rate, chemical properties, and target concentration. The concentrations of the pollutant before and after the air filter are continuously recorded by PID detector (ppb3000 RAE).

3.1.2. Photocatalytic oxidation experiments

In the previous design, the goal is to determine the adsorption ability of the filter in the absence of light and photocatalytic reactions. For evaluating the photocatalytic performance of titania,

some modifications are made to the previous design and the resulting set-up is shown in Figure 3.2.

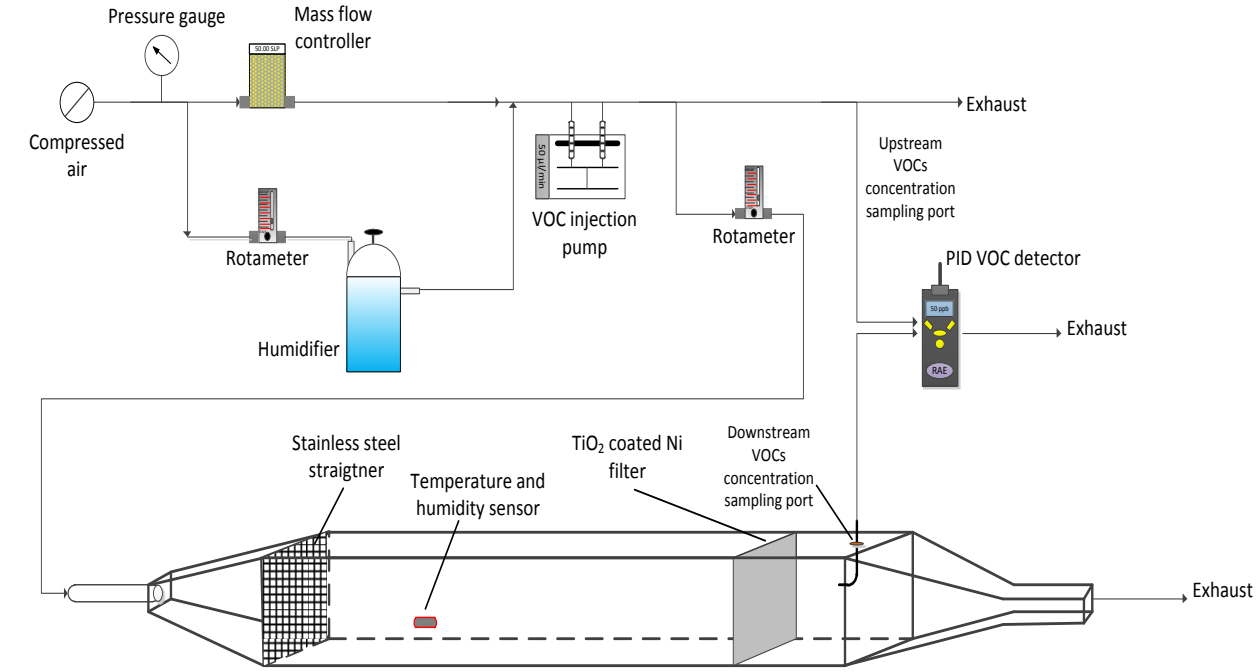

Figure 3.1 Schematic presentation of the experimental set-up for adsorption experiments

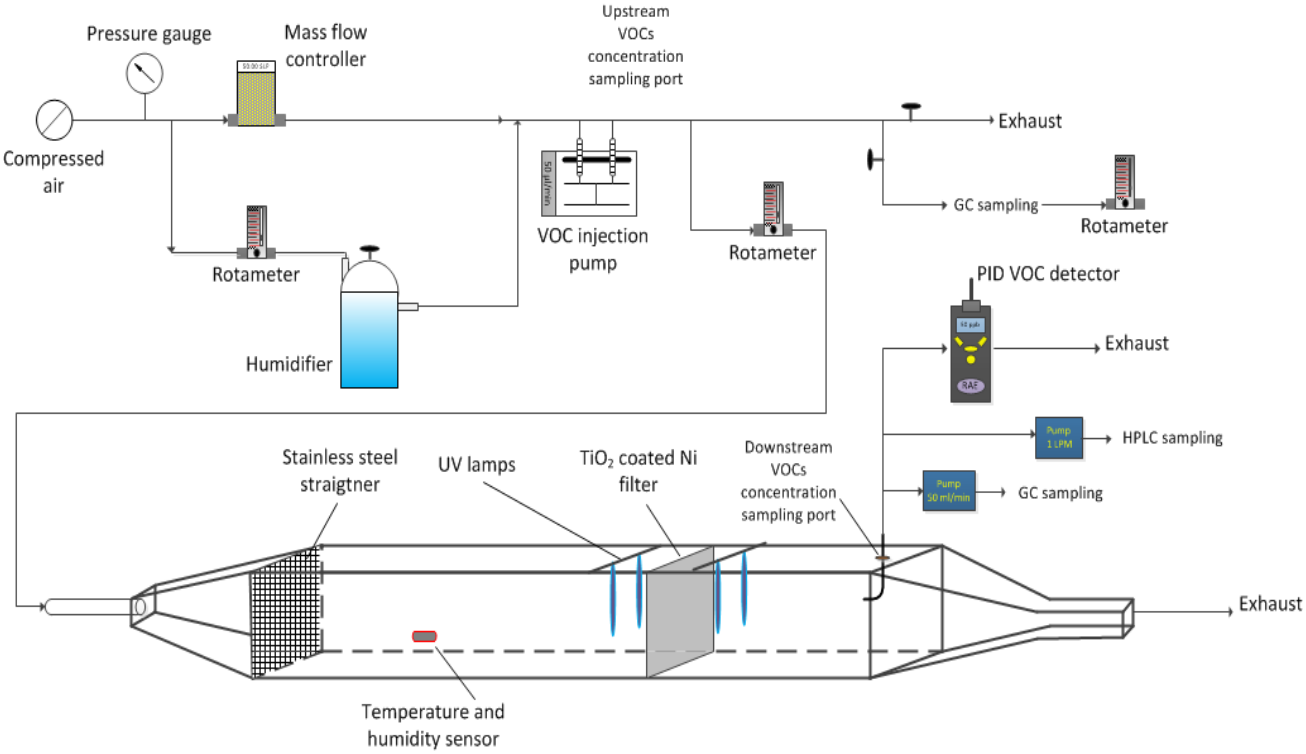

Figure 3.2 Schematic presentation of the experimental set-up for PCO experiments

Inside the photoreactor 4 UV lamps (Philips, TUV PL-S 5W/4P 1CT/5X10CC) are mounted which provide a total light intensity of 5 mW/cm^2. The distance between the UV lamps and the air filter on both sides is ~3 cm. The photoreactor was designed in a way that can contain 3 air filter (i.e. 8 UV lamps) in case it is desired to improve the removal efficiency. Performance indicators (e.g. removal efficiency, by-products generation, etc.) are calculated based on the data acquire from GC-MS and HPLC analyses. To do so, inlet and outlet concentrations of target VOCs as well as by-products generated during PCO reactions are determined using GC-MS and HPLC.

3.2. Experimental procedure

3.2.1. Air sampling and analytical methods

For GC-MS, air samples are taken periodically from both upstream and downstream sampling ports using an air pump (GilAir®) with 50 mL/min flow rate for calculated duration depending on the concentration of pollutants. These samples are collected by passing the air through an AirToxic® tube (SUPELCO) which is connected directly to the air pump. AirToxic® adsorbent tubes are stainless-steel tubes filled with Carbotrap B followed by Carbosieve adsorbent, which are utilized for capturing C3- C12 VOCs as in EPA TO-17 method. Before the sampling, GC tubes are conditioned for 30 minutes at 320 °C using helium (He) flow. The adsorbed VOCs in tubes are desorbed by automatic thermal desorber (Perkin-Elmer TurboMatrix® 650 ATD) and introduced to GC/MS (Perkin-Elmer Clarus® 500) with a capillary column (Perkin-Elmer Elite-VMS, 60m, 0.32 mm I.D., and 1.8 μm of film thickness). Two-stage desorption was applied in thermal desorption: the primary desorption at 240 °C for 4 minutes at 0.33 mL/s (1.22 in^3/min) of He flow; and the secondary desorption at 300 °C. Through inlet and outlet splits, 1% of analytes was introduced into GC column with 0.017 mL/s (0.062 in^3/min) of He flow. GC temperature program is at 40 °C hold for 5 min; 5 °C/min increase to 110 °C; 20 °C/min increase to 200 °C and hold for 15 min. EI-mode MS scanned from 40 to 150 m/z with a scanning time of 0.25 min.

For the HPLC analysis, the generated by-products and/or pollutants are absorbed on a high purity silica adsorbent coated with 2, 4-dinitrophenylhydrazine (2, 4-DNPH) (SUPLECO LpDNPH S10L, Sigma Aldrich). LpDNPH cartridges are capable of adsorbing and detecting carbonyls (e.g. aldehydes and ketones). It is noteworthy to mention that the sampling and analysis of by-

products are done in accordance with the US EPA TO-11a. The flow rate of the sampling pump for HPLC cartridge is 1 L/min and depending on the experiment the sampling duration varies. Once the sampling is finished, the absorbed compounds are extracted from the HPLC cartridge via washing pure acetonitrile. Afterwards, elutes are analyzed by the HPLC with ultraviolet detection (360 nm wavelength) (PerkinElmer Flexar) with a C18 Brownlee validated micro-bore column (150 mm x 4.6 mm ID, 5 μm film thickness). The injection volume is 20 μL. The mobile phases are 72% acetonitrile and 28% of deionized water with the total flow rate of 0.017 mL/s.

3.2.2. Photocatalytic experiment protocol

A step-by-step procedure is applied for the PCO tests in order to: (1) minimize the interference of adsorption capacity with actual performance of the photocatalyst and (2) provide enough time for the system to reach steady state condition in terms of irradiance, concentration, humidity, and temperature. The following stages are followed in all experiments determining PCO performance of either commercial titania samples or developed TiO_2 materials:

1) Installing the titania coated air filter inside the photoreactor in the absence of light or airflow.
2) Start recording the relative humidity and temperature data at the upstream (using RH&T sensors before air filter) and the target VOC concentration using PID at the downstream; [t=0]
3) Introduce the air stream with the desired humidity and flow rate into the reactor while simultaneously start pollutant injection with a calculated rate using syringe pump. For one hour 10 ppm of toluene or 20 ppm of MEK is considered as the inlet concentration with the goal to completely saturate titania before starting the PCO test. These concentrations were obtained from the adsorption tests and assure complete saturation of the filter with pollutant. Accordingly, after one hour the reading from PID can also guarantee reaching the 100% breakthrough of the filter; [t=1h]
4) After one hour adsorption in dark (stage 3), lamps are tuned on and we allow the system to run for 4 more hours to become stable; [t=5h]
5) GC and HPLC sampling for toluene PCO: t=5-5:20 1st GC sampling from both upstream and downstream ports; t=5:20-5:40 2nd GC sampling from both upstream and

downstream ports; t=5:40-6 3rd GC sampling from downstream port; t=5-6:30 1st HPLC sampling from downstream port.

HPLC sampling for MEK PCO: t=5-5:20 1st HPLC sampling from both upstream and downstream ports; t=5:20-5:40 2nd HPLC sampling from both upstream and downstream ports.

6) Once the samplings are done, the lamps are tuned off and the air filter is removed.

A number of points should be highlighted:

- Each air filter is tested only once and for each test a fresh photocatalyst is used.
- HPLC and GC samples of upstream in the absence of pollutant injection revealed that inlet air stream does not carry any components rather than nitrogen, oxygen and water vapor, and, thus, the generated by-products detected at downstream resulted from PCO reactions.
- The GC and HPLC sampling flows (50 mL/min and 1 L/min respectively) are monitored continuously using two flow meters (DryCal).

3.3. Photocatalyst coating

In order to evaluate the photocatalytic performance of titania samples, titania powder is deposited on a nickel foam substrate (Shanghai Tankii Alloy Material Co). The width, height, and thickness of the filter were 10, 10, and 0.1 cm, respectively. First, titania particles obtained from hydrothermal synthesis are pressed to form thin pellets, which then are crushed and sieved to the size of 35-60 meshes (250-500 μm). A specific quantity of photocatalyst is added to distilled water and the mixture is stirred for 6 h at room temperature to reach a homogeneous TiO_2 suspension (0.5 wt%). TiO_2 colloidal solution is coated on the Ni filter via a pipetting technique in which TiO_2 solution is placed drop by drop on the filter until the entire surface of the filter is covered with TiO_2 solution. The filter is dried at 80 ˚C for 1 h and the same coating procedure is repeated for the other side of the filter. Finally, the titania coated filter is dried overnight at 80 ˚C to remove water from the filter. The TiO_2 coated filter weight is measured and compared to that of the uncoated filter to calculate the coating density. In all experiments, the TiO_2 coating density on the substrate is kept at 1 ± 0.05 mg/cm^2. Prior to each PCO test, the TiO_2 coated filter is preheated in air oven at 80 ˚C for about 2 h to remove the physically adsorbed water vapor during storage.

3.4. Photocatalytic activity and health-risk measurements

Photocatalysts are compared in terms of total toluene/MEK removal efficiency, amount of generated by-products in the gas phase, reaction rate, and health-risk index.

Toluene/MEK single-pass removal efficiency and by-products generation are defined as follows:

$$\text{Single-pass removal efficiency, } \eta\ (\%) = \frac{(C_{in} - C_{out})}{C_{in}} \times 100 \tag{3.1}$$

where C_{in} and C_{out} are the upstream and downstream concentrations of toluene/MEK in ppb, respectively.

$$\text{By-product generation, } G_i\,(\text{ppb}) = C_{i,out} - C_{i,in} \tag{3.2}$$

where $C_{i,in}$ and $C_{i,out}$ are the upstream and downstream concentrations of by-product i in ppb, respectively.

The photocatalytic reaction rate is determined as follows:

$$\text{Reaction rate, } r_{PCO} = \frac{Q_{air} \times (C_{in} - C_{out})}{m \times M_{toluene/MEK}} \times 100 \tag{3.3}$$

where C_{in} and C_{out} are concentrations in g/m^3, m is the photocatalyst mass on nickel foam (g), M is the toluene/MEK molecular weight (g/mol), and Q_{air} is the air volumetric flow rate (m^3/min).

To determine the risk level to human health associated with each photocatalytic system, a health-related index (HRI) is defined based on the concentrations of by-products and the recommended exposure limit (REL) values proposed by NIOSH (National Institute for Occupational Safety and Health) [133].

$$\text{HRI} = \sum \frac{C_{i,out}}{REL_i} \tag{3.4}$$

Table 3.1 Health-related information of generated by-products

Pollutant	REL (ppm)	REL data source	IARC carcinogenic classification
Formaldehyde	0.016	NIOSH	Group 1, carcinogenic to humans
Acetaldehyde	0.078	OEHHA*	Group 2B, possibly carcinogenic to humans
Acetone	250	NIOSH	-

*Office of Environmental Health Hazards Assessments, California Environmental Protection Agency, U.S.

3.5. Characterization techniques

In order to acquire information related to the physical and chemical features of prepared titania samples including crystallinity, crystal phase and size, porosity, surface area, and surface chemistry various analytical techniques are exploited.

3.5.1. X-ray diffraction

The best and most applied approach to determine the existence of various phases in titania structure, degree of crystallinity, and crystal size is XRD. The crystalline structure and crystallite size are identified by X-ray diffraction (Bruker, D8 advance) with a monochromatized source of Cu-Kα radiation. The average crystal sizes of anatase, brookite, and rutile are estimated based on Scherrer formulae:

$$d_{hkl} = \frac{k\lambda}{\beta \cos 2\theta} \tag{3.5}$$

where λ is the wavelength of the Cu-Kα radiation (λ=0.15405 nm), θ the Bragg's diffraction angle, β the full width at half maximum intensity of the peak, and k a constant (0.89). For anatase, brookite, and rutile, [101], [121], and [110] peaks are respectively applied in Scherrer equation to determine the crystal size. Accordingly, the phase composition can be estimated from the integrated intensities of anatase [101], brookite [121], and rutile [110] peaks. For samples with more than one crystalline phase, the mass fractions of brookite (W_B) and rutile (W_R) are calculated according to the following equations [134]:

$$W_B = \frac{2.721 A_B}{0.886 A_A + 2.721 A_B} \tag{3.6}$$

$$W_R = \frac{A_R}{0.884A_A + A_R} \tag{3.7}$$

where A_A, A_B, and A_R are, respectively, the integrated intensities of the anatase [101] and brookite [121], and rutile [110] peaks.

3.5.2. Nitrogen (N_2) adsorption-desorption isotherms

Nitrogen adsorption-desorption isotherms at liquid nitrogen temperature (77K) are measured with an AUTOSORB-1 (Quantrochrome Instruments Co.) nitrogen adsorption apparatus. The surface areas of the samples are evaluated by multipoint Brauner, Emmett, and Teller (BET) method using the adsorption data in the relative pressure (p/p_0) range 0.05-0.3. The pore size distributions are calculated from desorption branches of isotherms by the Density Functional Theory (DFT), assuming slit-like pores. Prior to N_2 adsorption analysis, samples are completely degassed at 120 °C for several hours (except the samples that synthesized at lower temperatures, which are degassed at 80 °C).

3.5.3. Electron microscopy

SEM and TEM are well-known and effective techniques to investigate the morphology and crystallographic properties of nano-sized materials. To investigate the surface morphology of TiO_2 samples scanning electron microscope (Hitachi S-4700 Model) or field emission SEM (FEI Quanta 450) is employed. Transmission electron microscopy and high-resolution transmission electron microscopy images along with the selected area electron diffraction (SAED) patterns are taken on a FEI Tecnai TF-20 S/TEM instrument.

3.5.4. Fourier transform infrared spectroscopy

FTIR analyses are performed using a Nicolet 6700 FTIR spectrometer (Thermo Fisher Scientific). Spectra are collected in a range of 4000–600 cm^{-1} at a resolution of 4 cm^{-1} and an absorbance detection limit of 0.001 a.u. Air spectrum, as background, is always subtracted from the obtained FTIR spectra in all experiments. The titania samples are degassed at 80 ˚C for 12 h before performing the FTIR analysis.

3.5.5. X-ray photoelectron spectroscopy

XPS is a quantitative method that measures the elemental composition and chemical state of the elements on a solid surface. Surface chemical compositions of photocatalysts are investigated

using an X-ray Photoelectron Spectroscopy (Thermo Scientific K-Alpha spectrometer, USA) equipped with an Al Kα excitation source and X-ray spot size of 200 μm in diameter. All the binding energies are referenced to the C 1s peak at 284.6 eV of the surface adventitious carbon.

3.5.6. Thermo gravimetric analysis

TGA is performed by using a TGA Q500/Discovery MS, in the 30-750 °C range in a nitrogen flux of ca. 90 mL/min. The temperature program is as follows: 10 °C/min from 30 to 120 °C, 15 min in isothermal condition at 120 °C, and 10 °C/min from 120 to 750 °C. Based on [135], weight loss in each temperature interval is assigned to the removal of different surface species: 30 to 120 °C → humidity, 120 to 300 °C → weakly bonded OH groups, and 300 to 600 °C → strongly bonded OH groups.

3.5.7. Photoluminescence spectra

Photoluminescence emission spectra can be utilized to explore the fate of photogenerated e^--h^+, considering that PL emission is generated by the recombination of free charge carriers. The PL emission spectra are measured using a PerkinElmer LS45 Fluorescence spectrometer. The excitation wavelength and the scanning speed are 300 nm and 500 nm/min, respectively, and the width of excitation and emission slits are 10.0 nm.

3.5.8. Hydroxyl radical analysis

In order to measure the amount of $^{\bullet}OH$ formed on the surface of UV-illuminated TiO_2, photoluminescence method with terephthalic acid (TA) as a probe molecule is employed. It is known that hydroxyl radicals rapidly react with TA and produce highly fluorescent 2-hydroxyterephthalic acid (2-HTA). Therefore, the intensity of the PL peak of 2-HTA is in proportion to the concentration of $^{\bullet}OH$ generated on photocatalyst. 100 mg TiO_2 is dispersed in 30 ml of an aqueous solution containing 2 mmol/L NaOH and 0.5 mmol/L TA in a glass dish with 9 cm diameter and 2 cm depth. The concentration of TA is chosen based on the work of Ishibashi et al. which indicated that in a solution with 10^{-3}-10^{-4} M TA, the hydroxylation reactions of TA proceed mainly by $^{\bullet}OH$ [136]. It has been shown that at this TA concentration, 2-HTA absorption or fluorescence quenching is not significant and the correlation between 2-HTA concentration and PL intensity is linear [137]. The solution is stirred for 20 min in darkness at ambient temperature to obtain a homogenous suspension prior to irradiation. For illumination, a 254-nm UV lamp (Philips, TUV PL-S 5W/4P) is horizontally placed 5 cm above the center of

the dish. After 15 min of illumination, 4 ml aliquot is drawn, and immediately filtered using a 0.22 μm syringe filter to remove TiO_2 particles and acquire a clear solution. The fluorescence emission intensity of 2-HTA is measured at 426 nm after excitation at 315 nm on the fluorescence spectrophotometer. The PMT voltage and width of excitation (and emission) slit are 600 V and 5 nm, respectively.

3.5.9. UV adsorption spectra

The UV-vis spectrum can be used to calculate the band gaps of semiconductor materials. Diffuse reflectance UV-visible spectra of samples are obtained over a range of 200-800 nm by a Perkin-Elmer Lambda 750 spectrophotometer, in which $BaSO_4$ is used as the background. The band gap energies are determined by plotting $(\alpha h\nu)^2$ versus energy of light ($h\nu$) (Tauc plot) where α is the absorption coefficient, h is the plank constant and v is the frequency. The extrapolation of the straight line from the Tauc region intercepts the x axis ($h\nu$) to give the direct band gap of the TiO_2 powder.

Chapter 4

4. Adsorption and photocatalytic oxidation performance of commercial titanium dioxide photocatalysts

4.1. Gas phase adsorption of toluene and MEK onto titanium dioxide: Detailed FTIR and adsorption isotherm studies

Adsorption of pollutants on photocatalyst surface plays a critical role in the efficacy of photocatalytic oxidation technology for air purification applications. It is upon the adsorption on the surface that pollutant molecules come into contact with highly active species/radicals (such as $OH^{\bullet}$ and $O_2^{\bullet -}$) and undergo photochemical reactions [138, 139]. From another perspective, since the recombination of e^--h^+ pairs takes places extremely fast (<25 μs [9]), the species that can act as charge carrier traps must be pre-adsorbed on the surface in order to make interfacial carrier trapping kinetically competitive to e^--h^+ recombination process. Although a great number of articles have been published on the performance of PCO systems, only a few studies have specifically focused on the adsorption of organic contaminants on TiO_2. More importantly, in most of the experiments dedicated to study the adsorption of VOCs on photocatalysts, the impact of relative humidity on the adsorption isotherms has not been fully investigated. On the other hand, the role of surface hydroxyl groups in the interaction of TiO_2 surface with adsorbates molecules other than water is still unclear. To address these research gaps, the main objective of this section is to provide a systematic adsorption study of toluene and MEK over titanium dioxide at different levels of relative humidity (0, 20, or 50%). The adsorption performances of six commercially available titanium dioxide photocatalysts (P25, PC500, PC105, UV100, PC-S7, and S5-300A) coated on nickel foam substrates were determined and adsorption isotherms were presented. Knowing the importance of hydroxyl groups in the adsorption process, FTIR analysis was employed to study the type and concentration of OH groups on titania surface and subsequently to determine the contribution of these groups to the adsorption of VOC molecules. Based on the structural properties of selected photocatalysts and the results obtained from FTIR analyses attempts are made to provide clear explanations for different adsorption trends observed for each titania sample and connect the key properties of the air filter to its adsorption capacity for toluene and MEK.

4.1.1. Methodology

4.1.1.1. Materials

P25 from Evonik®, PC500, PC105, PC-S7 and S5-300A from Cristal Global Companies, and UV100 from Hombikat® were selected titanium dioxide photocatalysts in this study. Some of the main characteristics of the photocatalysts are tabulated in Table 4.1 [27, 140, 141]. Toluene (99.9%) and MEK (99.9%) (Fisher Scientific Inc., Canada) were chosen as air contaminants and the relevant physical properties of these compounds are given in Table 4.2.

Table 4.1 Characteristics of titanium dioxide photocatalysts

Catalyst	Properties		
	BET (m^2/g)	Pore radius (nm)	Other remarks
P25	50	-	Non-porous material with interparticle pores
PC500	276	6.1	Type IV sorption isotherms indicates presence of mesopores
PC105	80	15.3	-
PC-S7	300	-	Neural to moderately alkaline pH
S5-300A	330	-	Acidic
UV100	330	<5	Agglomeration of small subparticles generates microporous

Table 4.2 Physical properties of selected VOCs

Compound	Family	Formula	Molecular weight (g/mol)	Boiling point (°C)	Dipole moment	Water solubility (g/L)
Toluene	Aromatics	C_7H_8	92.1	111.1	0.36	0.52
MEK	ketones	C_4H_8O	72.1	79.4	2.76	275

4.1.1.2. Experimental procedure

The experimental set-up design and operation are explained in details in section 3.1.1; therefore here, only some of the specific points during the adsorption tests are highlighted. After installing the filter, airflow with target humidity is introduced into the reactor and simultaneously the injection of VOC is initiated. The challenge compound is automatically injected by the syringe

pump into the airflow. The start of injection is considered as time zero, and the adsorption efficiency and amount adsorbed on titania is calculated based on this time scale. The concentrations of the pollutant before and after the air filter are continuously recorded by PID detector (ppb3000 RAE). Table 4.3 summarizes the main experimental conditions as well as the uncertainty level for some of the parameters. It is also worth mentioning that the nickel foam filter without coating showed marginal adsorption capacity toward MEK (θ = 0.00101 $g_{MEK}/g_{support}$) and toluene (θ = 0.00096 $g_{Toluene}/g_{support}$), meaning the adsorption capacity can be solely attributed to titania nanoparticles.

Table 4.3 Experimental conditions in adsorption tests

Parameter	Value	Unit
Inlet concentration	0.5 ± 0.04, 1 ± 0.05, 2 ± 0.1, 4 ± 0.1, 10 ± 0.15, 20 ± 0.2	ppm
Relative humidity	0, 20 ± 2, 50 ± 2	%
Volumetric flow rate	12 ± 0.2	L/min
Residence time	0.05	s
Temperature	19.5 ± 0.5	°C
TiO_2 concentration	1.5± 0.09	mg/cm^2

4.1.1.3. FTIR tests procedure

In order to identify the type and relative concentration of hydroxyl groups on the surface, FTIR analyses were performed on fresh titania powders (i.e. without VOC adsorption). Additionally, in order to minimize the interference between the –OH signals of adsorbed water and surface hydroxyls and also evaluate the thermal stability of various kinds of OH groups, titania powders were calcined at 100 ˚C for 12 h or at 325 ˚C for 3 h in air-oven before FTIR analysis.

A number of experiments were conducted on the static adsorption of toluene and MEK on different titania photocatalysts in dry condition. Briefly, 100 mg of fresh titania powder were placed inside a glass test tube and compressed air was passed over the sample for 30 min. Immediately, the system was sealed and a certain volume of liquid pollutant (100 µL for MEK and 25 µL for toluene) was introduced into the vial with a syringe, via a septum. It should be emphasized that the liquid was added dropwise to a glass wool at the bottom of the vial without directly contacting the titania sample. The amounts of injected VOCs were determined based on

the results of adsorption tests under dry conditions in the continuous system and guarantee complete saturation of the catalyst. After the adsorption equilibrium was reached at room temperature (about 5 h after the injection), IR spectra of the solid phase were collected.

4.1.1.4. Adsorption performance indicators

The adsorption efficiency was determined with the following expression:

$$\text{Adsorption efficiency, t (\%)} = (1-\frac{C_{out}^{(t)}}{C_{in}^{(t)}})\times 100 \quad (4.1)$$

where $C_{in}^{(t)}$ and $C_{out}^{(t)}$ are the upstream and downstream concentrations at time t(min), respectively.

In order to calculate the adsorption capacity of each TiO_2 nanopowder, the concentrations of challenge compound in air at the inlet and outlet of the reactor were measured. The adsorption capacity is defined as the ratio between the total mass of VOC adsorbed till the adsorption equilibrium time and the mass of titania on the support. The adsorption capacity (θ) was calculated as follows:

$$\theta = \frac{\int_0^{t_{equ}} Q(C_{in}^{(t)} - C_{out}^{(t)})dt}{m_{TiO_2}} \quad (4.2)$$

where t_{equ} is the elapsed time of adsorption test; Q is the airflow rate; and m_{TiO2} is the mass of TiO_2 coated on the nickel foam filter [142].

In this study, depending on TiO_2 photocatalyst and target VOC, Langmuir or Henry adsorption (for low toluene concentrations) has been used to model the results of adsorption tests.

For the Langmuir isotherm model the following functional form of isotherm was considered [143]:

$$\theta = \frac{\mu_{\max} K_a C}{1 + K_a C} \quad (4.3)$$

where θ is the amount of pollutant (toluene or MEK) adsorbed per mass of titanium dioxide on the filter, μ_{max} is the maximum amount adsorbed, K_a is the adsorption equilibrium constant, and C is the concentration of challenge compound.

When the concentration of pollutant in air is very low, the term K_aC will be much smaller than unity and can be neglected; therefore, equation 3 can be written as follows:

$$\theta = \mu_{max} K_a C = K_L C \quad (4.4)$$

In this equation, K_L incorporates the Langmuir adsorption constant and the maximum amount of adsorbed. As a result, a linear relation between θ and concentration at equilibrium can be expected in some cases.

The coverage value for each photocatalyst based on the adsorption capacity at 4 ppm and dry condition is calculated as follows:

$$\text{Coverage value} = \frac{\theta_{\text{Toluene/MEK at 4 ppm and 0\% RH}} \times \text{Avogadro's number}}{\text{Molecular weight of Toluene/MEK} \times \text{Surface area of photocatalyst}} \quad (4.5)$$

4.1.2. Results and discussion

4.1.2.1. Characterization of TiO_2 coated filters

The morphology and microstructure of TiO_2 coated filters were investigated by SEM. Figure 4.1 presents the SEM images of TiO_2 (UV100) coated on nickel foam filters at different magnifications. As can be observed, the nickel foam filter has a 3-D porous structure and the pore size ranges from 100 to 600 μm. Figure 4.1b demonstrates that UV100 nanoparticles are mainly deposited on filter surfaces and accumulated in the hexagonal void space of the foam. Figure 4.1c and d represent large magnifications of the filter coated with UV100 and clearly confirms the presence of macropores formed by the accumulation of nanoparticles, which facilitate the diffusion of pollutant molecules. In order to quantitatively determine the composition on the surface of the filter and acquire more information regarding the quality of coating, energy dispersive spectroscopy (INCA system, Oxford Instruments) was employed. Figure 4.2 and Table 4.4 present the obtained data from EDS analysis for the filters coated with PC500 and UV100. As can be inferred from the result of elemental composition, the surface of support material is entirely coated with titania (Spectrum 1 in Figure 4.2a and b and Spectrum 2 in Figure 4.2a) while on the sharp edges of all filters (such as Spectrum 2 in Figure 4.2b) poorer coating quality can be observed.

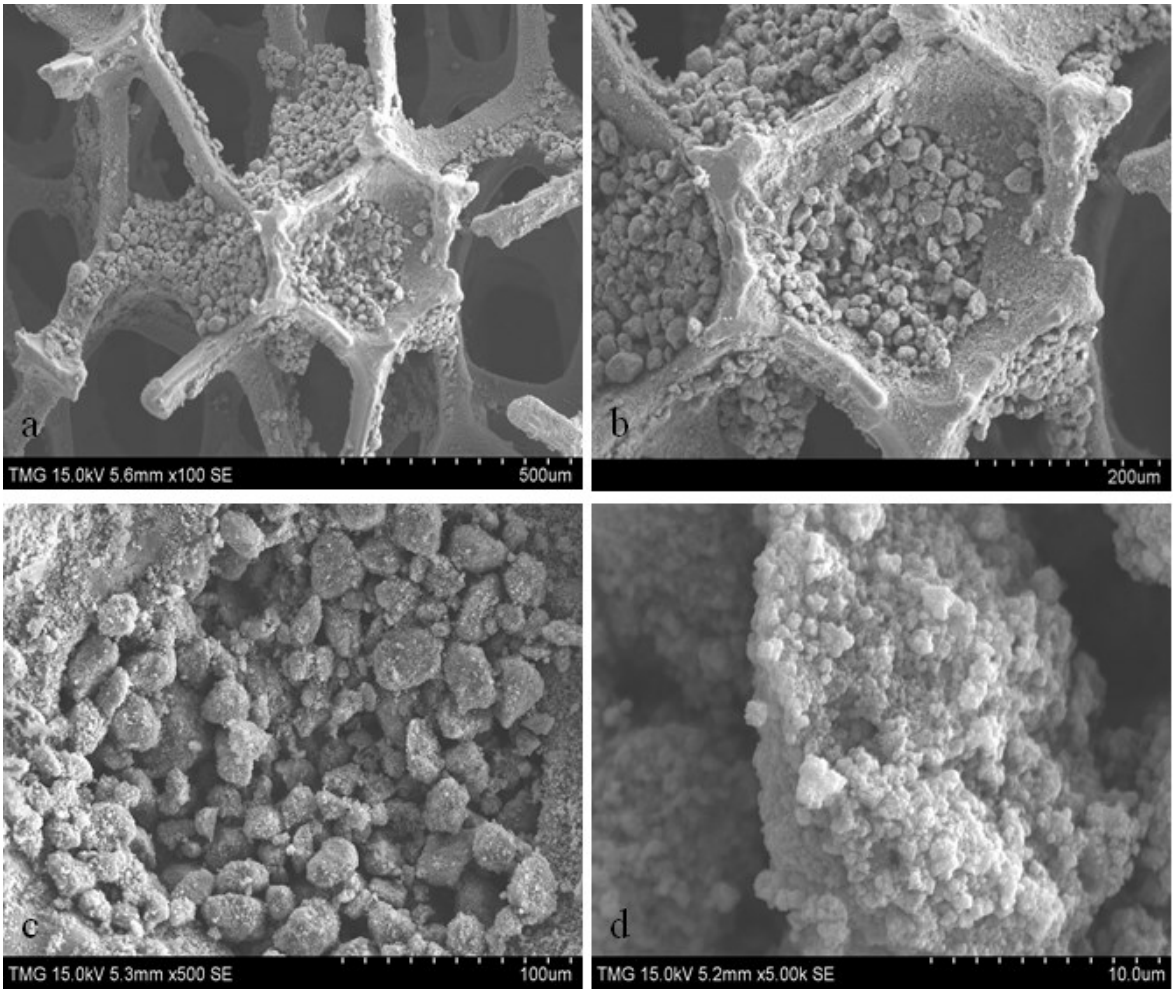

Figure 4.1 SEM images of UV100 coated nickel filters at different magnification

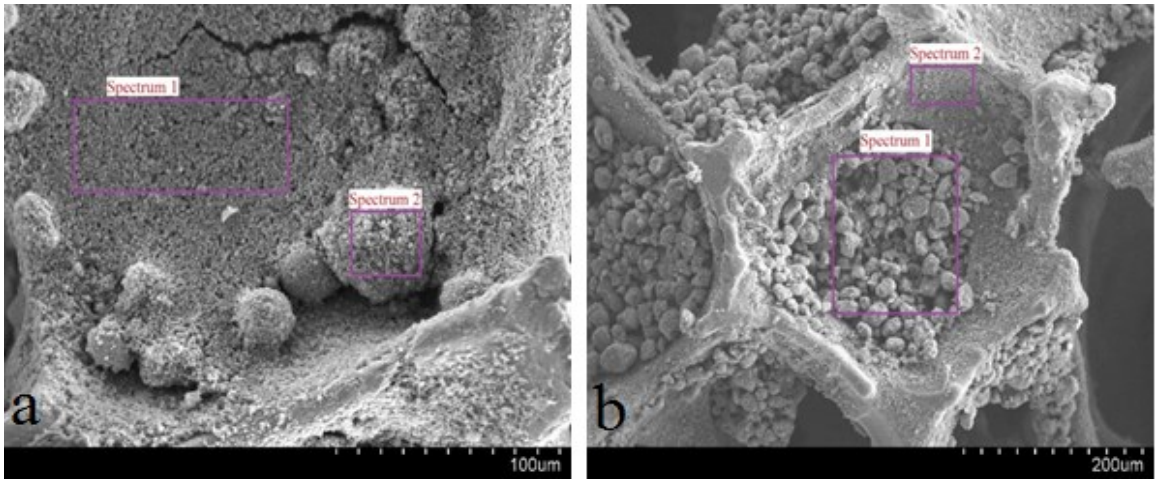

Figure 4.2 EDS analysis for selected TiO_2-coated nickel filters, (a) PC500 and (b) UV100

Table 4.4 Elemental composition of the surface of TiO_2-coated nickel filters

Spectrum	O (wt%)	Ti (wt%)	Ni (wt%)
		Figure 4.2a	
Spectrum 1	51.13	46.79	2.08
Spectrum 2	46.5	50.35	3.15
		Figure 4.2b	
Spectrum 1	40.37	56.3	3.33
Spectrum 2	20.87	20.28	58.85

4.1.2.2. Characterization of surface hydroxyl groups

Hydroxyl groups on TiO_2 surface are believed to be effective active centres for gaseous VOCs adsorption and thereby their nature and distribution can be the determining factor of TiO_2 behavior [29, 94, 144]. FTIR is one of the suitable techniques to study surface hydroxyls and adsorption of water molecules on metal oxides. Consequently, numerous experimental and theoretical works have been published on water adsorption on titania surface and characterization of surface hydroxyls by means of FTIR spectroscopy [145, 146]. In order to find a correlation between catalyst adsorption performance and the type and concentration of hydroxyl groups, FTIR analyses have been done on fresh and calcined titania powders. Figure 4.3 demonstrates the FTIR spectra of titania samples (fresh and calcined) in the OH spectral region, 3800 to 2800 cm^{-1}. All untreated titania samples (red curves) exhibit a broad and intense IR absorption in the 3600-2800 cm^{-1} range. The absorption in this region is widely attributed to different types of hydroxyl groups with acid/base character, water molecules coordinatively adsorbed on surface Ti^{4+} cations, and un-dissociated water molecules bonded via weak hydrogen bonds to each other and/or to OH-groups of solid [27, 146-149]. Noticeably, the IR absorption for S5-300A in this region is more intense compared to other samples, which can be an indicator of higher amount of adsorbed water/OH groups on the surface. It is noteworthy that unlike other samples, the spectra of PC-S7 in the 3600-2800 cm^{-1} range has a maximum at 3150-3050 cm^{-1} which has been specifically assigned to the molecular adsorption of water on titania surface [144]. The bands at frequencies higher than 3600 cm^{-1} are generally assigned to the stretching mode (υ_{OH}) of all -OH species free from hydrogen bonding interactions [27, 144]. In this regard, the band at 3663 cm^{-1} can be assigned to OH groups with more basic character [94, 148, 150] while the one at 3625 cm^{-}

[1] is assignable to acidic hydroxyl groups [94, 150, 151] or adsorbed water [147, 152]. All titania photocatalysts possess a sharp adsorption band at 3700-3695 cm^{-1} which is widely accepted that results from isolated hydroxyl groups [29, 146, 153]. The strong band at 3728 cm^{-1} which exits in the spectra of all samples is also assigned to the stretching mode of isolated hydroxyls [147]. It has been proposed that υ_{OH} bands at frequencies higher than 3680 cm^{-1} can be assigned to terminal hydroxyl groups (Ti-OH), while bands at lower frequencies can be due to bridged -OH (Ti-OH-Ti) [147, 149]. It is to be noted that fresh PC105 and P25 show much more intense absorption bands in the 3700-3695 cm^{-1} range which implies larger population of isolated linear hydroxyl groups on the surface of these samples.

In order to provide a clearer view of spectral components at 3750-3600 cm^{-1} range (i.e. without the interference of adsorbed water), two thermal treatments were examined. In the first procedure, samples were dried at 100 ˚C for 12 h, which resulted in a substantial decrement in the intensity of IR absorbance in 3600-2800 cm^{-1} range due to the removal of physically bound water as shown in Figure 4.3 (green curves). The more significant decrease in spectra of PC105 and S5-300A in this region may be ascribed to the higher amount of removed weakly adsorbed water. For P25, PC500, S5-300A and PC105, the treatment at 100 ˚C did not considerably change the positions of the bands in the 3750-3600 cm^{-1} range and only moderately reduced the adsorption intensities. In the case of PC-S7, the absorption intensity for almost all the bands in this region greatly decreased after drying at 100 ˚C. In all spectra after treatment, a new band at 3646 cm^{-1} appeared, which according to the literature and the behavior may be assigned to another type of isolated hydroxyl group [147]. For P25, PC500, PC105, and UV100 a new band located at 3670 cm^{-1} was seen in the spectra which has been ascribed to bridging –OH group [27, 151]. Interestingly, in the case of UV100 some bands in the 3750-3600 cm^{-1} region became stronger with thermal treatment. It led us to believe that many of the OH groups of UV100 were freed from H-bond to water upon drying and gave rise to sharper bands/subbands in these frequencies. In the second thermal treatment, samples were calcined at 325 ˚C for 3 h, which made the spectra much less complex in the 3750-3600 cm^{-1} region and smoother in the 3600-2800 cm^{-1} range (as shown in Figure 4.3 (blue curves)). The calcination at this temperature should practically remove all the signals of adsorbed water and not considerably affect free OH species [154]. Nevertheless, it should be mentioned that the presence of trace amount of water in the samples was inevitable due to sample handling and preparation during FTIR analysis.

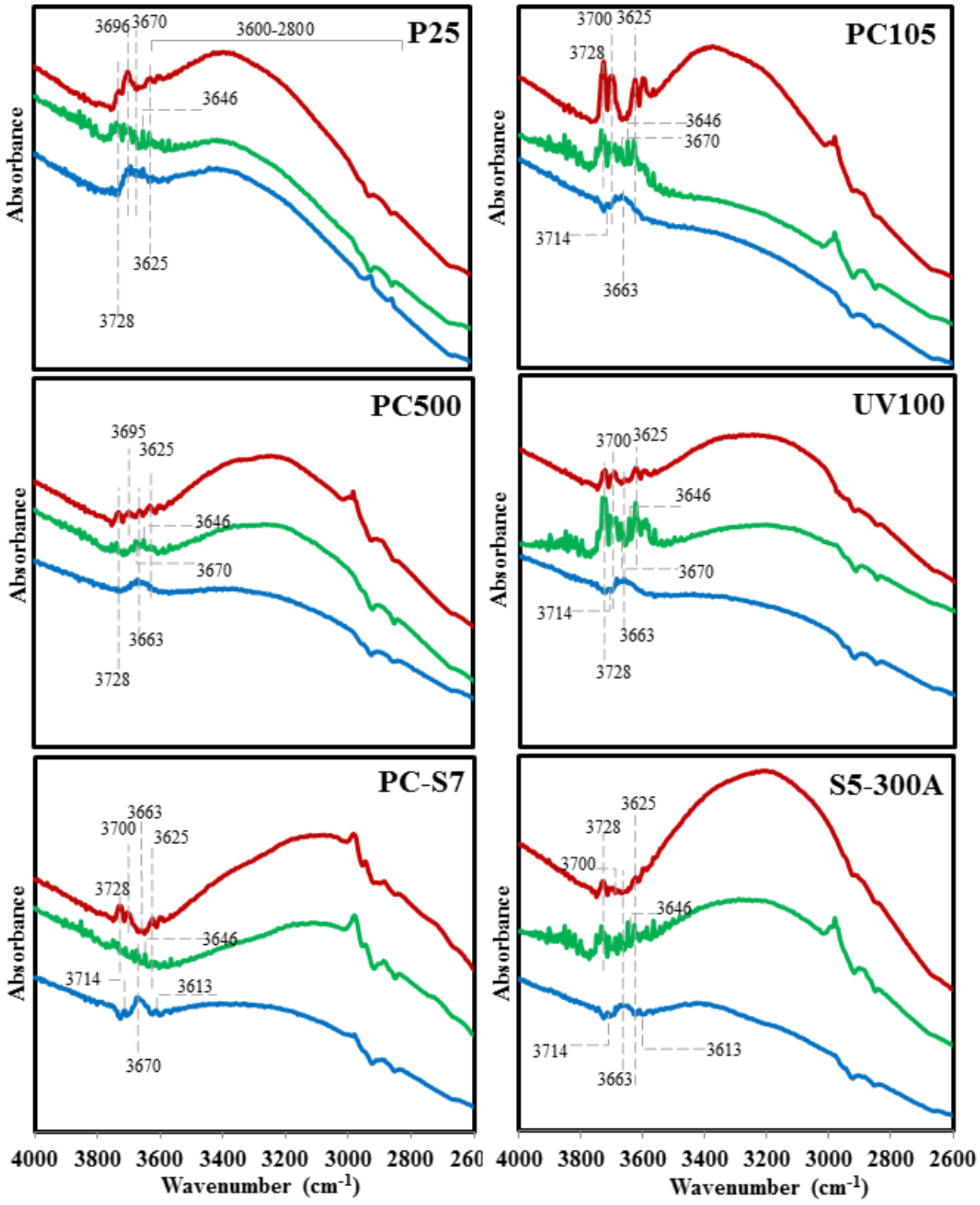

Figure 4.3 FTIR spectra of the TiO2 samples in the hydroxyl group region: fresh (red); dried at 100 ˚C for 12 h (green); calcined at 325 ˚C for 3 h (blue)

After calcination, for all samples, there is a broad and dominant peak between 3728-3625 cm^{-1} with maximum at ca. 3663 cm^{-1} and some shoulders which can be assigned to OH groups with basic character as well as other types of isolated hydroxyls [94, 148, 150, 152]. Two bands at 3714 and 3613 cm^{-1} appeared in the spectra of some samples upon calcination can be assigned to isolated OH group bound to the anatase phase [147] and free OH groups [109].

4.1.2.3. Adsorption efficiency at dry condition

Figure 4.4 shows the variations of toluene adsorption efficiency with time for different TiO_2 photocatalysts for experiments conducted in dry air. For all samples, the complete toluene removal efficiency (i.e. 100%) during the first few minutes of adsorption is followed by a sharp decline over the first hour. UV100, PC500, and S5-300A (Group 1) demonstrated significantly superior adsorption ability with respect to P25, PC105, and PC-S7 (Group 2). As can be observed, the complete saturation (i.e. zero toluene uptake) of Group 2 samples reached 50 min after injection started while on the titania samples from Group 1, the adsorption was prolonged for almost 6 h. Nevertheless, even in the case of Group 1, the adsorption efficiency decreased from 70-100% at t = 20 min to 5-18% at t = 120 min, indicating weak interaction between toluene and titania.

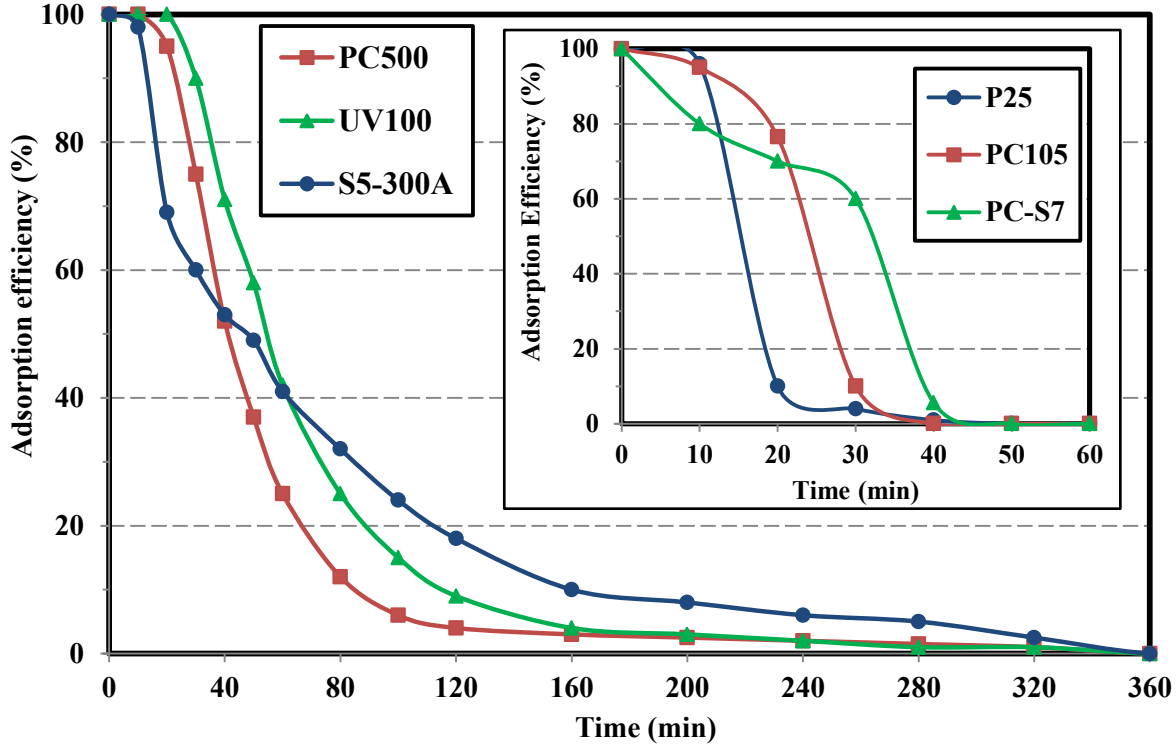

Figure 4.4 Toluene adsorption efficiency with time at 0% RH and 1 ppm concentration

Figure 4.5 depicts the MEK adsorption efficiency with time for various TiO_2 samples at 0% relative humidity and concentration of 1 ppm. For Group 1 catalysts, the adsorption efficiency experiences a slight reduction from 100% to 80% in the first 200 min followed by a steady and gradual decrease until it reaches 100% breakthrough after 1400-1800 min. On the other hand, Group 2 samples indicate a substantial efficiency loss in the first 200 min of the adsorption test and have MEK adsorption efficiencies smaller than 10% after only 500 min. Among various adsorbents, PC500 offers a remarkable MEK adsorption efficiency (>90%) within the first 300 min of operation which is roughly 12-18% higher than the rest of the samples in Group 1.

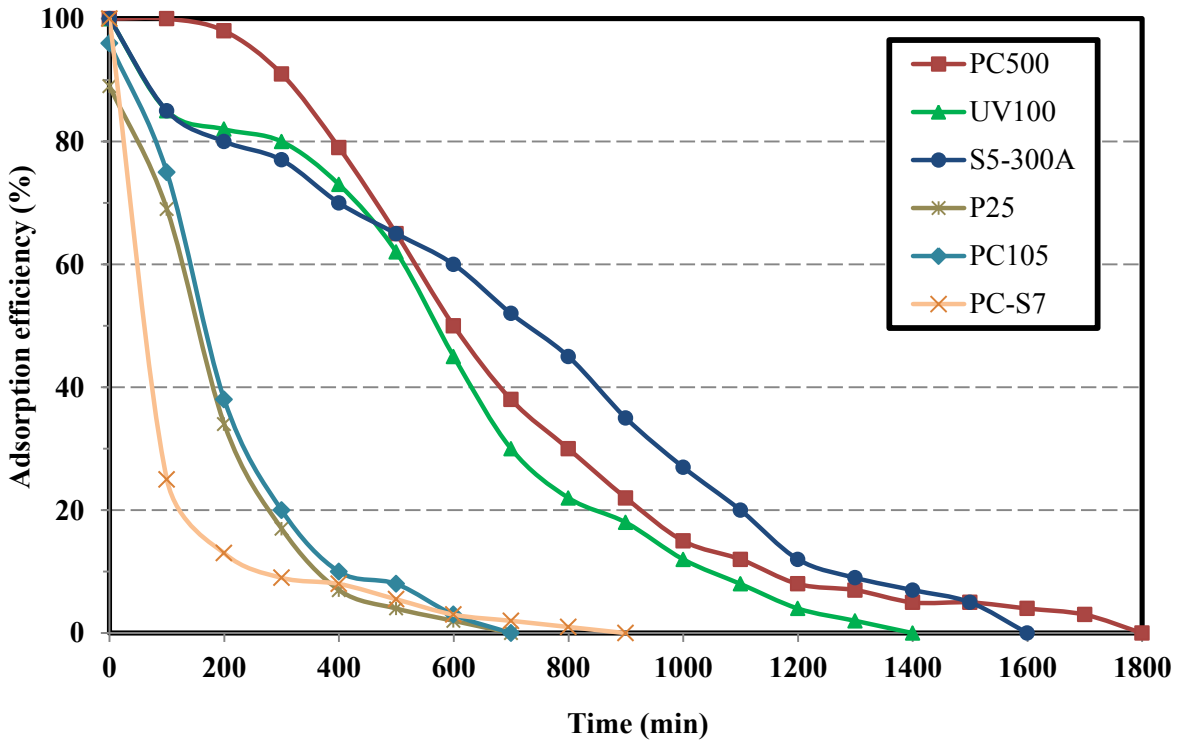

Figure 4.5 MEK adsorption efficiency with time at 0% RH and 1 ppm concentration

As presented in Table 4.1, PC500, UV100, and S5-300A possess much larger BET surface areas with respect to P25 and PC105. Accordingly, it seems reasonable to acquire higher adsorption capacity for Group 1 samples since larger surface area offers more available adsorption sites for molecular diffusion of pollutants. Regarding Group 2 samples, marginal superiority of PC105 over P25 in terms of adsorption capacity for toluene and MEK can be justified by comparing these samples surface areas. In contrast, in spite of its high surface area (300 m^2/g), PC-S7 has surprisingly low adsorption efficiency, even in comparison to P25, which holds very low BET

surface area. This might be partly originated from the huge amount of water present on fresh PC-S7 surface which barricades the access of toluene to the surface adsorption sites.

4.1.2.4. Adsorption isotherms at dry condition

Figure 4.6 displays the equilibrium adsorption isotherms for toluene for different titania samples in the absence of humidity. Once the adsorption equilibrium is reached, the rates of VOC desorption and adsorption on the surface is equal and, therefore, it can be easily recognized by comparing the concentration of target VOC upstream and downstream of the adsorbent. As could be predicted from adsorption efficiency results, Group 1 samples have much higher θ values than Group 2. Except P25 and PC105, all adsorption isotherms for toluene acceptably match with the Langmuir adsorption model in the concentration range (0.5-10 ppm).

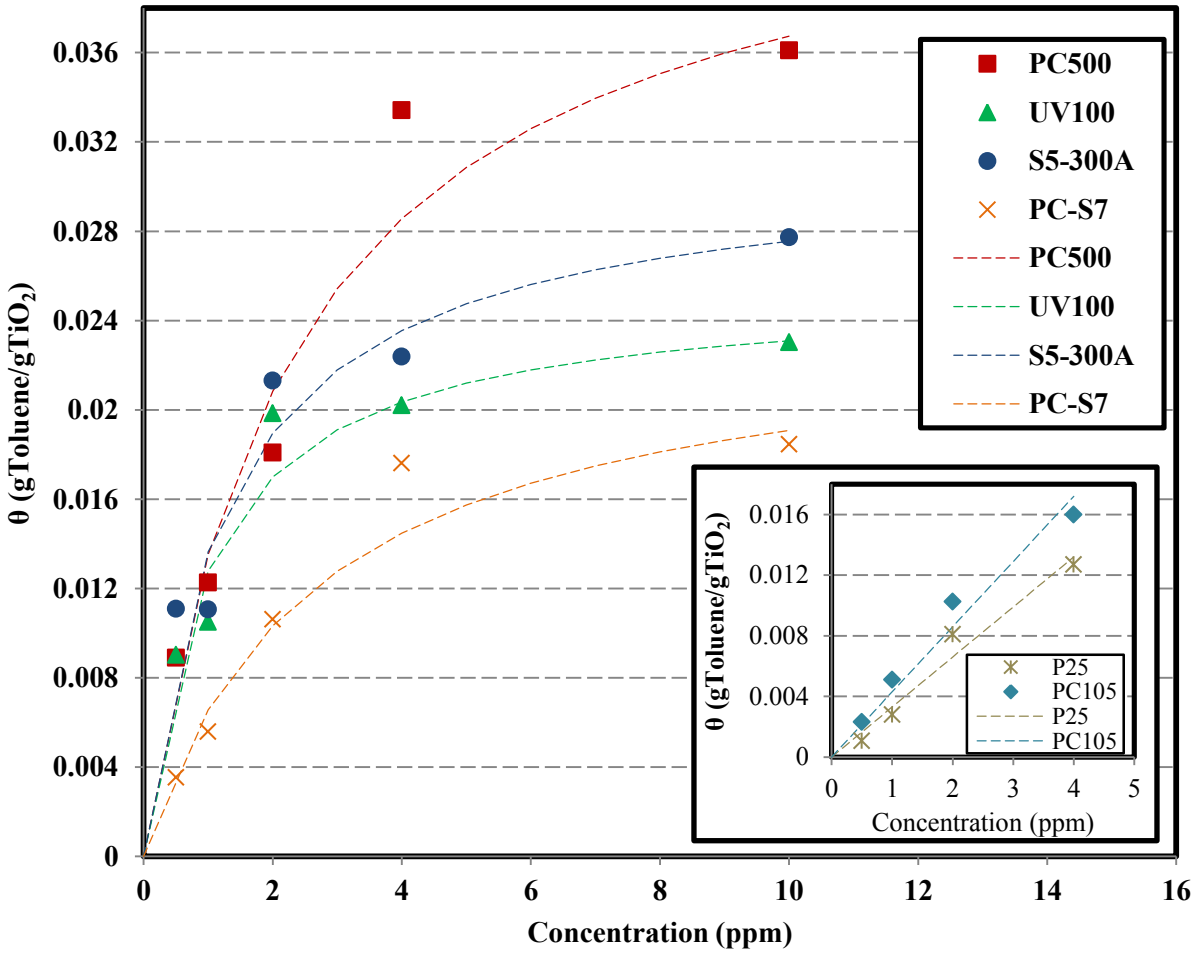

Figure 4.6 Adsorption isotherms for toluene under dry condition (dashed line: regression using Langmuir isotherm model and Langmuir parameters given in Table 4.5)

For P25 and PC105, the simplified form of Langmuir isotherm (Henry model) reproduces the experimental results obtained from toluene adsorption in low concentrations with greater accuracy. Consequently, one can deduce that the adsorption behavior of P25 and PC105 follow ideal monolayer adsorption (conceptual basis for Langmuir model) at low ppm toluene concentrations (0.5-4 ppm). Zhong et al. [155] also reported that toluene (0.5-5 ppm) adsorption isotherm onto TiO_2 (surface area = 105.7 m^2/g) is Henry type. Similarly, Demeestere et al. [156] investigated the adsorption of toluene on P25 at 0% and 57.8% relative humidity and acquired linear relationship between θ and equilibrium concentration. As represented in Table 4.5, Group 1 samples possess the highest maximum adsorption capacities (μ_{max}) which follow the sequence: PC500 > S5-300A > UV100. For P25 and PC105, the values of K_L determined from Henry model are given in Table 4.5 instead of μ_{max} and K_a.

Equilibrium adsorption isotherms of MEK for different photocatalysts in the absence of humidity are presented in Figure 4.7. Similar to the isotherms for toluene, Group 1 titania catalysts offer much higher adsorption capacity than Group 2. In the case of MEK, all the experimental data for MEK adsorption, in the concentration range of 1-20 ppm, could be represented by Langmuir model with sufficient accuracy. The main difference that can be easily noticed by comparing Figure 4.6 and Figure 4.7 is the wider gaps between the adsorption capacities for Group 1 and Group 2 samples for MEK. For instance, at 10 ppm, the adsorption capacity for Group 2 is 0.025-0.05 g_{MEK}/g_{TiO2} (PC105 > PC-S7 > P25), while Group 1 samples provide much higher values: 0.171, 0.145, and 0.120 g_{MEK}/g_{TiO2} for S5-300A, PC500, and UV100, respectively. One possible explanation is that due to better interaction between TiO_2 and MEK, the key properties of photocatalyst in adsorption such as surface area and porosity become more influential. As can be seen in Table 4.5, the maximum adsorption capacity follows the order: S5-300A > PC500 > UV100 > PC105 > PC-S7 > P25 which is in good agreement with the experimental data given in Figure 4.7. On the other hand, μ_{max} values for MEK are much higher than the ones for toluene, which once again, reveals that titania has greater affinity toward MEK compared to toluene.

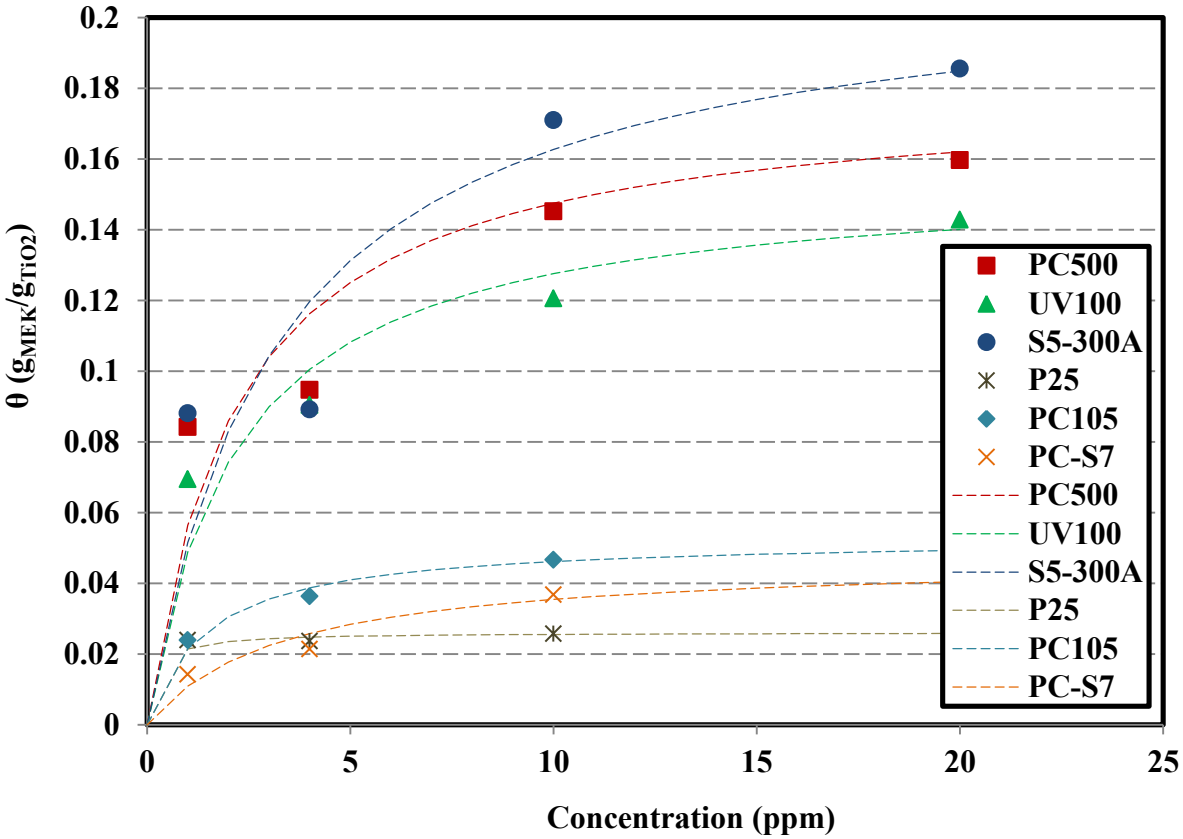

Figure 4.7 Adsorption isotherms for MEK under dry condition (dashed line: regression using Langmuir isotherm model and Langmuir parameters given in Table 4.5)

4.1.2.5. Adsorption isotherms in the presence of humidity

It is well known that water vapor can bond to various types of OH surface groups on TiO_2 via hydrogen bond. Additionally, water molecules can form a well-organized multilayer film, which drastically weaken the attraction forces between VOC molecules and TiO_2 surface [100, 157]. Hagglund et al. [158] reported that the coverage of water molecules on TiO_2 with 250 m^2/g surface area at 25% RH is between 0.3 ML and 3 ML (1 ML= bilayer of water molecules). In another study, Goodman et al. [159] calculated that P25 surface is covered with a monolayer and 2 layers of water at RH = 11% and RH = 57%, respectively. The second detrimental effect of humidity is that water molecules compete with VOCs for adsorption sites available on TiO_2. Taking into account the high concentration of water vapor (thousands of ppm) and very low concentration of VOCs (tens of ppb), clearly water vapor can overpower the adsorption of VOCs over TiO_2 [100, 160]. Besides that, since hydrogen bonding for water is stronger than van der Waals interactions for most VOCs, the adsorption of water on titania is more favorable [155].

Table 4.5 Langmuir parameters for toluene and MEK adsorption on various photocatalysts under dry and humid conditions

		Toluene			MEK		
	RH%	μmax ($g_{Toluene}/g_{TiO2}$)	K_a (ppm^{-1})	R^2	μmax (g_{MEK}/g_{TiO2})	K_a (ppm^{-1})	R^2
P25	0	-	0.0033[a]	0.96	0.0261	4.558	0.99
PC105	0	-	0.0043[a]	0.95	0.0529	0.6882	0.99
PC-S7	0	0.0242	0.3727	0.96	0.0472	0.3024	0.92
PC500	0	0.0454	0.4245	0.97	0.1754	0.4709	0.98
	20	0.0172	0.1272	0.97	0.1366	0.1254	0.99
	50	0.0116	0.0979	0.98	0.1207	0.0972	0.97
UV100	0	0.0254	1.0175	0.99	0.1554	0.4587	0.99
	20	0.0066	0.4583	0.97	0.1095	0.1069	0.97
	50	0.0043	0.2435	0.97	0.0943	0.0785	0.93
S5-300A	0	0.0311	0.7831	0.98	0.214	0.3174	0.95
	20	0.0094	0.2809	0.98	0.1258	0.0762	0.98
	50	0.0057	0.2230	0.96	0.1136	0.0522	0.98

[a] For adsorption of toluene over P25 and PC105 at dry condition, these values represent K_L calculated based Henry adsorption model.

In order to quantitatively assess the impact of humidity on the adsorption of toluene and MEK, PC500, UV100 and S5-300A, which showed superior performance in dry condition, were tested in humid air (20% and 50% RH). The adsorption isotherms of toluene at different humidity levels over Group 1 samples are depicted in Figure 4.8. As the RH is increased from 0 to 20%, the amount of adsorbed toluene drastically decreases for all three samples. This sharp decline in the adsorbent capacity for organic molecules can be partly ascribed to the adsorbed water film, which physically hinders the contact between TiO_2 and toluene. In order for toluene to be adsorbed on the surface, the water layer must accommodate toluene non-polar molecules, which necessitates the reorientation of water molecules and change in entropy which are highly unfavorable [161]. On the other hand, considering the hydrophobic nature of toluene, it is very unlikely that toluene molecules be able to attach to or dissolve in the water film on titania surface. In this regard, similar trend was observed in the adsorption of cyclohexane,

chlorobenzene, and benzene over P25 and ascribed to the hydrophobicity of these compounds [36, 40, 162]. Besides that, considering the concentration of water and toluene in the upstream air (~ 5100 ppm vs. 0.5-10 ppm), the adsorption competition between water molecule and toluene for active sites can play an important role. Taking into account that both water molecule and toluene can be adsorbed on the same receptor sites, a competitive interaction can be expected.

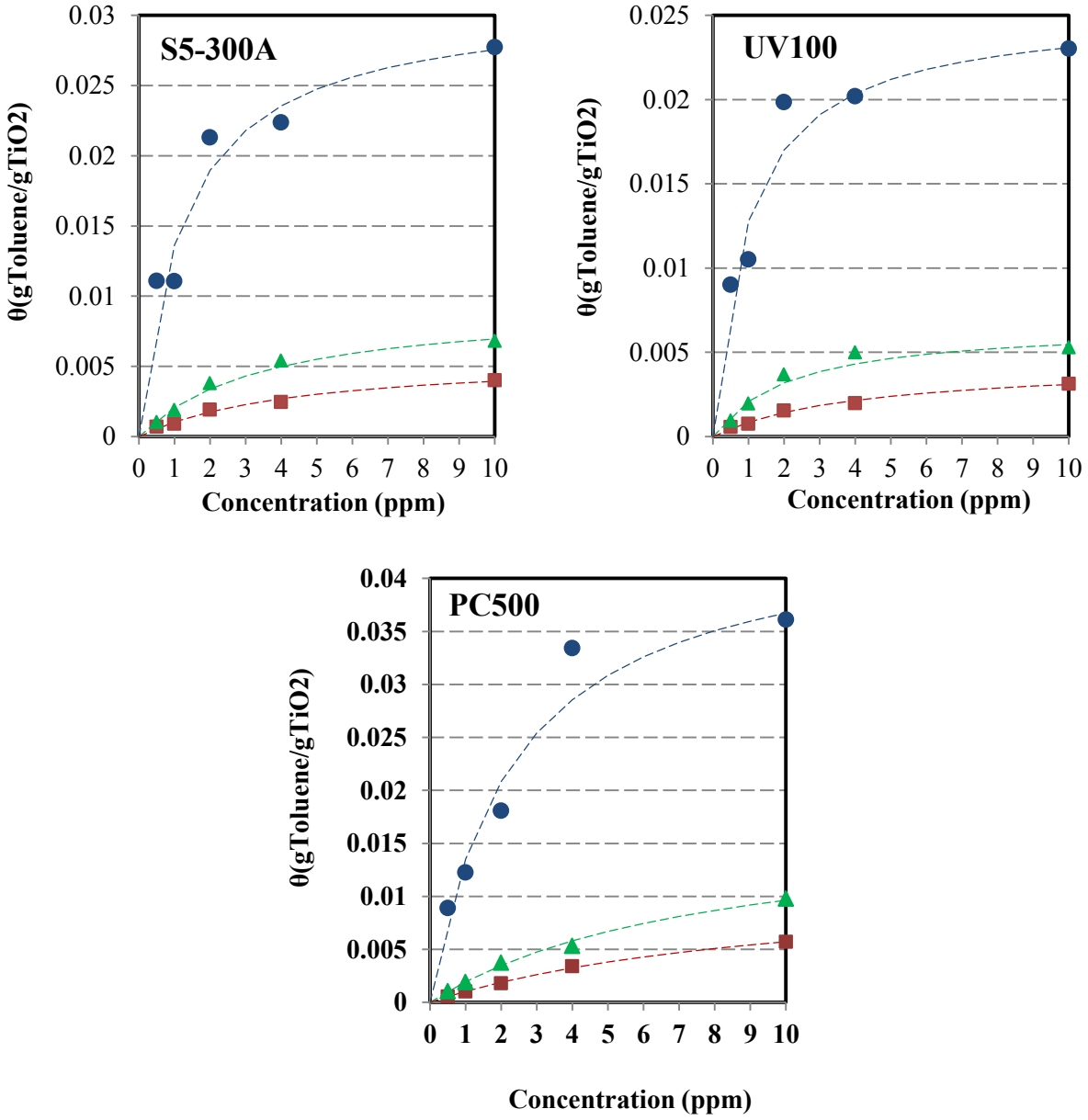

Figure 4.8 Adsorption isotherms of toluene over Group 1 photocatalysts at 0% (●), 20% (▲), and 50% (■) relative humidity (dashed line: regression using Langmuir model and Langmuir parameters given in Table 4.5)

As noted, at 500 ppb concentration the adsorption capacity is almost equal to zero for both humidity levels and on all photocatalysts due to the absolute dominance of water molecule over toluene in competition for active sites. Moreover, at low concentrations (≤ 4 ppm) and 20% or 50% RH, the difference between toluene adsorption capacities of Group 1 samples is imperceptible, pointing out that regardless of the titania surface area and surface chemistry, water molecule can be very detrimental to adsorption. The Langmuir parameters determined from adsorption isotherms of toluene at 20% and 50% RH are summarized in Table 4.5. In terms of maximum adsorption capacity, PC500 by far outperforms UV100 and S5-300A under both humidity levels despite the fact that its surface area is smaller than UV100 and S5-300A. The Langmuir adsorption constant (K_a) significantly reduces with increasing the humidity level.

Figure 4.9 displays the adsorption isotherms of MEK for Group 1 samples at different humidity levels. As can be seen, by increasing the relative humidity from 0 to 20%, the adsorption capacity experiences a considerable decline. This observation validates that even for compounds which are water soluble and polar (such as MEK), the inhibitive effect of humidity can still be significant [100]. Likewise, Kibanova et al. [41] demonstrated that in spite of formaldehyde hydrophilicity, its adsorption on P25 in the presence of humidity was strongly reduced. This can be explained by taking into account that even for polar organic molecules that can form H-bond with water, the adsorption of organic molecule entails disruption in the well-organized water network on titania surface [163]. As evident from Figure 4.8 and Figure 4.9, compared to toluene, the values of (θ_{dry}- $\theta_{Humid}/\theta_{dry}$) for all titania samples are much smaller in the case of MEK. The less intense impact of humidity on the adsorption of MEK is due to the hydrophilic character of MEK and its high water solubility (275 g/L). This is understandable since MEK can more easily penetrate the water layer and/or compete with water molecules for adsorption sites [36]. Considering the Langmuir parameters for MEK adsorption in Table 4.5, in all cases, the maximum adsorption capacities are substantially larger than those for toluene adsorption and follow the order: PC500 > S5-300A > UV100. At 20 and 50% relative humidity, the considerable decrement in MEK maximum adsorption capacities and K_a values underlines the fact that MEK is precluded from contacting titania despite its strong affinity owing to its large dipole moment.

In order to explain this behavior, it should be highlighted that considering the surface areas of photocatalysts tested (Group 1) in humid condition, according to the literature [158, 159] at RH

= 20% incomplete surface coverage (< monolayer of water molecules) and at RH = 50% multiple layers of water molecules (> bilayer) can be envisaged. Consequently, it seems logical to assume that when the surface is not completely covered with water, VOC molecules can adsorb on the unoccupied fraction of titania.

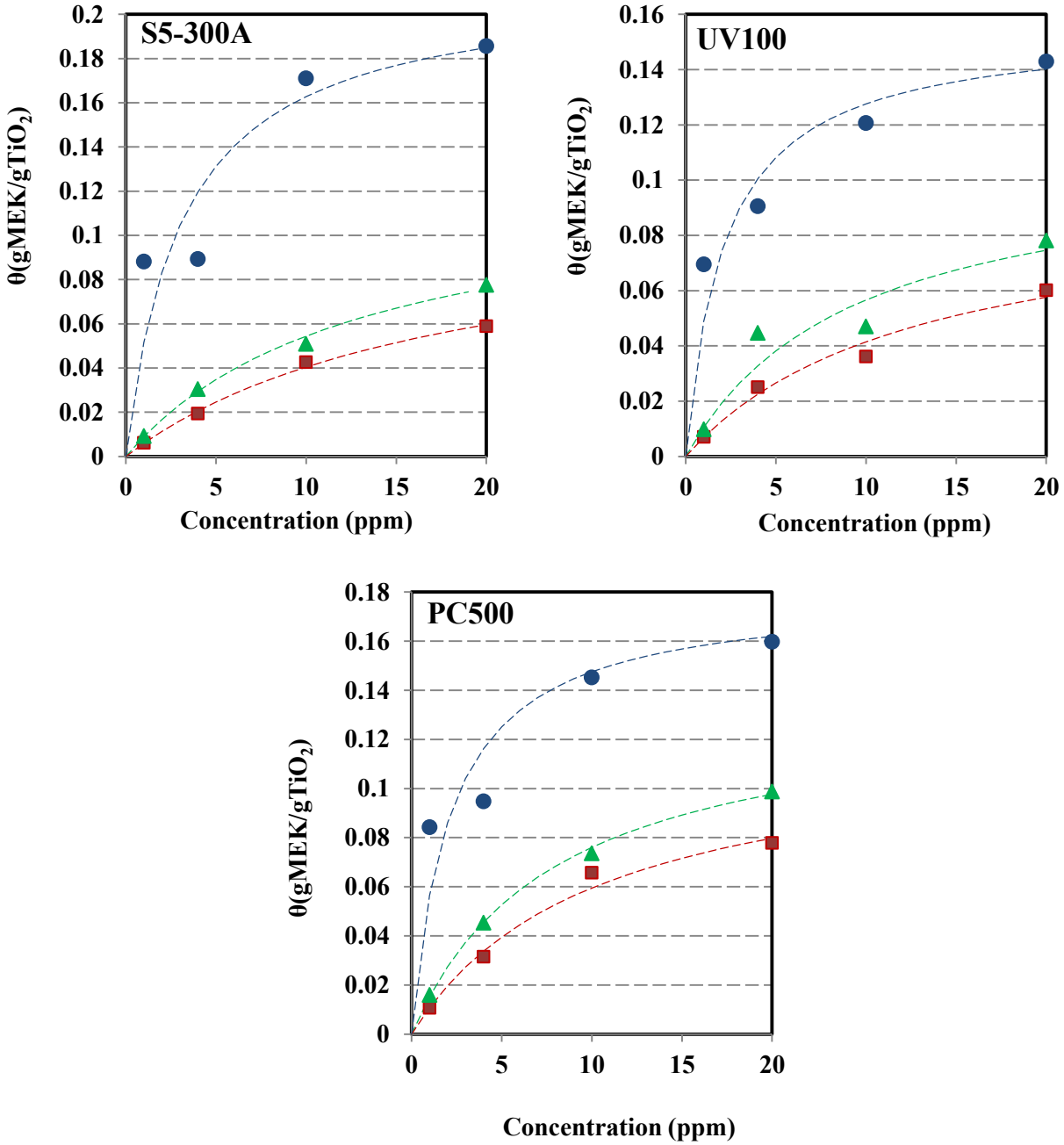

Figure 4.9 Adsorption isotherms of MEK over Group 1 photocatalysts at 0% (●), 20% (▲), and 50% (■) relative humidity (dashed line: regression using Langmuir model and Langmuir parameters given in Table 4.5)

4.1.2.6. FTIR characterization of adsorbed toluene and MEK

To more closely investigate the interactions between challenge VOC and the titania samples, static adsorption of toluene and MEK on titania was conducted and subsequently solid phase was characterized by FTIR spectroscopy. It should be mentioned that only the data of Group 1 samples are reported here for the sake of brevity, being the behavior of the Group 2 titania markedly similar. Figure 4.10 demonstrates the FTIR spectra of Group 1 photocatalysts after being exposed to gas-phase toluene for 5 h. As can be seen in this figure, most surface toluene bands are at frequencies similar to those of liquid toluene (gray curve). In this regard, the bands in Figure 4.10 are 1030 and 1179 (δ(CH) [164]), 1379 and 1459 (symmetric and asymmetric bending modes of the methyl group [109, 164, 165]), 1495 and 1604 (υ(C=C) aromatic ring [148, 165]), 2915 (υ(CH_3) [27, 150, 164]), and 3025, 3060 and 3085 cm^{-1} (υ(CH) of aromatic ring [148, 164]). The broad band between 1640-1620 cm^{-1} with a maximum at 1635 cm^{-1}, which is present in all samples, is assignable to bending mode adsorbed water [145, 148]. In the low frequency range (1800-600 cm^{-1}), beside the new absorption bands due to toluene adsorbed on the surface, no notable difference between the spectra of titania after and before adsorption was observed. In the high frequency range, several bands appeared in the range of 3100-2800 cm^{-1} which result from toluene adsorption on the surface.

The following facts can be deduced from comparing the spectra of titania before and after interaction with toluene in the high frequency range:

- For all samples, there is a redshift for band at 3728 to 3715 cm^{-1} due to the interaction between terminal isolated hydroxyl and toluene.
- The peak at 3700 cm^{-1} for UV100 and S5-300A and 3695 cm^{-1} for PC500 is considerably reduced and a new band appeared at 3686 cm^{-1} which might be attributed to the redshift of band in 3700-3695 cm^{-1}(isolated hydroxyl groups).
- For PC500 and S5-300A the band at 3625 cm^{-1} (sign of acidic OH groups) and for PC500 the band at 3663 cm^{-1} (sign of basic OH groups) completely disappeared after toluene adsorption.
- For UV100, after saturation of titania with toluene a complex band between 3675 and 3500 cm^{-1} appeared which could be ascribed to the sum effect of interactions of OH groups (positioned at 3663, 3625 and 3600 cm^{-1}) and Π electrons of toluene [150].

- For PC500, the broad band in the 3600-2800 cm^{-1} region (H-bonded OH groups) became stronger after adsorption test.

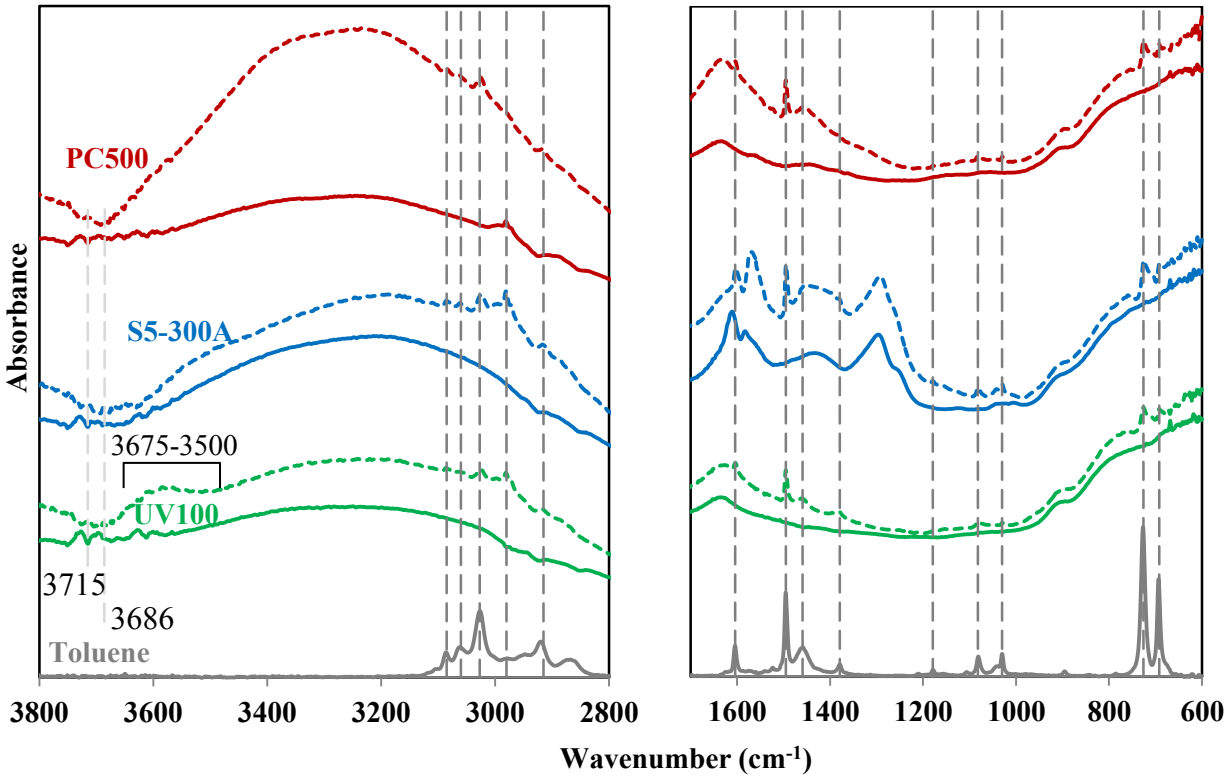

Figure 4.10 FTIR spectra of liquid toluene and Group 1 TiO_2 samples before (solid lines) and after (dashed lines) adsorption of toluene

The amounts of adsorbed toluene on Group 1 catalysts, presented in Figure 4.6, agree well with the intensity of the FTIR peaks in Figure 4.10 and can be ranked as PC500 > S5-300A > UV100. From the FTIR results, it may be inferred that toluene dominantly interact with the isolated hydroxyl groups of titania and to a much smaller extent with H-bounded OH groups.

The FTIR spectra of titania samples when brought into contact with MEK are represented in Figure 4.11. Similar to toluene, all surface MEK bands, except the band at 1713 cm^{-1}, are at frequencies similar to those of liquid MEK (gray curve). The main bands of the liquid MEK in Figure 4.11 are 1170 (C-CO-C bend), 1365, 1415, and 1460 (C-H bending [166]), 1713 (C=O stretching [166-168]), and bands between 2980-2880 cm^{-1} (C-H stretching [166]).

In the low frequency range of Figure 4.11, three sharp peaks at 1170, 1365, and 1711-1707 cm^{-1} appeared in the titania samples after being in contact with MEK for 5 h because of the adsorption of the MEK molecules on the surface. In particular, the carbonyl band (originally at 1713 cm^{-1})

red shifted to 1711 cm^{-1} for UV100 and S5-300 and to 1707 cm^{-1} for PC500 which reveals that binding MEK molecules occurs with engagement of carbonyl groups [145, 166]. Verbruggen et al. [145] proposed two adsorption mechanism for acetaldehyde on P25: via OH-Ti and carbonyl bonding to Ti^{4+}, while in our study, only the former was observed in all FTIR experiments (both Group 1 and 2). It is noteworthy that the intensities of bands due to adsorbed MEK on different titania samples (dashed lines in Figure 4.11) follow the order of S5-300A > PC500 > UV100 which corresponds well with the data presented in Figure 4.7.

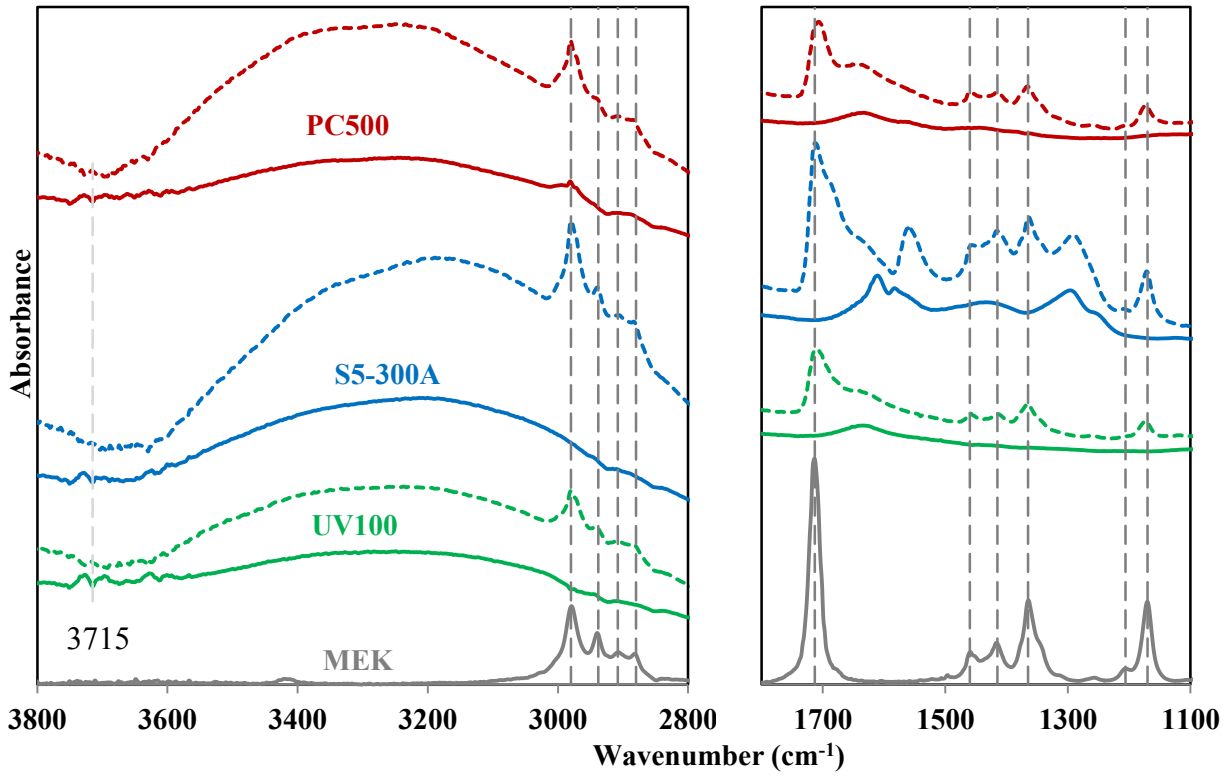

Figure 4.11 FTIR spectra of liquid MEK and Group 1 TiO_2 samples before (solid lines) and after (dashed lines) adsorption of MEK

In the high frequency region titania photocatalysts experienced significant changes upon contact with MEK which can be summarized as follows:

- For all samples, the new bands at 2980-2880 cm^{-1} are attributable to adsorbed MEK on titania surface.
- The broad band between 3600-2800 cm^{-1} in original spectra became more intense especially in the case of S5-300A and PC500, showing presence of huge amount of adsorbed MEK via H-bounded hydroxyl groups.

- Similar to toluene static adsorption, there is a redshift for band at 3728 to 3715 cm^{-1} due to the interaction between terminal isolated hydroxyls and MEK.
- For all titania photocatalysts, the rest of the bands related to free OH groups in the range of 3700-3600 cm^{-1} completely disappeared or significantly diminished after adsorption of MEK.

4.1.2.7. Interaction between VOCs and titania photocatalysts

Regarding the adsorption of ketones (e.g. MEK) on TiO_2, it has been suggested that the high electron-donor ability of carbonyl group facilitates adsorption via H-bonding to the surface hydroxyl groups of titania [169, 170]. Unlike MEK which can be chemisorbed on titania via H-bonding, physisorption of toluene on TiO_2 surface is non-dissociative and could take place through weak Π-bonding to surface hydroxyls [34, 171]. It is also noteworthy that the main inter-molecular forces mediating the interactions between aromatics and titania surface are of van der Waals type, while for ketones, the carbonyl group high dipole moment leads to stronger dipole-dipole interactions [155]. The aforementioned facts along with more polar and water soluble nature of MEK result in greater adsorption of MEK compared to toluene on titania surface. This could also be recognized by comparing the intensity growth of the wide band in 3600-2800 cm^{-1} region before and after adsorption of toluene (Figure 4.10) and MEK (Figure 4.11). Similar trend was observed by Zhong et al. [155] in a study on the adsorption of VOCs on TiO_2 coated fiberglass fibers. They found out that the adsorption capacity follows the sequence: alcohols > ketones and terpenes > aromatics > alkanes. Similarly, Alberici and Jardim [172] found the following order for affinity between various VOCs and P25: alcohols > ketones > aromatics > alkanes. In the presence of humidity, the interactions between organic molecules and TiO_2 surface are greatly altered. The adsorbed water film on hydrophilic titania diminishes the accessibility of organic vapors to active sites. Therefore, the adsorption capacity is mostly affected by the diffusion and dissolution of the pollutant into the water layer which depends on the hydrophilicity of the VOC. Accordingly, it appears that higher hydrophilicity would bring about greater sorption capacity for the VOC.

The calculated coverage values for different photocatalysts are given in Table 4.6. Kirchnerova et al. [173] attained 3.5 and 2.8 molecules $_{n\text{-butanol}}/nm^2$ on P25 and UV100, respectively, in humid air at 580 ppm concentration. For ethanol adsorption on P25 (inlet concentration of 10-200 ppm)

and 2-propanol adsorption on anatase titania, 2.8 and 2.22 molecules/nm^2 were reported, respectively [143, 174]. Data presented in Table 4.6 reveals that despite the fact that Group 1 samples offer higher adsorption capacity for MEK and toluene, once the contribution of surface area is removed (i.e. coverage value), P25 and PC105 significantly surpassed other photocatalysts in terms of the number of adsorbed VOC molecule per unit area. FTIR results show that the concentrations of free hydroxyl groups on P25 and PC105 are the largest among all samples which can support the higher coverage values obtained on P25 and PC105.

Table 4.6 Coverage values for MEK and toluene at dry condition and 4 ppm inlet concentration

		P25	PC500	UV100	PC105	PC-S7	S5-300A
Coverage value (molecule/nm^2)	MEK	3.96	2.87	2.29	3.79	0.59	2.26
	Toluene	1.66	0.79	0.40	1.29	0.38	0.44

4.2. Photocatalytic degradation of toluene and MEK: Impact of operating parameters on removal efficiency and by-products generation

Together with the properties of air filter (i.e. surface area, adsorbability, crystallinity, etc.), operating conditions including relative humidity, airflow rate, and light intensity can also affect different steps of photocatalysis. Consequently, the VOC removal efficiency and the amount and type of generated by-products vary significantly with these parameters. Relative humidity exerts great influence on both the adsorption process (section 4.1) and the rate of photocatalytic reaction mainly due to the involvement of water in formation of hydroxyl radicals. ASHRAE Standard 62.1-2016 suggests relative humidity to be kept under 65% in occupied spaces and EPA recommends the range of 30 to 50% for an indoor environment. Thus, it is of great practical importance to assess the performance of new catalytic air purification technologies at these recommended conditions for humidity. Assessing the performance under long residence times (up to several minutes) is a main shortcoming in most of the previous laboratory studies which can lead to considerable overestimation of the capability of air cleaners. In air handling units of buildings, the contact time between the air and the catalytic filter is normally in the range of tens of milliseconds. Finally, it is important to determine the photocatalytic performance at low concentrations, as in indoor environment the concentration of VOCs individually does not exceed tens of ppb. This point has been overlooked in earlier studies on indoor air treatment mainly due to analytical and technical challenges one encounters in experiments with VOCs in low ppb levels. Considering these issues, in this section the photocatalytic performance of PC500, UV100, and S5-300A (which exhibited the highest adsorption capacity for toluene and MEK (section 4.1)) and P25 (as a reference photocatalyst) were examined in wide ranges of key operating conditions including inlet concentration (100-1000 ppb), relative humidity (0-50% at 23 ˚C), light intensity (12.5-50 $W \cdot m^{-2}$), and residence time (0.02-0.1 sec). Considering the differences in the key properties of these photocatalysts (e.g. crystallinity and surface area), a comprehensive assessment of photocatalyst activity at wide ranges of operating conditions enables us to have a clearer understanding of parameters that govern the activity of a catalyst in PCO air purification.

4.2.1. Methodology

The experimental set-up design and operation are explained in details in section 3.1.2. Table 4.7 summarizes the experimental conditions at which PCO tests were conducted and the 95%

confidence interval associated with some of these parameters. Moreover, some of the PCO-relevant properties of selected photocatalysts are provided in Table 4.8.

Table 4.7 PCO tests experimental conditions (mean value ± 95% confidence interval)

Parameter	Value	Unit
Inlet concentration	101.8 ± 5.4, 1010 ± 29.8	ppb
Relative humidity	0, 19.9 ± 0.97, 48.7 ± 1.39	%
Volumetric flow rate	6, 12, 30	L/min
Residence time	0.02, 0.05, 0.1	s
Light intensity	12.5, 50	W/m^2
Temperature	23.3 ± 0.8	°C
TiO_2 concentration	1± 0.03	mg/cm^2

Table 4.8 Characteristics of titanium dioxide photocatalysts

Photocatalyst	Properties			
	BET (m^2/g)	Crystal size (nm)	Crystalline phase	Surface OH density ($/nm^2$)
P25	47	25.8	A (80%), R (20%)	4.8
PC500	276	5-10	Anatase	2.4
S5-300A	330	-	Anatase	-
UV100	330	9	Anatase	2.5

4.2.2. Results and discussion

4.2.2.1. Impact of relative humidity

Figure 4.12 illustrates the variations in toluene and MEK removal efficiencies with relative humidity on various TiO_2 photocatalysts. It shows that the increase of RH from 0 to 20% enhances the pollutant removal efficiency for all titania samples. This clearly indicates that low water vapor level promotes photocatalytic degradation of toluene and MEK. The adsorbed water molecules are oxidized by photo-generated positive holes and produce hydroxyl radicals, which are the main oxidizing agents in gas phase PCO. Consequently, one can deduce that the lack of sufficient amount of OH radicals at 0% RH leads to the inferior removal rate of challenge

compound with respect to that at 20% RH. On the other hand, water vapor can replenish the surface hydroxyl groups (via dissociative chemisorption of water on Ti^{4+} sites) which serve as adsorption sites for toluene and MEK [112, 175]. Upon further increment in RH to 50%, a significant drop in the removal efficiency is evidenced, more vividly in the case of toluene PCO. The first clear explanation is the adsorption competition between VOC and water molecules over adsorption sites on titania, which reduces the amount of VOC adsorbed on the catalyst. This is understandable since water, toluene, and MEK are all adsorbing on the same surface OH groups: water and MEK via hydrogen bonding, and toluene via weak Π-bonding [34, 176]. On the other hand, water vapor molecules carried with the air stream can generate a well-organized film on TiO_2 and can act as a physical barrier and impedes effective contact between pollutant and catalyst surface. Accordingly, VOC molecules must disorganize or break the water network (i.e. unfavorable change in entropy [36, 177]) to be adsorbed on titania and participate in the oxidation reactions [113]. It is noteworthy that the adverse impact of RH on the photocatalytic activity is more pronounced for toluene than MEK. This can be attributed to the fact that the water film can accommodate polar and water soluble molecules like MEK better than non-polar molecules of toluene. As can be seen in Figure 4.12, the best photocatalytic activities are achieved at 20% RH which also has been reported by other researchers as the optimal humidity content during PCO of toluene [34, 178]. Another interesting observation is that as RH increases, the role of catalyst surface area becomes more important; thus, in most cases the differences between removal efficiencies of P25 and other samples become greater. For instance, the difference in removal efficiency of toluene on P25 and S5-300A at dry condition is roughly 8%, while at RH=50% it is more than 44%. Understandably, the quantity and type of by-products are factors of reaction pathway, which in turn is affected by catalyst properties and experimental conditions. In the case of toluene, acetone, acetaldehyde, formaldehyde, benzaldehyde, benzene, benzyl alcohol, and benzoic acid were found to be the main by-products of photocatalytic degradation [178-180]. Regarding MEK PCO, Raillard et al. [131] reported that the main by-products are acetone, ethanol, acetaldehyde, acetic acid, methanol, formaldehyde, and formic acid.

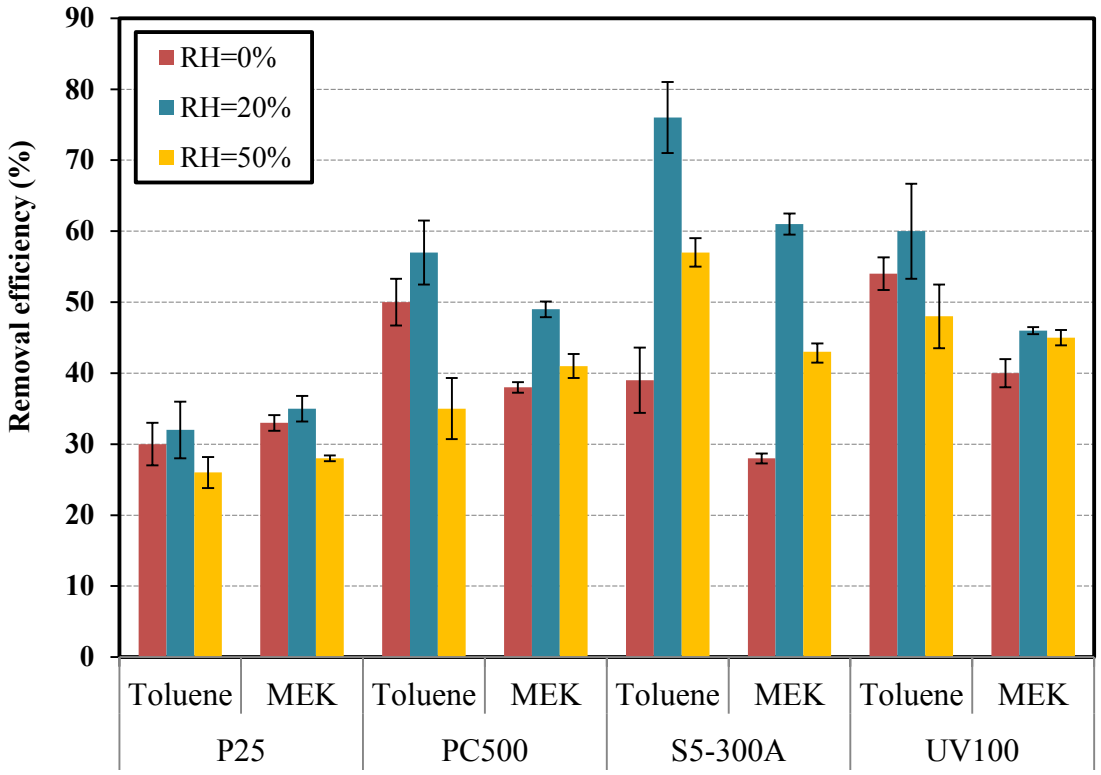

Figure 4.12 Effect of relative humidity on toluene and MEK removal efficiency. VOC inlet concentration=1 ppm, residence time=0.05 sec, light intensity=50 W/m^2. Error bar shows the minimum and maximum removal efficiencies for each experiment

In the present study, as summarized in Table 4.9, formaldehyde, acetaldehyde, and acetone are the detected gas phase by-products during the PCO of toluene and MEK. It is worth mentioning that during the PCO of toluene very small traces of benzaldehyde are also detected in the GC chromatograms. For all photocatalysts, a consistent trend is that more by-products are formed during degradation of MEK compared to toluene, which is in good agreement with previous studies [181, 182]. For MEK, by increasing RH, the quantities of formaldehyde and acetaldehyde diminish regardless of the photocatalyst type or the measured removal efficiency. This could be due to the presence of more hydroxyl radicals at 20 and 50% RH, which further the oxidation reactions toward complete mineralization to CO_2 and H_2O. Another possible explanation is that since these by-products are highly water-soluble, instead of becoming airborne, they can stay in the water layer formed on titania surface at high humidity levels. Interestingly, although VOC removal efficiency of P25 is lower in the presence of humidity with respect to other titania samples, the amount of by-products in the outlet air is higher for P25. This could be explained from two possible perspectives: 1) the degree of mineralization is higher on catalysts with larger

surface area due to the larger number of accessible active sites, and 2) the higher adsorption capacity of PC500, S5-300A, and UV100 decreases the amount of by-products in the outlet flow. Regarding the generated by-products during toluene PCO, even though toluene removal efficiencies are lower at RH=50% compared to those at 0 and 20% RH, the amounts of by-products are relatively higher, which could stem from a stronger competition between water and organic molecules at 50% RH and the presence of multi-layer water film on titania surface [178].

Table 4.9 Generated by-products during the PCO of toluene and MEK over various titania samples and at three humidity levels

MEK	P25			PC500			S5-300A			UV100		
RH (%)	0	20	50	0	20	50	0	20	50	0	20	50
Formaldehyde (ppb)	119.1	46.3	32.5	51.5	42.7	28.2	104.6	52.3	20.1	53.0	38.8	26.4
Acetaldehyde (ppb)	71.0	60.4	55.5	37.4	45.1	31.2	57.0	62.5	48.2	35.0	44.5	33.7
Acetone (ppb)	8.6	8.5	12.6	7.2	9.0	13.5	9.5	8.0	19.0	7.6	5.1	27.5
Toluene	P25			PC500			S5-300A			UV100		
RH (%)	0	20	50	0	20	50	0	20	50	0	20	50
Formaldehyde (ppb)	8.5	14.8	15.7	6.4	9.7	11.5	7.0	11.2	8.5	6.6	10.4	11.6
Acetaldehyde (ppb)	2.2	3.5	7.6	1.7	2.3	8.5	1.6	3.3	6.1	1.5	2.3	4.7
Acetone (ppb)	9.0	3.5	9.5	8.2	4.9	10.4	8.5	3.6	8.1	9.3	3.5	7.7

A possible mechanism is proposed in Figure 4.13 to explain the variations in the amount of by-products with relative humidity. In dry condition (Figure 4.13a), despite the fact that in the majority of experiments the removal efficiency is the highest, the amount of by-products is the lowest. At 0% RH, there is no water film on titania and no adsorption competition for the active sites of photocatalyst between water and formed by-products (and VOCs); thus, by-products can be easily adsorbed on free adsorption sites. Nevertheless, a part of produced by-products specifically light ones such as formaldehyde and acetaldehyde leaves the surface and enters the gas phase. At 60% RH (Figure 4.13c), even on high surface photocatalysts, a multi-layer water film can cover titania and gives rise to an extreme adsorption competition among reactants. This not only negatively affects the removal efficiency, but also forces a greater portion of by-products to detach from titania surface

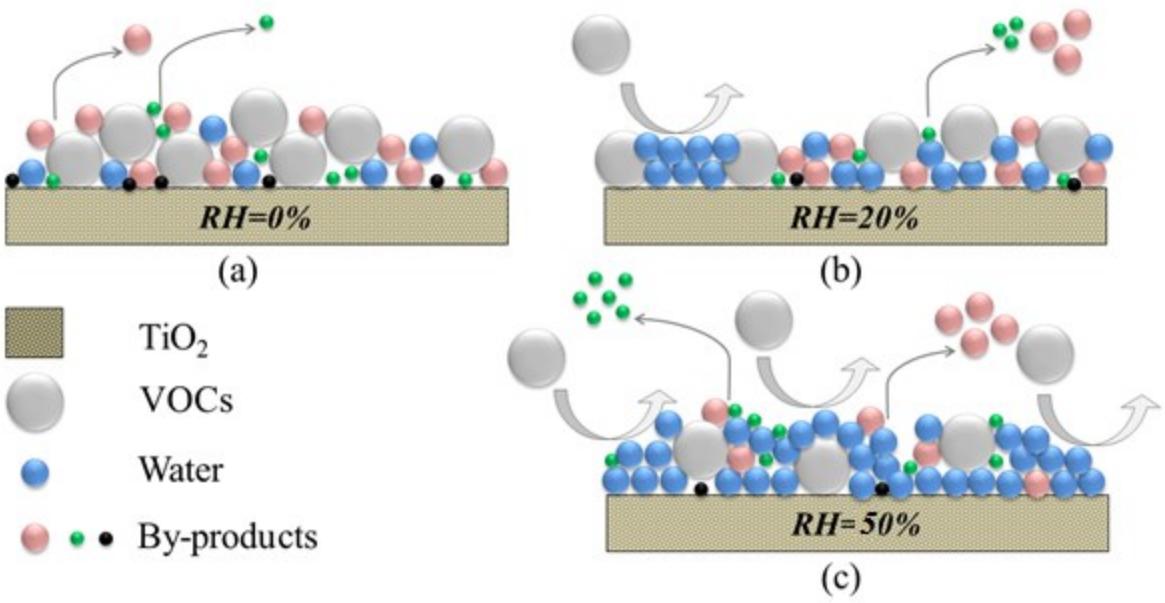

Figure 4.13 Possible effect of relative humidity level on by-product generation

4.2.2.2. Impact of airflow rate

The impact of residence time on the removal efficiency of MEK and toluene over various titania photocatalysts is presented in Figure 4.14. Taking into account the steady diminution in the removal efficiency of both MEK and toluene with decreasing residence time, clearly the prevalent factor in our experiments is the shorter residence time at higher airflow rates. By prolonging the residence time, the pollutants have longer time for adsorption on the surface and participating in oxidation reactions. Another less likely explanation is that apart from the heterogeneous reactions on the surface, gas phase reactions between the reactive species (e.g. hydroxyl and superoxide anion radicals) and VOC molecules are impaired at higher airflow rates because of the shorter contact time [92]. As depicted in Figure 4.14, the improvement in removal efficiency upon increasing the residence time is more noticeable for toluene with respect to that of MEK. For instance, as the residence time increased from 0.02 to 0.1 sec, toluene and MEK removal efficiencies respectively improved by 27% and 22% for P25, and 28% and 17% for PC500. In order to justify this observation, one should keep in mind that the affinity of titania surface toward MEK polar molecules is much stronger than that toward toluene since the former results from dipole-dipole interactions (due to carbonyl group in MEK) while the latter comes from van der Waals forces.

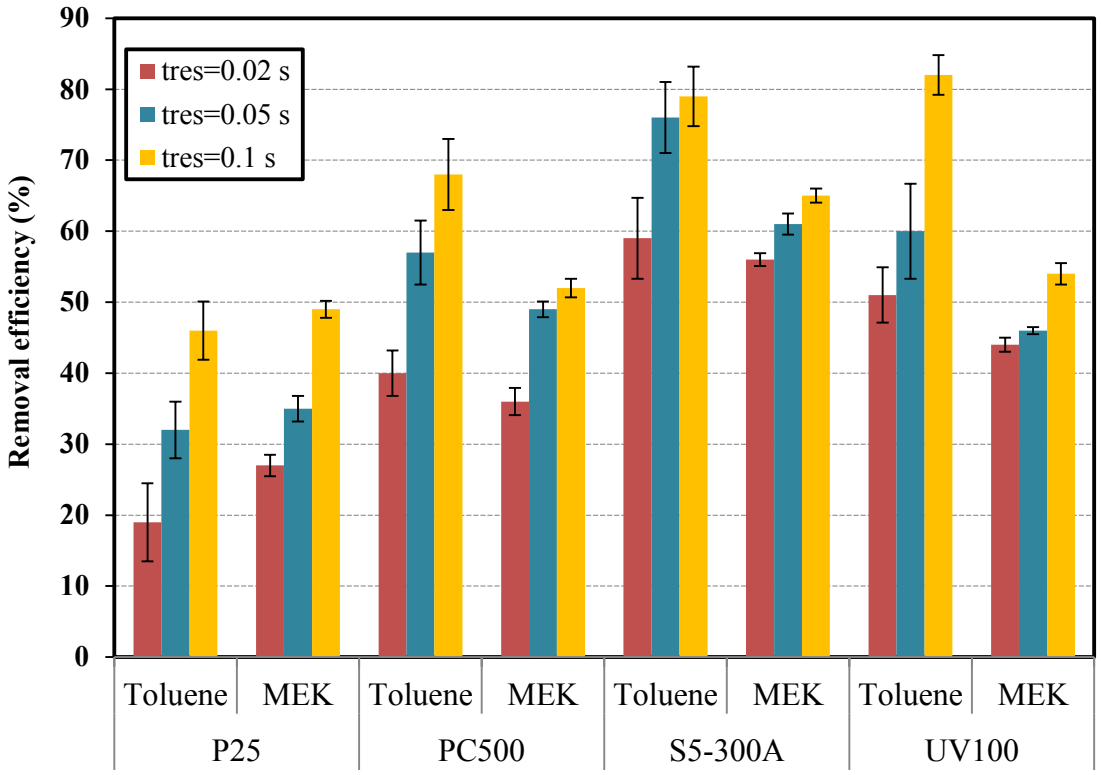

Figure 4.14 Effect of residence time on toluene and MEK removal efficiency. VOC inlet concentration=1 ppm, relative humidity=20%, light intensity=50 W/m^2. Error bar shows the minimum and maximum removal efficiencies for each experiment

P25 is a non-microporous material with large mesopores and macropores resulting from particles agglomeration; while, UV100 and PC500 have micro and meso porous structures. The meso and micropores can extend the presence of VOC molecules and intermediates on the TiO_2-coated filter and favor the photocatalytic activity. In fact, an interconnected porous structure can retard the escape of pollutants and increase the chance of adsorption on the active sites. In the case of non-porous P25, pollutants can more easily leave the catalyst surface in comparison to UV100 and PC500, resulting in a lower removal efficiency. Table 4.10 presents the amounts of by-products generated during the PCO of MEK and toluene at different residence times and on various photocatalysts. As noted, there is no correlation between the quantity of by-products and the residence time employed in the experiment. This could be due to the fact that two interconnected factors affect by-product generation at longer residence time: 1) more MEK/toluene molecules are oxidized and, thus, more intermediates and by-products are formed, and 2) by-products and intermediates have more time for complete mineralization to CO_2 and H_2O and/or adsorption on the surface. Since these factors counteract one another and are also

strongly influenced by the reaction pathways and the properties of photocatalyst, no evident trend could be underlined.

Table 4.10 Generated by-products during the PCO of toluene and MEK over various titania samples and at three residence times

MEK	P25			PC500			S5-300A			UV100		
Residence time (s)	0.02	0.05	0.1	0.02	0.05	0.1	0.02	0.05	0.1	0.02	0.05	0.1
Formaldehyde (ppb)	51.5	46.3	61.8	27.3	42.7	51.2	90.5	52.3	54.2	48.1	38.8	43.2
Acetaldehyde (ppb)	74.0	60.4	75.9	45.5	45.1	47.2	82.8	62.5	57.6	96.0	44.5	43.6
Acetone (ppb)	8.6	8.5	13.4	7.5	9.0	6.3	6.0	8.0	11.3	8.8	5.1	5.5
Toluene	P25			PC500			S5-300A			UV100		
Residence time (s)	0.02	0.05	0.1	0.02	0.05	0.1	0.02	0.05	0.1	0.02	0.05	0.1
Formaldehyde (ppb)	18.4	14.8	17.1	12.4	9.7	16.5	15.4	11.2	17.4	13.6	10.4	12.5
Acetaldehyde (ppb)	3.3	3.5	5.5	3.8	2.3	4.3	3.8	3.3	5.5	3.6	2.3	3.5
Acetone (ppb)	5.0	3.5	6.9	5.3	4.9	6.4	5.3	3.6	7.1	4.9	3.5	5.4

4.2.2.3. Impact of target VOC type and inlet concentration

Figure 4.15 illustrates the removal efficiency of toluene and MEK at two concentration levels on various TiO_2 samples. As could be expected, in all cases, the removal efficiency of the target pollutant at 100 ppb surpasses that at 1 ppm concentration. This stems from the fact that at higher VOC concentration the ratio of active sites on photocatalyst plus reactive species to VOC molecules drops and, consequently, more VOCs leave the reactor unreacted. On the other hand, as represented in Table 4.11, larger quantities of by-products are released into the gas phase during PCO at 1 ppm compared to 100 ppb for both MEK and toluene. Considering this, it is also reasonable to assume that at higher VOC concentration more active sites are occupied by intermediates and by-products. Therefore, there is a stronger competition between the original VOC and the existing by-products for adsorption on the catalyst (and reaction with the reactive radicals), which in turn leads to the inferior removal efficiency at 1 ppm. It is interesting to note that the increment in inlet concentration had the most adverse effect on the photocatalytic activity of P25 (up to 28% decrement in the removal efficiency), mainly because of its low surface area. By comparing the removal efficiencies of toluene and MEK, it can be easily seen that except in the case of P25, on all other titania samples at both concentration levels, toluene removal efficiencies are higher than those of MEK.

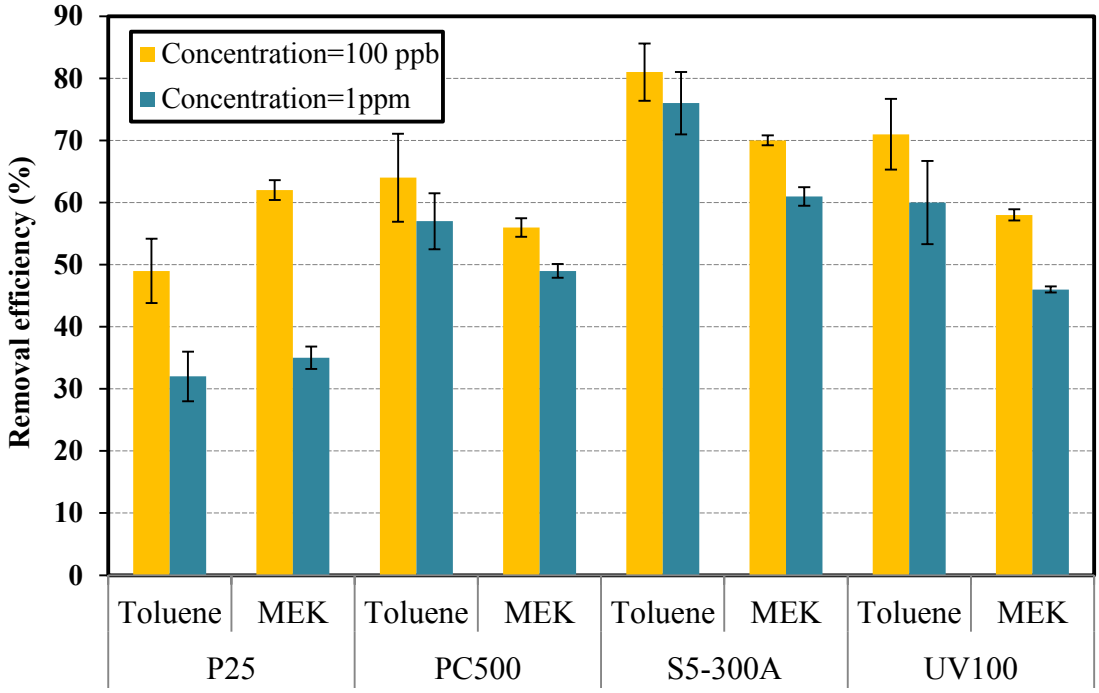

Figure 4.15 Effect of VOC inlet concentration and type on toluene and MEK removal efficiency. Residence time=0.05 sec, relative humidity=20%, light intensity=50 W/m^2. Error bar shows the minimum and maximum removal efficiencies for each experiment

One contributing factor is the higher reaction rate between $OH^{\bullet}$ and toluene, 6×10^{-12} cm^3 $molecule^{-1}$ s^{-1}, which is roughly 5 times larger than that of MEK [183]. One possible explanation for the lower removal efficiency of toluene compared to MEK on P25 is that the low surface area of P25 and weak interaction between the catalyst and toluene limit the adsorption process. In other words, it seems that in the case of toluene PCO over P25, the overall removal efficiency is controlled by the adsorption step instead of the oxidation reactions. Contrarily, for other samples, relatively high surface area along with the fast reaction rate of toluene with OH radicals outweighs the poor toluene adsorption in comparison to MEK, and ultimately brings about higher removal rate for MEK. Considering that the selected VOCs have very different polarities, the hydrophilicity/hydrophobicity character of photocatalyst can play an important role in the adsorption process and photocatalytic activity. In this regard, the hydroxyl group surface density has been suggested as a good measure of the hydrophilicity of titania surface. The values of surface OH density for P25, PC500, and UV100 are reported in Table 4.8. Although the surface OH density of P25 is twice that of UV100 and PC500, once we factor in the catalyst surface area, the total number of hydroxyl groups on PC500 and UV100 are 2.93 and 3.65 times higher than that of P25, respectively. On the other hand, the obtained data from FTIR analyses in the

previous section revealed that the population of surface OH groups on S5-300A is much greater than that on P25. Consequently, a possible reason for the superior photocatalytic performance of PC500, UV100 and S5-300A in terms of the removal efficiency and the amount of by-products could be the higher OH concentration on the surface that can promote the adsorption of VOC and its by-products. Another interesting trend which can be noticed for both toluene and MEK is that although the removal efficiency at 1 ppm on P25 is much smaller than that on PC500, the amount of by-products is higher for P25. This observation highlights the crucial impact of surface area on heterogeneous catalysis. Because of the low surface area, P25 cannot host both the incoming pollutants and by-products, which leads to not only lower removal efficiency but also an increased quantity of by-products in the outlet stream.

Table 4.11 Generated by-products during the PCO of toluene and MEK over various titania samples and at different inlet concentrations

MEK	P25		PC500		S5-300A		UV100	
Concentration	1 ppm	100 ppb	1 ppm	100 ppb	1 ppm	100 ppb	1 ppm	100 ppb
Formaldehyde (ppb)	46.3	5.8	42.7	8.5	52.3	8.5	38.8	5.5
Acetaldehyde (ppb)	60.4	8.7	45.1	8.6	62.5	7.5	44.5	6.9
Acetone (ppb)	8.5	6.8	9.0	9.1	8.0	7.3	5.1	6.1
Toluene	P25		PC500		S5-300A		UV100	
Concentration	1 ppm	100 ppb	1 ppm	100 ppb	1 ppm	100 ppb	1 ppm	100 ppb
Formaldehyde (ppb)	14.8	3.3	9.7	7.6	11.2	8.1	10.4	2.5
Acetaldehyde (ppb)	3.5	3.2	2.3	5.6	3.3	5.7	2.3	2.8
Acetone (ppb)	3.5	6.6	4.9	8.0	3.6	9.6	3.5	6.4

4.2.2.4. Impact of light intensity

The light intensity effect on the VOC removal efficiency and by-products generation is presented in Figure 4.16 and Table 4.12, respectively. It is well established that increasing the light intensity results in the generation of more electrons and holes which are key reactants in photocatalytic reactions and their shortage can greatly reduce the removal efficiency. Figure 4.16 illustrates that as the light intensity is lowered from 50 to 12.5 W/m^2, the removal efficiency considerably diminishes, however to different extents depending on the photocatalyst. It has been suggested that the co-presence of anatase and rutile particles in P25 and band bending in rutile particles prevent charge recombination [29, 30]. Additionally, with respect to P25 (80% anatase

and 20% rutile), other samples are pure anatase and so have slightly larger band gaps (anatase and rutile band-gaps are 3.23 and 3.02 eV, respectively). These bring about generation of smaller number of charge carriers and also faster recombination rate of electrons and holes. Moreover, it should be emphasized that PC500, UV100, and S5-300A have a lower degree of crystallinity compared to P25, which means larger number of defects in the crystalline structure and higher amount of amorphous titania in these samples [30, 184]. In this study, these factors lead to more efficient utilization of UV light and, therefore, less severe performance drop for P25 with respect to other samples. For instance, toluene and MEK removal efficiencies respectively decline by 18% and 11% over P25, and 27% and 25% over S5-300A when light intensity is reduced from 50 to 12.5 W/m^2.

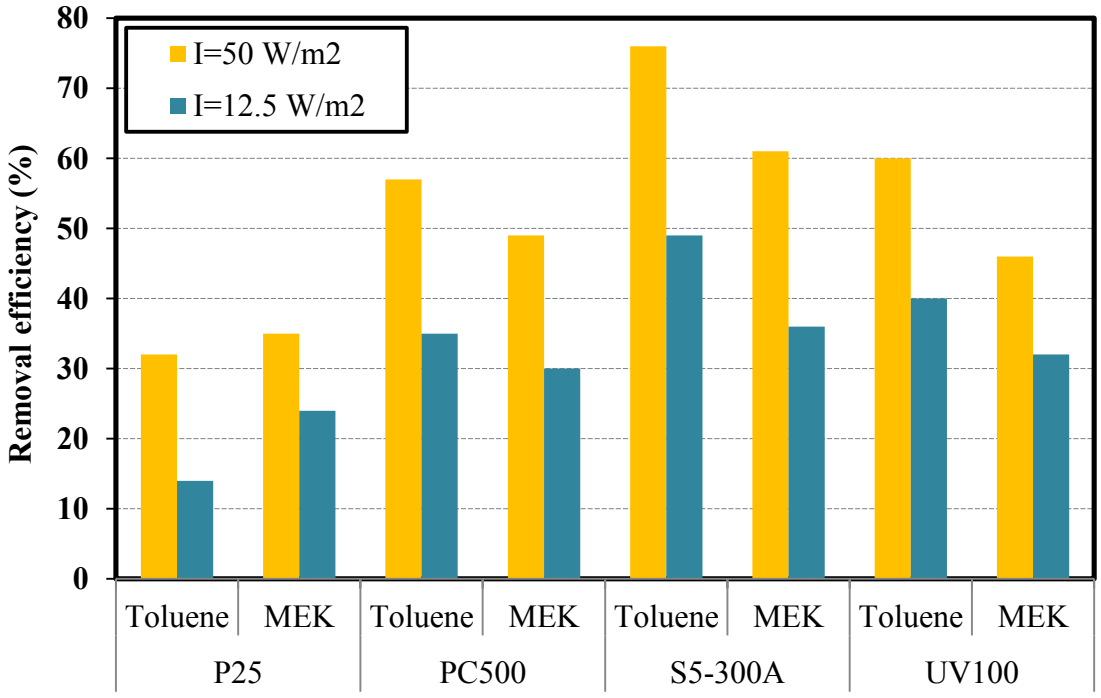

Figure 4.16 Effect of light intensity on toluene and MEK removal efficiency. VOC inlet concentration=1 ppm, residence time=0.05 sec, relative humidity=20%. Error bar shows the minimum and maximum removal efficiencies for each experiment

The negative influence of poor light utilization for PC500, UV100, and S5-300A is mitigated when the light intensity is high (i.e. 50 W/m^2) since sufficient amount of charge carriers are formed for photocatalytic reactions, even after considering the surface and bulk recombination. As a result, at 50 W/m^2, other features of photocatalyst such as surface area and adsorption capacity for VOC become more dominant and result in much better performance for PC500,

UV100, and S5-300A compared to P25. Another noted trend is that upon decrement in light intensity, toluene photocatalytic degradation is suppressed more severely in comparison to that of MEK. Decreasing light intensity from 50 to 12.5 W/m^2, toluene and MEK removal efficiency losses are in the range of 18-27% and 11-25% respectively, depending on the photocatalyst. To explain this observation, one should bear in mind that toluene (C_7H_8) needs more oxygen or hydroxyl radicals compared to MEK (C_4H_8O) for complete mineralization. As discussed before, at low light intensity, scarcity of reactive radicals can be anticipated (due to the smaller number of charge carries) which naturally results in harsher deterioration in toluene elimination rate. Low light intensity also negatively affects the amount of by-products in the outlet air since the number of charge carriers and, consequently, reactive radicals are not sufficient to degrade both the incoming pollutant and the generated intermediates/by-products. As can be seen in Table 4.12, even though the removal efficiency at 50 W/m^2 is much higher than that at 12.5 W/m^2, the amounts of by-products in the downstream are still comparable and in similar ranges.

Table 4.12 Generated by-products during the PCO of toluene and MEK over various titania samples and at different light intensities

MEK	P25		PC500		S5-300A		UV100	
Light intensity (W/m^2)	50	12.5	50	12.5	50	12.5	50	12.5
Formaldehyde (ppb)	46.3	34.3	42.7	35.3	52.3	33.1	38.8	22.3
Acetaldehyde (ppb)	60.4	38.0	45.1	48.5	62.5	56.5	44.5	36.2
Acetone (ppb)	8.5	10.7	9.0	7.2	8.0	17.3	5.1	27.4
Toluene	P25		PC500		S5-300A		UV100	
Light intensity (W/m^2)	50	12.5	50	12.5	50	12.5	50	12.5
Formaldehyde (ppb)	14.8	10.5	9.7	8.1	11.2	9.4	10.4	4.8
Acetaldehyde (ppb)	3.5	2.7	2.3	1.5	3.3	5.2	2.3	3.6
Acetone (ppb)	3.5	6.6	4.9	12.8	3.6	2.7	3.5	7.5

Chapter 5

5. Photocatalytic activity of hydrothermally/solvothermally prepared titanium dioxide photocatalysts

5.1. Impact of hydrothermal preparation time, temperature, and pressure

Given the immense impact of photocatalyst's features on performance, finely tailoring the crystalline and textural properties of TiO_2 for air purification is of great importance to enhance its activity, durability, and commercial acceptance. In this context, hydrothermal preparation parameters can be exploited to purposefully control the properties of final products. In this section, a series of porous TiO_2 photocatalysts are prepared, by systematically varying the preparation conditions including time, temperature, or pressure (i.e. filling ratio). Previous studies showed that hydrothermal time and temperature significantly affect the textural and crystalline structure of TiO_2. The ultimate goal is to explore preparation-property-performance relationships. The presented property-activity relationships can be utilized as potential design criteria for the development of new TiO_2 photocatalysts for air purification. To date, only a few works have been done on the impact of hydrothermal synthesis parameters on titania properties and its activity for indoor air purification. Therefore, there is a lack in understanding of how catalyst features influence the pollutant removal efficiency and by-products generation. The aim of the present study is to systematically investigate the effect of these preparation parameters on catalyst features and photocatalytic performance. This objective was addressed in three steps: (1) preparation of a number of photocatalysts by varying hydrothermal time, temperature, and pressure; (2) comprehensive characterization to obtain information on key properties of titania; and (3) photoactivity assessment and highlighting the preparation-property and property-performance relationships.

5.1.1. Methodology

5.1.1.1. Photocatalyst preparation

All chemicals used in this study were used as received without further purification. Distilled water was employed in the preparation of all titania samples. In a typical synthesis procedure, a calculated amount of TBOT ($Ti(OC_4H_9)_4$ from Aldrich) was added dropwise at a rate of 2

mL/min to distilled water in the absence of stirring at room temperature. The volume ratio of the reaction medium to TBOT in all experiments was fixed at 10. The solution aged for 24 h at ambient temperature (21 ˚C) and afterwards the white-yellow precipitates were filtered. The filtered solids were washed several times with distilled water until the washing solution reached pH of ca. 7, and subsequently dried at 80 ˚C for 12 h. In order to investigate the impact of reaction time, temperature, and pressure, hydrothermal reactions were conducted at different temperatures (100-220 ˚C), durations (1-48 h), and reactor filling ratios (20-90%). A specific amount of amorphous titania sample was placed in a 100 mL stainless steel autoclave with a Teflon liner and the liner was filled with distilled water until it reached the desired filling ratio. The mass ratio between the amorphous TiO_2 and water within the autoclave was kept at 0.025. The autoclave was heated at a rate of 3 ˚C/min to the target temperature, maintained at that temperature for the desired hydrothermal time, and finally cooled down to room temperature.

Table 5.1 Hydrothermal preparation conditions of different TiO_2 photocatalysts

	Preparation parameters		
Name*	Temperature (˚C)	Time (h)	Filling percentage (%)
H-Base	180	12	80
Ht-1	180	1	80
Ht-2	180	3	80
Ht-3	180	6	80
Ht-4	180	24	80
Ht-5	180	48	80
HT-1	100	12	80
HT-2	140	12	80
HT-3	200	12	80
HT-4	220	12	80
HP-1	180	12	20
HP-2	180	12	40
HP-3	180	12	60
HP-4	180	12	90

*In naming, t, T, and P respectively stand for time, temperature and pressure of hydrothermal reactions.

The resulting precipitate was filtered, washed with distilled water, and finally dried at 80 ˚C for 12 h as the post-synthesis thermal treatment. The hydrothermal preparation parameters as well as the assigned name to each photocatalyst are listed in Table 5.1.

The experimental set-up design and operation are explained in details in section 3.1.2. The experimental conditions for PCO tests of this section are given in Table 5.2.

Table 5.2. PCO tests experimental conditions

Parameter	Value	Unit
Inlet concentration	1005 ± 18.4	ppb
Relative humidity	20.5 ± 0.4	%
Volumetric flow rate	12	L/min
Residence time	0.05	s
Light intensity	5	mW/cm^2
Temperature	22.6 ± 0.7	°C
TiO_2 concentration	1± 0.05	mg/cm^2

5.1.2. Results and discussion

5.1.2.1. Photocatalyst characterization

5.1.2.1.1. Crystal structure

Figure 5.1a illustrates XRD patterns of TiO_2 samples treated for various durations at 180 ˚C and 80% filling ratio. Expectedly, the as-prepared sample (i.e. without undergoing hydrothermal treatment) is amorphous since the rate of hydrolysis reaction of titanium precursor in pure water at room temperature is low and, thus, the hydrolysis cannot proceed completely. Therefore, the TiO_2 sample before hydrothermal reactions contains a considerable amount of unhydrolyzed alkyls, which hinder crystallization by adsorbing on the surface of titania particles. Contrarily, samples underwent hydrothermal treatment show presence of both anatase, as the dominant crystal phase, and brookite. After hydrothermal treatment for only 1 h, a significant phase transformation from amorphous to crystalline titania is witnessed. The diffraction peaks of Ht-1 can be indexed to anatase (JCPDS No. 21-1272) and brookite TiO_2 (JCPDS No. 29-1360). By prolonging the hydrothermal synthesis duration to 3 h, anatase and brookite peaks intensities

increase, implying an improvement in crystallization. Additionally, the widths of the diffraction peaks at 2θ=25.28 ˚ (anatase (101) plane) and 2θ=30.80 ˚ (brookite (121) plane) decrease as the hydrothermal time increases from 1 to 3 h. The sharpening of diffraction peaks stems from the increment in anatase and brookite crystal sizes from 6.1 and 7.4 nm for Ht-1 to 6.9 and 7.7 nm for Ht-2. As a consistent behavior, extending the hydrothermal synthesis time results in gradual crystal size enlargement, higher degree of crystallinity, and lower amorphous TiO_2 content (see Table 5.3). After 6 h of hydrothermal treatment, the TiO_2 sample contains 81.5% anatase and 18.5% brookite phase. Notably, the brookite content (mass fraction) increased with hydrothermal time up to 6 h (18.5%) and from that point on experiences a downward trend. The sample undertaken 48 h of hydrothermal treatment possesses the highest relative anatase crystallinity and largest crystal sizes due to the advancement of crystallization process with time. The impact of hydrothermal temperature on the phase structures of titania samples is presented in Figure 5.1b. With raising the hydrothermal temperature, the XRD peaks intensities significantly grow and coherently the widths of diffraction peaks of anatase and brookite become smaller. These observations support the fact that higher temperature within autoclave leads to better crystallinity (i.e. smaller amorphous content) and crystal growth. This is due to the fact that Ostwald ripening process is improved at a higher hydrothermal temperature or a longer hydrothermal time. It is known that the primary driving force for simple crystal growth is the reduction in surface energy. According to Ostwald ripening phenomenon, growth of large particles at the expense of smaller particles (and concurrent morphology evolution) is driven by the tendency to minimize the area of high surface energy faces [185]. Even at temperatures as low as 100 ˚C, crystalline titania could be synthesized, which is beneficial in terms of energy requirement and obtaining large surface areas [186]. In order to compare the crystallinity of different samples, the intensity of the (101) diffraction peak of the anatase phase was regarded as a measure. The relative crystallinity was calculated by dividing the intensity of the (101) peak of each sample to that of H-Base. As shown in Table 5.3, the relative anatase crystallinity and crystal size steadily increase with hydrothermal temperature. For instance, at 100 ˚C the anatase and brookite crystal sizes are 5.9 and 7.3 nm, respectively, while at 220 ˚C these values reach 9.5 and 10 nm and the relative crystallinity almost doubles. Regarding the impact of hydrothermal temperature on phase composition, there are insignificant variations in anatase content among

samples prepared at temperature lower than 220 °C. The anatase content reaches its maximum at 220 °C, 89.7%, which indicates that high temperature favors anatase phase formation.

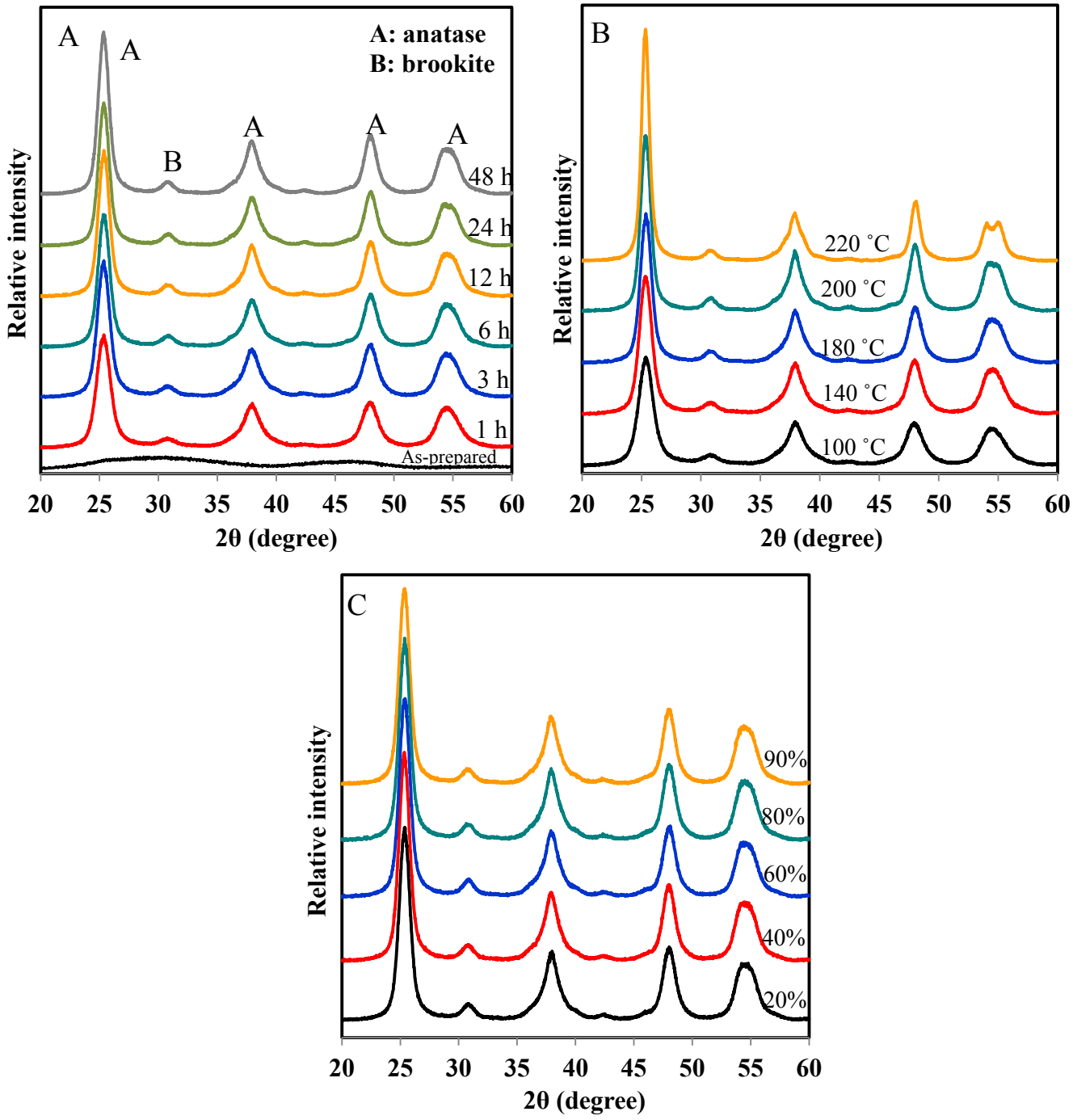

Figure 5.1 XRD patterns of photocatalysts prepared at different (a) hydrothermal durations, (b) hydrothermal temperatures, and (c) autoclave filling ratios

Filling ratio is defined as the volume of reaction medium to the volume of autoclave. During the hydrothermal synthesis, the pressure inside the system is the sum of the pressure generated by saturated water vapor and the pressure resulted from CO_2 evolution via decomposition of titanium precursor [187]. Accordingly, the filling ratio determines the pressure during TiO_2 crystallization. Despite its potential impact on the properties of yielded titania, this aspect of hydrothermal synthesis has rarely been discussed in previous works. Hsiao et al. [187] stated that the pressurized environment in the autoclave can improve the crystallization process.

Table 5.3 Crystalline and textural properties of titania photocatalysts prepared at various hydrothermal conditions and P25

Name	Amorphous content (%)	Crystalline phase (%)		Crystal size (nm)		Relative crystallinity	Surface area (m^2/g)	Band gap (eV)
		A	B	A	B			
P25	9.0	81.3	18.7 (R)	25.3	27.4 (R)	-	53.23	3.01
As-prepared	100	-	-	-	-	-	346.5	-
H-Base	14.6	83.4	16.6	7.6	8.3	1	155.5	3.20
Ht-1	17.4	84.6	15.4	6.1	7.4	0.80	219.1	3.19
Ht-2	16.0	82.8	17.2	6.9	7.7	0.93	181.0	3.21
Ht-3	14.6	81.5	18.5	7.3	8.0	0.96	168.4	3.19
Ht-4	14.7	89.0	11.0	7.9	8.5	1.14	148.3	3.21
Ht-5	12.6	92.3	7.7	8.8	9.2	1.34	134.9	3.21
HT-1	20.5	82.3	17.7	5.9	7.3	0.74	237.2	3.20
HT-2	15.9	83.1	16.9	6.9	7.9	0.90	183.5	3.19
HT-3	12.3	82.3	17.7	8.4	8.7	1.16	146.7	3.21
HT-4	11.0	89.7	10.3	9.5	10.0	1.47	139.1	3.22
HP-1	15.1	83.7	16.3	7.2	8.3	0.95	163.2	3.18
HP-2	14.5	83.2	16.8	8.4	8.9	1.04	151.4	3.22
HP-3	14.4	82.8	17.2	7.8	8.4	0.98	162.7	3.19
HP-4	14.4	81.5	18.5	7.7	8.7	0.97	165.3	3.21

* Relative anatase crystalinity is calculated by dividing the intensity of the anatase (101) diffraction peak to that of H-Base. A: anatase, B: brookite, R: rutile

Figure 5.1c depicts the XRD patterns of TiO_2 samples prepared at different autoclave filling ratios. As can be noted in Figure 5.1c and Table 5.3, the impact of autoclave filling ratio on crystallinity and crystal size is much less in comparison to that of hydrothermal temperature or

hydrothermal time. The relative crystallinity, phase composition and crystal size vary in narrow ranges by increasing the autoclave filling ratio and no consistent correlation between filling ratio and crystalline structure could be found. For example, the relative crystallinity increases by increasing the filling ratio from 20% to 40%, decreases at 60% and then increases when 80% filling ratio is applied. Evidently, simultaneous effects of pressure, temperature, and water allowed crystallization to occur at relatively lower temperature compared to "sol-gel route + calcination" [188]. It is believed that water molecules catalyze the rearrangement of the TiO_6 octahedra in the amorphous titania by adsorption to the titania surface reaction, accelerating crystallization [189] and along with high temperature and pressure in autoclave facilitate structural changes [190]. Figure 5.2 illustrates a graphical presentation of the crystalline structure of TiO_2 before and after hydrothermal synthesis at maximum time (Ht-5), temperature (HT-4), and pressure (HP-4). The crystalline and textural properties of as-prepared titania sample (100% amorphous and 346.5 m^2/g surface area) dramatically change after the hydrothermal treatment. As can be seen, a major portion of the amorphous titania (70.7-80.7%) transforms to crystalline anatase upon hydrothermal treatment. Compared to high hydrothermal time (48 h) or temperature (220 °C), high reactor filling ratio (i.e. pressure) leads to the formation of more brookite phase, 14.9%. The activation energy for anatase-to-brookite transformation is small (11.9 kJ/mol); while for brookite-to-rutile transformation much higher energy is required (163.8 kJ/mol) [134]. Therefore, the A→B transition can proceed at such low temperatures (100-220 °C) and results in the appearance of brookite phase after hydrothermal synthesis. Yu et al. [191] reported that the formation of brookite phase can be promoted in acidic environment. Considering that in our preparation method the reaction medium was non-acidic, it is reasonable to assume that the hydrothermal environment led to the formation of brookite phase.

5.1.2.1.2. Surface area and porosity

The influence of hydrothermal preparation factors on surface area and pore structure were investigated by nitrogen adsorption-desorption technique. The BET surface area of titania samples prepared at different preparation conditions are provided in Table 5.3. All yielded titania samples possess high surface area, a fact which underlines the advantage of hydrothermal preparation route. The BET surface area monotonically decreases with reaction time and hydrothermal temperature which is in good agreement with the XRD results.

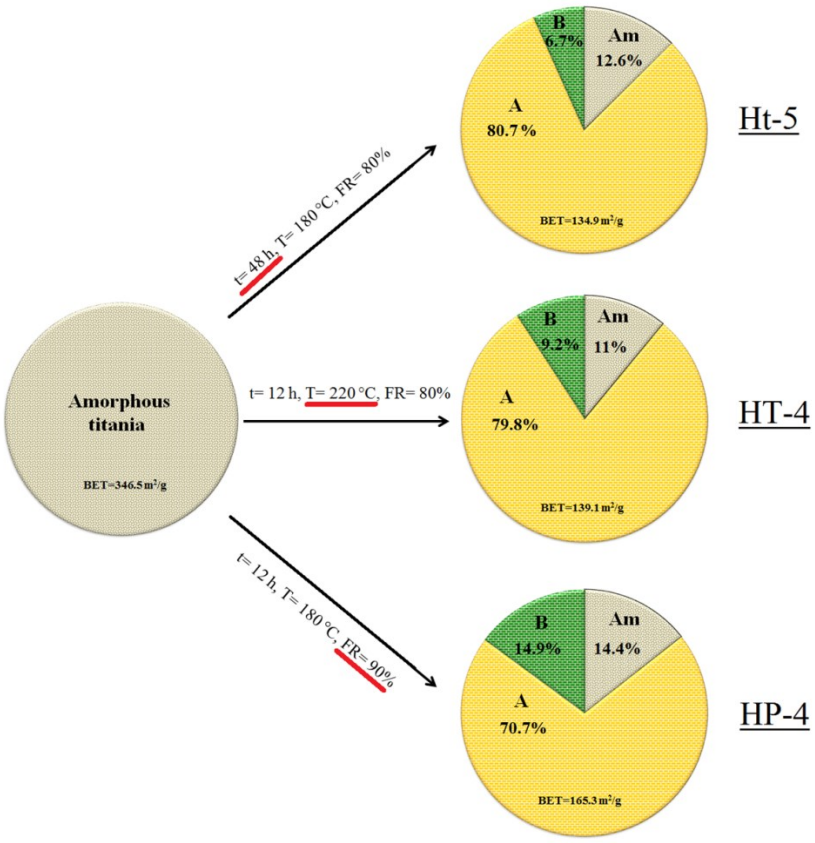

Figure 5.2 Graphical presentation of the impact of hydrothermal treatment on titania structure

As could also be predicted from the significant crystal growth, the surface area of the as-prepared sample decreases by 37% after 1 h of hydrothermal treatment. After this initial sharp drop, increasing the reaction time gradually diminishes the surface area until it reaches its minimum for Ht-5. Analogous to the influence of reaction time, rising the hydrothermal temperature leads to an almost linear reduction in the surface area of titania samples. As an instance, as the hydrothermal temperature is raised from 100 to 220 °C the surface area decreases from 237.2 to 139.1 m^2/g. Figure 5.3 and Figure 5.4 present the adsorption-desorption isotherms and the corresponding pore size distributions of as-prepared titania, Ht-1, H-Base and HT-4. Before hydrothermal treatment, the TiO_2 sample has a large surface area, 346.5 m^2/g, due to its amorphous structure. As shown in Figure 5.3a, the as-prepared TiO_2 exhibits isotherm of types I and IV (BDDT classification): at low relative pressures ($p_0/p < 0.1$), the isotherm shows a high adsorption due to the presence of micropores (type I) and the narrow and continuous hysteresis loop at higher relative pressures indicates the existence of mesopores (type IV). This is also in good agreement with the pore size distribution (Figure 5.4a) which confirms a huge amount of

micropores (pore width < 2 nm) and smaller amount of mesopores (2 < pore width < 50 nm) in the as-prepared sample structure. All the other samples show isotherms of type IV with hysteresis loops appearing at high relative pressures, indicating the presence of mesopores. The shapes of hysteresis loop are of type H2, associated with narrow necks and wider bodies (ink-bottle pores). By increasing the hydrothermal time from 1 h to 12 h (Ht-1 and H-Base respectively), the hysteresis loop shifts slightly to a region with higher relative pressure, implying an increment in the average pore size. Regarding the impact of hydrothermal temperature, by rising the temperature from 180 to 220 °C (H-Base and HT-4 respectively), the hysteresis loop moves rightward and downward to a region with higher relative pressure and lower adsorbed volume, showing increment in pore size and decrement in specific surface area. All hydrothermally-prepared samples appear to possess a considerable amount of mesopores within their porous structures which could explain the high surface areas. The increment in pore sizes and the reduction in surface area at more severe hydrothermal conditions (i.e. longer time, higher temperature, and higher filling ratio) can be explained as follows. Considering the fact that smaller pores bear greater stress than the bigger ones, during hydrothermal synthesis smaller pores collapse sooner. Secondly, as evidenced by XRD analyses, at harsher hydrothermal conditions, larger crystals are formed due to the crystal growth and, thus, pores result from the aggregation of these crystals would be bigger

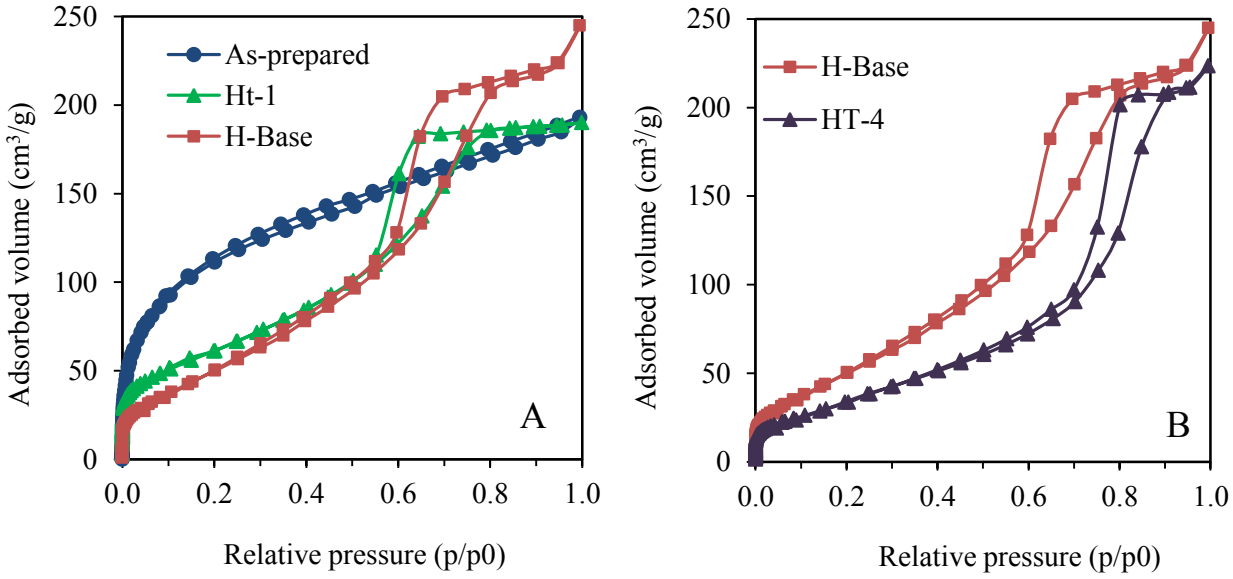

Figure 5.3 Nitrogen adsorption–desorption isotherms of hydrothermally-prepared titania photocatalysts; Impact of hydrothermal preparation time (a) and temperature (b)

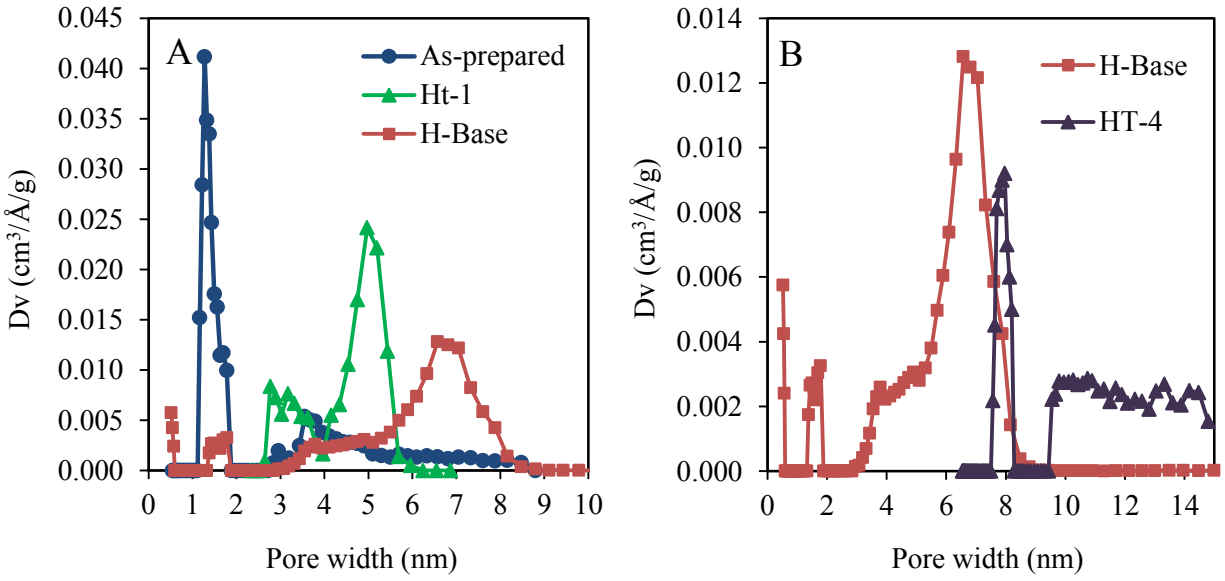

Figure 5.4 Pore-size distribution of hydrothermally-prepared titania photocatalysts; Impact of hydrothermal preparation time (a) and temperature (b)

5.1.2.1.3. SEM and TEM

The macroporous structure of the yielded titania powder was directly examined by scanning electron microscopy. The SEM images of H-Base (treated at 180 °C for 12 h and 80% filling ratio) are presented in Figure 5.5. In Figure 5.5a, it can be clearly seen that the yielded titania sample possesses macroporous structure with pore size ranging from 0.5-3 µm. Judging from Figure 5.5b (side view of H-Base sample), H-Base exhibits a disordered macroporous frameworks with continuous walls with thickness of about 4-8 µm extend through the whole particle. The type of reaction medium can greatly influence the pore size and shape of macroporous structure. It was proposed that when the dominant solvent in the reactor is water meso-macroporous structure with macrochannels and mesoporous walls can be expected [192]. The well-oriented macroporous channels are arranged parallel to each other and perpendicular to the outer surface of the particle. The macroporous channels formed during the hydrothermal synthesis not only can facilitate the mass transfer of pollutants molecules to the active sites of titania, but also serve as paths for emitted photons to reach the particle's interior regions. As it is shown in the inset of Figure 5.5b, a portion of titania particles fused together in the form of dimers or trimmers instead of incorporating in the main structure of macro/micro porous titania. This could result from the attachment of titania particles via the condensation reaction, considering the abundance of surface OH groups on TiO_2 particles. Upon the contact between

TBOT droplet and water in the first step of preparation procedure, a semipermeable TiO_2 layer forms on the droplet surface. This layer divides the subsequent hydrolysis and condensation reactions. These reactions proceed inwardly, and approximately perpendicular to the external surface of the particles, as the distilled water diffuses through the outer membrane. This produces microphase-separated regions of TiO_2 nanoparticles and water/alcohol channels within the TBOT droplets that undergo spontaneous radial patterning caused by the hydrodynamic flow of the solvent [193]. We suggest that the mesoporosity is partly due to the intraparticle porosity and partly due to interparticle porosity. The SEM results along with the information extracted from N_2 adsorption-desorption indicate that H-Base has a trimodal pore structure of a micro-meso-macro porous system. Moreover, the microstructure of the nickel foam filter coated with H-Base photocatalyst is presented in Figure 5.5c and d. The nickel foam filter shows a 3-D porous network with pore sizes ranging from 100 to 800 μm. As seen, titania nanoparticles are mostly deposited on the filter framework and in some regions particles filled the oval-shape void spaces.

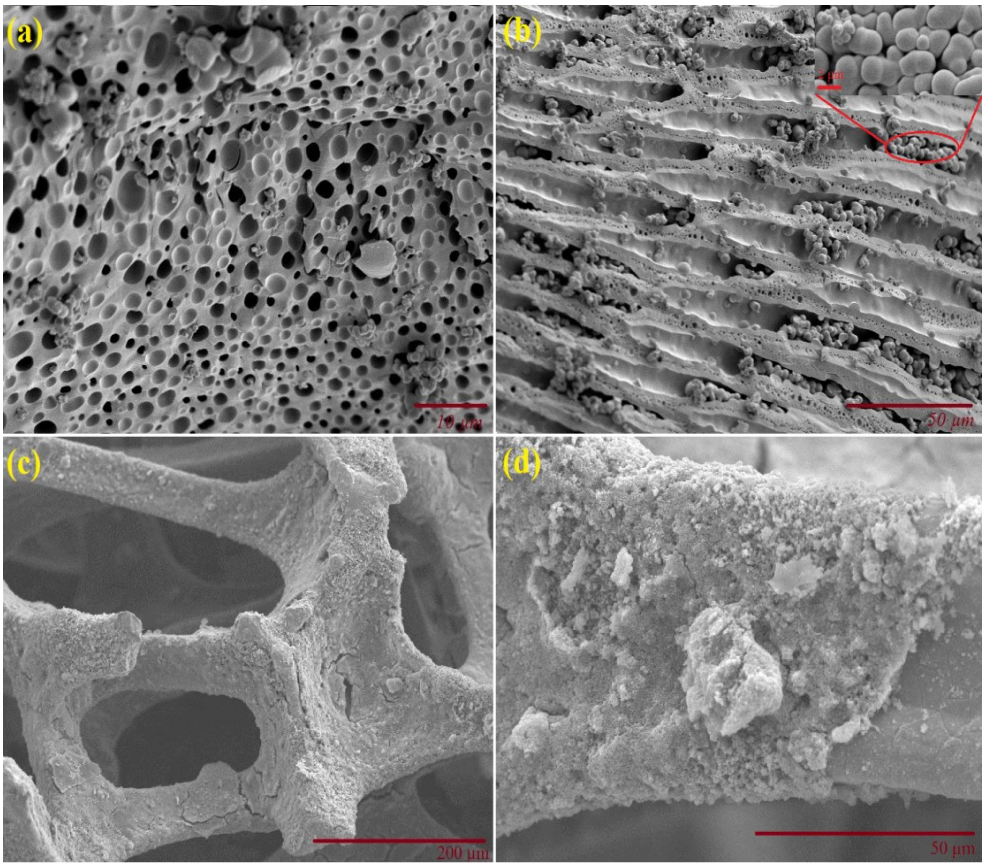

Figure 5.5 (a and b) SEM images of porous TiO_2 hydrothermally prepared at 180 °C and 80% filling ratio for 12 h (H-Base). (c and d) SEM images of H-Base photocatalyst coated on nickel form filter

In order to directly study the microstructure and crystal shape, size, and phase, TEM imaging was performed. Figure 5.6 illustrates TEM and HRTEM images of the sample hydrothermally treated at 180 °C and 80% filling ratio for 12 h. As can be seen in Figure 5.6b, the anatase and brookite crystal sizes are approximately 7.33 and 8.81 nm, respectively. The particle size distribution of the H-Base sample measured from TEM analysis is depicted in Figure 5.6d. Most crystals are between 6 and 10 nm in diameter and the mean size of the counted particles is roughly 7.5 nm. These values are consistent with the crystal sizes calculated by Scherrer equation based on the XRD results for H-Base (7.6 nm for anatase and 8.3 nm for brookite). Absence of long-range ordered mesostructure in TEM images led us to believe that a part of mesoporosity was caused by the aggregation of the primary titania particles (i.e. interparticle porosity), as shown in Figure 5.6b. In Figure 5.6c the lattice fringes of the titania can be easily recognized which confirms high crystallinity of the sample. The lattice plane of anatase (101) with interlayer spacing of ca. 0.35 nm [194] can be observed in the HRTEM images.

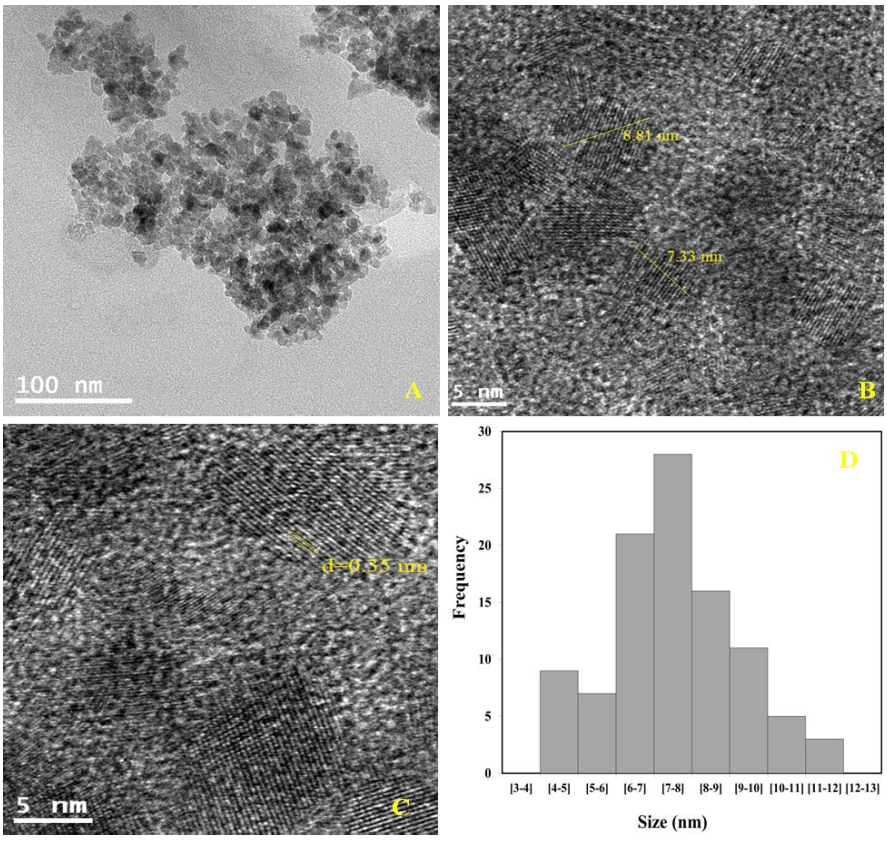

Figure 5.6 TEM (a) and HRTEM (b and c) images of H-Base. (d) Particle size distribution histogram of H-Base sample measured from the TEM imaging in a (the graph is based on the measurement of the size of 100 nanoparticles)

5.1.2.1.4. Hydroxyl radical analysis

Photocatalyst ability to produce hydroxyl radicals has an enormous influence on the efficacy of PCO system in removal and mineralization of air contaminants. The yield of $^{\bullet}OH$ radicals depends on the competition between oxidation of surface OH groups/water by holes and e^{-}-h^{+} recombination. Thus, the measurement of the formation rate of hydroxyl radicals can provide useful information to better understand the connections between catalyst features and its photocatalytic activity. Hydroxyl radical has a very short lifetime (~10^{-9} s) and high reactivity, which make it difficult to be directly measured. Consequently, a variety of indirect techniques including electron spin resonance (ESR), UV/vis absorption spectroscopy, luminescence and fluorescence have been employed [195].

In this study, the fluorescence spectrometry was applied to determine the formation rate of hydroxyl radicals on different hydrothermally-prepared samples. Figure 5.7a illustrates the PL spectra of TiO_2 samples synthesized under different hydrothermal durations at 180 °C and 80% filling ratio. No PL was seen for the base solution (mixture of TA and NaOH) or the TiO_2 solution in the absence of illumination which indicates that the source of PL is 2-HTA [136]. The as-prepared amorphous titania (i.e. only underwent a drying step) shows a minimal PL intensity at 426 nm, arising from the lack of crystallinity which induces more e^{-}-h^{+} recombination and smaller number of available holes for $^{\bullet}OH$ production. A steady increment in PL intensity is witnessed with prolonging the hydrothermal reaction time from 1 to 48 h which can mainly be ascribed to the enhancement in crystallinity. Regarding the impact of hydrothermal temperature, in the range of 100 to 200 °C, PL intensity exhibits an upward trend and reaches its optimum value at 200 °C. The PL intensity of HT-4 was much lower than that of HT-3 despite its superior crystallinity (see Table 5.3), which could probably stem from the reduction in surface area and surface hydroxyl groups population at a higher hydrothermal reaction temperature. In the case of autoclave filling ratio, the PL intensity does not correspond with the pressure inside the reactor, but it agrees to some extent with samples crystallinity. The relationship between the surface area normalized PL intensity (calculated based on data in Figure 5.7 and Table 5.3) and relative anatase crystallinity is depicted in Figure 5.8. Even though there are some biases in the linear correlation, a good proportionality between the two parameters can be noticed in Figure 5.8. The normalized PL intensity almost linearly grows with improvement in anatase relative crystallinity. Since the PL intensity is proportional to 2-HTA concentration, which is generated by the reaction

between •OH and TA, once the contribution of surface area is removed, the quality of crystallinity mainly controls the formation rate of •OH. It is important to point out that given the high pH of solution and low concentration of TA, the direct oxidation of TA by photogenerated holes is unlikely and can be ruled out [196].

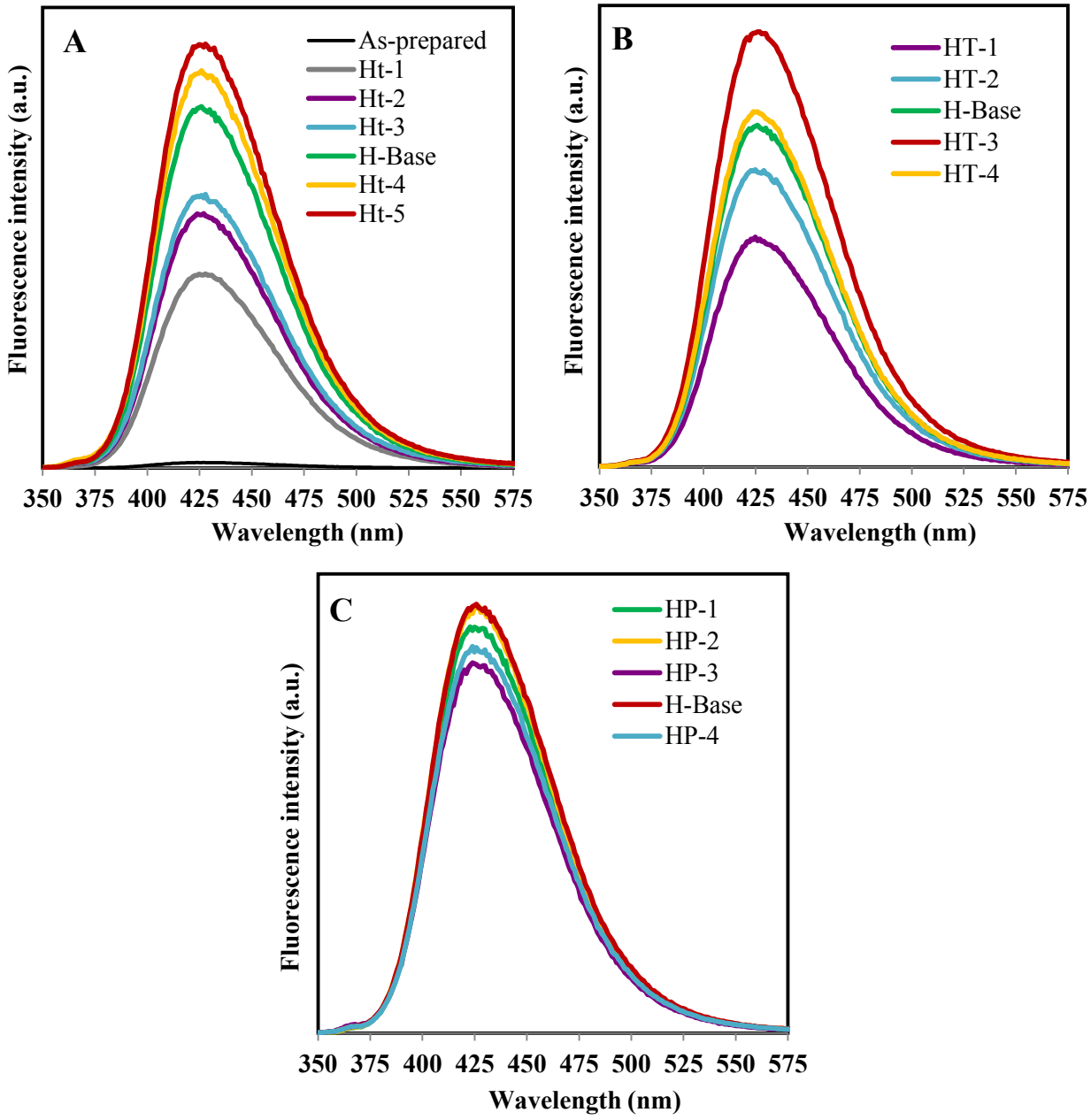

Figure 5.7 Variations in Photoluminescence spectra of titania photocatalysts with (a) hydrothermal duration, (b) hydrothermal temperature, and (c) autoclave filling ratio

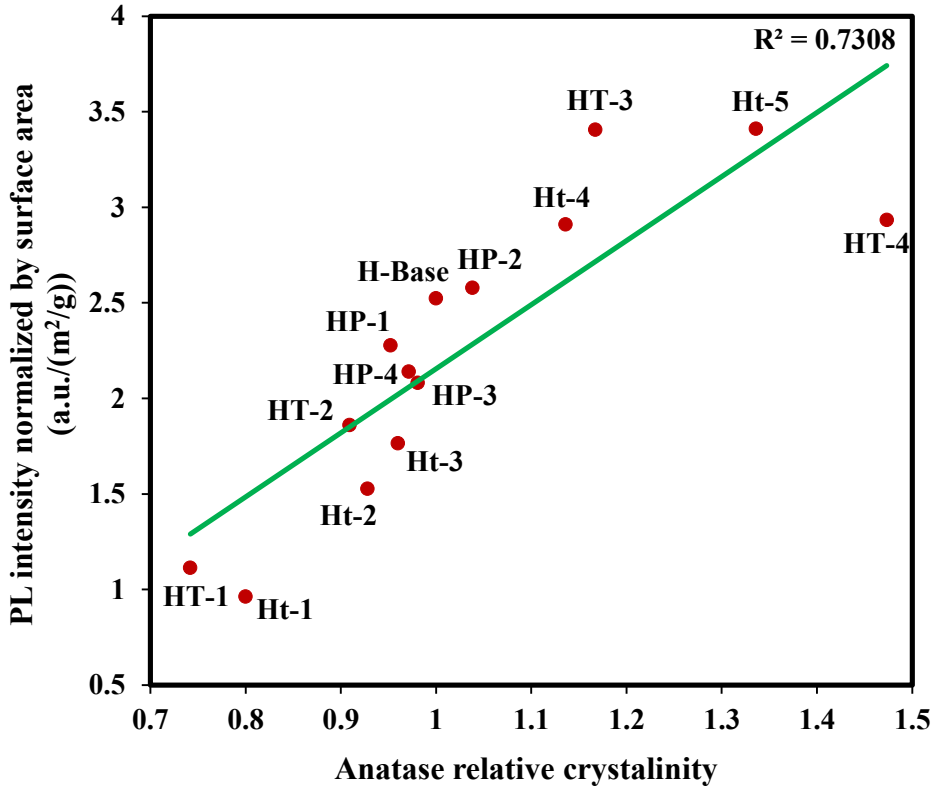

Figure 5.8 Dependence of surface area normalized fluorescence intensity (a.u./(m^2/g)) on the relative anatase crystallinity of various titania photocatalysts

5.1.2.1.5. UV-vis

The UV-vis absorbance spectra of titania samples with different hydrothermal synthesis conditions are illustrated in Figure 5.9. As can be seen in this figure, TiO_2 only effectively absorb the UV light with wavelength shorter than 410-420 nm, which is consistent with previous studies [197]. The significant absorption around 350-400 nm can be ascribed to the excitation of electrons from the valence band to the conduction band ($O_{2p} \rightarrow Ti_{3d}$). It is evident that all the titania samples have very similar absorption profiles (and absorption edges) in the range of 250-800 nm, indicating that their band gaps should fall within a narrow range. The band gap energies are determined by plotting $(\alpha h\nu)^2$ versus energy of light ($h\nu$) (Tauc plot) where α is the absorption coefficient, h is the plank constant and v is the frequency. The extrapolation of the straight line from the Tauc region intercepts the x axis ($h\nu$) to give the direct band gap of the TiO_2 powder. The band gap energies of pure anatase and brookite phases are 3.23 and 3.14 eV, respectively. As reported in Table 5.3, the band gap energies of the mixed-phase TiO_2 samples,

estimated from the Tauc plot, are very close and between 3.14 and 3.23 eV depending on the phase composition.

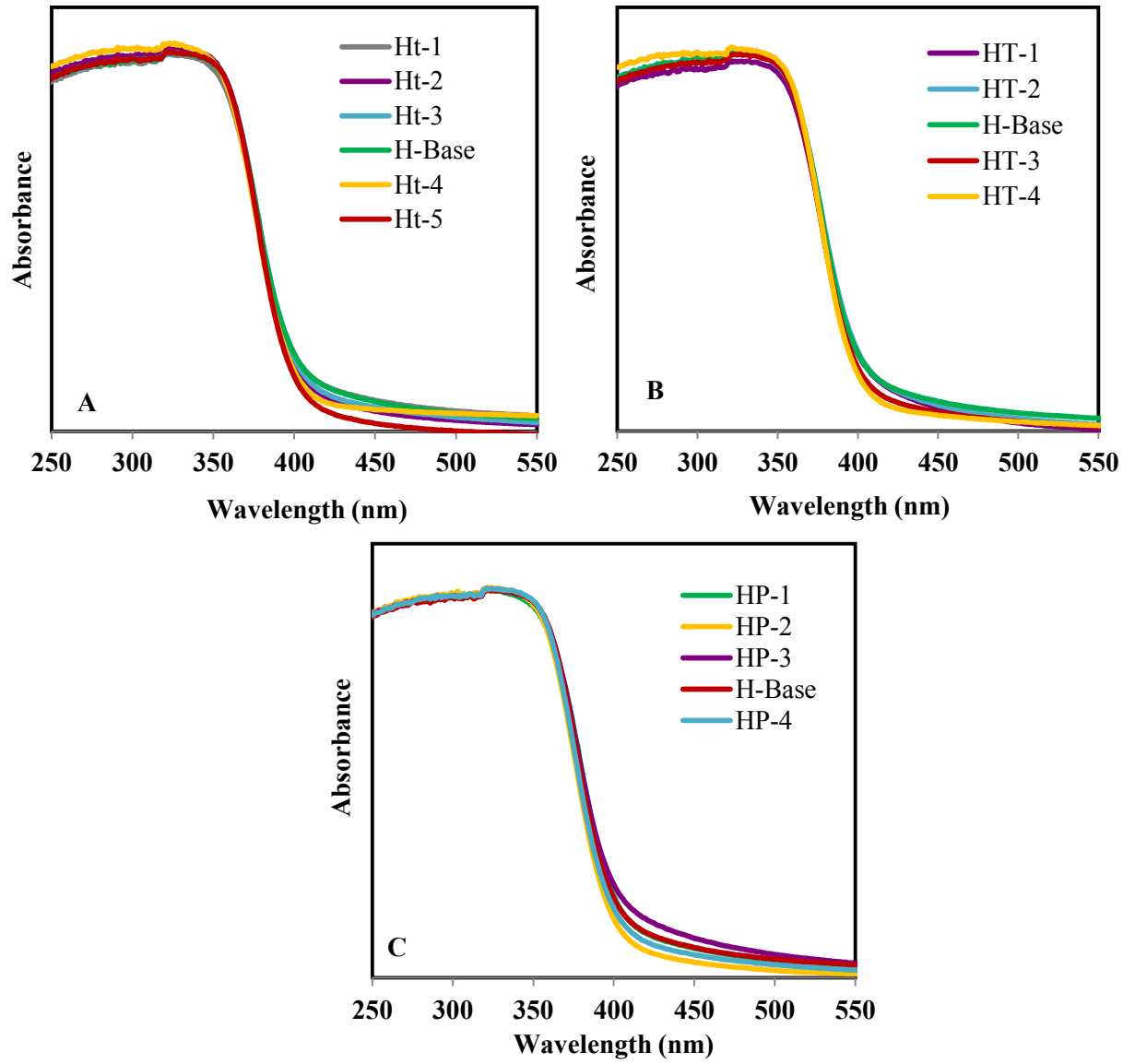

Figure 5.9 Variations in UV-vis absorbance spectra of titania photocatalysts with (a) hydrothermal duration, (b) hydrothermal temperature, and (c) autoclave filling ratio

5.1.2.1.6. FTIR

Figure 5.10 shows the FTIR characterization of the titania samples in the OH spectral region, 3800-2600 cm^{-1}. Considering that the FTIR spectra of some of the samples are almost similar, for the sake of brevity, in Figure 5.10 only some of the spectra are represented. As can be noted, the surfaces of all titania powders are abundant with OH groups, judging from the appearance of

a broad and strong IR absorption in the 3600-2800 cm^{-1} range. Regarding the as-prepared sample and HT-1, several bands are observed in the 2975-2850 cm^{-1} range, which could be assigned to the C-H stretching vibration. This indicates that even after 12 h of hydrothermal treatment at 100 ˚C, still there are some unhydrolyzed butoxy groups (or other residual organic moieties originating from the starting alkoxides) in titania structure. By comparing the broad band in the 3600-2800 cm^{-1} region in samples underwent hydrothermal reactions, it can be seen that the IR absorption gradually diminishes as the reaction time or autoclave temperature is increased. This is partly due to the fact that as the hydrothermal reactions proceed, many surface hydroxyl groups are consumed in condensation reactions to form Ti-O-Ti networks. Except the as-prepared sample, in all FTIR spectra of samples prepared at different temperatures and durations, three sharp peaks at 3693, 3670, and ~3630 cm^{-1} are detected.

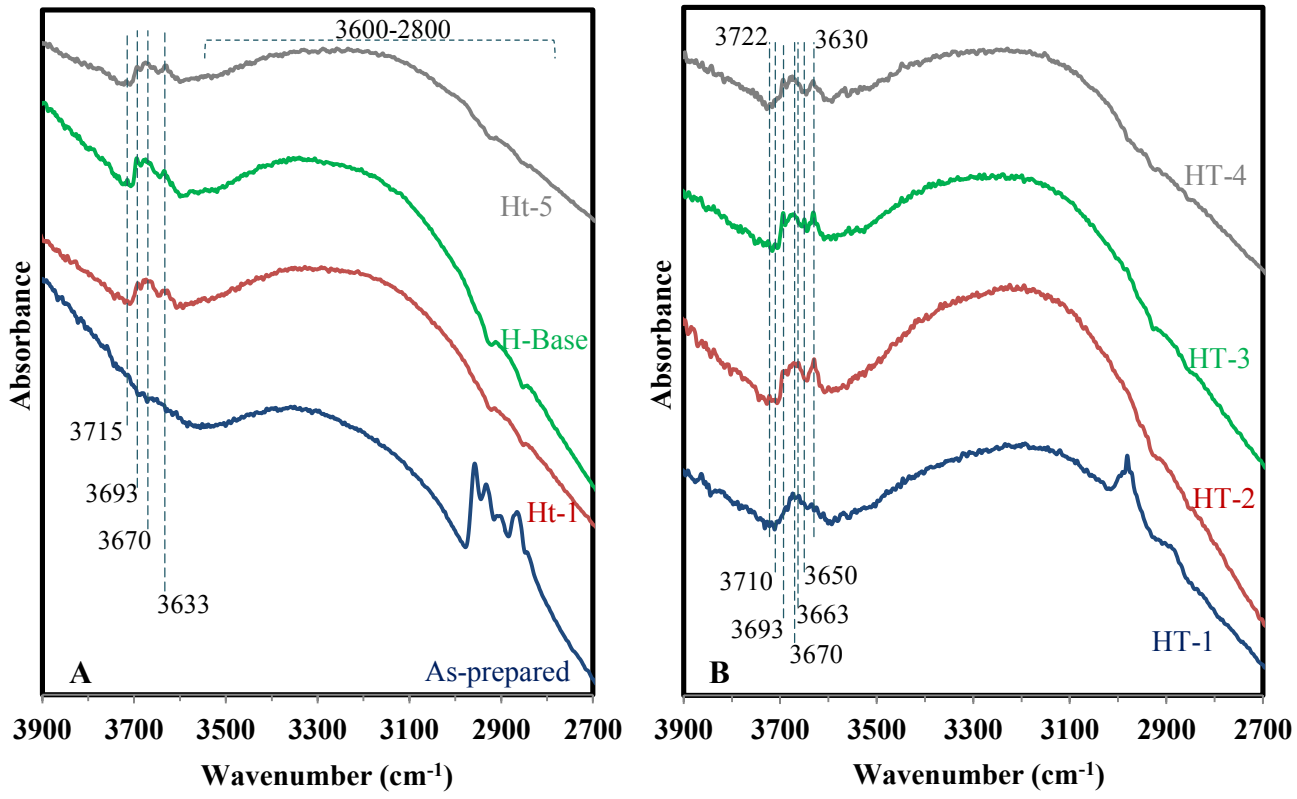

Figure 5.10 FTIR spectra of the TiO_2 samples in the hydroxyl group region: (a) impact of hydrothermal time and (b) impact of hydrothermal temperature

Generally, bands at frequencies greater than 3600 cm^{-1} are ascribed to the stretching mode of –OH species free from hydrogen bonding interactions [27, 144]. Some studies suggested that the bands at frequencies higher than 3680 cm^{-1} might belong to terminal hydroxyl groups (Ti−OH)

and bands at lower frequencies can be sign of bridged −OH (Ti−OH−Ti) [147]. More specifically, the band at 3693 cm^{-1} is suggested to be a signature of isolated hydroxyl groups on titania [29]. It is interesting to note that the band at 3693 cm^{-1} has its highest intensity in the case of H-Base and HT-3. In all spectra a sharp band located at 3670 cm^{-1} can be noticed which is due to the presence of bridging −OH group [27]. Only on HT-3, a small and sharp peak appears at 3650 cm^{-1} which could be attributed to a type of isolated hydroxyl group [147]. In section 4.1, we showed that the isolated hydroxyl groups, located at 3722-3693 cm^{-1}, have strong interaction with toluene and MEK molecules.

5.1.2.2. Photocatalytic activity

The photocatalytic activity of yielded photocatalysts was assessed through photocatalytic oxidation of toluene and MEK in air at room temperature. For comparison, the activity of P25, which is widely recognized as a highly efficient photocatalyst under UV light, is also evaluated. As could be easily inferred from the characterization data, hydrothermal time should have a great influence on the removal efficiency (and reaction rate) of toluene and MEK. Considering Figure 5.11, the as-prepared titania sample exhibits minor toluene and MEK removal efficiencies in comparison to samples underwent hydrothermal treatment mainly due to its amorphous structure, which triggers fast e^--h^+ recombination. The sample prepared at 180 ˚C for 1 h (Ht-1) shows high toluene and MEK removal efficiencies, 41% and 34%, respectively, which are higher than (for toluene) and equal to (for MEK) those of P25. The good photoactivity of Ht-1 could be mainly attributed to the formation of anatase crystals, large surface area, and mesoporous structure. After this point, VOC removal efficiency variation with hydrothermal time displays different trends depending on the challenge compound. In the case of toluene which has much weaker interaction with titania surface with respect to MEK, the significant surface area (and porosity) decrement from Ht-1 to Ht-2 overpowers the marginal enhancement in crystallinity and causes ~20% drop in the removal efficiency. This clearly indicates that the adsorption process affects the photocatalytic oxidation of toluene to a greater extent than that of MEK. By prolonging the reaction time from 3 to 12 h (i.e. Ht-2 to H-Base), toluene removal efficiency and reaction rate progressively increase and reach their optimum values, 48.7 % and 11.95×10^{-5} mol/(min.g), showing improvement over P25 with 34% removal efficiency and 8.35×10^{-5} mol/(min.g) reaction rate. Further increment in the reaction time (from 12 to 48 h) results in a sharp decline in toluene removal efficiency, most probably due to the reduction in surface area,

porosity, and surface OH density. On the other hand, MEK removal efficiency monotonically enhances with hydrothermal time, reaches its maximum value on Ht-4, and experiences a minor drop for the sample that underwent 48 h hydrothermal treatment. Besides the improvement in crystallinity which surely contributes to the upward trend of MEK removal efficiency with hydrothermal time, one should bear in mind that anatase is the most active polymorph of titania in gaseous PCO and in our experiments anatase phase content increases with the hydrothermal time. Notably, MEK removal efficiency and reaction rate on Ht-4 is almost two times higher than that on P25. This superiority can be attributed to Ht-4 large surface area (thrice P25), good crystallinity, proper crystal size, and high mesoporosity.

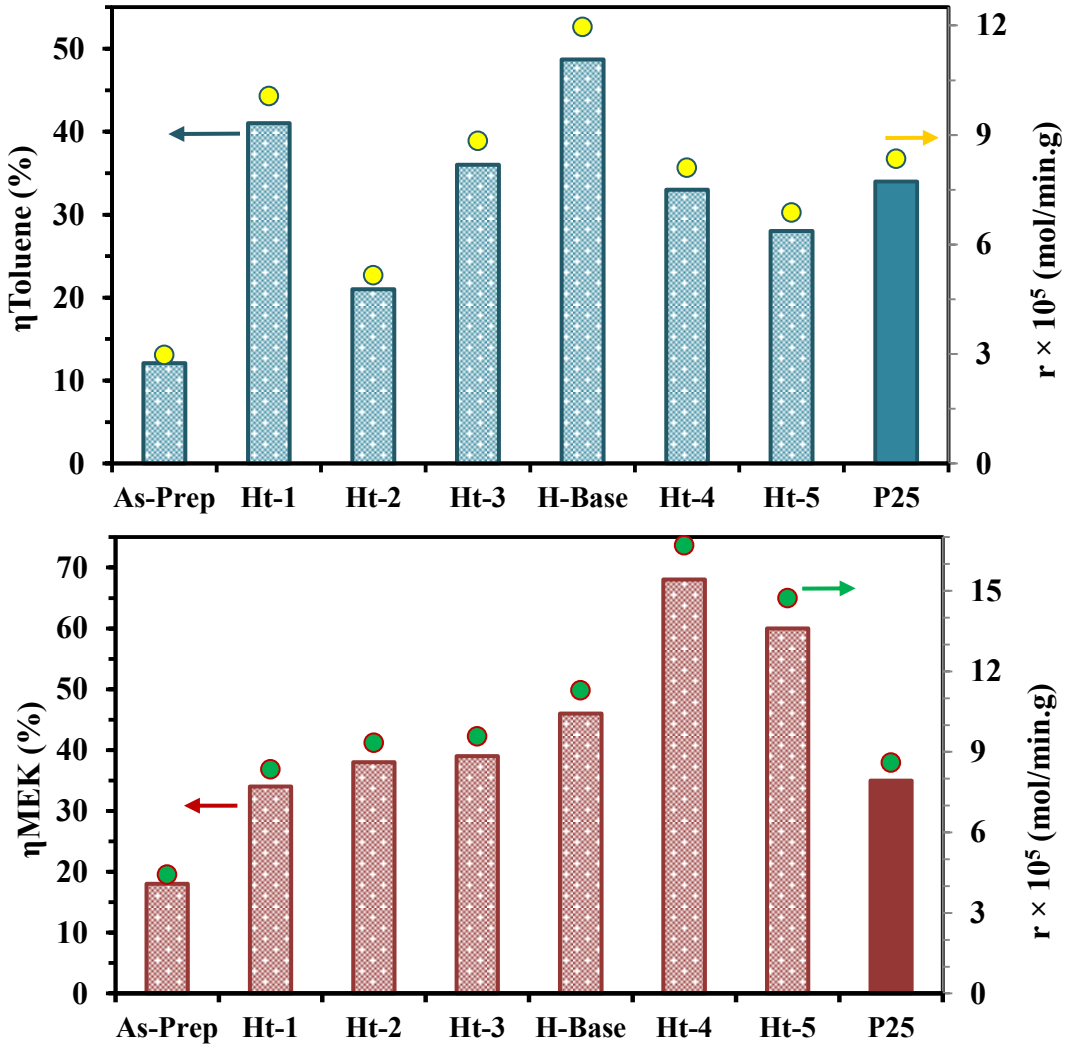

Figure 5.11 Toluene and MEK removal efficiency and reaction rate for the as-prepared titania, hydrothermally-prepared TiO_2 samples synthesized at different durations (1-48 h), and P25

As noted in Figure 5.12, the trends of MEK and toluene removal efficiency (and reaction rate) with hydrothermal temperature are fairly similar. With employing a higher hydrothermal temperature, the obtained photocatalyst performs better mainly owed to the substantial enhancement in crystallinity and crystal growth. The observed trends indicate that the greater crystallinity at higher hydrothermal temperatures counteracted the reduction in the surface area and the net effect was positive. Many researchers proposed that the co-presence of two TiO_2 crystal phases can extend the e^--h^+ pairs lifetime and, therefore, boost the quantum efficiency. Based on the obtained results, it appears that the biphasic titania photocatalyst with 82.3% anatase and 17.7% brookite (HT-3) offers the optimum photocatalytic activity towards the selected VOCs under the employed experimental conditions. It is noteworthy that higher hydrothermal temperature can also bring about a better contact between the two crystalline phases which is crucial for a successful charge carrier transfer from one phase to another. Another possible explanation for achieving the highest photocatalytic activity over HT-3 could be its crystal size, considering that the charge carrier recombination can take place both in the bulk and on the surface of TiO_2. It is known that with crystal growth the bulk recombination becomes more significant; consequently, one can envisage a crystal size at which the best trade-off between surface and bulk recombinations exists. The fluorescence spectrometry data can be useful to better justify this point since photocatalyst capability to produce $^{\bullet}OH$ is closely connected to the population of available holes, which in turn is a measure of the effectiveness of charge carrier separation. As can be seen in Figure 5.7b, HT-3 possesses the largest PL intensity amongst samples treated at different hydrothermal temperatures, which might be partly ascribed to its ideal crystal size that enhances the e^--h^+ separation and subsequently the removal of challenge compounds. Additionally, although the removal efficiency does not always match the population of hydroxyl groups on titania surface in our study, as showed in Figure 5.10b, the IR absorbance for HT-3 in the OH spectral region is stronger than that for HT-4. As mentioned before, surface OH groups are extremely important adsorption centers for VOC molecules. MEK can be adsorbed on the surface via H-bonding between its carbonyl group and surface OH groups, and toluene adsorption mainly occurs through weak Π-bonding to surface hydroxyls [176]. Therefore, the lower concentration of OH groups along with the smaller surface area and porosity can explain the inferior photocatalytic performance of HT-4 with respect to HT-3.

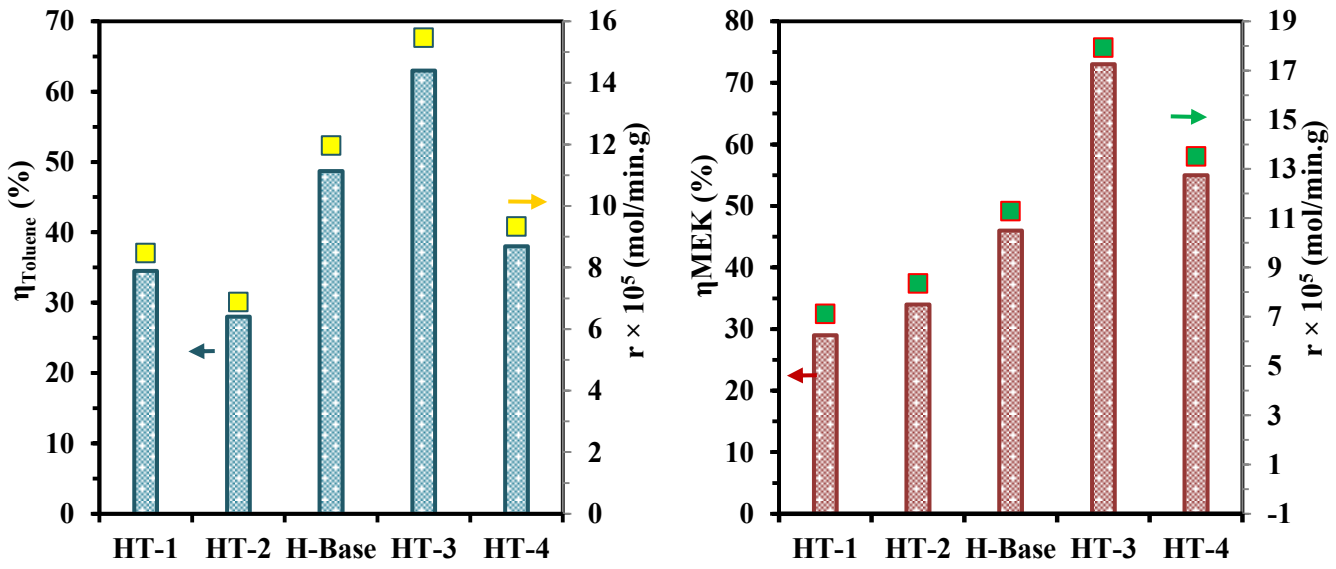

Figure 5.12 Toluene and MEK removal efficiency and reaction rate for hydrothermally-prepared TiO_2 samples synthesized at different hydrothermal temperatures (100-220 °C)

Figure 5.13 illustrates toluene and MEK removal efficiencies (and reaction rate) for titania powders synthesized at 180 °C for 12h with different reactor filling ratios. Evidently, the removal efficiencies cannot be correlated with the applied filling ratio which is reasonable taking into account that the variations in photocatalysts characteristics with this preparation parameter were unpredictable as well. Nonetheless, it is worth highlighting that the impact of autoclave filling ratio on toluene and MEK photocatalytic oxidation is much less with respect to that of the other preparation parameters, namely hydrothermal temperature and time. Considering Figure 5.13, H-Base (180 °C, 12h, and 80%) indicates the highest removal efficiency for both toluene and MEK, which is in good agreement with the results reported in Figure 5.7c on the PL intensity of these samples. On the other hand, although HP-3 has comparable surface area and crystallinity to those of other HP samples, it has the lowest toluene removal efficiency (31.4%) and the third lowest MEK removal efficiency (29%), which could result from its poor ability to produce hydroxyl radicals as can be evidenced in Figure 5.7c.

Table 5.4 summarizes the amounts of detected by-products in the gas phase during the PCO of toluene and MEK on various titania samples. By comparing the data in Table 5.4 and Figure 5.11 to Figure 5.13, it can be noted that though many of the samples outperformed P25 in MEK/toluene degradation, the amounts of by-products in the outlet stream are considerably larger for P25.

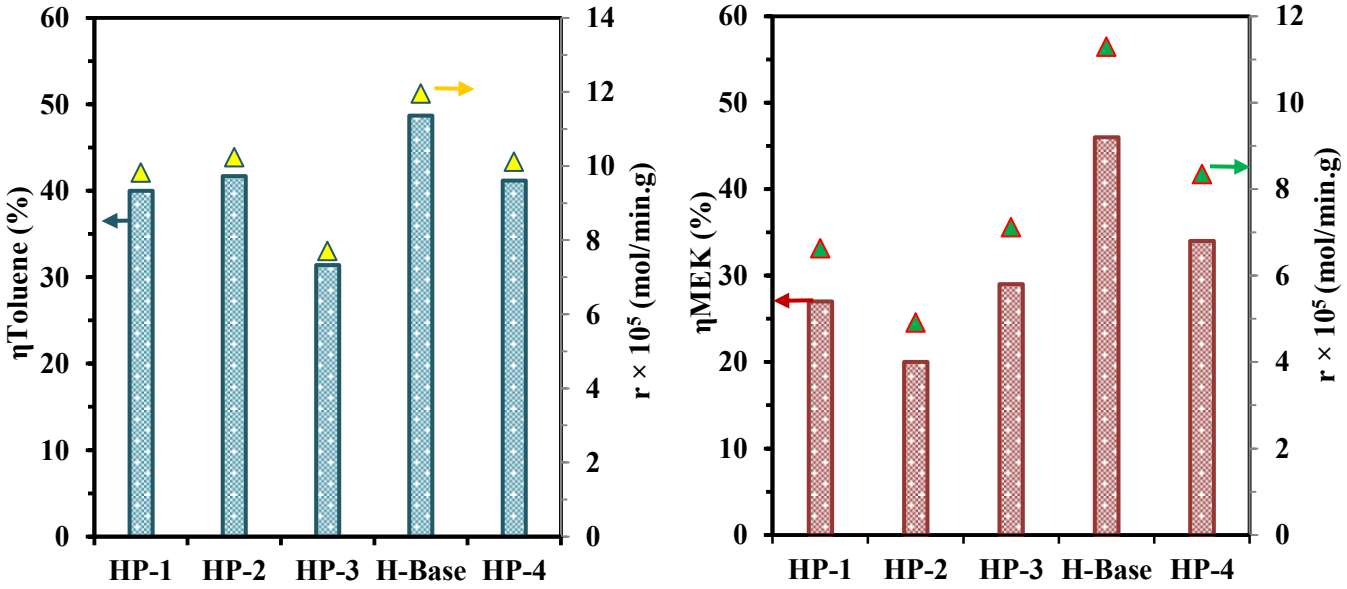

Figure 5.13 Toluene and MEK removal efficiency and reaction rate for hydrothermally-prepared TiO_2 samples synthesized at different autoclave filling ratios (20-90%)

This observation can be described from two perspectives: (i) the complete conversion of challenge compounds to CO_2 and H_2O is greater on the hydrothermally prepared samples or (ii) generated by-products during PCO reactions are more efficiently adsorbed on the prepared samples compared to P25. Both views can be explained by considering the larger surface area of hydrothermally prepared samples, which provide a larger number of accessible active sites for chemical reactions (i.e. more complete mineralization) and more adsorption sites for by-products (i.e. less adsorption competition). Additionally, the porous structure of fabricated titania photocatalysts can retard the desorption of by-products (or intermediates) from the surface to the gas phase and, thus, boost the possibility of participation in further oxidation reactions. In some of the PCO experiments, propionaldehyde is found in the outlet air, while in other cases formaldehyde, acetaldehyde and acetone are the only by-products. One reason might be the low concentration of propionaldehyde which was lower than the detection limit of the HPLC. Regardless of the photocatalyst and the achieved efficiency, as a consistent trend, more by-products are generated during MEK degradation compared to that of toluene which agrees with previous works on toluene and MEK photocatalytic oxidation studies [181]. This might be attributed to the severe adsorption competition between MEK and generated by-products during its oxidation and/or the strong adsorption of toluene by-products (e.g. benzoic acid and benzaldehyde) on titania.

Table 5.4 Generated by-products in the gas phase during photocatalytic degradation of toluene and MEK on various titania photocatalysts (all values are in ppb)

Photocatalyst	Toluene			MEK			
	Formaldehyde	Acetaldehyde	Acetone	Formaldehyde	Acetaldehyde	Acetone	Propionaldehyde
P25	14.7	3.4	3.4	46.3	60.4	8.5	-
As-prepared	20.8	6.0	5.9	17.5	9.4	-	6.0
H-Base	13.0	4.6	-	43.9	45.6	-	-
Ht-1	13.2	4.6	6.5	33.3	31.7	-	-
Ht-2	11.3	3.9	5.7	35.8	34.4	-	6.1
Ht-3	13.7	5.3	6.4	36.6	34.4	6.7	4.6
Ht-4	12.5	4.4	5.1	38.2	37.2	-	-
Ht-5	12.6	5.0	6.2	40.0	36.5	10.8	5.3
HT-1	8.4	3.3	-	32.7	30.6	7.6	-
HT-2	10.7	4.5	6.1	38.2	35.6	7.8	-
HT-3	17.5	7.3	6.6	35.8	34.4	7.4	-
HT-4	16.2	5.8	5.8	34.6	33.0	7.1	-
HP-1	10.4	4.5	7.0	42.5	35.8	6.2	-
HP-2	10.8	4.5	10.5	40.0	33.0	-	-
HP-3	9.5	3.1	5.6	43.1	40.6	-	-
HP-4	9.9	5.3	8.4	37.4	36.7	-	-

In this study, crystallinity, crystal size, phase composition, surface area, porosity, surface OH density, and $^{\bullet}OH$ generation ability are the main factors. On the one hand, these parameters are interconnected and can negatively/positively (and to different magnitudes) affect photocatalytic processes. On the other hand, similar to many examples in the field of catalysis, there are thresholds for photocatalyst properties, at which sharp changes in the activity are seen due to a small variation in a property. For instance, in terms of relative crystallinity, surface area, band gap, $^{\bullet}OH$ generation and crystal size, there are very small differences between Ht-3 and HP-1. These samples mainly differ from each other in the anatase content, 81.5 vs 83.7%. Evidently, this slight difference in phase composition could lead to 12% difference in MEK removal efficiency. The above-mentioned issues along with the non-linear correlation between each photocatalyst feature and its activity could account for the absence of any mechanistic property-performance relationships. Nevertheless, as can be noted in Figure 5.14 in the majority of cases, there is an acceptable level of proportionality between MEK/toluene removal efficiency and PL intensity. Especially for MEK photocatalytic degradation, removal efficiencies over Ht-series

and HT-series photocatalysts correspond very well with their PL intensities (coefficient of determination (R^2)=0.82). The positive correlations in Figure 5.14 point out that generally higher PL intensity (or •OH generation efficiency) brings about better VOC removal efficiencies.

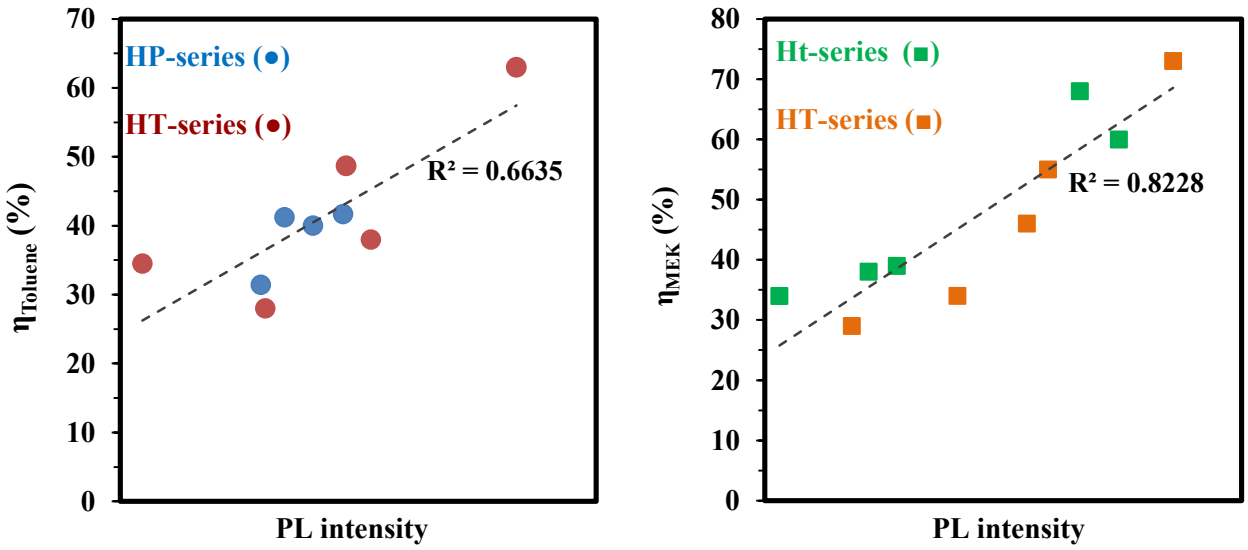

Figure 5.14 Dependence of toluene and MEK removal efficiency on PL intensity

5.2. Impact of hydrothermal medium pH and type of acid/base

Altering the pH of hydrothermal reaction medium (e.g. via addition of acid/base) is a facile and efficient method to adjust the degree of crystallinity and crystal phase of TiO_2. Proper selection of the acidity of reaction medium and type of additive can enable synthesis of bi/tri phasic titanium dioxides which are believed to be superior to single phase materials. Furthermore, the desired pore structure can be achieved in one pot synthesis by controlling the hydrolysis and polycondensation rates of the pre-selected titanium sources on the basis of the chemistry of metal alkoxides. In this section we indicated that a good control over the key features of catalysts could be achieved by varying the pH of the starting aqueous solution (pH=2-12) and the type of acid (chloric, formic, acetic, nitric, and sulfuric) during preparation. To gain more insight into the impact of main operating conditions on PCO processes, experiments were conducted at wide ranges of inlet concentration, relative humidity, and residence time. Considering the formation of carcinogenic compounds during MEK oxidation, the health-risk associated with gaseous by-products was also assessed. To our best knowledge, there are only a few studies on photocatalytic oxidation of methyl ethyl ketone in air; therefore, the performance, by-products, reaction mechanism, and health aspects of MEK degradation over titania are not fully investigated. The obtained photocatalytic activities were justified by underlining the role of key characteristics of photocatalysts in each step of heterogeneous photocatalysis. Furthermore, the influence of operating conditions on MEK removal efficiency, by-products generation, and health-risk index were explained. A tentative reaction pathway for MEK photodegradation was proposed, comprising H-abstraction, ß C-C scissions, surface reactions, radicals recombinations, and mineralization.

5.2.1. Methodology

5.2.1.1. Photocatalyst preparation

In a typical synthesis procedure, a specific volume of TBOT was added slowly (~ 2 mL/min) to an aqueous solution (containing acid/base with the desired molarity and pH, Table 5.5) in a 250 ml beaker without stirring. The volume ratio of the aqueous solution to TBOT in all experiments was kept at 10.4. After aging for 24 h at ambient temperature (21 ˚C), the mixture and the formed precipitates were carefully transferred to a 100 mL Teflon-lined stainless steel autoclave. The autoclave filling was approximately 80% in the preparation of all samples. Subsequently, the

autoclave was heated at a rate of 3 ˚C/min to 180 ˚C in an air oven, maintained at 180 ˚C for 12 h, and then cooled down to room temperature at rate of -3 ˚C/min. After hydrothermal reaction, the solution was filtered and the precipitates were washed several times with distilled water until the washing solution reached pH of ca. 6. The resulting white-yellow solids were dried at 100 ˚C for 12 h to remove water and obtain the final titania samples for characterization and performance evaluation. The properties of aqueous solution during hydrothermal preparation and the assigned name to each photocatalyst are given in Table 5.5. The experimental set-up design and operation are explained in details in section 3.1.2. The experimental conditions at which PCO tests were performed in this section are given in Table 5.6.

Table 5.5 Hydrothermal reaction medium of TiO_2 photocatalysts

Name	Reaction medium	Solution pH	Acid/base concentration (mol/L)
H-SA2	Sulfuric acid (H_2SO_4)	2	0.01
H-SA4		4	0.0001
H-NA2	Nitric acid (HNO_3)	2	0.01
H-NA4		4	0.0001
H-HCA2	Hydrochloric acid (HCl)	2	0.01
H-HCA4		4	0.0001
H-FA2	Formic acid (HCOOH)	2	0.5
H-FA4		4	0.00015
H-AA2	Acetic acid (CH_3COOH)	2	5
H-AA4		4	0.0006
H-Base	Pure water	6	-
H-A10	Ammonium hydroxide	10	0.0007
H-A12		12	6

Table 5.6 PCO tests experimental conditions

Parameter	Value	Unit
Inlet concentration	101.8 ± 5.4, 504.7 ± 11.6, 1002 ± 29.8	ppb
Relative humidity	0, 18.8 ± 1.1, 50.2 ± 3.4	%
Volumetric flow rate	20, 30, 50	L/min
Residence time	0.012, 0.02, 0.03	s
Light intensity	5	mW/cm^2
TiO_2 concentration	1± 0.04	mg/cm^2

5.2.2. Results and discussion

5.2.2.1. Photocatalyst characterization

5.2.2.1.1. Crystal structure

Figure 5.15a depicts the XRD patterns of TiO_2 prepared in neutral (pH~6) and alkaline solutions (pH=10 and 12). The diffraction peaks at 25.3° and 30.8° respectively correspond to the anatase (101) plane and brookite (121) plane. By increasing the pH of hydrothermal solution (i.e. increasing ammonia concentration), the brookite phase content steadily diminishes and ultimately at pH=12 the brookite phase completely disappears. At higher pH values stronger and narrower diffractions peaks for anatase are obtained, implying the enhancement in crystallinity and substantial crystal growth. The average anatase crystal size (Table 5.7) for H-Base, H-A10, and H-A12 are 7.6, 10.7, and 18.8 nm, respectively, which is in good agreement with the peak sharpening seen in Figure 5.15a. The improvement in crystallinity mainly stems from the fact that in a more basic reaction solution a larger population of hydroxyl groups are available for hydrolysis of titanium butoxide precursor. Figure 5.15b and Figure 5.15c present the influence of acid type (sulfuric, nitric, acetic, formic, or hydrochloric) with pH=2 and pH=4, respectively, on phase structure. For all TiO_2 samples sharp peaks are seen at 25.3°, indicating formation of anatase crystals even at very low pH under hydrothermal conditions. Compared to other acids, HNO_3 more effectively catalyzes brookite phase formation (18.9% for H-NA2), which was also witnessed in titania preparation via sol–gel and hydrothermal methods [82]. The ability of acids to promote anatase formation followed the sequence of formic > sulfuric > acetic > nitric ~ chloric. By comparing the values for relative crystallinity (Table 5.7), it is evident that basic hydrothermal solution leads to a significantly better crystallinity with respect to acidic or neutral solutions. In acidic solutions, due to the OH groups deficit, titanium precursor cannot be completely hydrolyzed and, therefore, a great quantity of unhydrolyzed alkyl groups exist in the reaction medium. These unhydrolyzed alkyl groups impede the coagulation and flocculation of titania particles (via electrostatic repulsion) and consequently the crystallization process [198]. Sulfuric acid and formic acid respectively result in the lowest (1.00-1.06) and highest (1.20-1.46) crystallinities among the investigated acids. It is possible that Cl^-, NO_3^-, or SO_4^{2-} ions (or their complexes) remained in the precursors or crystal structure and caused disturbance in titanium dioxide crystallization.

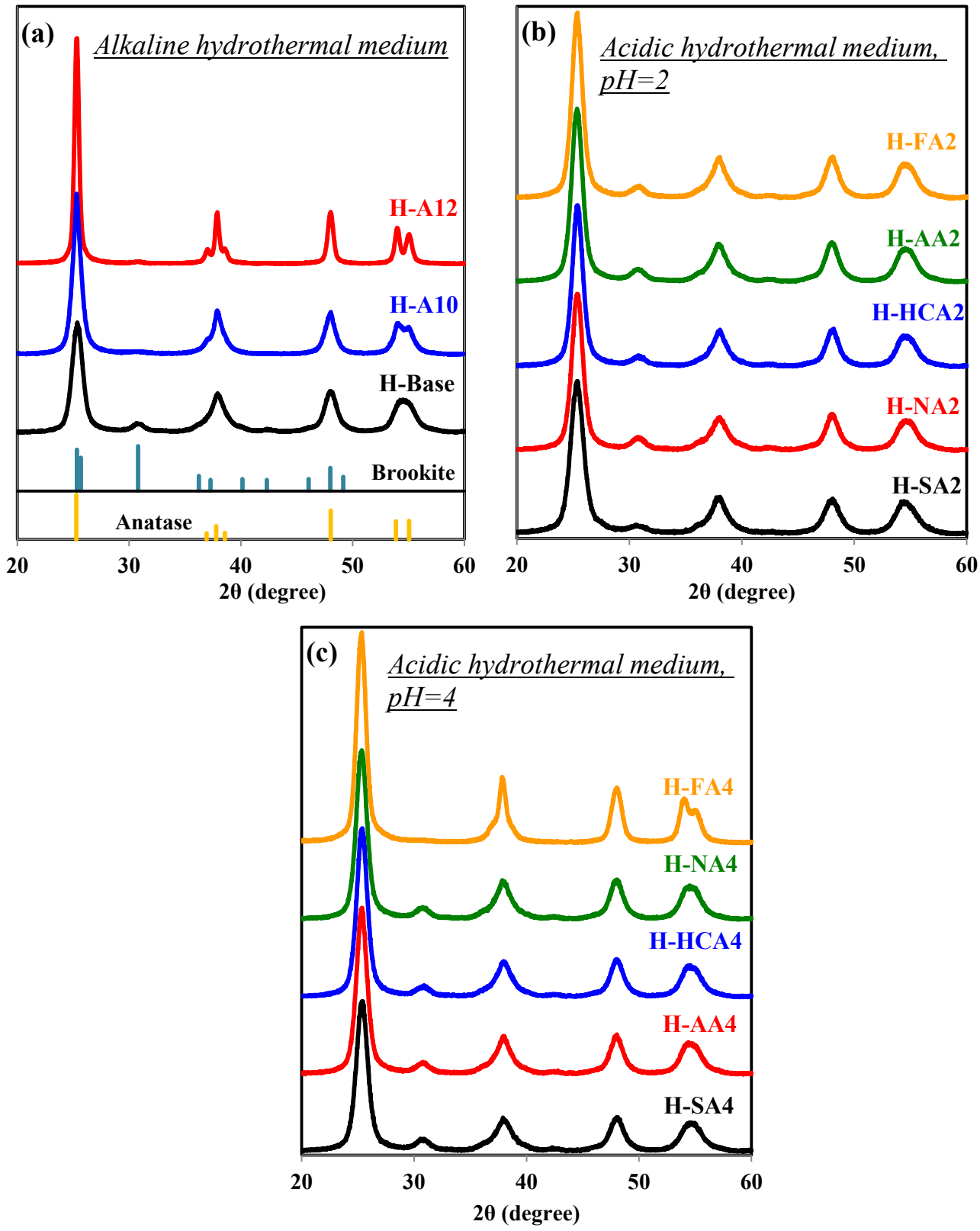

Figure 5.15 XRD patterns of anatase and brookite TiO_2 (JCPDS database) and photocatalysts prepared under neutral/basic (a) and acidic environments (b and c)

Table 5.7 Crystalline, textural, and optical properties of titania photocatalysts

Sample	Relative crystallinity [a]	Phase content (%)		Crystal size (nm)		Surface area (m^2/g)	PL intensity [b]	Fluorescence intensity [c]
		Anatase	Brookite	Anatase	Brookite			
P25	4.17	81.3	18.7 (rutile)	25.3	27.4 (rutile)	53.23	-	-
H-Base	1.32	83.4	16.6	7.6	8.3	155.5	2177.5	279
H-SA2	1.00	88.7	11.3	6.7	7.5	216.1	893.7	323
H-SA4	1.06	86.1	13.9	8.3	7.9	179.8	3007.3	313
H-NA2	1.02	81.1	18.9	7.9	7.6	188.0	2162.0	310
H-NA4	1.20	83.7	16.3	8.1	8.0	173.0	2735.8	285
H-HCA2	1.05	85.2	14.8	7.5	7.6	180.5	2253.6	320
H-HCA4	1.19	82.7	17.3	8.2	7.9	161.0	2020.2	303
H-FA2	1.20	86.3	13.7	8.2	8.5	163.2	2100.0	297
H-FA4	1.46	100.0	0	9.2	-	151.2	2350.6	283
H-AA2	1.10	82.2	17.8	7.7	8.0	175.4	2385.4	306
H-AA4	1.17	84.3	15.7	8.2	8.0	171.9	2181.3	295
H-A10	1.90	97.8	2.2	10.7	-	121.0	2050.0	270
H-A12	2.65	100.0	0	17.5	-	82.9	3208.7	277

[a] Relative crystallinity is defined as the ratio between the intensity of (101) peak of each sample to that of H-SA2. [b] PL intensity is the magnitude of fluorescence spectrum (presented in Figure 5.20) at ca. 425 nm. [c] Fluorescence intensity is the magnitude of fluorescence spectrum (presented in Figure 5.19) at ca. 390 nm.

It is particularly noteworthy that none of the hydrothermal solutions provided the right conditions for rutile formation which could be explained from different standpoints. According to the Ostwald step rule, the titania phase with the lowest surface energy first nucleates in the reaction medium. Since surface energy is inversely correlated to molar volume and anatase has a much higher molar volume with respect to rutile [199], anatase formation is preferred. The other justification is mainly related to the arrangements of octahedra in different phases of titania. In anatase, the TiO_6 octahedra are surrounded by eight octahedra: four edge-shared and four corner-shared, while in rutile, each octahedron is surrounded by ten octahedra: eight corner-shared and two edge-shared [15, 200]. The edge-shared bonding between two octahedra requires two juxtaposed hydrolysis and condensation reactions while only one reaction is needed for corner-shared bonding. Considering this, at mildly acidic, neutral and basic conditions, due to the sufficient concentration of hydroxide ions, the probability of edge-shared bonding is larger; hence, anatase is the major phase observed in our experiments. Additionally, the formation of

anatase at pH=2 might be better explained by considering the status of TiO_6 octahedra in the reaction medium. Under acidic environment, protonation of surface Ti-OH groups [201] results in good dispersion of TiO_6 octahedra in the amorphous phase. These protonated surfaces (i.e. $Ti\text{-}OH_2^+$) can combine with hydroxyl groups of other octahedra to form Ti-O-Ti bonds by dehydration (i.e. oxolation). It is suggested that this mechanism promotes face-sharing polycondensation and thus anatase formation [202, 203]. It should be also mentioned that SO_4^{2-} and CH_3COO^- ions have strong affinity toward titanium atom in aqueous solution which hinders the structural rearrangement and phase transformation [199, 204]. This gives anatase formation a kinetic advantage over rutile in terms of lower activation energy for crystallization. Regarding the formation of brookite in the acidic and neutral solutions, it is to be noted that the activation energy for anatase → brookite transformation is smaller (11.9 kJ/mol) than that of brookite → rutile (163.8 kJ/mol) [134], consequently under low hydrothermal temperature of 180 °C, the former process prevails. On the other hand, Yu et al. [191] put forward an explanation for the formation of brookite phase in the acidic environment containing chloride ions. Considering the fact that the ligand field strength of chloride ion is greater than that of the butoxy group, Cl can replace the butoxy group (i.e. OC_2H_9) in $Ti(OH)_x(OC_2H_9)_x$ complex formed during hydrolysis. In the aqueous solution, $Ti(OH)_2(Cl)_2$ exists in the form of $Ti(OH)_2Cl_2(H_2O)_2$, which is believed to be the precursor of brookite [205].

5.2.2.1.2. Surface area and porosity

Nitrogen sorption analysis can be used to gain insights into the catalyst pore texture and specific surface area. Figure 5.16a and Figure 5.16b exhibit the N_2 adsorption-desorption isotherms and the pore size distributions of H-Base, H-A12, and H-SA2, respectively. As can be seen in Figure 5.16a, H-Base and H-SA2 both indicate isotherms of type IV (BDDT classification) with the hysteresis loops around $0.50 < p_0/p < 0.85$. The type IV isotherms suggest that the porosity in these samples is mainly due to the existence of mesopores. The hysteresis loops of H-Base and H-SA2 have a triangular shape with steep desorption branch which can be categorized as type H2 hysteresis loop, associated with narrow necks and wider bodies (ink-bottle pores). Additionally, the isotherm of H-SA2 also shows a very small H3 type hysteresis loop at $0.9 < p_0/p < 1.0$, suggesting a bimodal pore size distribution in the mesoporous region. The isotherm of H-A12 is of type II unlike the other samples and the hysteresis loop appears at higher relative pressure, $0.70 < p_0/p < 1.0$, indicating formation of larger mesopores. The steep increment in the

adsorption branch (seen in H-A12) is attributed to the capillary condensation of N_2 within titania mesopores (2-50 nm). Moreover, the shape of H-A12 hysteresis loop is of type H3, which could be observed in slit-like pores result from aggregation of plate-like particles. With increasing the pH of the reaction medium, the hysteresis loop shifts rightward and downward to the region with smaller adsorbed N_2 volume and higher relative pressure. This implies that in a more basic environment photocatalyst with larger pores and smaller specific surface area can be obtained. The increment in catalyst pore size with pH could also be noticed in the pore size distributions presented in Figure 5.16b. The photocatalyst prepared at pH=2 shows a relatively narrow pore size distribution mainly between 3.4 and 14 nm, centered at 7.3 nm. For higher pH values, the pore size distributions become wider and center at larger pore sizes: 10.5 nm for H-Base and 15.1 nm for H-A12. This can be mainly attributed to the enlargement of anatase crystals in more alkaline conditions which upon aggregation form larger mesopores. The BET surface areas of TiO_2 photocatalysts prepared at different hydrothermal media are listed in Table 5.7. It can be noticed that the hydrothermally-synthesized samples have much larger surface areas (82.9-216.1 m^2/g) compared to commercial P25 (53.23 m^2/g). On the other hand, in general, the surface area substantially diminishes as the pH value of hydrothermal solution increases. For instance, the surface areas of titania samples prepared in pure water (H-Base) and concentrated ammonia (H-A12) are respectively 28% and 61% smaller than H-SA2. At each acidic pH level (i.e. 2 or 4), comparable specific surface areas are seen for different acids.

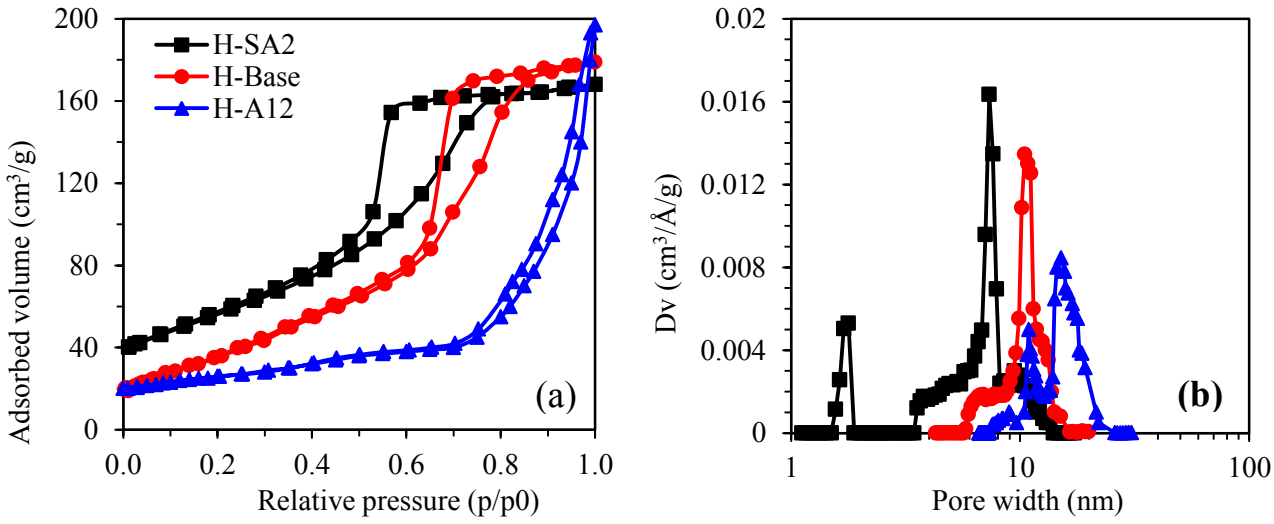

Figure 5.16 Nitrogen adsorption–desorption isotherms and pore-size distribution of H-Base, H-SA2, and H-A12

5.2.2.1.3. Morphological structure

The porous structure of TiO_2 photocatalysts in the micrometer range was studied by scanning electron microscopy. Figure 5.17 demonstrates the SEM images of H-SA2, H-Base, and H-A12 at two different magnifications, in which the macroporous structure of catalysts can be easily seen. Basically, three forms of porosity can be noticed: (i) long and well-oriented macrochannels that are parallel to each other and perpendicular to the outer surface of the particle, (ii) surface macropores of 0.8-9.3 μm in size, and (iii) porous walls with pores mostly smaller than 0.5 μm. Considering the fact that no surfactant or template was used in the preparation process, the macropores sizes differ and a certain degree of randomness can be seen in the structure of the samples. In the course of titanium precursor hydrolysis and subsequent condensation reactions, butanol was released into the aqueous solution, which could create microphase-separated regions of solid Ti particles and water-alcohol channels. This can provide the right condition for the formation of macrochannels which are observed in the SEM images. The hydrothermal route could successfully advance titanium dioxide crystallization while maintaining the hierarchically porous network initially formed during hydrolysis and aging processes. It is noteworthy that these open-ended tubelike macrochannels can facilitate the diffusion of VOC molecules to the active sites of titania and also serve as paths for emitted photons to reach particle's interior regions.

TEM was employed to further elucidate the microstructure of hydrothermally-prepared TiO_2 photocatalysts. Figure 5.18 presents the TEM and HR-TEM images along with dark-field imaging of H-Base, H-SA2, and H-A12. No long-range ordered mesoporous structure can be seen in Figure 5.18a, d, or g, which indicates that a major portion of mesopores are originated from the aggregation of small titania crystals (i.e. interparticle porosity). This could be more easily observed in the dark-field images of the samples, brought in Figure 5.18b, e, and h. In good accordance with the BET results, depending on the sample, mesopores ranging from ca. 2 nm to ca. 30 nm in size are formed due to the accumulation of TiO_2 nanocrystals. As the pH of reaction medium is raised from 2 to 12 (i.e. H-SA2 to H-A12), the interparticle pore size grows as well, which could be deduced from the enlargement of white dots in the dark field images. The HR-TEM images reveal that the crystallinity and crystal size are improved in more alkaline preparation environments. Anatase crystal sizes measured directly from HR-TEM images (Figure 5.18c, f, and i) are about 7, 6.5, and 15.5 nm for H-Base, H-SA2, and H-A12,

respectively. The clarity of lattice fringes of titania crystals in HR-TEM images, specifically in Figure 5.18i, suggests high degree of crystallinity for all samples.

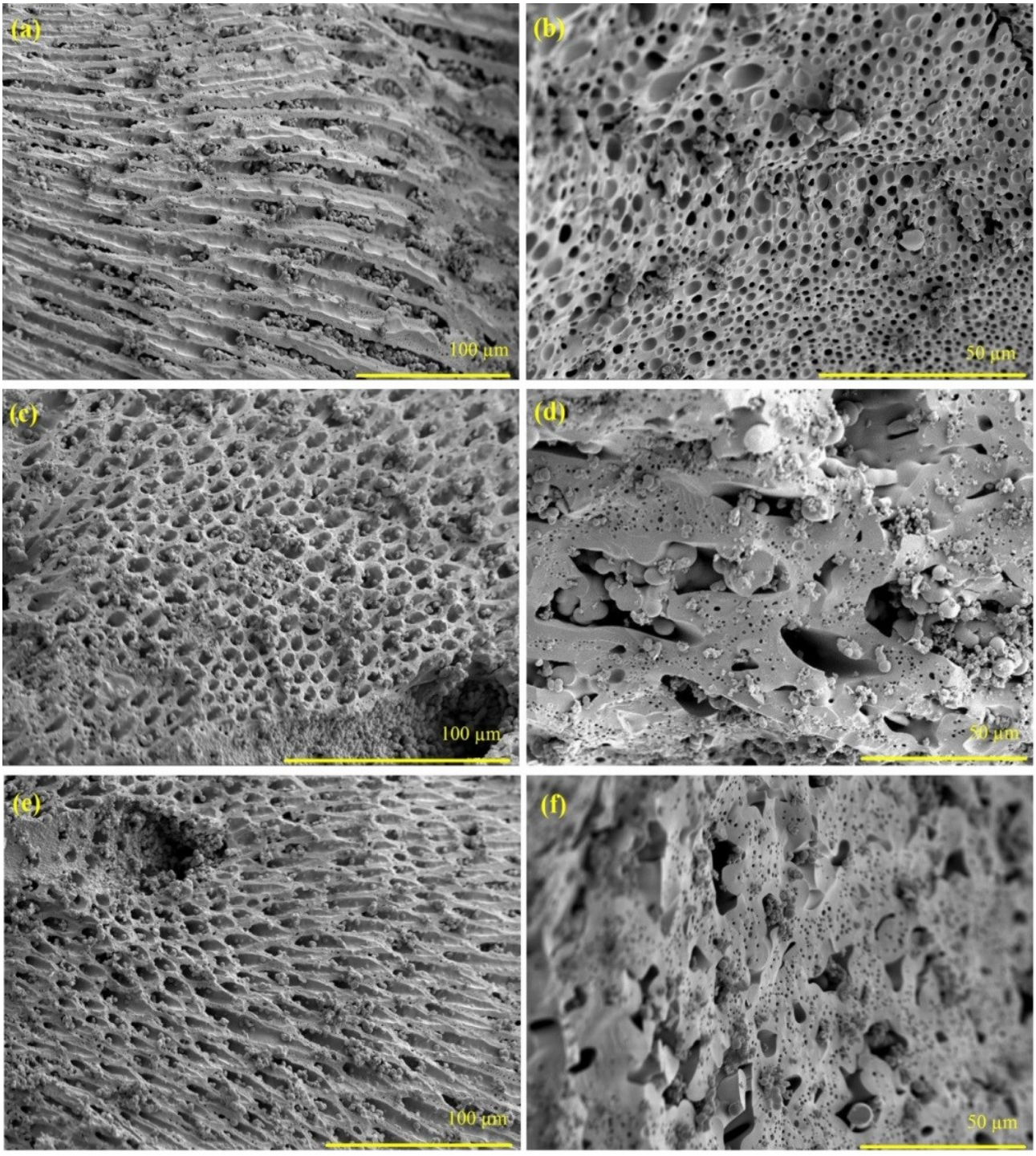

Figure 5.17 SEM images of (a, b) H-Base, (c, d) H-SA2, and (e, f) H-A12

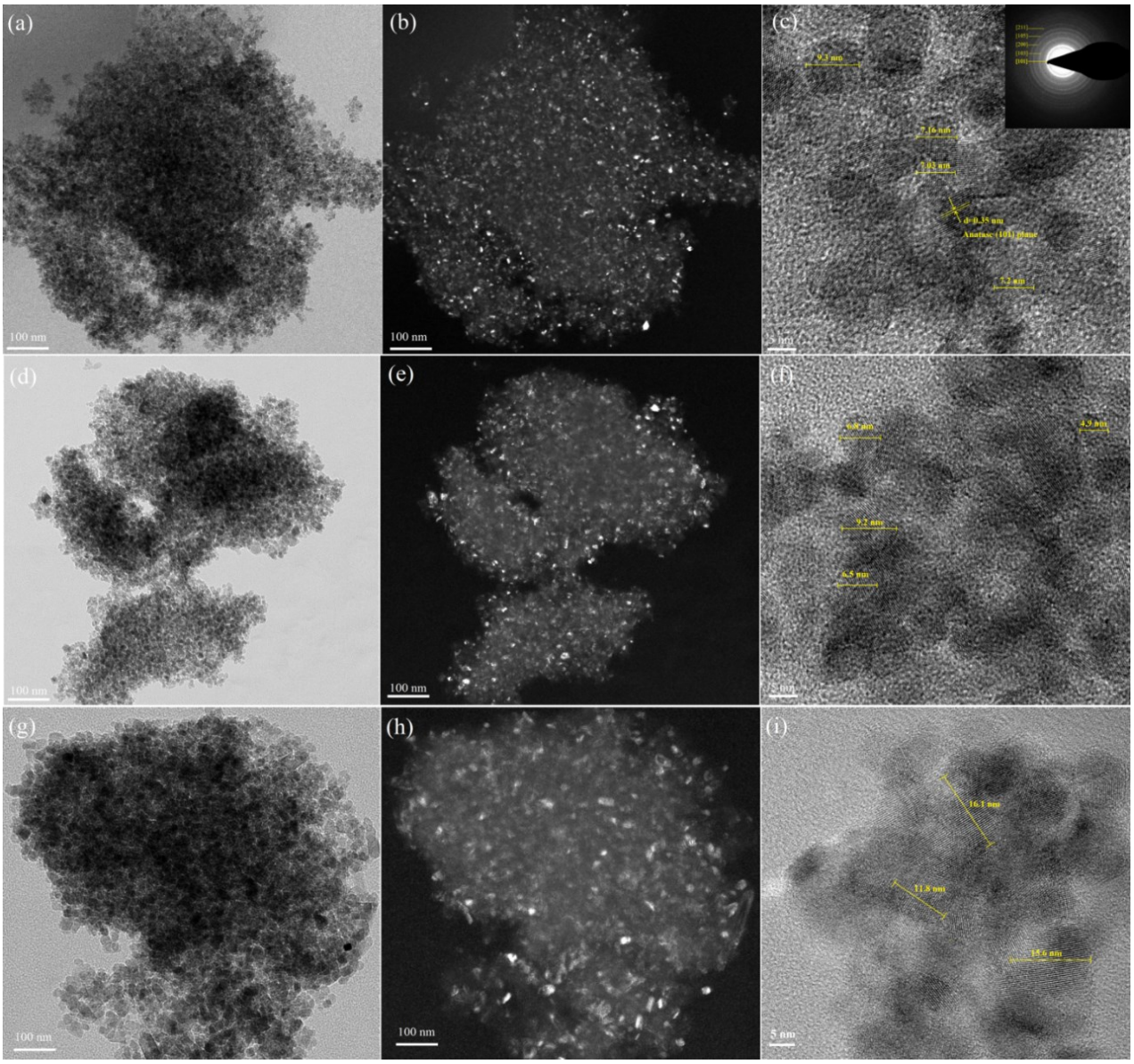

Figure 5.18 TEM and HR-TEM images of (a, b, c) H-Base, (d, e, f) H-SA2, and (g, h, i) H-A12. Inset of (c): SAED pattern of H-Base.

The lattice fringes are around 3.5Å, corresponding to the (101) plane of anatase [194]. The polycrystalline anatase phase is, demonstrated by SAED pattern (inset in Figure 5.18c), complying with the results of the XRD analysis. Clear diffraction rings indexable to anatase (*d*-spacings and (*hkl)* values: 0.352 (101), 0.243 (103), 0.189 (200), 0.169 (105), and 0.166 nm (211); JCPDS no. 21-1272) further shows that H-Base has good crystallinity. It is worth mentioning that the particle size distributions of yielded titania samples (not shown) were fairly narrow. Producing uniformly sized or monodispersed particles is in fact one of the known

advantages of hydrothermal route. The reason is that in the hydrothermal route, crystallization and crystal growth occur in a homogeneous condition, therefore, the crystal size distribution is fairly narrow.

5.2.2.1.4. Photoluminescence and hydroxyl radical analyses

Photoluminescence spectroscopy can be employed to investigate the efficiency of charge carriers generation and separation. Considering the fact that electron-hole recombination in titanium dioxide results in PL emission, PL analysis provides valuable information on the availability of electrons and holes for photocatalytic reactions [206]. The PL spectra of photocatalysts prepared in various hydrothermal reaction media are illustrated in Figure 5.19. To facilitate the comparison between different spectra, only some samples are represented in Figure 5.19 and instead all fluorescence intensities (at 390 nm) are listed in Table 5.7. In the wavelength range of 330-570 nm, the shapes of spectra are very similar and only small shifts can be noticed for the main emission peaks. Deconvolution of H-SA2 spectrum is presented in the inset of Figure 5.19, which indicates that the spectra consist of one strong peak at about 390 and four weaker peaks at 424, 445.5, 489, and 532 nm. The strong peak at about 390 nm (depending on the catalyst) is due to the emission of band gap transition, with the energy of light close to the band gap energy of anatase (387.5 nm) [207]. This peak gets slightly red shifted to the right for samples prepared at higher pH values due to the improved crystallinity. The emission peak appears at 424 nm can be attributed to the indirect band edge allowed transitions and self-trapped excitations localized in TiO_6 octahedra [208, 209]. The latter is the result of interaction between conduction band electrons (on Ti 3d orbital) and holes in the O 2p orbital of TiO_2 [206]. The emission bands at 445.5 and 489 nm can be assigned to excitonic PL, which mainly originate from surface oxygen vacancies, crystal defects, and/or self-trapped excitations in TiO_6 [29, 210]. It is noteworthy that oxygen vacancy is an intrinsic defect in TiO_2 lattice which traps the e^-/h^+ and creates the intermediate energy states in the forbidden gap. There is also a PL band at 532 nm, which can be attributed to the oxygen vacancies, impurities and defects [211]. Figure 5.19 reveals that the emission intensity to a great extent agrees with photocatalyst crystallinity. In this regard, H-SA2 with the lowest crystallinity among prepared samples exhibits the highest PL intensity, suggesting significant charge carriers recombination. On the other hand, H-A12 and H-Base, which comparatively possess higher crystallinities, show weaker PL emissions. Enhancement in

photocatalyst crystallinity reduces the number of crystal defects that potentially instigate the recombination of electrons and holes.

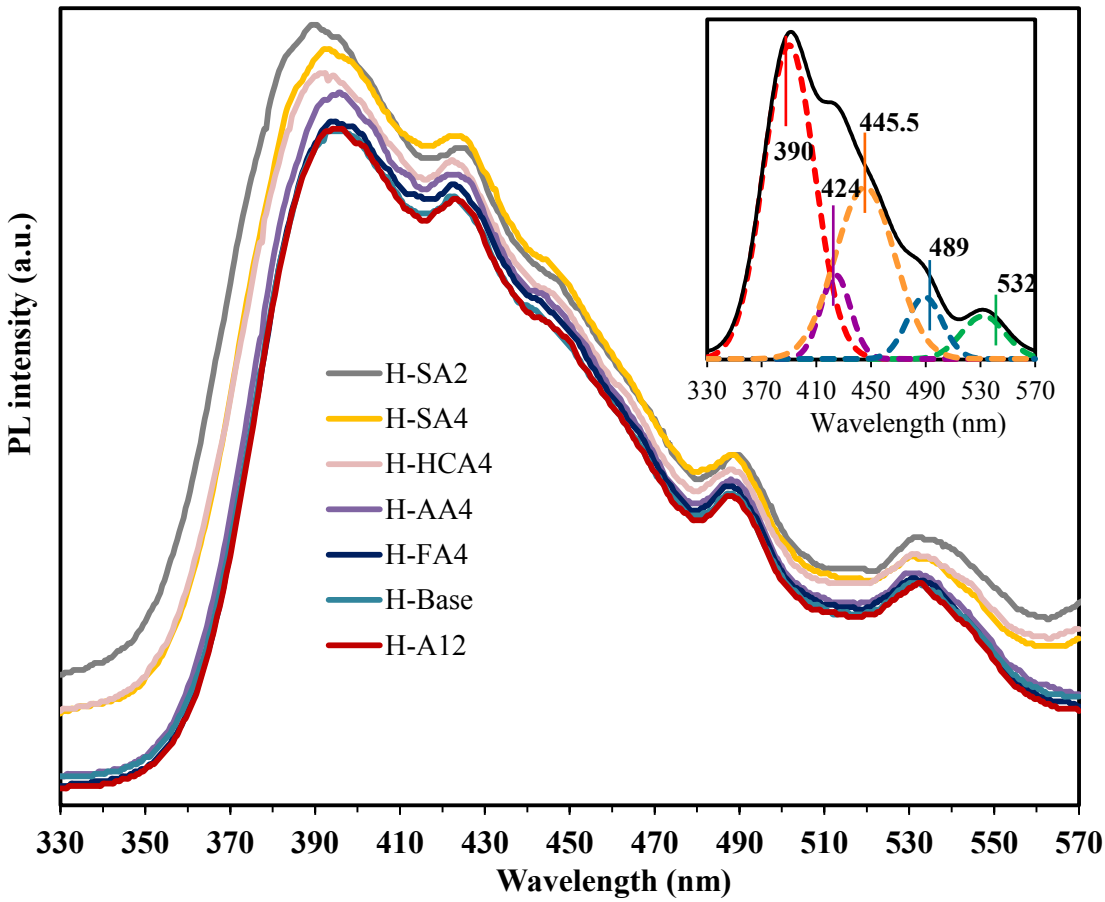

Figure 5.19 Photoluminescence spectra, inset: deconvolution of H-SA2 spectrum

Fluorescence spectrometry technique with TA as probe molecule was used to compare the ability of titania samples to produce ˙OH. Hydroxyl radicals quickly react with TA and produce highly fluorescent 2-HTA; thus, intensity of the PL peak of 2-HTA is proportional to the population of •OH on the surface of photocatalyst. The PL spectra of TiO_2 photocatalysts prepared at different hydrothermal conditions are demonstrated in Figure 5.20. The inset of Figure 5.20 depicts the fluorescence spectra that are obtained from supernatant liquid of H-Base titania irradiated for different durations (from 5 to 60 min). The linearity of PL intensity with time suggests that the number of generated ˙OHs is proportional to irradiation time. For the sake of clarity, only sufficiently distinct PL spectra are depicted in Figure 5.20 and the maximum PL intensities at 425 nm for all samples are listed in Table 5.7. H-SA2 has a relatively small PL intensity, which

is obviously related to its low crystallinity that substantially increases the chance of charge carriers recombination. By increasing the pH value of the reaction medium to 4, an increment in the PL intensity is seen for all acids except hydrochloric acid (Table 5.7), which surprisingly shows a small diminution in PL intensity for H-HCA4. The enhancement in crystallinity results in fewer recombinations, more e^--h^+ pairs, and higher concentrations of $^{\bullet}OH$ (i.e. 2-HTA) which could explain the stronger fluorescence emissions.

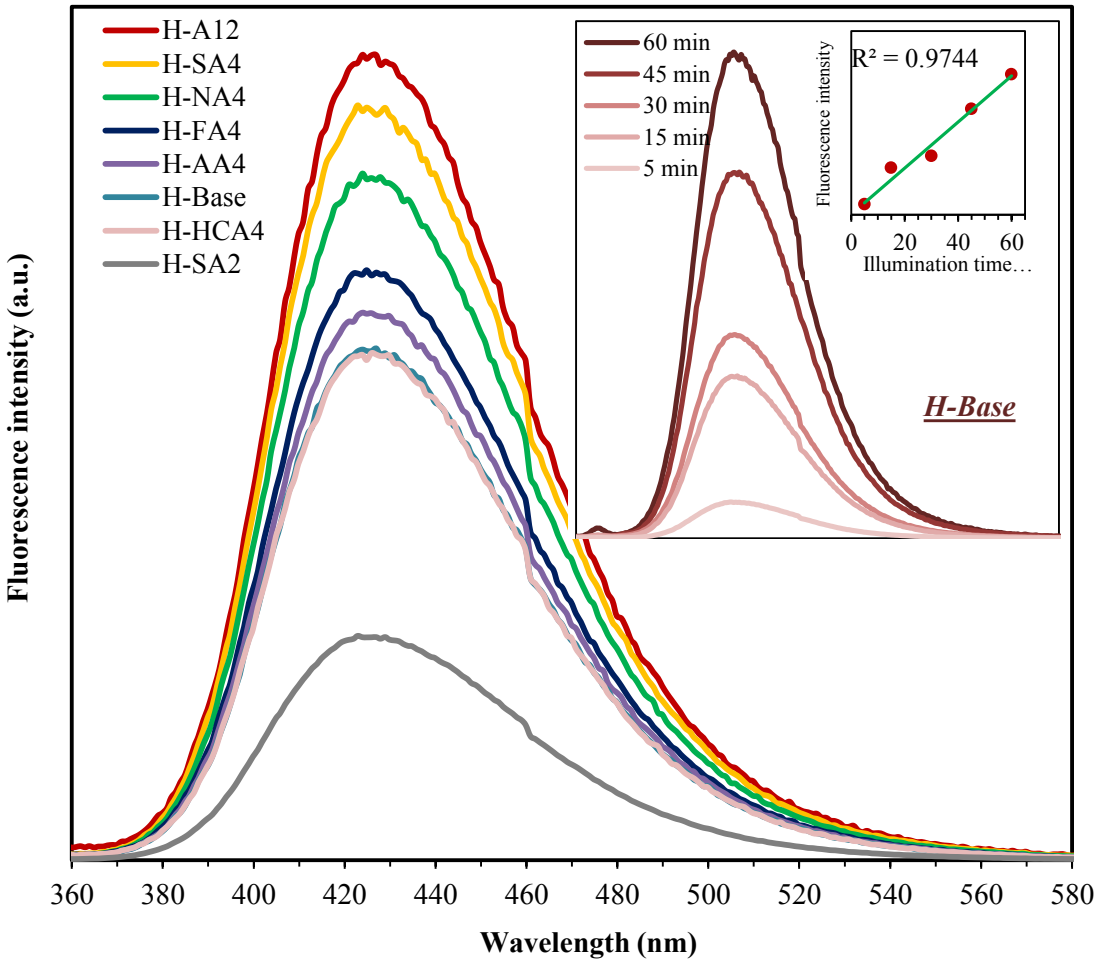

Figure 5.20 Fluorescence spectra, inset: variation in fluorescence intensity of H-Base irradiated for various durations

Despite the fact that the relative crystallinity of H-HCA4 is greater than H-HCA2 (1.19 vs. 1.05), H-HCA2 has slightly larger PL intensity compared to H-HCA4 (2253.6 vs. 2020.2 a.u.). This could be rationalized by comparing the key properties of H-HCA2 and H-HCA4: (i) H-HCA4 has a larger brookite content (17.3 vs 14.8%) and (ii) H-HCA4 specific surface area is roughly 11% smaller than H-HCA2, both (i) and (ii) contributing to lower PL intensity. By employing an

alkaline hydrothermal solution (i.e. H-A12) an increase in the PL intensity can be noted which could be anticipated given the huge gap between the relative crystallinity of H-A12 and other samples. Figure 5.21 demonstrates the variations in PL intensity and fluorescence intensity with relative crystallinity of photocatalysts (reported in Table 5.7). The blue circles represent the connection between photocatalyst relative crystallinity and charge carrier separation efficiency. The negative correlation between the PL intensity and degree of crystallinity implies that the recombination process is less severe in TiO_2 samples with higher crystallinity. On the other hand, surface area normalized fluorescence intensity (calculated based on the data in Figure 5.20 and Table 5.7) and relative crystallinity exhibit an acceptable level of proportionality (red trend line, R^2=0.79). The positive correlation suggests that a greater number of $^{\bullet}OH$s can be produced on the surface of titania samples with better crystallinity. On the basis of this trend, it can be concluded that once the contribution of surface area is excluded, among various features of catalyst (e.g. crystallinity, anatase content, crystal size, and band gap), the governing factor in generation of hydroxyls radicals on TiO_2 is crystallinity.

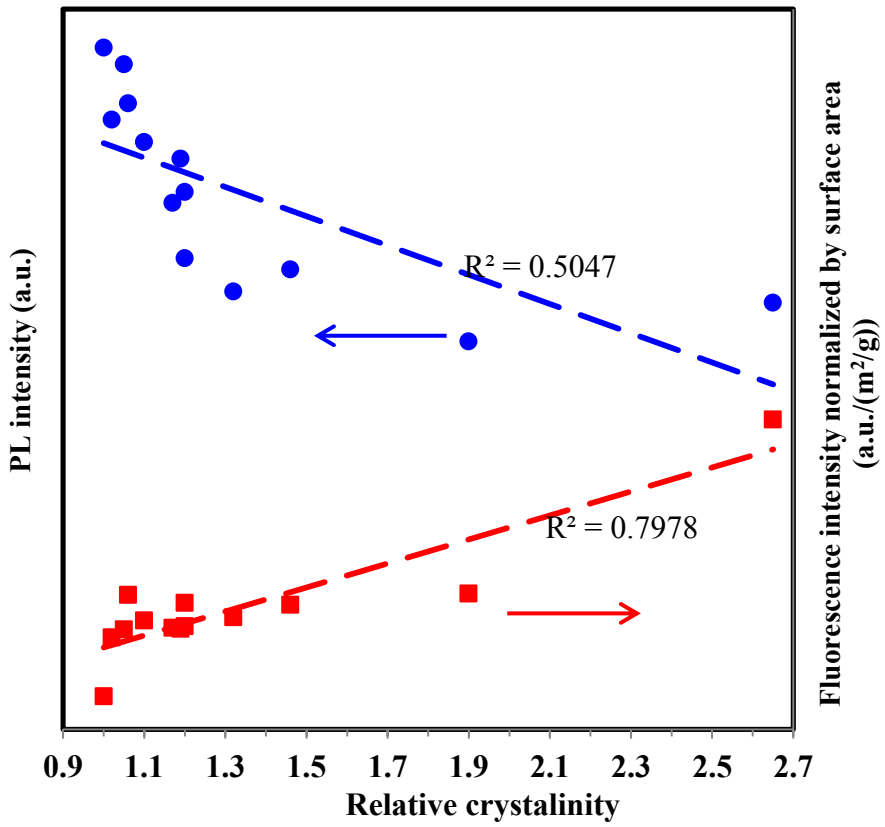

Figure 5.21 Dependence of PL and normalized fluorescence intensities on photocatalyst crystallinity

5.2.2.1.5. XPS

XPS is considered a reliable method to acquire information regarding the chemical states and surface chemical compositions of photocatalysts. The XPS survey spectra of H-SA2, H-A12, and H-Base are presented in Figure 5.22, indicating that all three titania samples contain Ti, O, and C elements. Besides small quantities of carbon and sulfur (only for H-SA2), no other impurities were observed in the XPS surveys. The C1s peak located at a binding energy of approximately 285 eV is assigned to adventitious carbon.

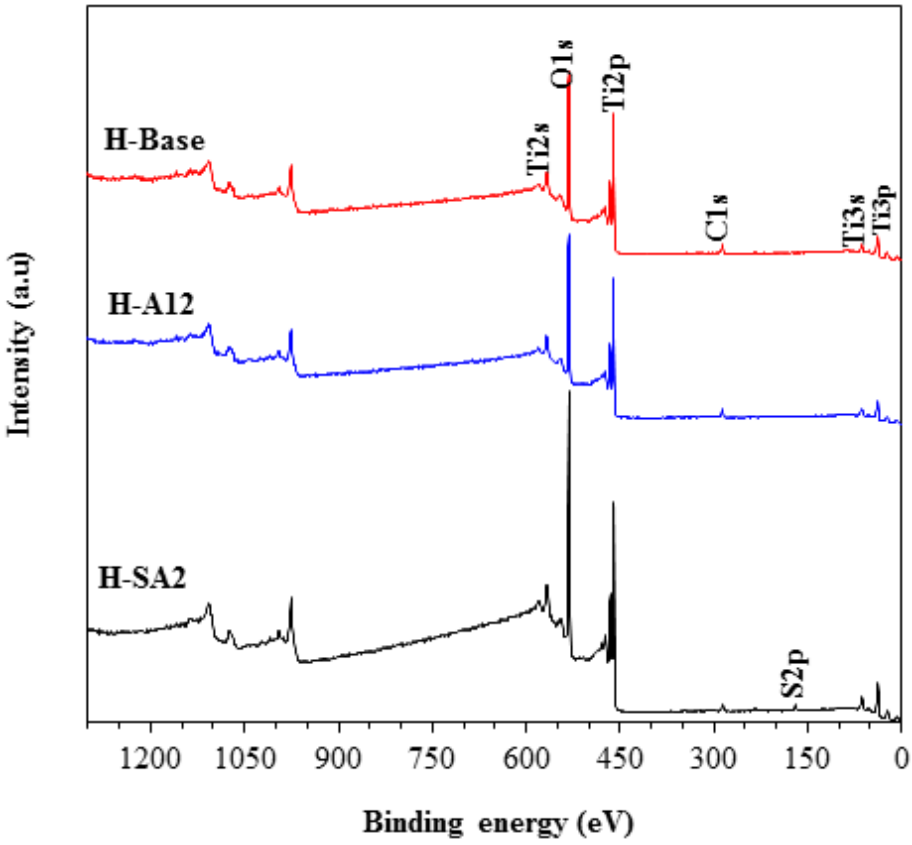

Figure 5.22 XPS survey spectra of H-Base, H-SA2, and H-A12

Figure 5.23a shows high-resolution XPS spectra of O1s region after Gaussian curve fitting, revealing presence of different types of oxygen on photocatalyst surface. The O1s can be mainly fitted into two peaks: a main peak at 530.3 eV and a smaller one at 531.8 eV which are respectively ascribed to lattice oxygen (Ti –O) in TiO_2 crystals and surface hydroxyl group (Ti–OH) [43, 212]. The peak area of hydroxyl groups of H-SA2 sample is much larger than those of H-Base and H-A12, indicating that the former contains more hydroxyl groups. As reported in

Table 5.8, the OH/O_{tot} ratio for photocatalysts declines with increasing the pH of hydrothermal reaction medium. This is due to the fact that at a higher pH, hydrothermal reactions further proceed; thus, many surface hydroxyl groups are consumed in condensation reactions to form Ti-O-Ti networks. Additionally, the stronger OH peak for H-SA2 can also be partly attributed to its larger surface area compared to the other two samples. Figure 5.23b illustrates the high resolution XPS spectra of C1s region of photocatalysts. The C 1s region can be deconvoluted for three peaks at bindings energy of 284.7, 286.2, and 288.7 eV. The main peak (at 284.7 eV) represents carbons in saturated hydrocarbon groups (C-C and C-H) [213] which could result from residual carbon in the hydrothermally-prepared samples or the adventitious carbon. The small peaks at 286.3 and 288.7 eV, respectively correspond to hydroxyl carbon (C–OH) and carboxyl carbon (C=O) [214, 215].

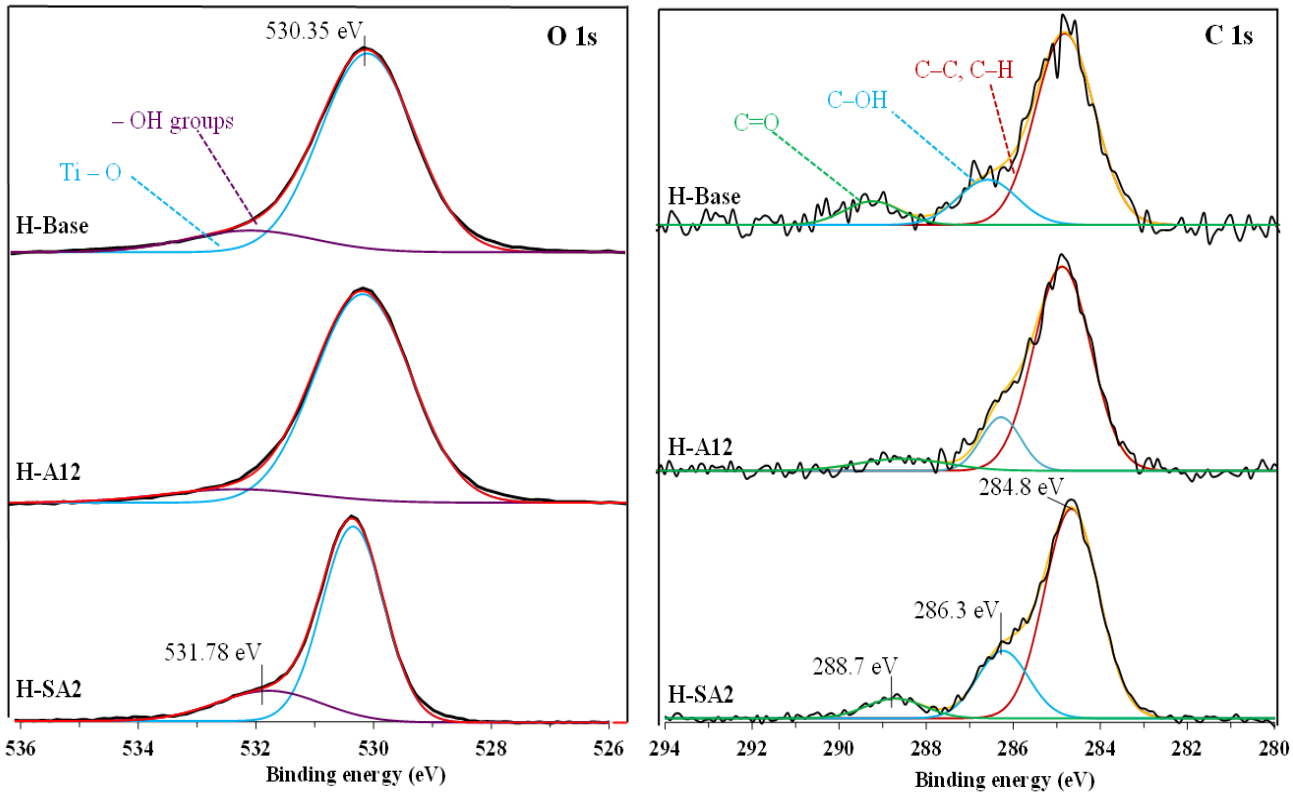

Figure 5.23 High resolution XPS spectra of O1s and C 1s region

The atomic ratios of Ti to O of all samples are in good agreement with the nominal atomic composition of TiO_2. The carbon can be attributed to the residual carbon from the sample and

adventitious hydrocarbon from XPS instrument itself. Excessive O element could come from the chemisorption of water on the samples [216].

Table 5.8 Elemental surface composition (atomic %) and ratio of hydroxyl groups oxygen to lattice oxygen

Photocatalyst	Element				OH/O_{tot}
	Ti	O	C	S	
H-Base	25.8	64.6	9.6	-	0.15
H-A12	26.5	63.0	10.5	-	0.09
H-SA2	25.4	64.4	7.5	2.7	0.25

5.2.2.2. Photocatalytic activity

The overall performance of a photocatalyst strongly depends on a number of factors including crystallinity, crystal size, surface area, porosity, crystalline phase, charge-separation efficiency, light harvesting ability, surface chemistry, and the ability to produce $^{\bullet}$OHs. Besides, the magnitude of influence of each factor on the performance of photocatalyst is closely linked to the key operating conditions such as relative humidity, inlet concentration, airflow rate and light intensity.

5.2.2.2.1. Impact of airflow rate

Figure 5.24 demonstrates the variation in removal efficiency of various photocatalysts with residence time in the range of 0.012-0.03 s. For all photocatalysts higher values of removal efficiency are reached at longer residence times since MEK molecules have more time to penetrate the boundary layer, adsorb on the surface, and react with the active species (e.g. hydroxyl radicals). However, it is interesting to note that the extent of the influence of residence time on the performance is closely related to the characteristics of photocatalyst, specifically surface area. As can be seen in Figure 5.24, depending on the residence time, the maximum removal efficiency of MEK is achieved over different titania photocatalysts: H-NA4 at 0.012 s (36.9%), and H-A10 at 0.02 s (48.0%) and 0.03 s (61.4%). This is understandable considering the fact that at shorter residence times the role of surface area (and porosity) in the overall VOC removal is more dominant with respect to that of crystallinity. In other words, for a catalyst with small surface area (e.g. H-A10), the short residence time severely limits the mass transfer of pollutants from the bulk to the surface and adjacent to the active sites/species. As a result, in the

case of H-A10, even though the high degree of crystallinity can guarantee a large density of OH radicals on the surface, the inefficient adsorption does not bring MEK molecules into contact with •OHs and, thus, impairs the removal efficiency. In contrast, at a longer residence time (i.e. 0.02 or 0.03 s), more MEK molecules are available on the surface of H-A10 and the oxidation reactions will be the determining step. To better understand this point it could be helpful to compare the relative performance drops (defined as: $1 - \frac{\eta_{t=0.012\ s}}{\eta_{t=0.03\ s}}$) of H-NA4 and H-A10. The relative performance drops for H-NA4 and H-A10 are 0.33 and 0.42, respectively, which clearly points to the fact that H-A10 is more sensitive to the changes in airflow rate. Except H-A12, all other hydrothermally synthesized TiO_2 samples significantly outperform P25 in MEK removal efficiency primarily due to the large surface area, multiscale porous structure, and sufficiently high crystalinity.

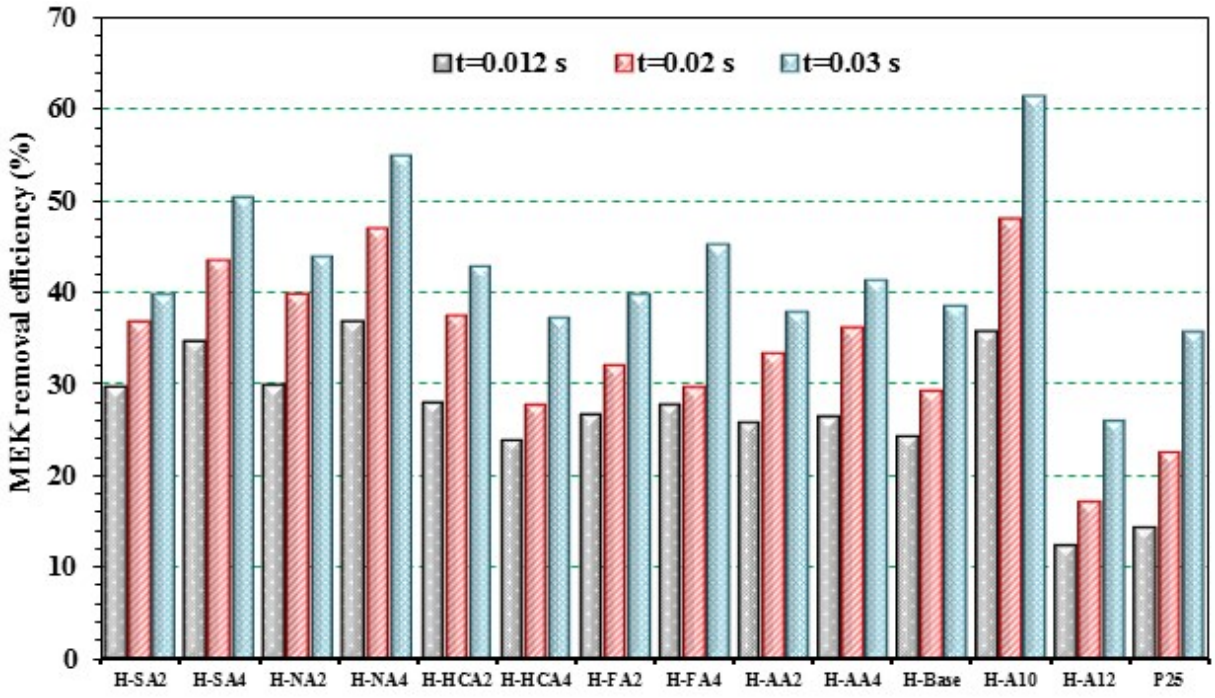

Figure 5.24 Effect of residence time on MEK removal efficiency over various photocatalysts

Figure 5.25 presents the corresponding by-products generation for the hydrothermally-prepared catalysts and P25. In the outlet air stream formaldehyde, acetaldehyde, acetone and traces of propionaldehyde were detected as unwanted by-products along with CO_2 as the main product. As a general trend, the total amount of by-products grows with the residence time clearly due to the increment in degradation rate. At longer residence times, more MEK molecules can adsorb on

the surface and participate in the catalytic reactions, leading to formation of larger amounts of intermediates/by-products. However, since intermediates/by-products as well have a higher chance of reaction and re-adsorption on the surface as the airflow rate decreases, the increase in the amount of by-products does not exactly correspond with the enhancement in the efficiency. For instance, MEK removal efficiency enhances from 35.7% at t_{res}=0.012 s to 61.4% at t_{res}=0.03 s, while the total amount of by-products increased from 144.7 ppb to only 211.5 ppb. On the other hand, it can be noticed that in the majority of cases and especially at t_{res}=0.012 s, despite the fact that the removal efficiency is much higher on the high-surface-area and hierarchically porous samples than on P25, the amounts of by-products are comparatively lower. The reason is that the multimodal porous TiO_2 with an interconnected structure more efficiently traps the intermediates, barricades their release to the gas phase, and advances total mineralization.

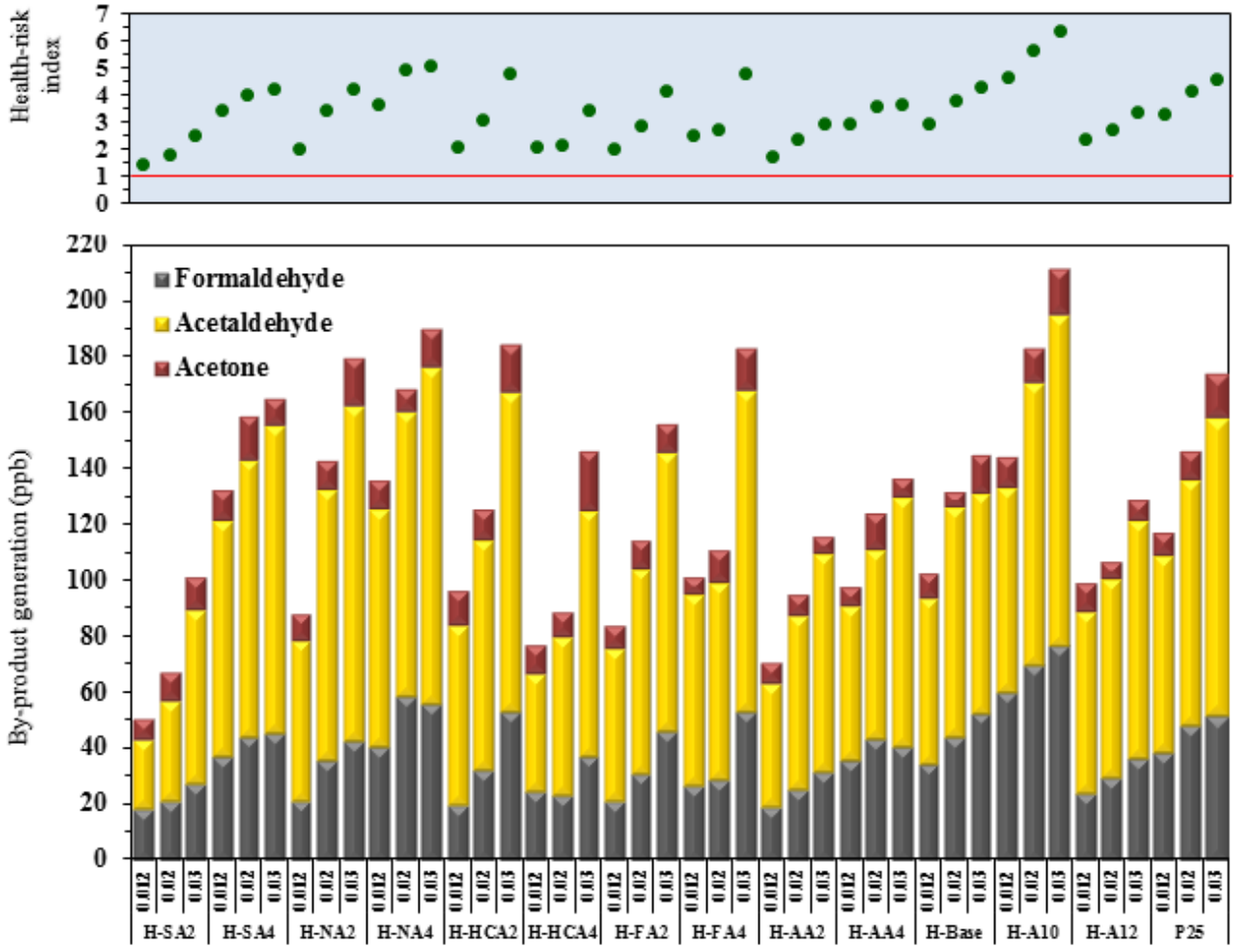

Figure 5.25 Effect of residence time on by-products generation during MEK photocatalytic degradation

Generation of unwanted by-products is one of the main shortcomings of photocatalytic air purification. It has been demonstrated that under severe operating conditions, the treated air may exert even more health risks to human because it carries by-products which are more harmful than the original contaminant [217, 218]. Consequently, in the present study we analyze this issue by assessing the health-risk index for generated by-products during PCO of MEK under various operating conditions. The top graph in Figure 5.25 displays the variation in HRI with the residence time over different photocatalysts. As could be expected from the trends of by-products generation, the higher the residence time is, the larger the HRI is. The HRI value varies between 1.47 and 6.32, which is reasonable considering that the inlet concentration of MEK is 1000 ppb. Among the generated by-products, formaldehyde is the most hazardous one with a REL value of 16 ppb and known to be a carcinogen. Consequently, the amount of formaldehyde in the outlet stream most severely affects the HRI value.

5.2.2.2.2. Impact of relative humidity

Presence of high concentrations of water vapor (up to 22000 ppm) in air especially during summer is a serious yet inevitable barrier against efficient removal of pollutants. In this study, the impact of relative humidity on the efficacy of developed titania samples is investigated by performing the PCO tests at three humidity levels: 0, 20, and 50%. As can be seen in Figure 5.26, the response of photocatalyst to the increment in relative humidity (from 0 to 50%) follows one of two trends: (i) steady reduction in MEK removal efficiency or (ii) presence of an optimum performance at 20% relative humidity. The first trend can chiefly be attributed to the adsorption competition between water and MEK molecules over the active sites of titania. In addition, the strong hydrogen bonds between water molecules and surface hydroxyl groups result in the formation of a water film on TiO_2. The water film diminishes the attraction forces between MEK molecules and titania and exacerbates the adsorption process. This adverse effect is less noticeable for photocatalysts with large surface area (e.g. H-SA2, H-NA2, etc.) since these samples are more capable of hosting both MEK and water molecules. For instance, MEK removal efficiency over H-SA2, H-NA2, and H-HCA2 only drop by 3.6, 4.3, and 1.6% respectively as humidity increases from 0 to 50%. It is important to note that the hydrophilic character and high water solubility (i.e. polar) of MEK enable it to diffuse through or adsorb on the water film which lessen the influence of humidity on the adsorption process.

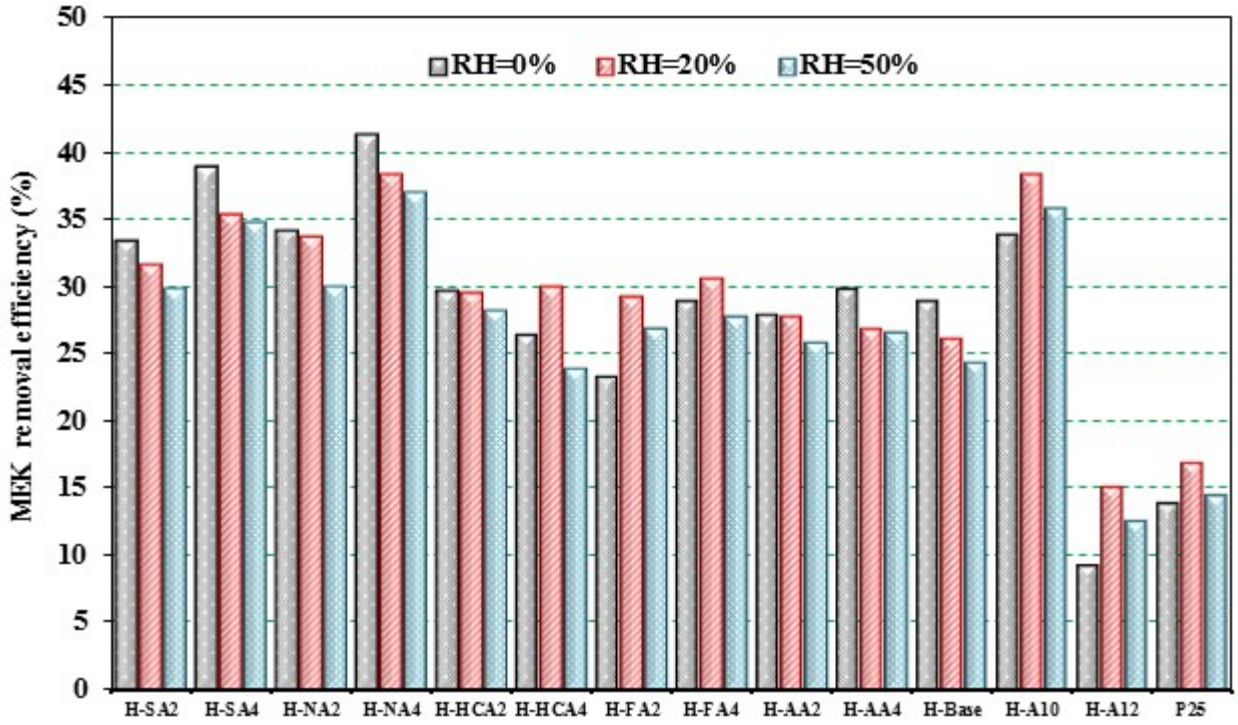

Figure 5.26 Effect of relative humidity on MEK removal efficiency over various photocatalysts

In the second trend, which is mostly observed for photocatalysts with small porosity and surface area, MEK removal efficiency firstly improves with humidity, peaks at humidity of 20%, and afterwards decreases. To explain this behavior one should keep in mind that besides surface hydroxyls, water vapor is the major source of •OHs. Water molecules on the surface of titania react with holes and produce •OHs, the main oxidant during MEK degradation. Therefore, it is logical to presume that for low surface area (i.e. highly crystalline) TiO_2 catalysts which also have low OH density, at dry condition, the precursor for •OH formation is missing, leading to a substantial performance drop. As an example, when humidity increases from 0 to 20%, MEK removal efficiency over H-A12 grows by roughly 63% compared to its initial value simply because more •OHs are available for oxidation of MEK. Further increment in relative humidity (i.e. 50%) deteriorates the efficiency since the inhibiting effect of adsorption competition overpowers the promoting effect of •OH formation. Humidity level can also influence the amount and type of generated by-products as depicted in Figure 5.27. In general, the amount of by-products increases with relative humidity because the adsorption competition between the intermediates/by-products and water molecules for active sites of titania becomes more severe. Nevertheless, it should be highlighted that the abundance of hydroxyl radicals at higher humidity

levels can boost the total mineralization and reduce the by-products. As a result, in some cases (e.g. H-Sa2, H-FA4, and H-A12) the amount of by-products at 50% is equal or even lower than that at 20%. Compared to the residence time, HRI is less sensitive to the changes in relative humidity and mainly fluctuates between 1 and 3. H-SA2 offers the safest PCO system (HRI=1.41-1.52) since its superior surface area, OH population, and adsorption capacity prevent the desorption of by-products from the surface to the air.

5.2.2.2.3. Impact of pollutant inlet concentration

The influence of MEK inlet concentration on removal efficiency over various TiO_2 samples is illustrated in Figure 5.28. In line with previous studies, raising the pollutant concentration leads to a sharp decline in removal efficiency (between 8-22.9%) in all cases.

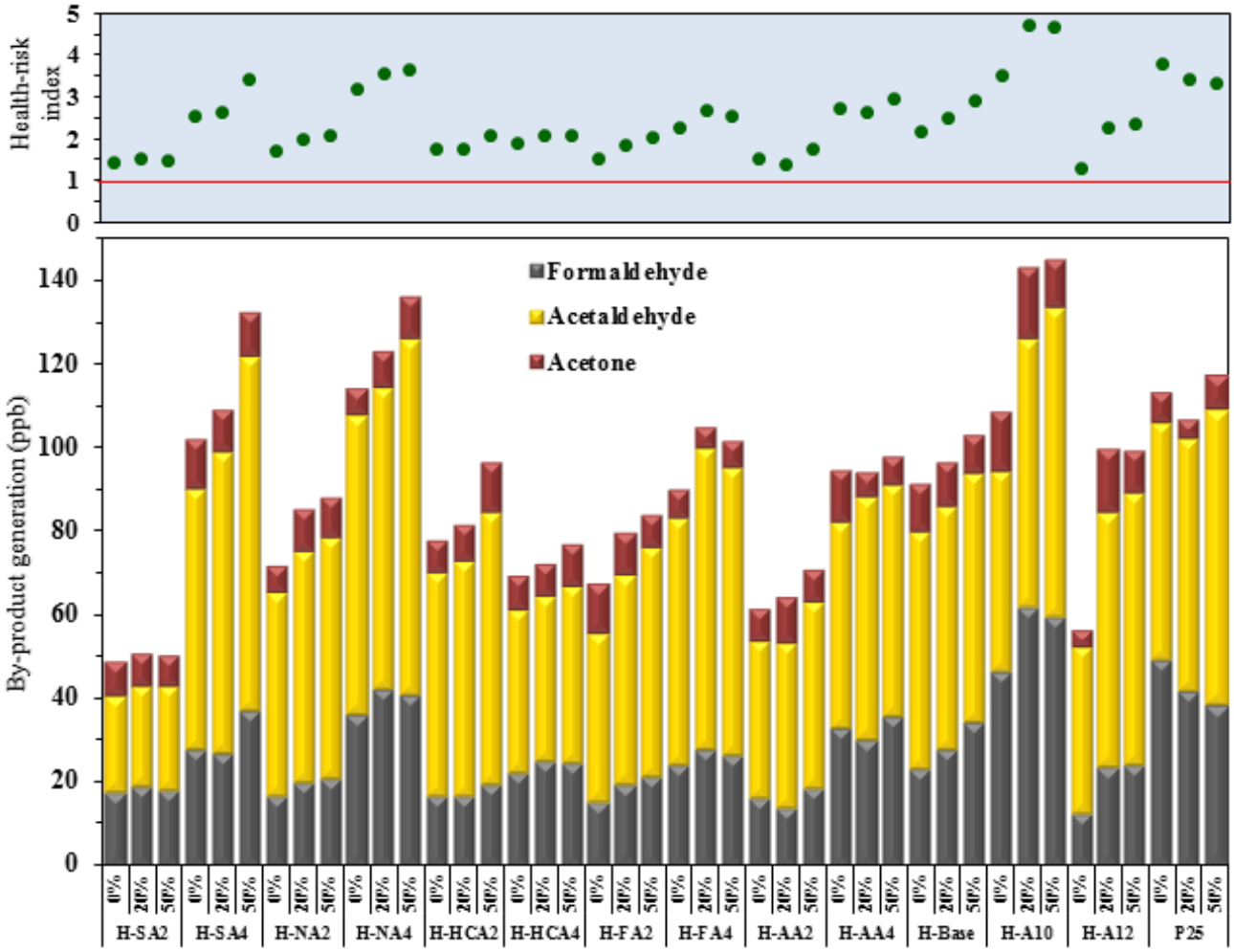

Figure 5.27 Effect of relative humidity on by-products generation during MEK photocatalytic degradation

This is understandable considering that the ratio of the number of "active/adsorptive sites + reactive species" to that of incoming MEK molecules decreases as the concentration increases. As a consequence, a greater number of MEK molecules cannot participate in the degradation reactions with $^{\bullet}$OHs. It is noteworthy that in indoor environment (i.e. office, residential, and commercial buildings) although there are numerous pollutants, the concentration of each VOC normally does not go beyond 20 ppb. Therefore, the values of removal efficiency at $[C_{MEK}]$=100 ppb are better representatives of the actual performance of the developed photocatalysts. By raising the hydrothermal medium pH from 2 to 4, MEK removal efficiency improves for all samples except with hydrochloric acid. At $[C_{MEK}]$=100 ppb, H-SA4, H-NA4, H-FA4, and H-AA4 outperform their counterparts prepared at pH=2 by 6.2, 11.9, 3.7 and 1.5% respectively. The observed behavior can be mainly attributed to the improvement in crystallinity of titania samples at higher pH values which results in higher quantum efficiency and lower recombination of e^--h^+ pairs. This indicates that for these samples the improvement in crystallinity outweighs the decline in surface area and porosity; therefore, the net effect of increasing solution pH is positive. On the other hand, the upward trend in MEK removal efficiency with pH corresponds well with the ability of these photocatalysts to create $^{\bullet}$OHs. For sulfuric, nitric, and formic acids, PL intensity is greater for the catalyst prepared at pH of 4, which implies larger concentration of hydroxyl radicals. Interestingly, for hydrochloric acid, both MEK removal efficiency and PL intensity experience downward trends by increasing the aqueous solution pH. Porosity and surface area diminution, and the increase in brookite phase content might be considered as the main reasons for the efficiency (and PL intensity) drop from H-HCA2 to H-HCA4. H-SA2 has the lowest crystallinity among the samples which leads to an extremely low PL intensity (893.7 a.u.); nevertheless, it reaches a comparable MEK removal efficiency. A certain contributing factor is H-SA2 surface area (and porosity) which exceeds all other samples prepared in acidic environments by 13-30% and provides H-SA2 a great advantage in the adsorption step. The photocatalyst prepared in ammonia alkaline solution with pH of 10 achieves the highest MEK removal efficiency, 61.4%, which is 26% higher than that of P25. The relative crystallinity and surface area of H-A10 are 1.9 and 121 m^2/g respectively, which apparently offer the best trade-off between these two contradictory features. In photocatalysis, charge carriers must reach and be stabilized at the surface of titania for e^-/h^+ transfer processes [198]. These phenomena are extremely hampered by recombination of e^--h^+ pairs in bulk and on the surface of photocatalyst.

Bulk and surface recombinations exacerbate with increment and decrement in crystal size, respectively. Consequently, it is logical to presume that at a specific crystal size the optimum balance between bulk and surface recombinations can be reached. Fluorescence spectrometry (OH radical generation) and photoluminescence results support the superior performance of H-A10. H-A10 has the second highest surface area normalized PL intensity (16.94 a.u./(m^2/g)), indicating the presence of a large number of hydroxyl radicals on the surface owed to satisfactory e^--h^+ separation. On the other hand, the weak PL emission for H-A10 also confirms the long lifetime of charge carriers on H-A10. It was witnessed that further increment in the hydrothermal solution pH (i.e. from 10 to 12) entails a drastic fall in MEK removal efficiency to 26%. H-A12 has the highest degree of crystallinity and PL intensity which are advantageous to PCO processes. However, the low surface area, decline in mesoporosity, small population of surface hydroxyl groups, and excessive crystal growth could be held accountable for the inferior activity of H-A12.

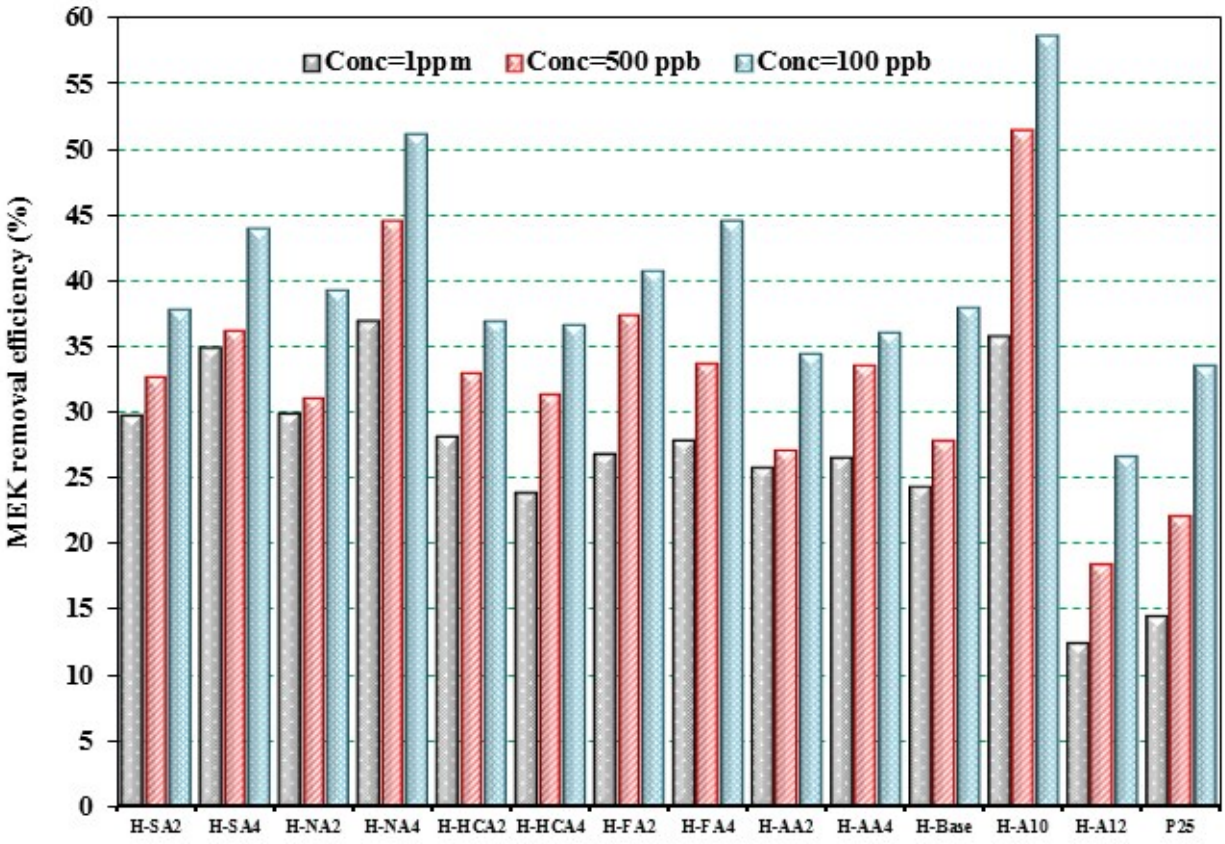

Figure 5.28 Effect of inlet concentration on MEK removal efficiency over various photocatalysts

It is worth noting that in our experiments photocatalysts with 100% anatase phase (i.e. H-A12 and H-FA4) do not possess the highest photoactivity, which is in contrary to the common belief that anatase is the most active polymorph of titania. The quantity and type of generated by-products during the experiments with different MEK concentrations are demonstrated in Figure 5.29. Expectedly, when the inlet concentration is higher a greater number of MEK molecules are decomposed or partially oxidized and thus more by-products are produced. Considering the top graph in Figure 5.29, the lowest health-hazards are obtained over H-SA2 for two reasons: small MEK degradation and large surface area, both of which contribute to lower HRI values. H-SA2 216.1 m^2/g surface area offers ample adsorption/active sites which can host incoming MEK molecules as well as the by-products generated throughout the PCO process. On the other hand, properly interconnected pores not only ease the diffusion of by-products (and MEK) into H-SA2 interiors, but act as trap and prevent the reintroduction of by-products (or intermediates) back to the gas phase. H-A10 and H-NA4 produce the largest quantities of by-products which is logical considering that they possess the highest removal efficiencies. It is interesting to note that although P25 has the second lowest MEK removal efficiency, it generates/releases a considerable amount of by-products. P25 small surface area in comparison to other titania samples brings about a severe adsorption competition among MEK, by-products, and water molecules. Therefore, light by-products such as acetone and formaldehyde are desorbed from the surface before undergoing the oxidation reactions toward complete mineralization. It has been suggested that the HRI value should not exceed 1 in order to assure a safe photocatalytic air purification system. As can be noted from the top graph in Figure 5.29, in most cases where the inlet concentration is 100 or 500 ppb, HRI is smaller or very close to one. Consequently, if we consider the application of these PCO systems under actual operating conditions, the generated by-products will not pose serious health issues.

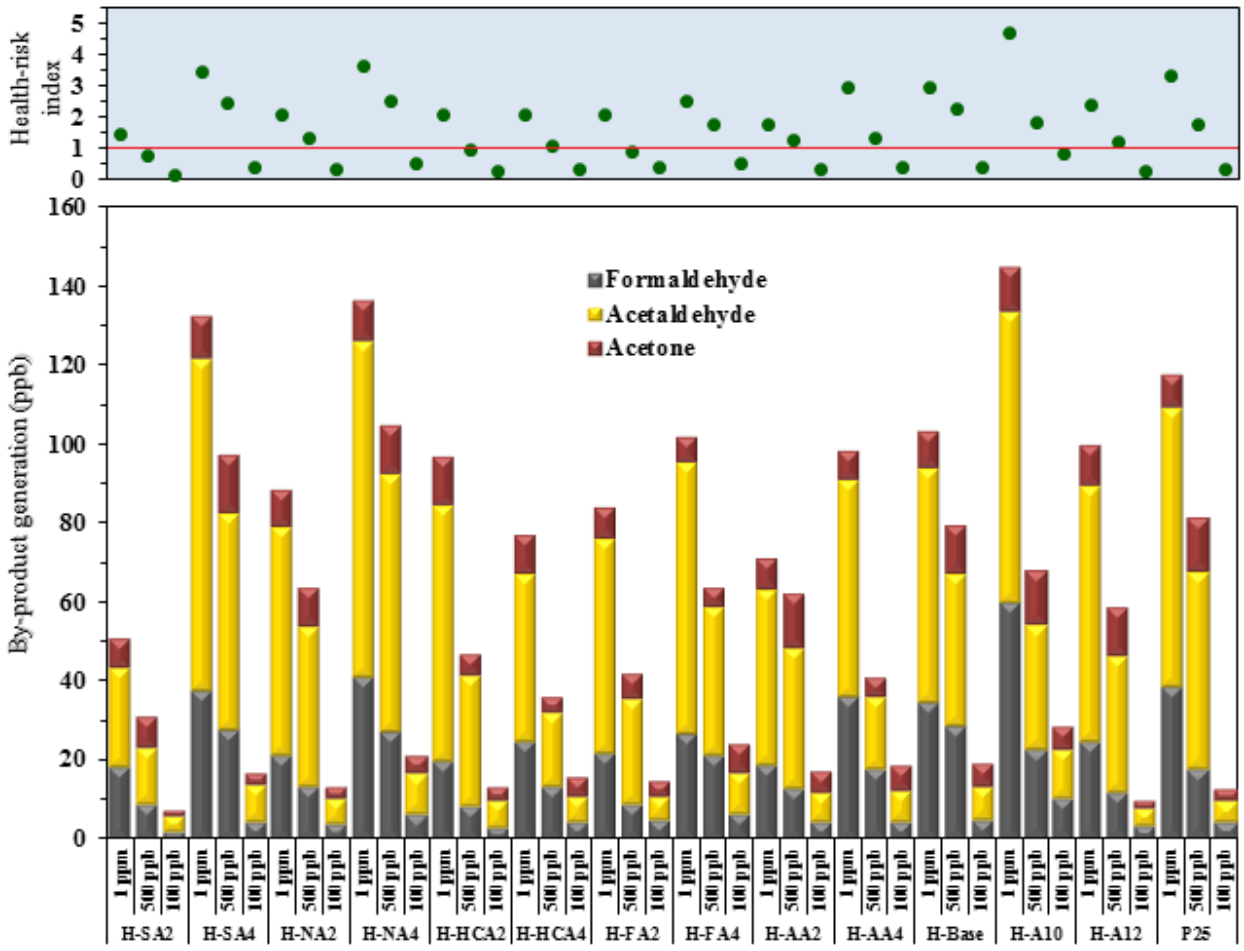

Figure 5.29 Effect of inlet concentration on by-products generation during MEK photocatalytic degradation

5.2.2.3. MEK degradation pathway

Based on the detected compounds in the gas-phase in this work and the intermediates/by-products reported in literature [217-221], a possible reaction pathway for photocatalytic oxidation of MEK is developed (Figure 5.30). In step I, illumination of titanium dioxide leads to creation of electrons and holes, which subsequently react with water, oxygen, and OH groups on the surface and generate strong oxidants. MEK molecules react with the photogenerated positive holes and/or $^{\bullet}$OHs to form alkyl radicals (H-abstraction). Through C-C scissions (step II) alkyl radicals break down into smaller alkyl radicals and various organic compounds including ketenes, ketones, propionaldehyde and propionic acid. Further surface reactions and radicals recombination result in the formation of ethanol, acetaldehyde, methanol and acetic acid. It has been suggested that during beta scissions several alkanes and alkenes might be produced (step

IV) although not detected in the gas phase [221]. Besides its direct formation in step III, acetaldehyde can also be formed via oxidation of ethanol. Then, acetaldehyde itself is oxidized to formaldehyde, acetic acid and methanol. A major portion of these light compounds go through further oxidation reactions and eventually are converted to CO_2 and water.

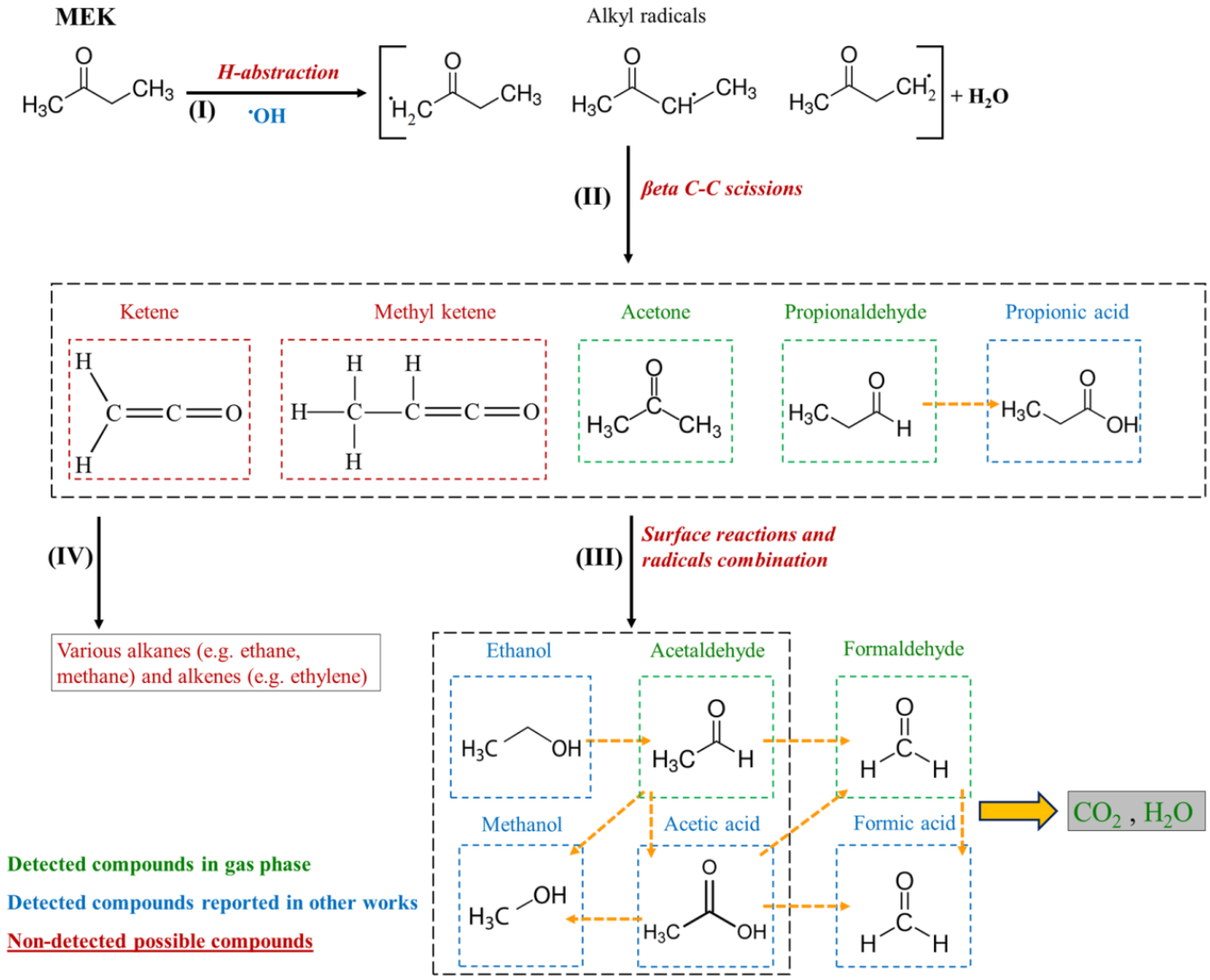

Figure 5.30 Possible reaction pathway for photocatalytic oxidation of MEK over titanium dioxide

5.3. Impact of photocatalyst morphology

As indicated in previous sections, activity of a photocatalyst depends on a large number of factors including crystallinity, crystal phase, crystal size, surface area, surface OH density, porosity, pore size, band gap, and ability to generate OH radicals. The fact that photocatalyst properties have non-linear and intertwined correlations with photoactivity makes property-performance prediction even more difficult and accounts for the absence of any mechanistic relationships between photocatalyst physicochemical features and VOC abatement ability. Structural dimensionality of TiO_2 has also a great impact on its properties and photocatalytic activity towards air contaminants. Numerous TiO_2 morphologies, such as nanoparticles, microspheres, nanotubes, nanosheets, hollow spheres, and hierarchically porous have been fabricated and tested for different applications [222]. Nevertheless, controllable fabrication of various titania structures with desired morphologies and architectures at micro- and nanoscale is still regarded an experimental challenge in material science. There are at most a handful of studies in which different TiO_2 designs have been compared for photocatalytic reactions; however, in these works a critical point has been overlooked which does not allow to draw any clear conclusion regarding the superiority of a specific morphology. It is extremely difficult and perhaps unreasonable to claim that a specific morphology outperformances others knowing that the developed morphologies have considerably different characteristics (i.e. crystallinity, surface area, etc.). This is quite an important point when we compare 0-D (e.g. nanoparticles and microspheres), 1-D (e.g. nanotubes and nanowires), 2-D (e.g. nanosheets and nanoplatelets), and 3-D (hierarchically porous) architectures. In addition, considering the fact that the applied conditions for evaluating the photocatalytic activity vary markedly in different researches, it is not possible to exploit the available data in literature to determine which design offers the best performance for photocatalytic air purification. In the quest for properly answering this question, we fabricated seven different titanium dioxide structures namely solid microspheres, mesoporous microspheres, hollow spheres, nanotubes, nanosheets, 3-D sea urchin-like, and 3-D hierarchically porous, and examined their efficiencies for removal of MEK. With deliberately adjusting the key parameters (e.g. hydrothermal time, temperature, pH, additives, solvent, etc.) based on our understanding of the physical/chemical phenomena during the synthesis and extensive literature review, we were able to reach the desired morphologies while keeping the variations in photocatalysts' crystallinity, crystalline composition, and surface area in narrow

ranges. This allows one to better make a comparison between different TiO_2 designs since the most influential features of these photocatalysts (i.e. crystallinity, crystal phase, and specific surface area) are, to a great extent, identical.

5.3.1. Methodology

5.3.1.1. Photocatalyst preparation

5.3.1.1.1. Solid microspheres

In a typical preparation procedure, 0.4 mL 0.1 M potassium chloride (from Fischer) aqueous solution was added slowly to 100 mL anhydrous ethanol under continuous stirring (400 rpm) at room temperature [223]. Then, 2.5 mL titanium tetra isopropoxide (from Fischer) was added dropwise to the above mixture. The resulted solution was stirred for 20 min and then aged for 24 h in a static state at ambient temperature. After aging, the precipitates were collected by means of centrifugation and washed three times with distilled water and ethanol successively. The obtained solids were dried in vacuum oven at 120 °C for 20 h. In the next step, 0.4 g of the amorphous titania was dispersed in 70 mL distilled water and stirred for 20 min. The slurry was transferred to a 100 mL stainless steel autoclave with a Teflon liner to undertake the hydrothermal treatment. The autoclave was heated at a rate of 3 ˚C/min to 180 ˚C, maintained at that temperature for 12 h, and finally cooled down (-3 ˚C/min) to room temperature. The resulting precipitate was separated from the solution by a similar procedure to that explained in the first step. Finally, the solid microspheres were dried under vacuum at 80 ˚C for 12 h. This sample hereafter is denoted as TSMS.

5.3.1.1.2. Mesoporous microspheres

For preparation of mesoporous anatase microspheres titanium tetrabutoxide and concentrated sulfuric acid were used. In a typical preparation route, 1.4 mL of TBOT was added dropwise to 80 mL H_2SO_4 2 M and stirred for 20 min to obtained a transparent solution. Afterwards, the solution was transferred into a 100 mL Teflon lined stainless steel autoclave and perfectly sealed. The autoclave was heated up in the electric oven at a rate of 3 ˚C/min to 160 ˚C, maintained at that temperature for 6 h, and cooled down (-3 ˚C/min) to room temperature. After the reaction, the formed solids in the liner were collected by centrifuge and washed with distilled water. This

process was repeated several times until the washing solution reached neutral pH value. Finally, the white product was dried in air at 70 ˚C for 12 h. This sample hereafter is denoted as TMMS.

5.3.1.1.3. Hollow spheres

First, 0.4160 g $Ti(SO_4)_2$ (from Sigma Aldrich, $Ti(SO_4).xH_2O+H_2SO_4$, 99%) was dissolved in 80 mL distilled water and stirred for 15 min at 300 rpm. This solution was mixed with 0.0177 g NH_4F (from Fisher) under vigorous stirring (600 rpm) for another 20 min [224]. The concentrations of titanium precursor and fluoride were 0.02 M and 0.006 M, respectively, in the reaction medium. The resulting mixture was poured into a 100 mL Teflon lined stainless steel autoclave and the hydrothermal synthesis was conducted at 180 ˚C for 12 h. After the reaction, the autoclave was allowed to cool down to room temperature (took roughly 6 h). The precipitates were filtered, washed with water several times, and dried at 100 ˚C for 12 h. This sample is denoted as THS.

5.3.1.1.4. Nanosheets

In a typical experiment, 14.56 mL TTIP and 2.0 g TiF_4 (from Fisher) were placed inside the liner cup. Then 4.88 mL 2-propanol, 1.2 mL H_2O and 0.4 mL HCl (to adjust the pH of initial solution) were added to the cup respectively [225, 226]. After sealing the stainless steel autoclave, the reactor was brought to 180 °C at a rate of 3˚C/min, allowed to react for 24 h at 180 °C inside the hot air oven, and left to cool overnight. The resulting white-gray precipitate was washed by bath sonication in 50 mL of 2-propanol for 30 min and subsequently centrifuged. The washing-centrifugation procedure was repeated three times and afterwards the solids were dried at 80 ˚C for 12 h. This sample hereafter is denoted as TNS.

5.3.1.1.5. Nanotubes

Crystalline nanotubes were prepared via hydrothermal treatment of P25 powder followed by thermal post-treatment. 2 g P25 powder was added to 80 mL NaOH 7.5 M and stirred for 30 min at 400 rpm to obtain a homogeneous slurry [227, 228]. The solution was transferred to a 100 mL Teflon lined autoclave and heated to 160 ˚C at a rate of ~ 10 ˚C/min and maintained at this temperature for 24 h. Afterwards, the products were washed with 0.1 M HCl and distilled water and filtered. The washing-filtering procedure was repeated until pH value of the rinsing solution was almost 6.5. The precipitates were dried in vacuum oven at 80 ˚C for 12 h. Finally, as-synthesized titanate nanotubes were calcined at 450 ˚C for 2 h. This sample is denoted as TNT.

5.3.1.1.6. 3-D sea urchin-like

These TiO_2 structures were fabricated via ethylene glycol (EG)-assisted solvothermal treatment [229]. In a typical experiment, 0.5 mL TBOT and 26 mL NaOH 1 M (aqueous solution) were mixed and stirred for 10 min at ambient temperature. To enhance the dispersion of TBOT precursor into the solution, a 5 min ultrasonication was applied. Then, 53 mL ethylene glycol (from Fischer) was added to the solution and vigorously mixed for another 10 min. The resulting white solution was transferred to the Teflon-lined hydrothermal reactor and heated at 180 ˚C for 12 h. Afterwards, the products were washed with 0.1 M HCl and distilled water and filtered. The washing-filtering procedure was repeated until the pH value of the rinsing solution reached 6. The precipitates were dried at 50 ˚C for 12 h and subsequently calcined at 550 ˚C for 2 h to enhance the crystallinity of the as-synthesized urchin-like titania. This sample is denoted as TSU.

5.3.1.1.7. 3-D hierarchically porous

To synthesis 3-D hierarchically porous titania, the preparation route explained in section 5.2 with minor modifications has been employed. TBOT was added to 0.01 M nitric acid aqueous solution. After aging for 24 h, the solution was transferred to autoclave and underwent hydrothermal reactions at 180 ˚C for 6 h. After separation, the resulting solids were calcined at 350 ˚C for 6 h. This sample hereafter is denoted as THP.

The experimental set-up design and operation are explained in details in section 3.1.2. The experimental conditions at which PCO tests were performed for photocatalysts of this section are given in Table 5.9.

Table 5.9 PCO tests experimental conditions

Parameter	Value	Unit
Inlet concentration	1006 ± 11.1	ppb
Relative humidity	18.5± 1.3	%
Volumetric flow rate	12	L/min
Residence time	0.05	s
Light intensity	5	mW/cm^2
Temperature	21.3 ± 1.5	°C
TiO_2 concentration	0.92± 0.02	mg/cm^2

5.3.2. Results and discussions

5.3.2.1. Morphological evolution

5.3.2.1.1. Titania solid and mesoporous microspheres

The morphology of yielded titanium dioxide solid microspheres was first examined by FE-SEM. Figure 5.31 illustrates the SEM images of TiO_2 products at different magnifications. As it can be seen, the preparation route resulted in well-defined solid spheres with sizes of about 0.3 to 0.8 μm. The spheres have rough surfaces (Figure 5.31c and d), indicating crystallization of TiO_2 and growth of TiO_2 crystallites. The formation of such structures can be explained by Van der Waals forces exist between particles. To lower the surface energy, the nucleated particles tend to form agglomerates with various geometries. Under these conditions, by forming spherical agglomerates the minimum surface-to-volume ratio and thus minimum surface free energy can be reached.

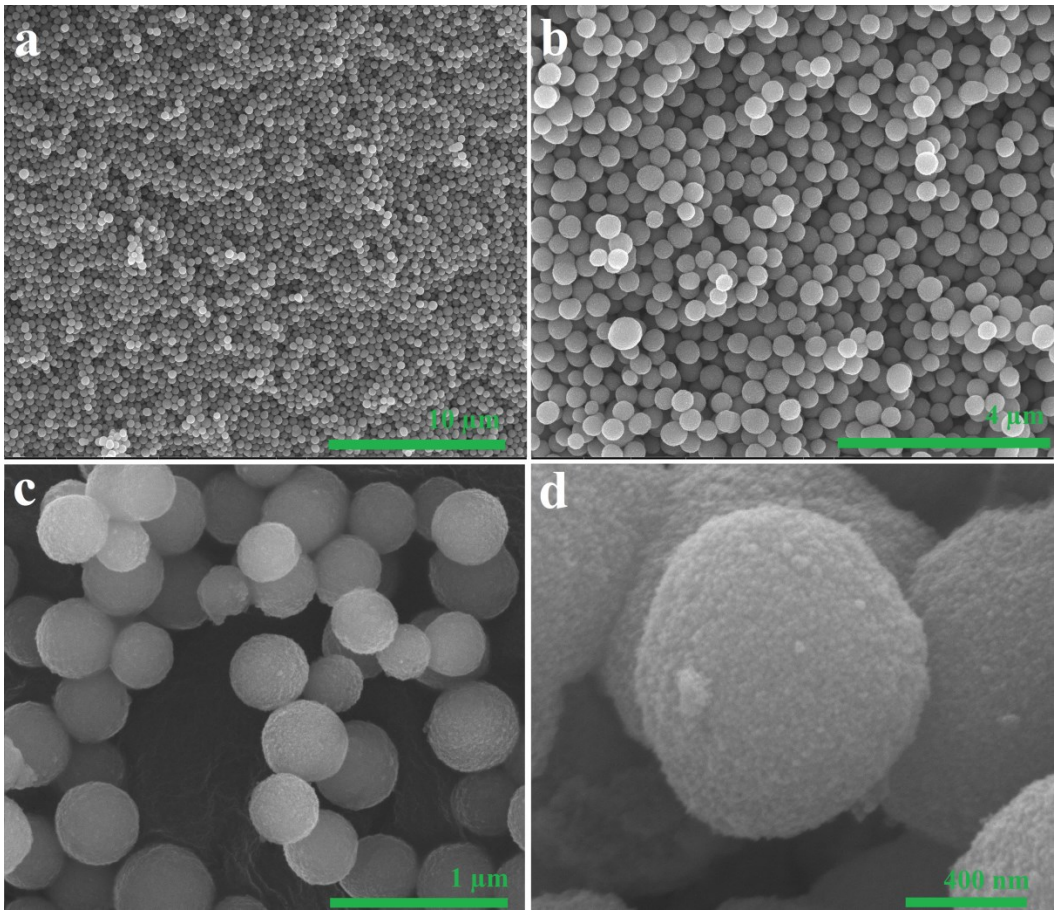

Figure 5.31 FE-SEM images of TSMS with well-defined spherical shape

To more closely investigate the structure of microspheres, TEM analysis was performed on the sample. TEM images (Figure 5.32a) further confirm that the prepared samples are solid spheres ca. 300-800 nm in size. TEM images also reveal that each sphere is composed of numerous nanocrystals of ca. 6-10 nm diameter, which is comparable to the grain size calculated from Scherrer equation (Table 5.10) based on XRD [101] diffraction peak (Figure 5.32b). The high degree of crystallinity could be deduced easily from the well-defined lattice fringes shown in the enlarged section of Figure 5.32c. This observation implies that the amorphous phase of TiO_2 could be successfully converted to anatase by undergoing a mild hydrothermal treatment. It can be noticed that a large number of mesopores are originated from the tightly interconnected TiO_2 nanoparticles evolved from amorphous titania during the hydrothermal reaction.

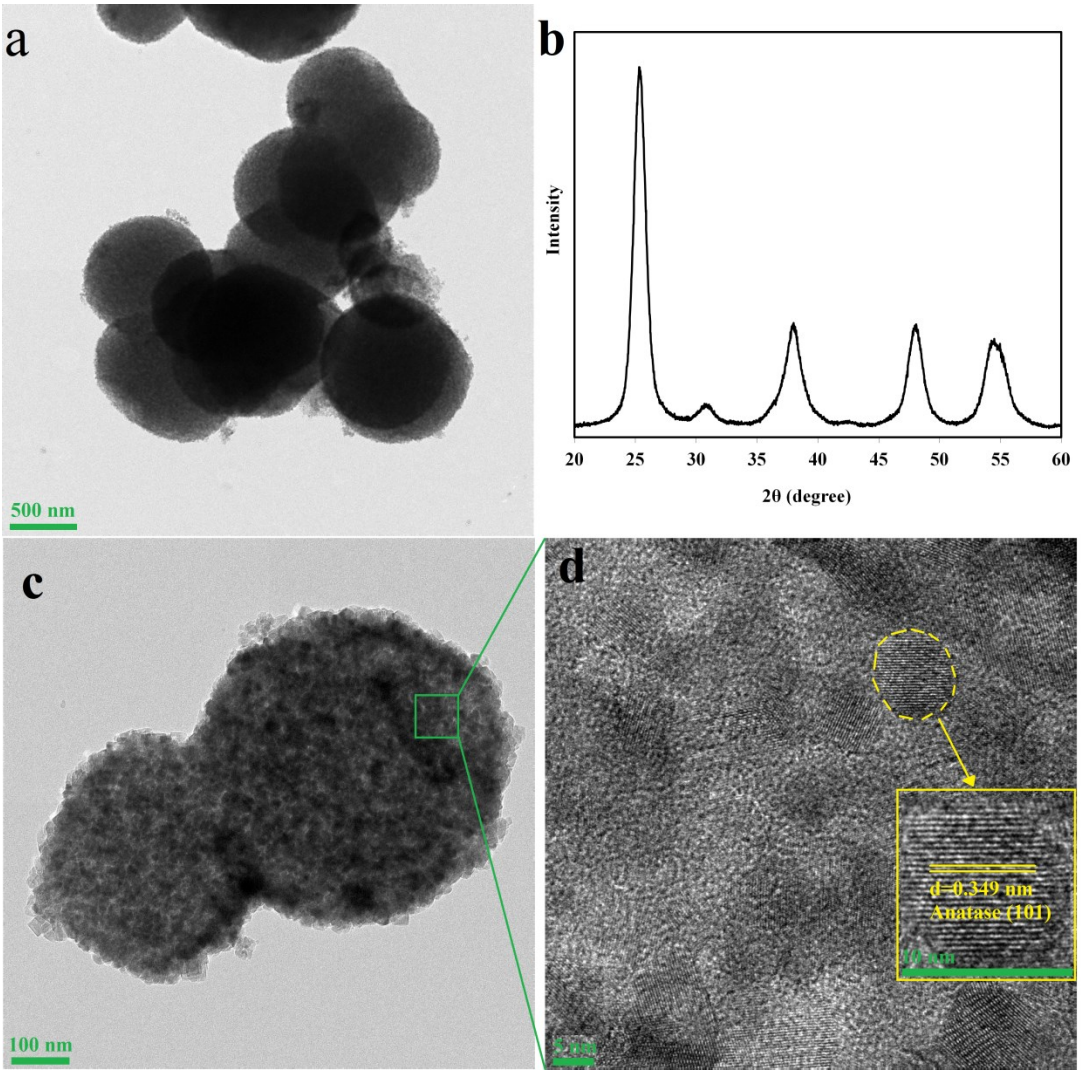

Figure 5.32 TEM image (a and c), XRD pattern (b), and HR-TEM image of TSMS

Figure 5.33 presents the XPS survey spectrum along with high-resolution spectra of O 1s, Ti 2p, and C 1s. TSMS powder contains mainly Ti, O, and C elements and very small amount of Cl. The Cl contamination might come from KCl during preparation. The high-resolution XPS spectra of O1s region demonstrate that the titania sample possesses a huge amount of surface hydroxyl group (the strong peak at 531.78 eV). Regarding the Ti 2p spectra, the peaks at 464.8 and 459.1 eV are attributed to Ti^{4+} 2p 1/2 and Ti^{4+} 2p 3/2 respectively, showing the oxidation state of the Ti element is the same as the bulk TiO_2. In addition, the small peak located at 457.9 eV is attributed to Ti^{3+} 2p 3/2. The existence of this peak reveals that there are two types of titanium species on the surface of TSMS. Ti(III) oxide has a smaller band gap with respect to TiO_2 and its energy level falls within the VB and CB of TiO_2. It has been suggested that the electron in the VB of Ti(III) oxide can be excited to the CB of TiO_2, resulting in superior e^--h^+ separation and visible light activity [230]. In the high-resolution XPS spectra of C 1s region, a relatively intense peak is found at 286.9 eV. The peak at this binding energy is usually attributed to hydroxyl carbon (C–OH), which could have been originated from the use of ethanol during synthesis or release of isopropanol during the hydrothermal reactions.

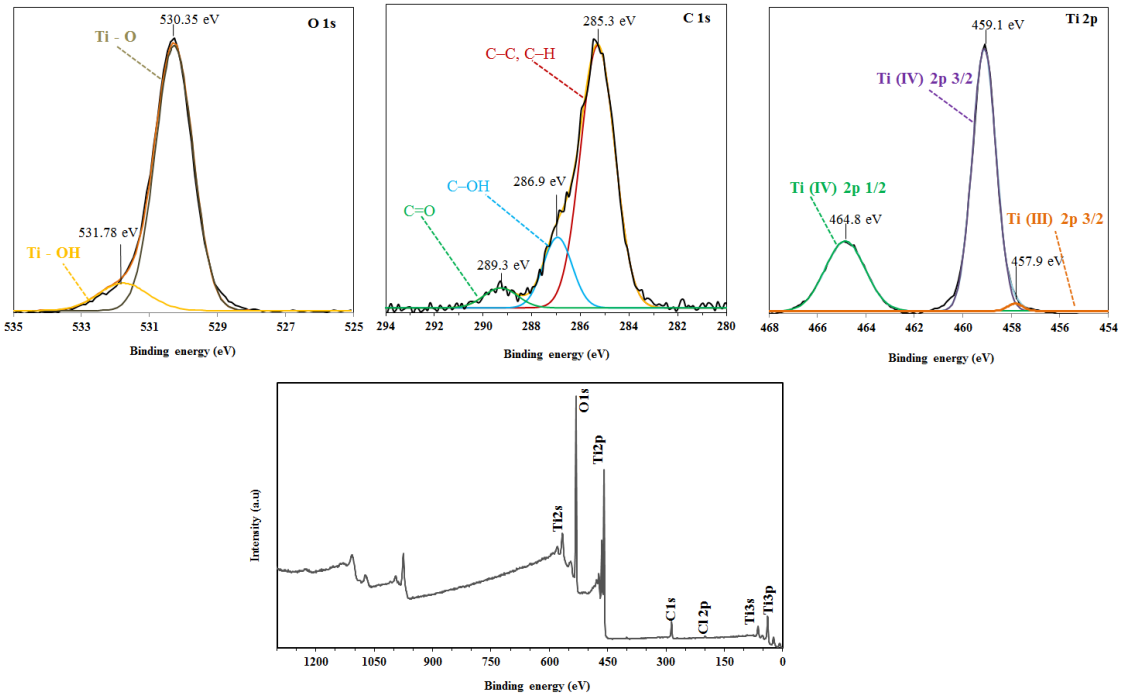

Figure 5.33 XPS survey spectra and high resolution XPS spectra of O 1s, C 1s, and Ti 2p regions of TSMS

Figure 5.34 depicts the SEM and TEM images of hierarchically mesoporous anatase microspheres. Considering Figure 5.34a, the developed titania illustrates a spherical morphology with an average diameter of about 3.5 μm. The high-magnification image of the surface of microsphere (Figure 5.34b) shows that the surface is covered with numerous tiny square nanoplates. To verify the hierarchical structure, samples were ground in a mortar to break the microspheres and inspect the interior regions. The cross-sectional SEM image of a broken microsphere is presented in the inset of Figure 5.34a, which indicates that the sphere is composed of 1-D nanorods that are aligned radially from the center. The corresponding HR-TEM image and X-ray diffraction are presented in Figure 5.34c and d, respectively. As could also be interfered from the high-resolution SEM image, the HR-TEM analysis reveals that the nanoplates size varies considerably. Based on Figure 5.34c, the anatase crystal size ranges mainly between 11 and 17 nm. The lattice fringes of titania can be easily recognized which confirms high crystallinity of TMMS. Moreover, the lattice plane of anatase (101) with interlayer spacing of ca. 0.35 nm [194] can be observed in the HR-TEM image. The XRD patterns for the mesoporous microspheres matches well with the anatase phase TiO_2 and the sharpness of diffraction peaks implies high degree of crystallinity. Using the (101) reflection peak and Scherrer equation, the average anatase crystal size was estimated to be 16.6 nm, which agree well with the crystal sizes seen in the HR-TEM image.

Under the hydrothermal conditions, the following hydrolysis reactions take place:

$$Ti(OBu)_4 + nH_2O \rightarrow (OBu)_{4-n}Ti(OH)_n + nBuOH (n = 1-4) \quad (5.1)$$

$$\equiv Ti-OH + HO-Ti \equiv \ \rightarrow \ \equiv TiOTi \equiv + H_2O \quad (5.2)$$

$$\equiv Ti-OBu + HO-Ti \equiv \ \rightarrow \ \equiv TiOTi \equiv + BuOH \quad (5.3)$$

Considering the high hydrolysis rate of TBOT precursor, the nucleation and growth can be very fast and lead to formation of large precipitates. In this context, using sulfuric acid in the hydrothermal solution can slow down the hydrolysis and titania growth rates and, consequently, offers a better control over the morphology. This was visually evidenced in the preparation stage: during the mixing process which lasted 20 min, the reaction solution was completely clear and no solid particle was seen.

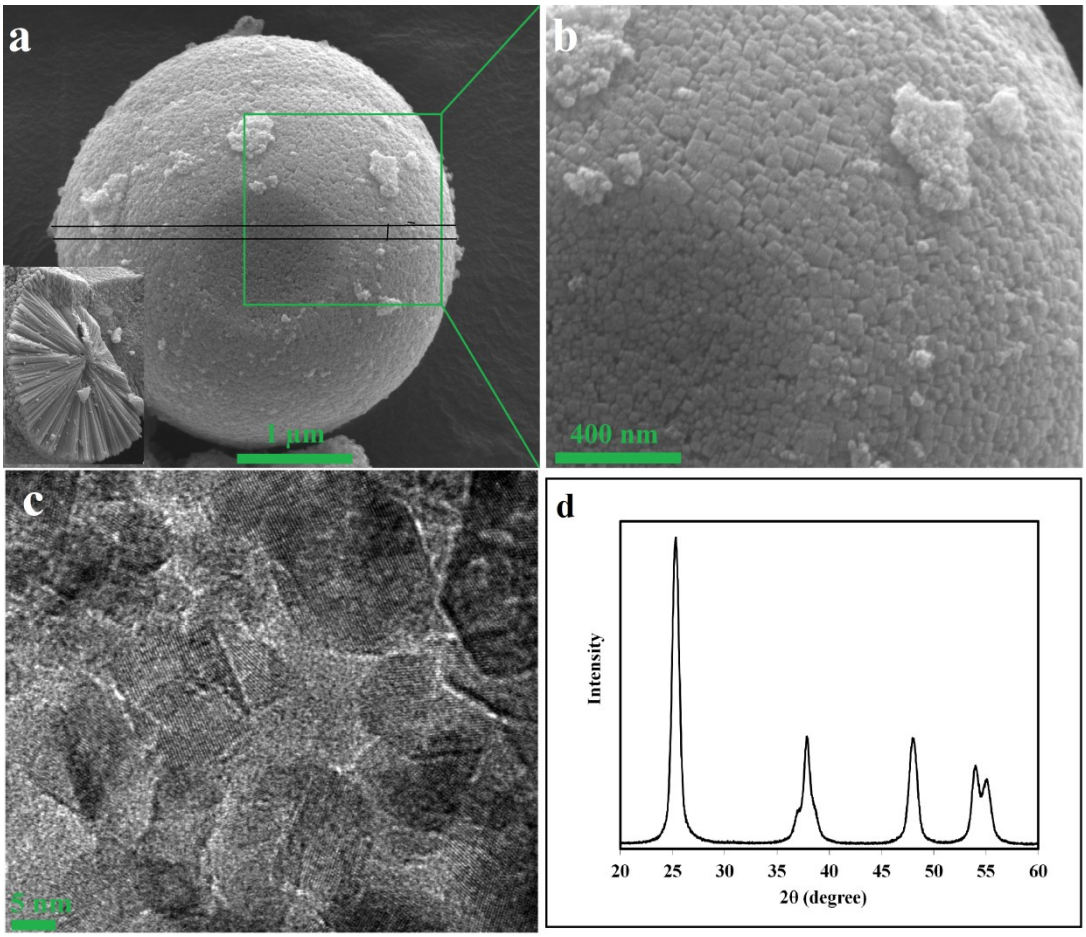

Figure 5.34 SEM images (a and b), HR-TEM image (c), and XRD pattern of TMMS

5.3.2.1.2. Titania hollow spheres

Porous hollow spheres could be successfully fabricated by a single-step hydrothermal method in the absence of any organic/inorganic templates. Field emission SEM analysis was employed to investigate the morphology of yielded hollow nanostructures (Figure 5.35). Figure 5.35a represents the low-magnification image of the sample, revealing that the aggregates are in fact composed of a large number of micro-size spheres with diameters of about 1 μm. Higher magnification images (Figure 5.35b, c and d) clearly show the porous structures and hollow interiors of microspheres. It is noteworthy that the preparation of titania samples without NH_4F resulted in solid TiO_2 aggregates, pointing to the fact that the presence of fluoride ions is essential to reach THS. The SEM image of a single hollow sphere in Figure 5.35d indicates that the solid shell of the hollow structure is actually composed of numerous aggregated

nanoparticles. This could be better appreciated in the TEM images (Figure 5.36) which show that the walls are made of nanoparticles with their sizes in the range of 9-22 nm.

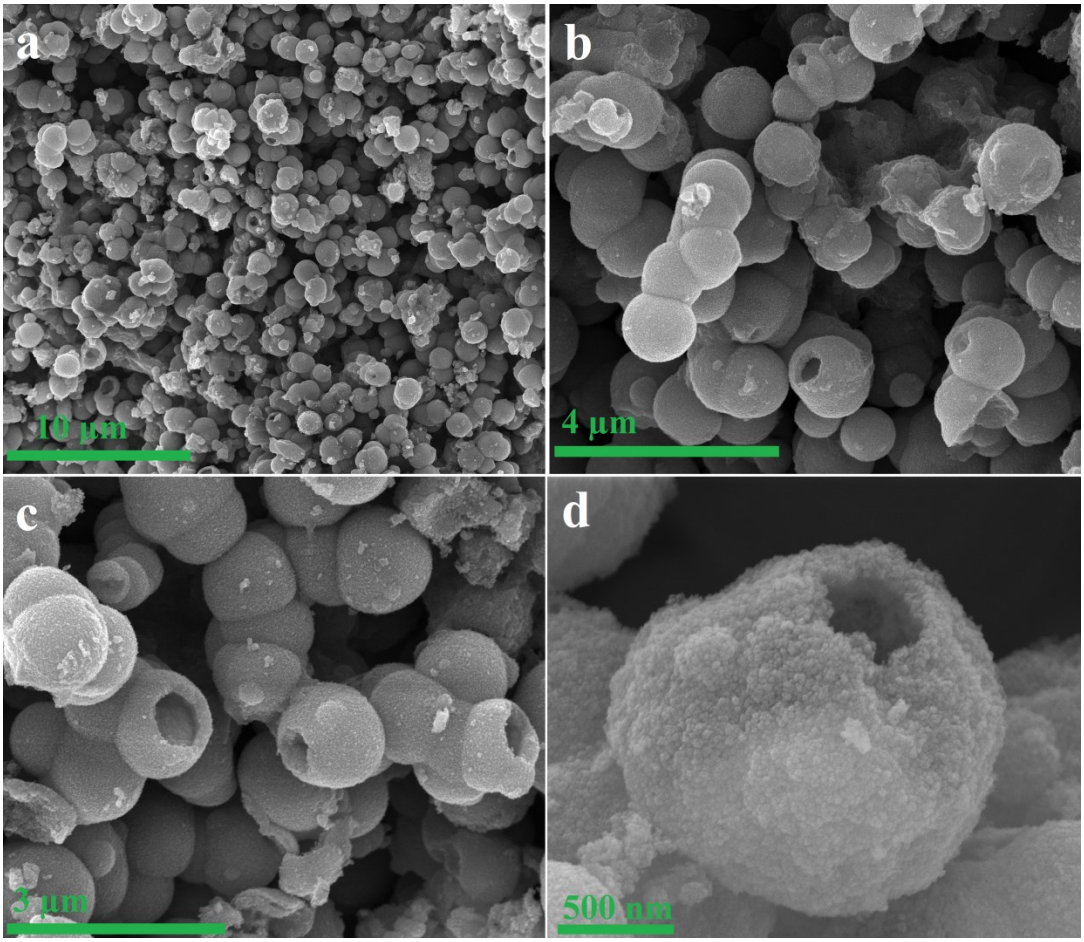

Figure 5.35 FE-SEM images of THS

The hollow structure of THS was also evidenced via TEM analysis as shown in Figure 5.36. The electron density difference between the dark exterior part of the sphere and its clearer center confirms the formation of hollow structures. Crystallization initiates at the surface of solid spheres due to the direct contact with aqueous medium and continues until the surface layer and the medium reaches equilibrium. Subsequently, due to the higher solubility and surface energy of amorphous core compared to the outer surface, the dissolution (via F^- ions) and hollowing processes preferentially act on the center of sphere rather than the outer regions. In this regard, it has been previously suggested that the fluoride ions help the dissolution of the particles interiors and also facilitate the mass transfer from the core to the surface [50].

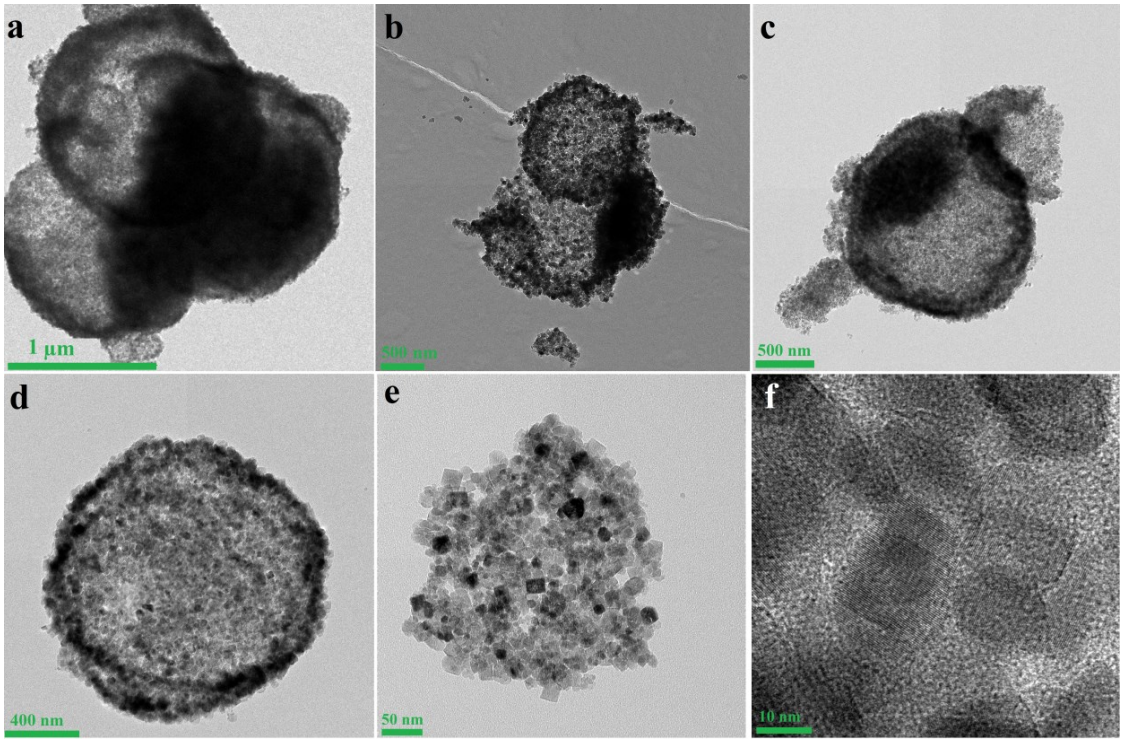

Figure 5.36 TEM (a, b, c, and d) and HR-TEM (e and f) images of THS

Hydrolysis of NH_4F during the hydrothermal treatment brings about the release of hydrofluoric acid in the reaction environment. Consequently, a localized high concentration HF zone in the vicinity of TiO_2 particles might be expected. Under the hydrothermal conditions, the hollow spheres are gradually produced through chemical etching/dissolution of the amorphous titania particles by HF followed by recrystallization of the surface of particles (dissolution-redeposition process). Based on HR-TEM images (Figure 5.36), it could be deduced that the developed THS have unexpectedly high anatase crystallinity considering the relatively low temperature and short reaction time. The high crystalline quality of yielded titania originates mostly from in-situ dissolution–recrystallization in the presence of fluoride ions (reactions (4) and (5)).

$$4H^+ + TiO_2 + 6F^- \rightarrow TiF_6^{2-} + 2H_2O \ (dissolution) \qquad (5.4)$$

$$TiF_6^{2-} + 2H_2O \rightarrow 4H^+ + TiO_2 + 6F^- \ (recrystalization) \qquad (5.5)$$

Additionally, the higher electronegativity of fluoride anion with respect to that of SO_4^{2-} allows effective nucleophilic substitution, which can diminish the reactivity of titanium precursor. This process can inhibit the fast formation of small anatase nuclei and enable further crystal growth

due to the presence of a large number of unreacted titanium complexes in the reaction medium. As can be noted in both SEM and TEM images, there are many semi-hollow or broken microspheres in the sample. This could result from the deficit of HF in some regions (due to the slow hydrolysis of NH_4F) during the hydrothermal synthesis, which does not provide perfect conditions for hollowing process and lead to appearance of semi-hollow spheres. The XPS survey spectra of THS (Figure 5.37) show that the hydrothermally-prepared sample contains Ti, O, C, and F elements. A small peak at 684 eV was found in the survey spectra which can be assigned to F 1s coming from NH_4F during preparation. This peak originates from surface fluoride (≡Ti-F) formed by ligand exchange between fluorine and surface hydroxyl groups (i.e. physically adsorbed F^-). As can be vividly seen in the high-resolution spectra of F 1s, no signal for F^- in the lattice of TiO_2 (binding energy of ca. 688.5 eV) exits. In acidic hydrothermal environment, lattice substitution of F for O is inhibited by relatively fast TiO_2 crystallization and growth via in situ dissolution-recrystallization.

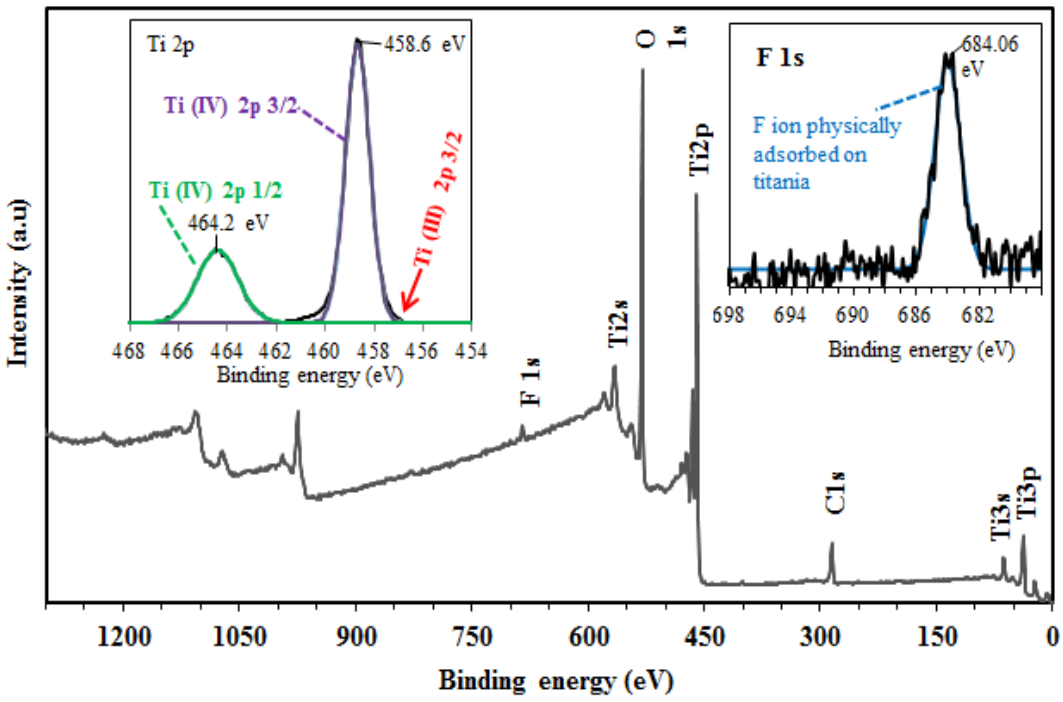

Figure 5.37 XPS survey spectra and high resolution XPS spectra of F 1s and Ti 2p regions of THS

We also studied the Ti chemical states by XPS to gain some insights about the existence of defects (e.g. oxygen vacancy) on TiO_2 surface. The molar ratio between Ti^{4+} and Ti^{3+} species is considered as a measure of oxygen vacancy concentration [231]. The negligible area of Ti(III) peak (Figure 5.37) signifies that there are a small number of oxygen vacancies on the surface of hollow spheres.

5.3.2.1.3. Titania nanosheets

Owing to their fundamental importance, synthesis of well-faceted anatase TiO_2 crystals with high percentage of [001] exposed facet has gained enormous interest in the field of photocatalysis. In the present work, we could achieve titania nanosheets with high crystalinity and aspect ratio via a solvothermal route at relatively low hydrothermal temperature. One of the main advantages of the developed solvothermal route, compared to conventional hydrolytic route, is that in this procedure the direct use of highly toxic HF can be avoided. Instead of hydrofluoric acid, TiF_4 is applied as the source of structure directing agent (i.e. fluorine) along with 2-propanol as the protective capping agent. Figure 5.38 and Figure 5.39 show the TEM and HR-TEM images of solvothermally-prepared TiO_2 nanosheets, respectively. Clearly, the sample consists of well-defined sheet-shaped structures with a rectangular outline with lateral dimensions of approximately 50-70 nm. Based on the high-resolution TEM images (Figure 5.39) and Figure 5.38c and d, the thickness of the sheet is about 4.5-6.5 nm. The lattice spacing parallel to the top and bottom facets (highlighted in Figure 5.39a) is 0.233 nm, corresponding to the [001] planes of anatase titania. The crystallographic planes (determined in the TEM images) for the face-on and edge-on orientations confirm that the thickness of the nanosheets is oriented along the [001] direction of the anatase unit cell. Moreover, Figure 5.39b shows an average interfacial angle of 67.5 °, which is consistent with the theoretical angle between the [001] and [101] lattice planes of anatase (68.3 ± 0.3°). On the basis of the hypothesized geometry (Figure 5.39b inset) and the average dimensions (thickness and lateral lengths) of nanosheets observed in TEM analysis, the percentage of [001] facets of the developed TNS is estimated to be around 83%. It is to be noted that not all nanoparticles have the truncated octahedra shape with [001] and [101] facets as the face and edge planes, respectively. Nonetheless, TEM analysis could reliably illustrate that the majority of platelets have high [001] facet exposed.

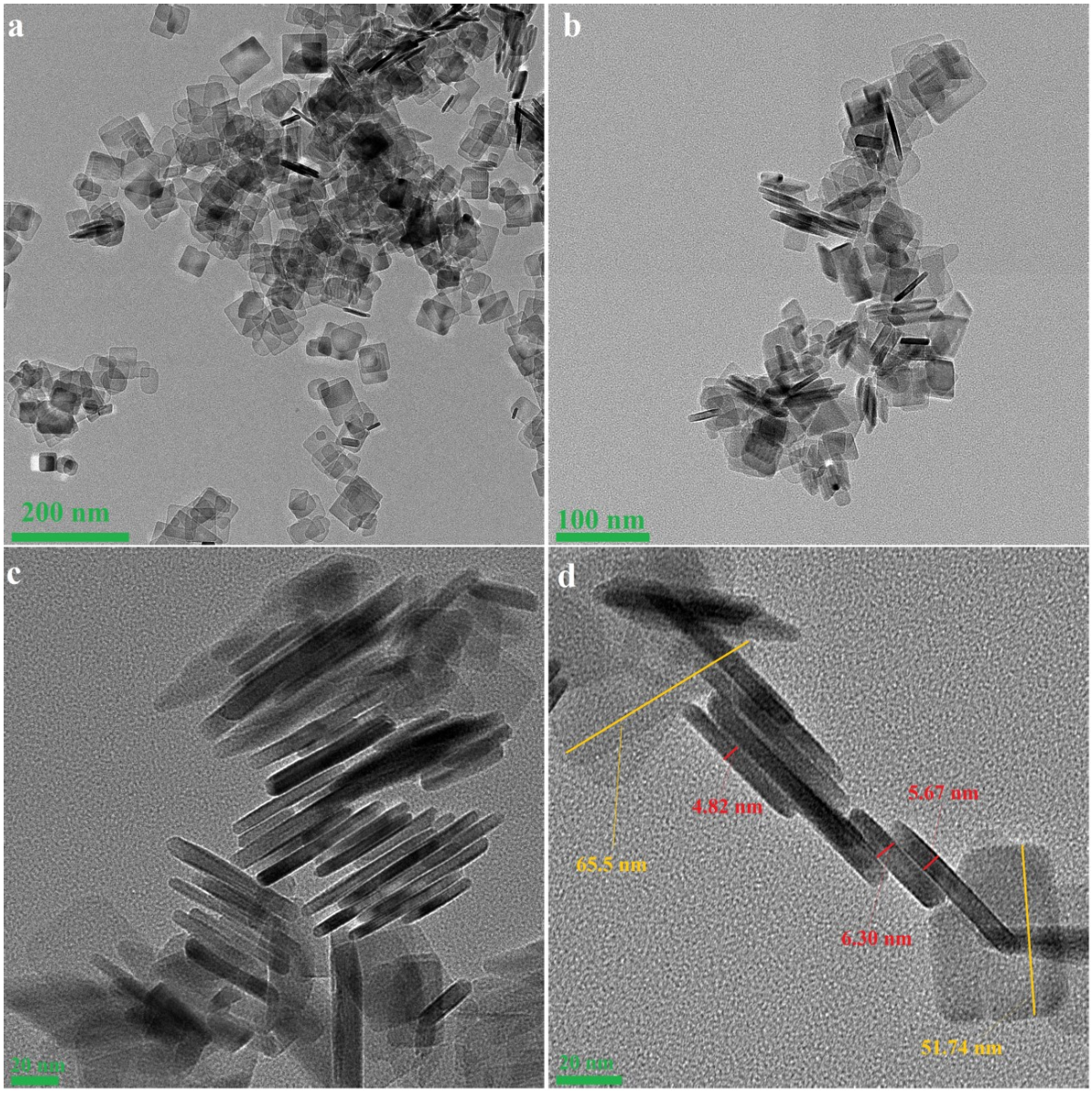

Figure 5.38 TEM images of TNS. (a and b) face-on and (c and d) edge-on orientations

Regarding the formation of nanosheet morphology, theoretical calculation indicated that fluoride ion can act as a structural directing agent via preferential adsorption on [001] anatase facets. Upon fluoride adsorption, the surface energy of the [001] facet becomes lower than that of [101]; therefore, the crystal growth proceeds along the [101] facet. On the other hand, in the present reaction route, 2-propanol can act as protecting agent to control the isotropic growth of anatase crystals as well. Under acidic conditions, 2-propanol dissociates and forms an alkoxy group ($((CH_3)_2CHO^-$) bound to coordinatively unsaturated Ti^{4+} cations on different facets [232]. Since

the density of 5-fold Ti on [001] is higher than that of [101], more alcohol can adhere to the [001] facet, inhibiting the crystal growth along the [001] direction. Besides the above-mentioned role of 2-propanol in TNS synthesis, the results of DFT calculations [232] suggest that the coadsorption of 2-propanol can strengthen the adsorption of fluorine to the [001] facet.

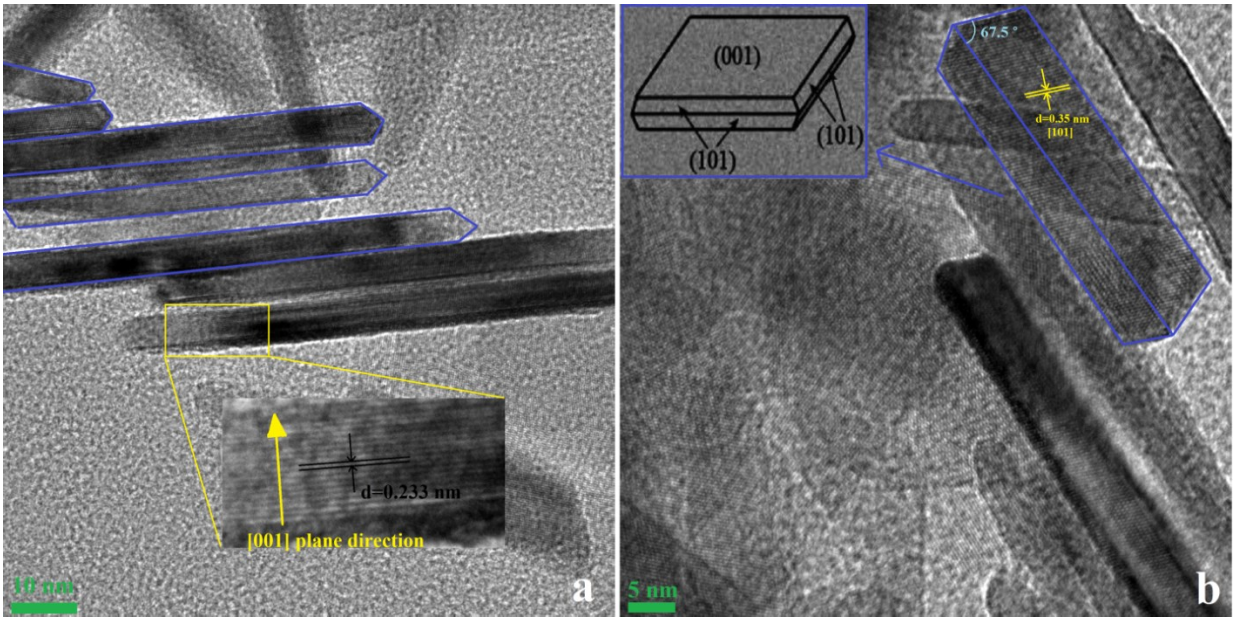

Figure 5.39 HR-TEM images of TNS. Inset of (b): assumed geometry of truncated octahedra

Figure 5.40 depicts the XPS survey spectrum of TNS. Sharp photoelectron peaks are seen at binding energies of 460 (Ti 2p), 531 (O 1s), 685 (F 1s), and 285 eV (C 1s). The F 1s peak only consists of one component with binding energy of 684.06 eV (similar to hollow spheres) which is related to fluorinated TiO_2 surface (≡Ti-F). The XPS analysis clearly points to the fact that the atomic incorporation of F atoms into the lattice did not occur under the employed hydrothermal conditions. Interestingly, the O 1s peak associated with the surface hydroxyl groups is very small for the prepared nanosheets compared to that in other morphologies. One contributing factor is certainly the ligand exchange between the surface OH groups and fluoride anions during the hydrothermal treatment. Regarding the C 1s peak, a quite intense peak (compared to other morphologies) appears at 286.7 eV, which may result from surface oxidation of the aliphatic chains and adsorbed 2-propanol. Moreover, the small peak at 288.07 eV can be attributed to the presence of carboxylate impurities.

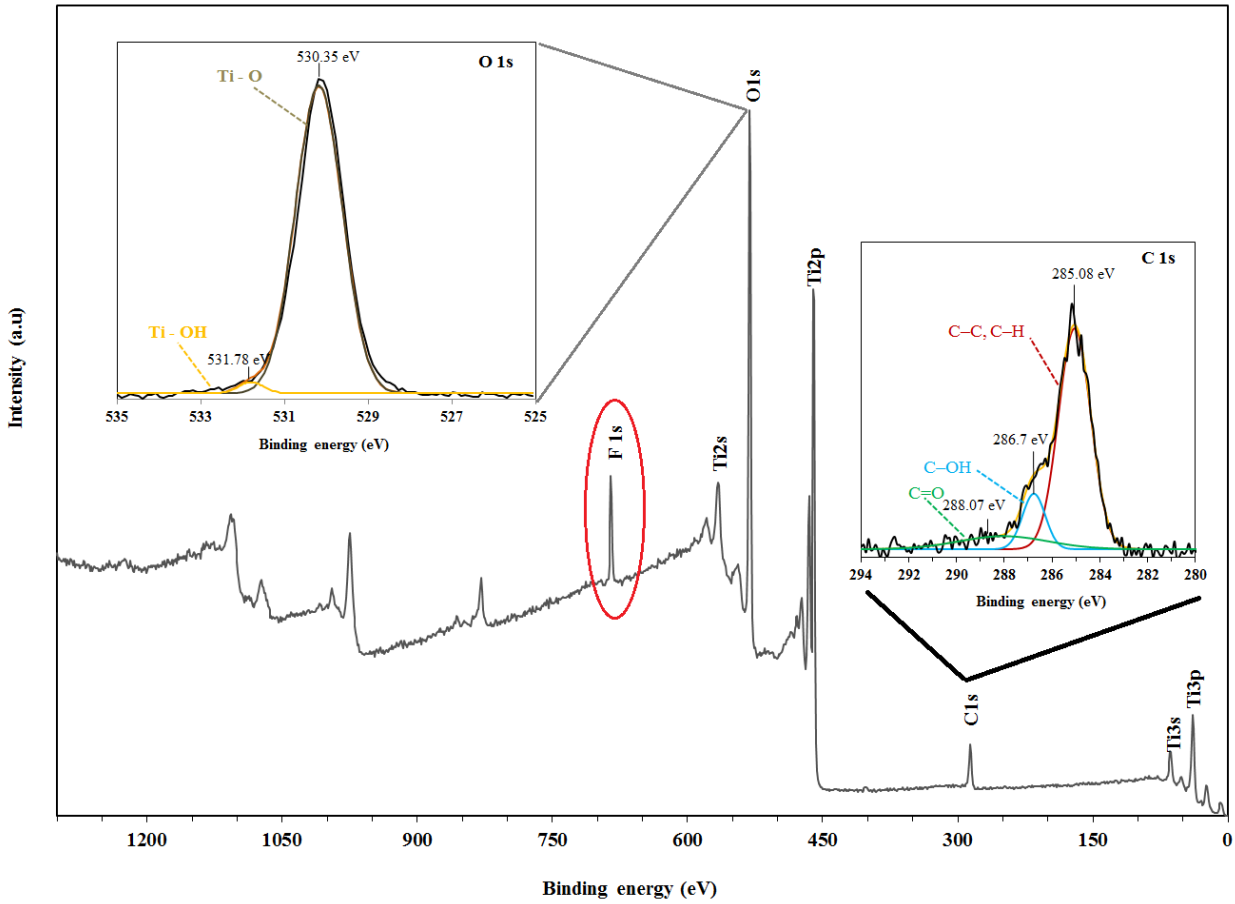

Figure 5.40 XPS survey spectra and high resolution XPS spectra of C 1s and O 1s regions of TNS

5.3.2.1.4. Titania nanotubes

As one of the pioneers, Kasuga et al. [233] successfully fabricated Ti-based nanotubular structures via a facile hydrothermal route through the transformation of TiO_2 nanoparticles into nanotubes. Since then, many groups developed TiO_2 nanotubes by hydrothermal or thermal post treatment techniques [234-236]. Most studies synthesized titania nanotubes by hydrothermal treatment of P25 or anatase/rutile powders in concentrated solution of NaOH or KOH [83, 237, 238]. However, as-synthesized nanotubes usually show very little photocatalytic activity due to the fact that the crystalline structure mainly consists of various hydrogen or sodium titanates (e.g. $Na_2Ti_3O_7$, $H_2Ti_3O_7$, $H_2Ti_6O_{13}$, $H_2Ti_8O_{17}$, etc.) instead of the highly active anatase polymorph. In the present study, a two-step preparation method was used to fabricate anatase TNT with high degree of crystallinity: (i) transformation of P25 powder into titanate nanotubes via hydrothermal treatment in highly alkaline solution of NaOH, and (ii) transformation of titanate nanotubes to anatase nanotubes via calcination (reactions (6) and (7)).

$$H_2Ti_2O_4(OH)_2 \rightarrow H_2O + H_2Ti_2O_5 \quad (5.6)$$

$$H_2Ti_2O_5 \rightarrow H_2O + 2TiO_2 \quad (5.7)$$

The main experimental challenge was to retain the nanotubular structure during calcination since at high temperatures TNT tends to agglomerate and evolve into anatase nanoparticles. Accordingly, the hydrothermal preparation conditions (e.g. molarity of NaOH, hydrothermal temperature/time, and acid washing) and calcination temperature must be adjusted carefully to obtain anatase TNT. Figure 5.41 represents the TEM image of TiO_2 after hydrothermal treatment at 160 °C for 24 h followed by calcination at 450 °C for 2 h. The tube sizes are difficult to be estimated with acceptable accuracy from TEM images, however, the inner diameter mainly ranges between 6-10 nm. Considering Figure 5.41c, nanotubes have a multiwall morphology and the distance between successive layers is approximately 0.726 nm. As can be seen from the XRD patterns in Figure 5.41d, all the diffraction peaks of TNT can be indexed to anatase phase. This observation is in good agreement with previous works that reported only anatase phase was formed after calcination of H-titanate nanotubes at high temperatures [239]. There are several possible formation mechanisms for titania nanotubes [240-242]. It has been proposed that the mechanism of transformation of titania nanoparticles precursor into tubular structure entails a scrolling/wrapping of single-layer titanate nanosheets [241].

The absence of sodium contamination (judged from the XPS results) demonstrates the good ion-exchange ability of the layered titanates, which facilitated the removal of Na during the acid washing step. Trace amount of Cl on the surface of TNT is found in the survey spectra which most probably came from the acid washing step. Judging from the high-resolution spectrum of O 1s region, the final calcination at high temperature removes a significant portion of the surface OH groups. Additionally, post-thermal treatment substantially improved the degree of crystalinity (sharpness of peaks in Figure 5.41d) and only a small number of surface defects (e.g. oxygen vacancy) exist in the yielded TNT (low intensity of Ti(III) 2p 3/2 peak in Figure 5.42).

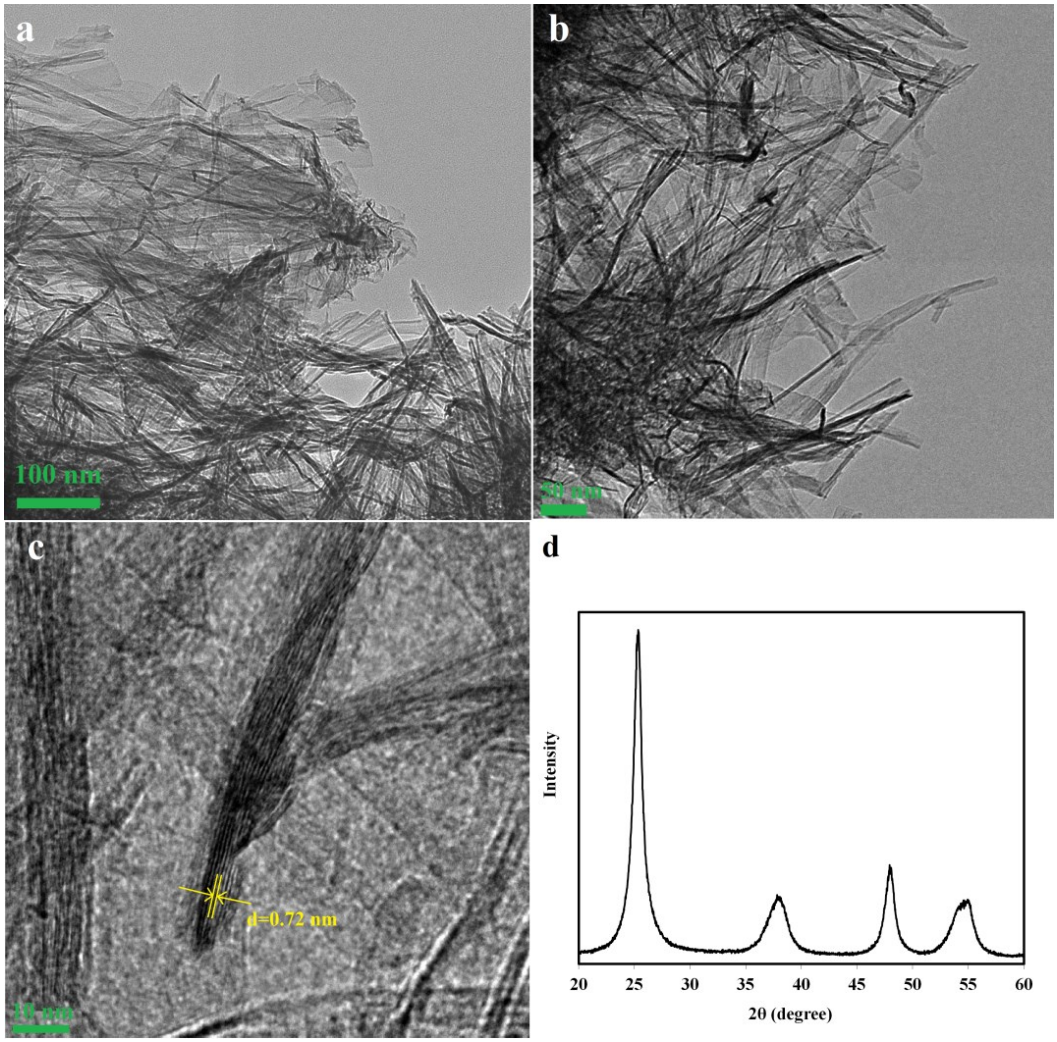

Figure 5.41 TEM images (a and b), HR-TEM image (c), and XRD pattern of TNT

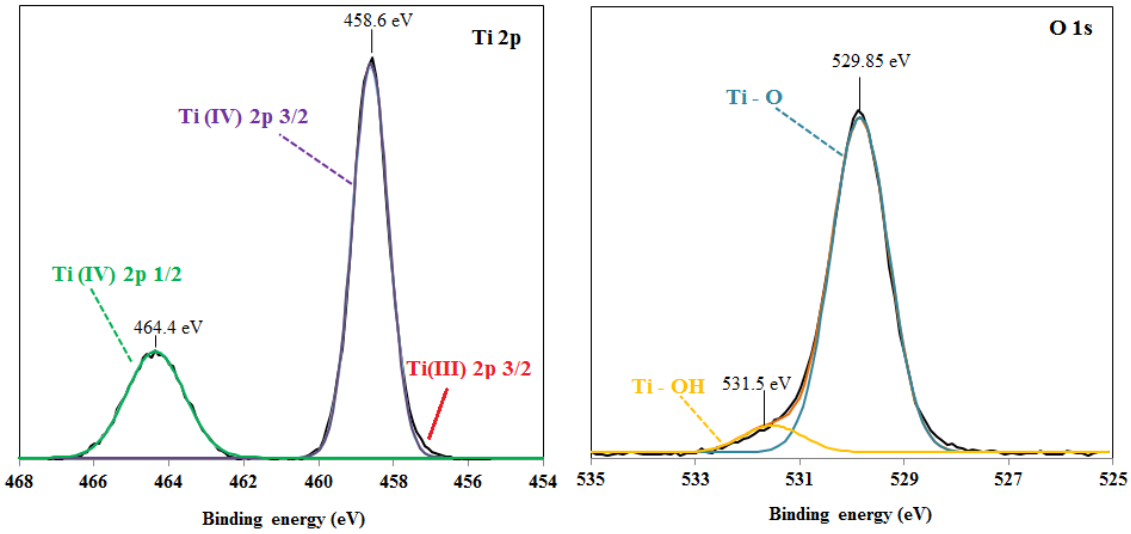

Figure 5.42 XPS spectra of O 1s and Ti 2p regions of TNT

5.3.2.1.5. Titania 3-D sea-urchin like

Figure 5.43 presents the FE-SEM images and XRD pattern of solvothermally prepared urchin-like structure. In the present work, by sea urchin-like morphology we mean three dimensional micrometer-sized titania particles, which are basically composed of numerous one dimensional rod-like (or spindle-like) structures along the radial direction from the core to the surface. It needs to be highlighted that similar to TNT, the as-prepared TSU showed very low crystallinity, which necessitated a post-thermal treatment to reach anatase phase and promote sufficient crystal growth. Taking into account the properties of the solvent (i.e. ethylene glycol), having a poor crystallinity for the as-prepared TSU is understandable. The large dielectric constant of EG (38.7 at 20 °C) leads to high solubility of TiO_2 nuclei because of the increased solvation energy [243]. This, together with the high boiling point of EG (197.8 °C) reduces the supersaturation degree, slows down the rate of crystallization, and ultimately deteriorates the crystalline quality. Despite its beneficial impact on crystallinity, it was noticed that the calcination process adversely affects the urchin-like morphology and causes a slight sintering (Figure 5.43a) and inevitable deformation. Regarding the formation mechanism of TSU, it is believed that the initial reaction between TBOT and NaOH aqueous solution results in the formation of primary TiO_2 nuclei/crystals due to fast TBOT hydrolysis (as was also experimentally witnessed during the preparation). Upon subsequent addition of EG, these primary particles act as support surfaces for agglomeration and growth of spindle-like structures. In this context, Jiang et al. [244] reported preparation of metal oxide nanowires via an EG-mediated synthesis route. As a result, it is hypothesized that EG is responsible for further nucleation and anisotropic growth of rods. Based on the XPS survey spectra, no impurity (e.g. Na or Cl) was introduced into (or remained on) the surface of TSU during the solvothermal treatment and acid washing steps. Figure 5.44 shows high-resolution XPS spectra of O1s region after Gaussian curve fitting, revealing presence of three different oxygen species on TSU surface. Strong peaks at 530.5 and 531.8 eV are respectively ascribed to lattice oxygen and surface OH. Interestingly, unlike the impact of calcination on TNT, TSU exhibits a considerable amount of surface OH in spite of being calcined at 550 °C, suggesting that these OH groups are strongly bonded to the surface. Additionally, a third peak appeared at 533.44 eV, which cannot be attributed to any compound containing oxygen and its source is unknown to us at the moment.

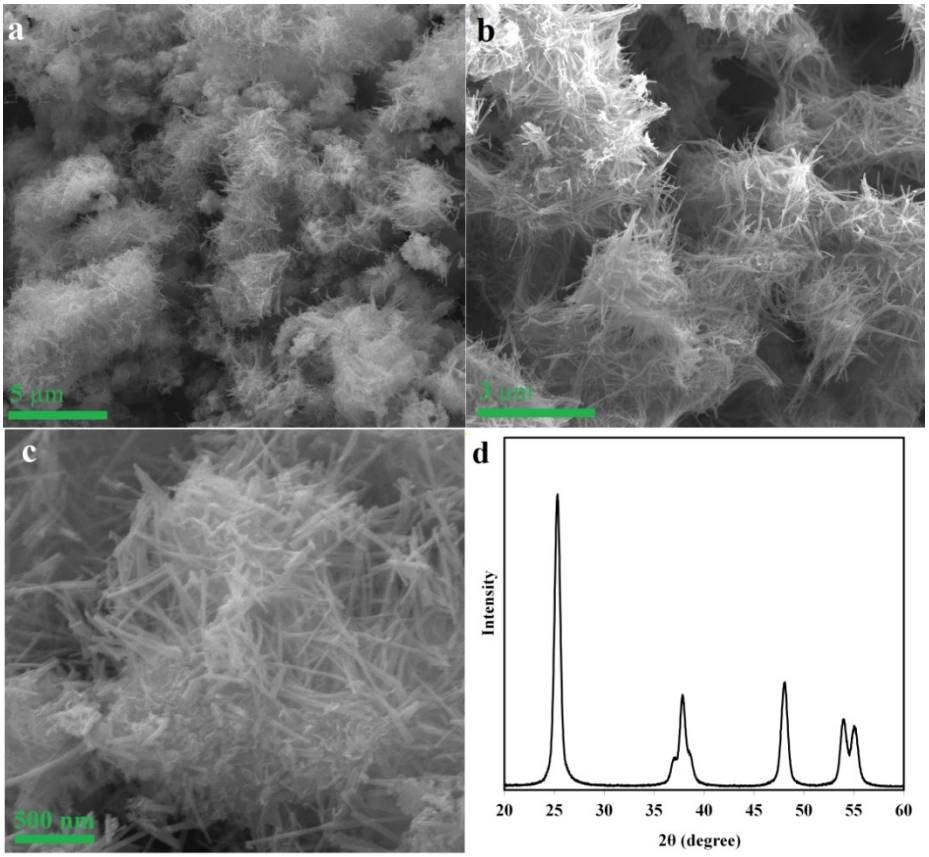

Figure 5.43 FE-SEM images (a, b, and c) and XRD pattern (d) of TSU

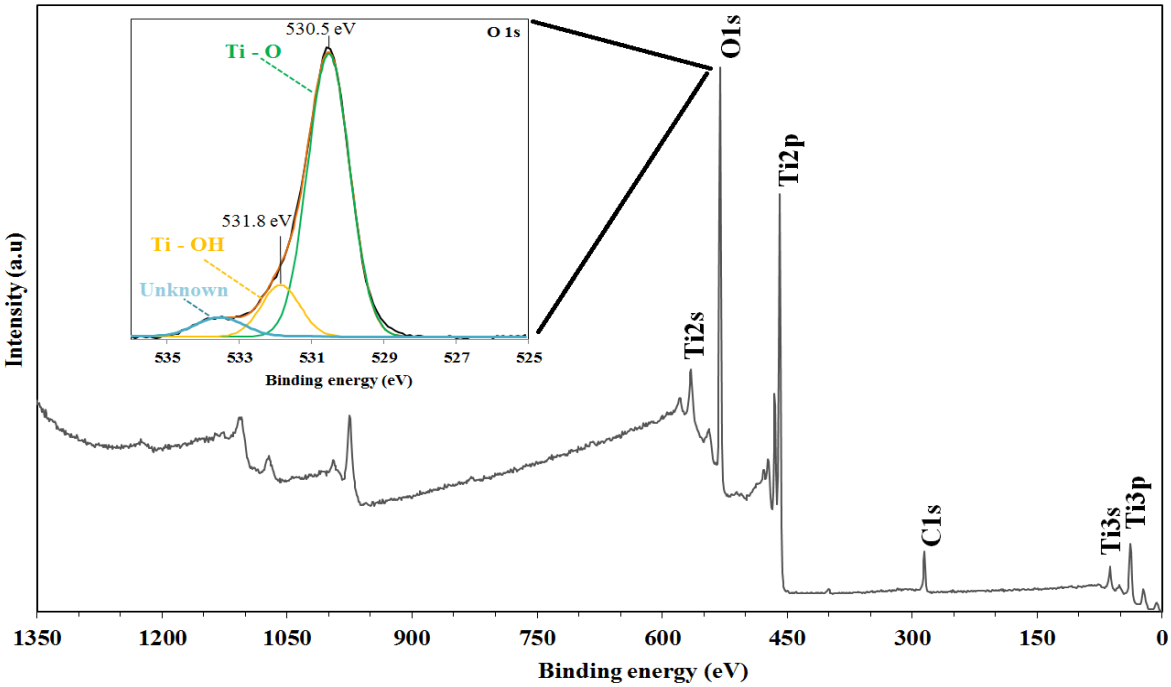

Figure 5.44 XPS survey spectra and high resolution XPS spectra of O 1s region of TSU

5.3.2.2. Photocatalytic activity

To demonstrate the intricate structure-function relationship, the photocatalytic activity of titania photocatalysts with various morphologies was examined by degradation of MEK. For comparison, the photocatalytic activity of P25 was also measured under identical conditions. The key characteristics of photocatalysts and P25 are provided in Table 5.10. Except P25, anatase is the main phase in all photocatalysts. As can be noted from Table 5.10, the relative crystallinity and surface area vary in fairly narrow spectra: 1-1.23 and 77.6-90 m^2/g, respectively. Figure 5.45 displays the comparison of photocatalytic activity (and by-products generation) of developed titania samples. Interestingly, despite the fact that crystal phase, degree of crystallinity, and surface area do not differ considerably, these morphologies exhibit distinct photocatalytic activities, which we believe stem from the intrinsic merits offered by each architecture.

Table 5.10 Crystalline, textural, and surface properties of titania photocatalysts

Photocatalyst	Crystal phase [a]	crystal size (nm)	Relative crystallinity [b]	Surface area (m^2/g)	OH/O_{tot} [c]	OH_T density $\times 10^{-19}$ (OH groups/m^2) [d]	Ti^{4+}/Ti^{3+} [e]
TSMS	A, B	10.40	1.06	82.50	0.120	3.02	55.5
TMMS	A	16.60	1.13	77.60	0.080	2.21	70.4
THS	A	18.00	1.17	88.20	0.078	1.88	ND [f]
TNS	A	17.40	1.12	80.30	0.020	1.64	ND
TNT	A	13.50	1.00	90.00	0.080	3.21	ND
TSU	A	18.50	1.23	79.10	0.150	3.36	82.3
THP	A, B	12.70	1.10	85.50	0.130	3.31	60.7
P25	A, R	25.30	2.86	53.23	0.14	1.02	ND

[a] A: anatase, B: brookite, R: rutile; [b] Relative anatase crystalinity is calculated by dividing the intensity of the anatase (101) diffraction peak to that of TNT; [c] Calculated based on high-resolution XPS spectra of O 1s region; [d] Calculated based on TGA analysis; [e] Calculated based on high-resolution XPS spectra of Ti 2p region; [f] Negligible Ti^{3+} peak

0-D TiO_2 photocatalysts are the most utilized architectures in photocatalytic air purification. Considering the fact that photocatalytic reactions happen on the surface of catalyst, it is ideal to maximize the exposure of photocatalyst to light and air stream in order to improve the quantum efficiency and mass transfer rate. In this regard, TiO_2 microspheres has been the focus of numerous researches owing to their small primary particle size, high surface-to-volume ratio,

large surface area, and high pore volume. In our experiments, MEK removal efficiency over TSMS, 31.8%, is the lowest among all prepared samples, and even lower than P25. Apparently, the yielded solid microspheres do not provide any structural advantage over nanoparticles.

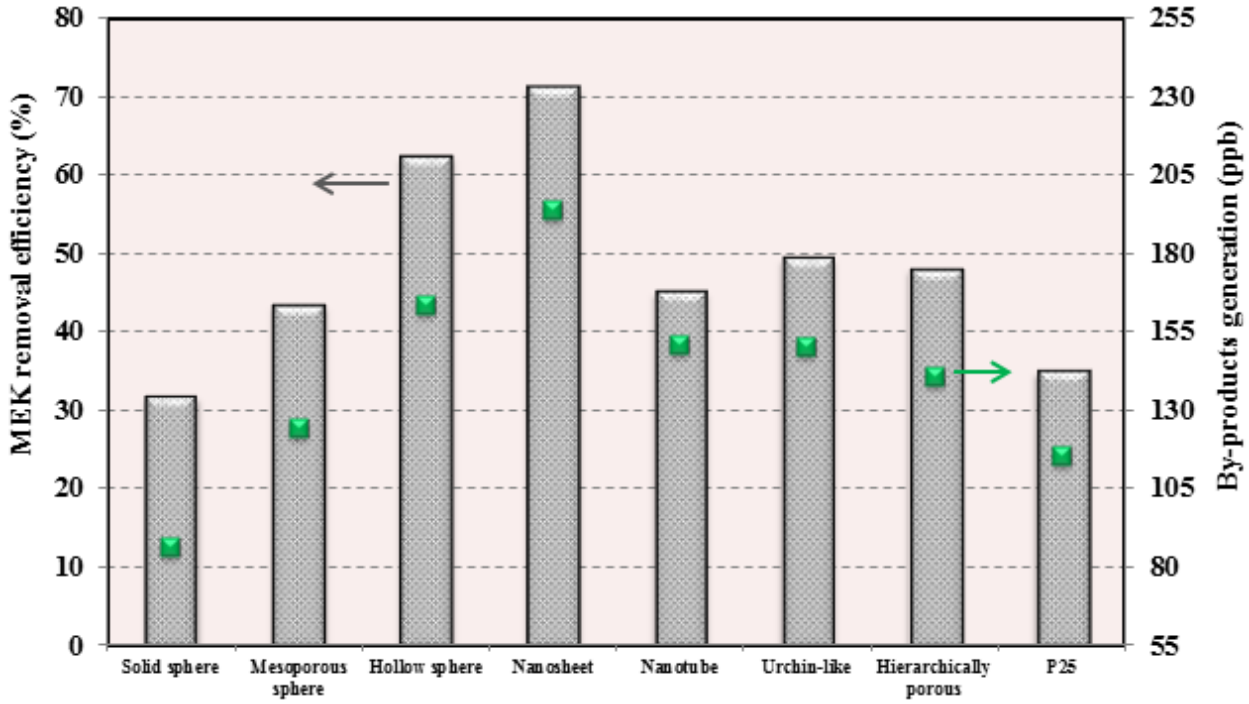

Figure 5.45 MEK removal efficiency and total by-product generation over different morphologies

One possible justification for TSMS low activity might be the low crystallinity and existence of surface defects (Table 5.10). As highlighted before, a small Ti^{4+}/Ti^{3+} ratio signifies presence of oxygen vacancies in the crystalline framework of TiO_2. Oxygen vacancies are ideal recombination sites for photogenerated charge carries and can greatly diminish the population of hydroxyl radicals. With respect to TSMS, mesoporous microspheres show higher photocatalytic activity towards MEK. This may be mainly attributed to the fact that for TMMS, the hierarchical mesoporous structure composed of highly crystalline TiO_2 nanorods can facilitate the adsorption and desorption of reactants and products, respectively. Furthermore, the degree of crystallinity and population of surface defects provide TMMS marginal advantage over TSMS. Nonetheless, both these structures may suffer from the difficulty in electron transfer between neighboring spheres, considering the small contact area among the micrometer spheres. Titania hollow spheres offer the second highest MEK removal efficiency (62.5%) among investigated morphologies and comparatively small amount of gaseous by-products (164 ppb). A number of factors contribute to the superior photocatalytic performance of THS which are elaborated

below. It is believed that the hollow structure allows multireflections of UV light inside hollow spheres (Figure 5.46), endowing THS with increased light harvesting ability, a larger number of e^--h^+ pairs, and consequently higher photoactivity. The porous shell and hollow structure also provide efficient transport pathways for MEK molecules (and by-products) to the interior regions of THS and subsequent entrapment of these organics, which boosts the probability of collision with reactive species. As witnessed in XPS spectra (Figure 5.37), there is a small amount of physically adsorbed fluorine on the surface of THS. It has been suggested that surface ≡Ti-F groups can trap electrons owed to high electronegativity of fluorine and, as a result, suppress the recombination [245]. Lastly, surface-fluorinated catalysts are able to generate free OH radicals (not surface-bound •OH) [246, 247] (reactions (8) and (9)), which has larger redox potential compared to surface-adsorbed •OH [246, 248]. These radicals can presumably move within the water film formed on hydrophilic titanium dioxide and react with MEK molecules in the liquid phase.

$$\equiv Ti - OH + h_{vb}^{+} \rightarrow \equiv Ti - OH \cdot \quad (5.8)$$

$$\equiv Ti - F + OH^{-} + h_{vb}^{+} \rightarrow \equiv Ti - F + \cdot OH_{free} + H^{+} \quad (5.9)$$

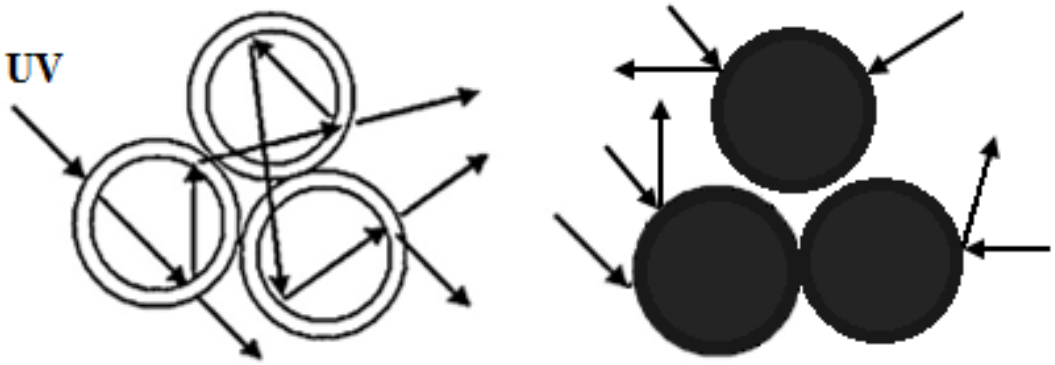

Figure 5.46 Schematic illustration of multiple reflections within hollow

According to our research, titanium dioxide nanosheets by far are superior to all other morphologies in degradation of pollutants in air. TNS exhibit an excellent MEK removal efficiency, 71.3%, which is roughly two times higher than the removal obtained by P25. More surprisingly, considering Table 5.10, THS do not possess the highest crystallinity or surface area and even have the lowest OH surface density. In the following part, we elucidate several possible

reasons for such unique activity observed for THS. Nanosheets are nano-sized flake-shape materials with a flat surface, small thickness and cross-sectional dimensions up to several tens of micrometers. It is widely accepted that for anatase TiO_2, [001] facets are more reactive than the thermodynamically more stable [101] facets [207, 232, 249]. The surface energy of different facets of anatase TiO_2 follows the sequence of [110] 1.09 > [001] 0.9 > [100] 0.53 > [101] 0.44 $J.m^{-2}$ [250]. The synergistic effect due to the copresence of [001] and [101] facets and the transport directions of photogenerated charge carriers are depicted in Figure 5.47. Photogenerated holes and electrons preferentially migrate toward [001] and [101] facets, respectively [251, 252]. Consequently, $OH^{\bullet}$ or oxidation sites are mainly located on [001] facets while $O_2^{\bullet-}$ or reduction sites are generated on [101] facets. Keeping this in mind, one can conclude that the copresence of both facets in TiO_2 nanocrystals can greatly enhance the photocatalytic activity. Another less investigated factor for superior activity of THS can be the higher density of uncoordinated titanium atoms on [001] facet [225, 252]. It has been proposed that unsaturated five-coordinated Ti atoms sites take part in the formation of terminal Ti-OH species, which are well-known active adsorption sites for VOC molecules [253]. Finally, similar to THS, surface fluorination can enhance the charge carriers separation and boost the number of reactive species (e.g. $OH^{\bullet}$ and $O_2^{\bullet-}$).

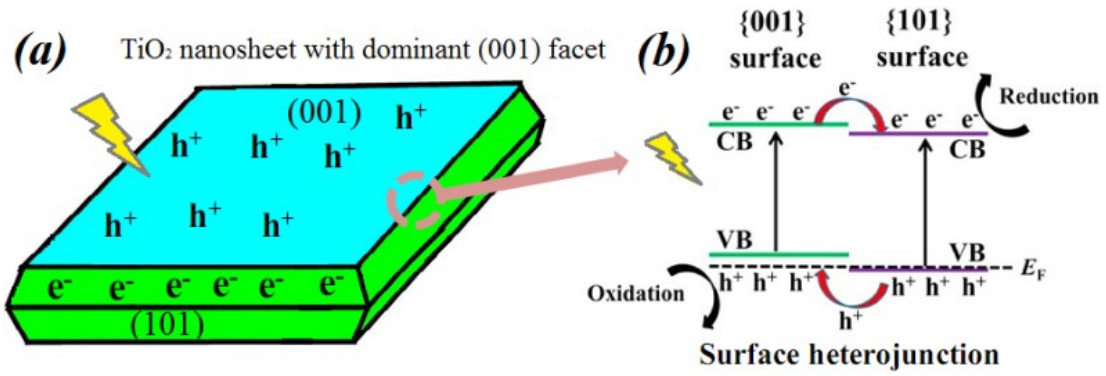

Figure 5.47 (a) Schematic illustration of the spatial separation of h^+ and e^- on TiO_2 nanosheets and (b) surface heterojunction between [001] and [101] facets

Different from our expectation, fabricated 1-D titania nanotubes did not show very high photocatalytic activity (MEK removal efficiency=45.2%) in spite of their large surface area and high OH_T density compared to most of the samples. One source which could have impaired the activity of TNT might be the inadequate crystalline quality. During the synthesis, P25 crystals go through several stages of intercalation and deintercalation of guest molecules into and from the

crystal lattice. This would swell and distort the original crystal lattice and adversely affect the creation of electrons and holes. In addition, even though we did not detect titanate in the structure of TNT, small titanate contamination could deteriorate the photocatalytic activity. In addition, as shown in Figure 5.41, because of the calcination step, the ideal morphology of nanotubes is partly destructed, which can interfere with the interfacial charge transfer.

Hierarchically porous materials with multiscale porosity have drawn attention in photocatalysis due to their unique features that result in high pollutant removal rate and enhanced quantum efficiency. In these materials, large macropores facilitate light and pollutant molecules transport, pores in the mesoscopic scale provide large surface area, and meso/micro pores advance the adsorption process. In the present work, two members of this category were synthesized and tested: 3-D sea-urchin like and 3-D hierarchically porous. Both TSU and THP exhibit decent photocatalytic activities: 49.5 and 48.1% MEK removal efficiency, respectively. Similar to THS, these morphologies also benefit from good light harvesting ability (but probably not as influential as that for THS) as depicted in Figure 5.48. In THP, the macroporous channels could serve as light transfer paths for the distribution of photon energy onto the large surface of inner photoactive mesoporous frameworks. In the case of TSU, long spindle-like structures could offer pathways for fast electrons transfer while high crystallinity and small number of surface defects (Table 5.10) reduce the electron/hole recombination. The existence of small amount of brookite phase in THP could also lead to better charge separation (anatase/brookite heterojunction, discussed in section 5.1) and improve the photoactivity.

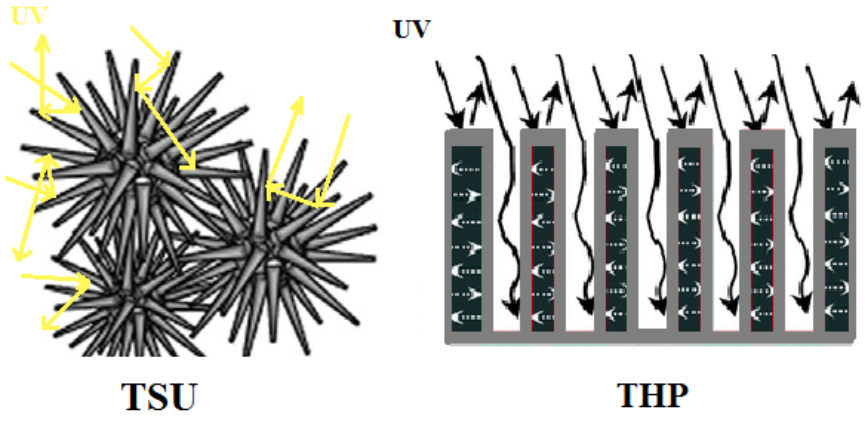

Figure 5.48 Schematic illustration of light harvesting ability of TSU and THP and pollutant transfer in THP

5.4. Impact of post-thermal treatment

High degree of crystallinity is an essential feature in photocatalytic oxidation reactions since surface and bulk defects can act as recombination centers for photogenerated charge carriers. Even though the titanium dioxide photocatalysts prepared via hydrothermal/solvothermal route exhibited good crystallinity, further improvement in crystallinity without substantial surface area loss and crystal growth could enhance the reaction rate due to the prolonged e^--h^+ lifetime. Calcination at high temperatures is a well-known procedure in order to increase the crystallinity of amorphous titania derived from sol-gel method. However, upon calcination the porous networks drastically collapse and undesired anatase-to-rutile phase transformation occurs. In this context, developing new approaches to synthesize highly crystalline and large-surface-area photocatalysts is of great importance. In this section, we examined the influence of a preliminary hydrothermal treatment prior to the calcination stage (300-800 °C) on the crystallinity, phase composition, porous structure, and anatase-to-rutile transition temperature. Furthermore, employing a novel solvothermal route, pure anatase titania was prepared in order to further investigate the impact of crystalline impurities and crystal size on structural evolution during calcination.

5.4.1. Methodology

5.4.1.1. Photocatalyst preparation

7 mL TBOT was added dropwise at a rate of 2 mL/min to 73 mL distilled water in the absence of stirring at room temperature. The solution aged for 24 h at ambient temperature (21 ˚C) and afterwards the precipitates were filtered. The filtered solids were washed several times with distilled water and subsequently dried at 80 ˚C for 12 h. 2.5 g of amorphous titania sample was placed in a 100 ml stainless steel autoclave with a Teflon liner and the liner was filled with distilled water until it reached 80% filling ratio. The autoclave was heated at a rate of 3 ˚C/min to 180 ˚C, maintained at that temperature for 12 h, and finally cooled down (-3 ˚C/min) to room temperature. The resulting precipitate was filtered, washed with distilled water, and dried at 80 ˚C for 12 h. Finally, the hydrothermally-prepared sample (denoted as H-T) was calcined at 300, 400, 500, 600, 700 or 800 °C for 2 h (denoted as H-Tx, where x represents the calcination temperature).

Pure anatase TiO_2 could be prepared by a facile solvothermal route with toluene as the solvent and TBOT as the titanium precursor. In a typical synthesis procedure, 5 mL TBOT was added dropwise to 45 mL toluene under vigorous mixing inside the Teflon liner to obtain a homogenous pale-yellow solution. Afterwards, the mixing was stopped and a glass vial (capacity=2 mL) containing 1 mL distilled water was fixed on the inner wall of the liner without any contact with the reaction solution (depicted in Figure 5.49). The hydrothermal reactor was sealed carefully and heated at a rate of 3 ˚C/min to 200 ˚C, maintained at that temperature for 12 h, and finally cooled down (-3 ˚C/min) to room temperature. With increasing the temperature during the solvothermal synthesis, the water slowly vaporizes and dissolves in the reaction medium, leading to controlled and slow hydrolysis of TBOT. The as-prepared powders were collected by centrifugation, washed three times with anhydrous ethanol, and finally dried at 80 °C for 20 h. It is noteworthy that upon addition of water to the centrifuged liquid, a small amount of precipitates were formed, indicating that the hydrolysis of TBOT was not complete. The solvothermally-prepared pure anatase (denoted as S-A) was finally calcined at 600 °C for 2 h (denoted as S-A600).

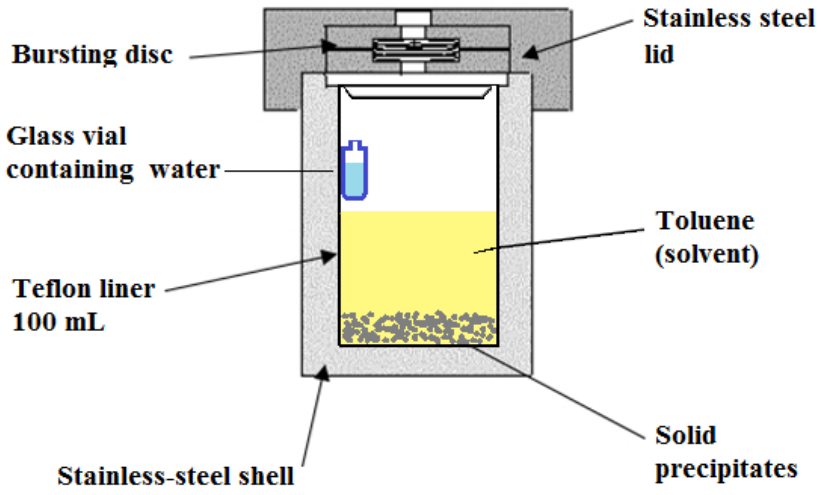

Figure 5.49 Schematic illustration of different parts of the stainless-steel autoclave during the solvothermal synthesis

The experimental set-up design and operation are explained in details in section 3.1.2. The experimental conditions at which PCO tests were performed for this section are given in Table 5.11.

Table 5.11 PCO tests experimental conditions

Parameter	Value	Unit
Pollutant	Toluene or MEK	
Inlet concentration	1034 ± 15.4	ppb
Relative humidity	20.5 ± 1.8	%
Volumetric flow rate	12	L/min
Residence time	0.05	s
Light intensity	5	mW/cm^2
Temperature	22.5 ± 0.5	°C
TiO_2 concentration	0.97± 0.06	mg/cm^2

5.4.2. Results and discussions

5.4.2.1. Photocatalyst characterization

The crystal composition and crystal size of titania samples were determined by XRD. Figure 5.50 illustrates the wide-angle XRD patterns of samples calcined at different temperatures. H-T shows a broad peak corresponding to (101) plane diffraction of anatase and a smaller one which is indexable to (121) plane diffraction of brookite. The broadening of the diffractions peaks stems from the small grain sizes of anatase (7.6 nm) and brookite crystals (8.3 nm) of H-T. The intensity of anatase and brookite peaks becomes stronger and sharper with increasing the calcination temperature up to 500 °C, indicating improvement in crystallinity and formation of larger crystals. Further increment in the calcination temperature to 600 °C results in complete disappearance of brookite phase; meanwhile, formation of a small amount of rutile in the sample is noticed via the obvious peak at 2θ=27.5° corresponding to (110) plane diffraction of rutile (JCPDS No. 21-1276). On the other hand, the crystal size of anatase substantially increases to 33.8 nm upon calcination at 600 °C, indicating significant crystal growth and sintering. The complete anatase-to-rutile phase transformation is seen at 800 °C, at which point the sample is 100% rutile.

Figure 5.51 displays the N_2 adsorption-desorption isotherms and pore size distributions for H-T, H-T400,and H-T600. H-T and H-T400 possess hysteresis loops with a stepwise adsorption and desorption branch (type IV isotherms), indicative of 3-D intersection of solid porous structures.

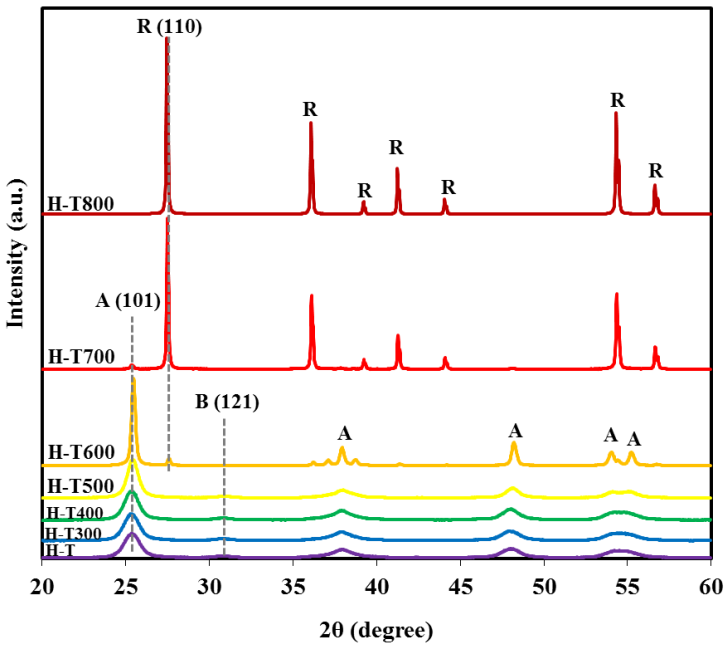

Figure 5.50 X-ray diffraction patterns of TiO_2 prepared under hydrothermal conditions and calcined at different temperatures

The shape of the hysteresis loops is of type H2, associated with narrow necks and wider bodies (ink-bottle pores). The porosity and surface area of photocatalysts gradually decrease with calcination temperature, as it is evident from the downward shift of the hysteresis loop (i.e. lower adsorbed volume) for H-T400 and H-T600. Considering the fact that a portion of the high surface area of H-T originates from its amorphous part (14.6%), when the calcination temperature is raised the amorphous content and, therefore, the surface area decline. Evidently, the pore size distribution of titania samples strongly depends on the calcination temperature. Prior to calcination, the H-T sample demonstrates a wider pore size distribution (1.6-8.8 nm) with a maximum peak of 6.6 nm. With calcination the pore size distribution range becomes narrower and shifts slightly to the right, implying increase in pore size. This could be mainly attributed to the partial collapse of the intra-aggregated pores and the crystal growth upon calcination. Unlike H-T, H-T400 shows a unimodal distribution of pores with a distribution of pores in the mesoscopic range and a mean pore diameter of 7.8 nm. Calcination of H-T at 600 °C brings about a dramatic decline in surface area to 14.6 m^2/g, resulting from the collapse of porous structure. This is further confirmed by the pore size distribution presented in Figure 5.51, which reveals that T-H600 has almost no mesoporosity.

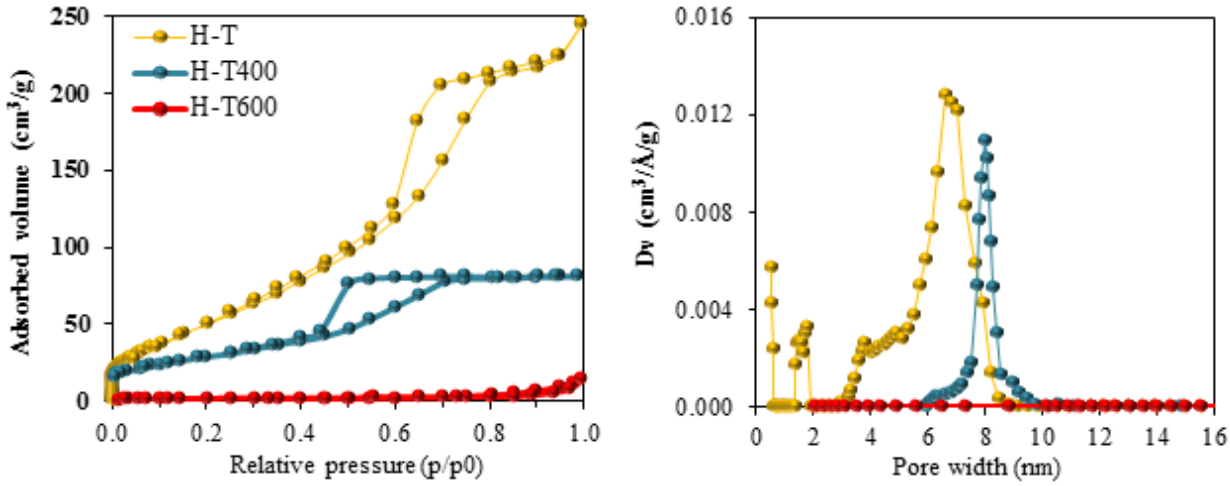

Figure 5.51 Nitrogen adsorption–desorption isotherms and pore-size distribution of H-T, H-T400, and H-T600

Table 5.12 Crystalline, textural, and optical properties of titania photocatalysts

Photocatalyst	Crystal size (nm)			Crystal composition (%)			Amorphous content (%)	Relative crystallinity	Surface area (m^2/g)	Band gap (eV)
	A	B	R	A	B	R				
H-T	7.6	8.3	-	83.4	16.6	-	14.6	1	155.5	3.2
H-T300	8.6	9	-	87.7	12.3	-	14.2	1.17	138.0	3.18
H-T400	10.3	13.4	-	91.5	8.5	-	13.5	1.29	116.1	3.18
H-T500	14.6	19.1	-	92.0	8.0	-	12.8	1.52	59.5	3.19
H-T600	33.8	-	46	93.2	-	6.8	9.3	3.4	14.6	3.1
H-T700	-	-	61.5	3.2	-	96.8	7.4	-	8.5	3.05
H-T800	-	-	72.1	-	-	100	3.5	-	2.2	3.02

Figure 5.52 summarizes the crystalline and textural variations with calcination temperature. As consistent trends, surface area and amorphous content gradually decline with calcination temperature up to 400-500 °C, and then have abrupt drops for higher temperatures. Similarly, crystal size exhibits small changes between 300-500 °C, and then experiences a drastic rise upon calcination at 600 and 700 °C. At this temperature, the crystallite size of anatase TiO_2 sharply increases because of the heat of the phase transformation from anatase/brookite to rutile. At 700 °C, the intensity of the anatase TiO_2 diffraction peak is almost negligible and the anatase mass fraction is less than 4%, which does not allow to calculate its crystal size accurately. Since rutile only appears at high temperatures, its crystal size is very large and ranges between 46 and 72.1 nm.

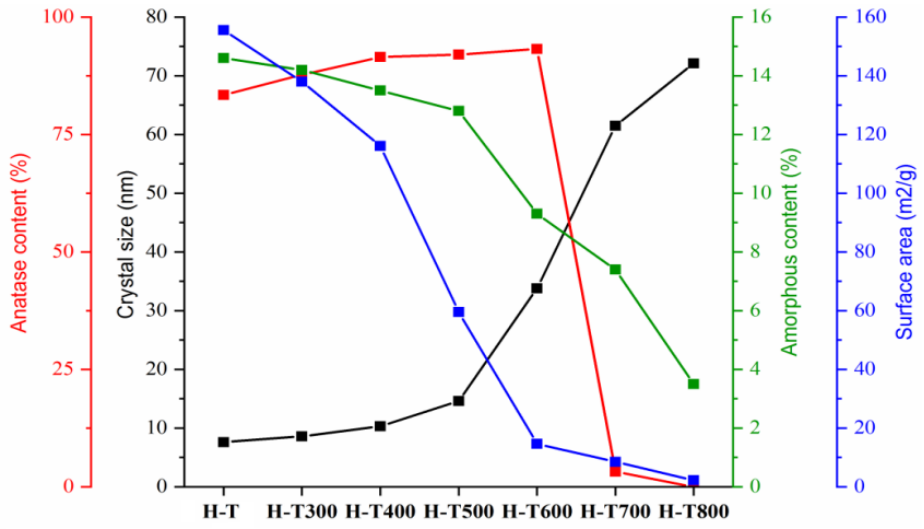

Figure 5.52 Variations in crystalline and textural properties of photocatalysts with calcination temperature

Table 5.12 reports the band gaps (estimated from the Tauc plot based on UV-vis analysis) of photocatalysts subjected to different calcination temperatures. The observed differences in the band gap can be ascribed to the fact that these samples have different crystalline compositions. Since the band gap of rutile (3.0 eV) is smaller than those of anatase and brookite (ca. 3.2 eV), with increasing the temperature lower bang gap energies are expected due to the formation of rutile phase. On the other hand, the band gap narrowing could be partly caused by the quantum size effects of semiconductors. In the quantum size effect, the band gap energy decreases as the crystallite size increases [254]. The FTIR spectra (Figure 5.53a) of selected samples show a broad peak between 3000-3500 cm^{-1} and four small peaks between 2633-3715 cm^{-1}. The absorption in 3000-3600 cm^{-1} region is usually ascribed to water molecules adsorbed on the surface via weak hydrogen bonds and some types of hydroxyl groups [144]. The bands at frequencies higher than 3600 cm^{-1} are generally assigned to the stretching mode of OH species free from hydrogen bonding interactions. The decrease in the intensities of these peaks with increased calcination temperature confirms the elimination of surface-adsorbed water and hydroxyl groups. Beside the water removal caused by the heat treatment, many surface hydroxyl groups are consumed in condensation reactions to form Ti-O-Ti networks. Figure 5.53b shows the PL spectra of H-T, H-T400, H-T600, and H-T800. The sharp PL peak around 390 nm can be attributed to the emission of band gap transition. Figure 5.53b reveals that the emission intensity decreases with calcination temperature, indicating that the recombination rate was decreased

gradually by eliminating the crystal defects in TiO_2 structure via calcination at higher temperatures. On interesting observation is that the PL intensity of H-T800 is slightly stronger than that of H-T600, although the former has a higher degree of crystallinity. This peculiar behavior may stem from the following facts. The crystal sizes of H-T600 and H-T800 are 33.8 (for anatase phase) and 72.1 nm (for rutile phase), respectively. It is well-known that the charge carriers bulk recombination becomes more prominent as the crystal size increase since electrons and holes must travel a longer distance to reach the surface and take part in photochemical reactions. The second reason is the efficient charge separation by anatase/rutile phase junction in H-T600 which reduces the probability of recombination (Figure 5.54).

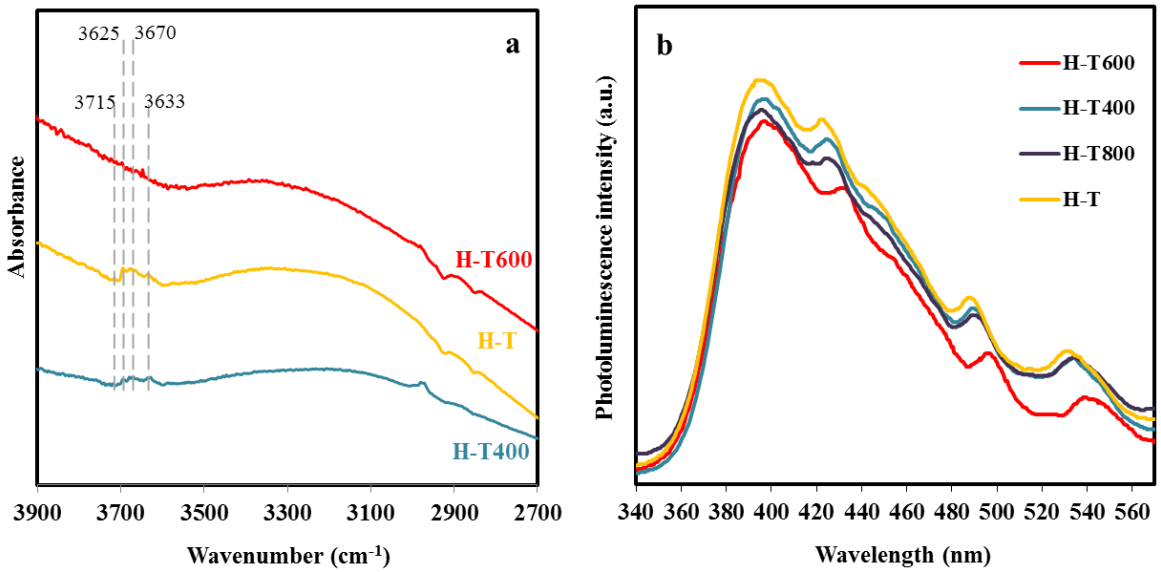

Figure 5.53 FTIR (a) and photoluminescence spectra (b) of selected photocatalysts

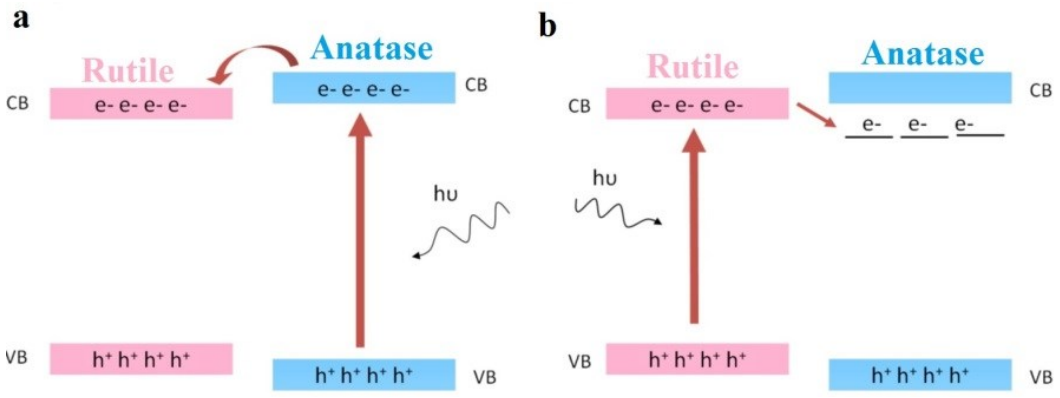

Figure 5.54 Possible charge transfer pathways between rutile and anatase: (a) from anatase to rutile; (b) from rutile to anatase [16]

In Table 5.13, a comparison is made between the properties of photocatalysts underwent two different preparation routes: (1) Route I: hydrothermal treatment + calcination (this work) and (2) Route II: direct calcination [255]. Considering the fact that the amorphous TiO_2 precursors used in both studies were synthesized under similar conditions, the differences in final products result only from the post thermal/hydrothermal treatments. As previously mentioned, it is believed that the hydrothermal treatment can effectively improve the thermal stability of anatase phase and delay the destruction of porous structure upon calcination. During the hydrothermal treatment, the amorphous titania gradually transforms into the crystalline form through further hydrolysis/polycondensation reactions and structural rearrangements. In contrast, during calcination, the amorphous powder undergoes rapid purification and thermal transformation before it could fully react and the crystallites develop well. Consequently, Route I theoretically can produce titanium dioxides with better crystallinity and fewer surface defects with respect to Route II. Firstly, a comparison between the surface areas of photocatalysts indicates that the decrement in the surface area of samples prepared via Route I with calcination temperature is not as marked as that of samples of Route II. This clearly implies that the hydrothermal treatment improves the thermal stability of the mesoporous framework. For instance, H-T600 possesses a surface area of 14.6 m^2/g while the corresponding sample obtained from Route II is actually nonporous with a very small surface area of 0.8 m^2/g. Similarly, regarding the crystal size and anatase-to-rutile transformation, Route I photocatalysts show superior results. The crystal sizes of Route I samples calcined at 300-800 °C are in the range of 8.6-72.1 nm, which is much smaller than those of the samples subjected to direct calcination (5.9-200 nm). On the other hand, even though in both methods rutile appears after calcination at 600 °C, the rutile phase content of H-T600 is only 6.8%, while the corresponding sample in Route II contains 12.6% rutile. This can be attributed to the fact that lattice defects (e.g. ion vacancies) and impurities can facilitate the nucleation of the rutile phase. This may partially support the argument that the increase in crystallinity during hydrothermal treatment would result in an elevation of the temperature for anatase-to-rutile transformation. As can be seen in Table 5.12, the rutile phase formation coincides exactly with the disappearance of brookite phase. Consequently, one may postulate that throughout the calcination rutile particles originate from brookite nuclei. To examine this hypothesis, a pure anatase titania sample (i.e. S-A) was prepared via a novel solvothermal method. The preparation parameters of the solvothermal method were adjusted in a way to obtain

a degree of crystallinity similar to that of H-T photocatalyst. Therefore, the only differences between H-T and S-A photocatalysts are the presence of brookite phase (16.6%) in H-T and the slightly larger anatase crystal size of S-A (8.1 vs. 7.6 nm). To investigate the thermal stability of S-A and assure removal of the solvent (i.e. toluene), TGA was conducted (Figure 5.55). Given the small weight loss up to 700 °C, it can be concluded that the S-A photocatalyst has an excellent thermal stability. In addition, the weight loss from 30-120 °C, which could be related to the evaporation of toluene and water, is only 1.23%, indicating that there cannot be a significant amount of toluene residue on S-A.

Table 5.13 Comparison between "hydrothermal+calcination" and direct calcination routes

T_{cal} (°C)	Route I (our work)							Route II ([255])				
	Phase (%)			Crystal size (nm)			Surface area (m^2/g)	Phase (%)		Crystal size (nm)		Surface area (m^2/g)
	A	B	R	A	B	R		A	R	A	R	
300	87.7	12.3	-	8.6	9	-	138.0	100	0	5.9	-	206
400	91.5	8.5	-	10.3	13.4	-	116.1	100	0	10.2	-	104
500	92.0	8.0	-	14.6	19.1	-	59.5	100	0	15.1	-	51
600	93.2	-	6.8	33.8	-	46	14.6	87.4	12.6	34.1	57.3	0.8
700	3.2	-	96.8	-	-	61.5	8.5	11.3	88.7	43.7	75.9	0.1
800	-	-	100	-	-	72.1	2.2	0	100	-	>200	0.02

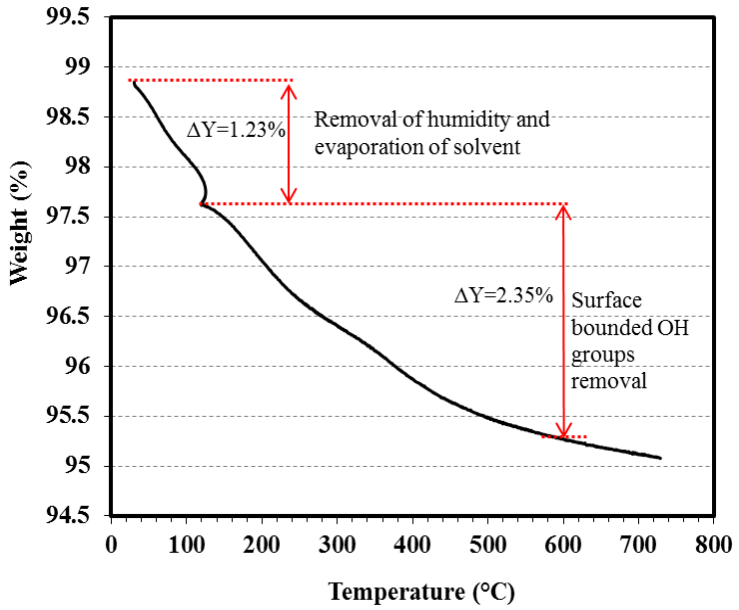

Figure 5.55 Weight percentage losses as a function of temperature for S-A sample

Figure 5.56 illustrates the XRD patterns of H-T, S-A, H-T600, and S-A600 (S-A calcined at 600 °C). Interestingly, unlike H-T600, the S-A600 sample does not show any diffraction peaks associated with the rutile phase. This reveals that the presence of a small amount of brookite contamination in the H-T600 sample led to the formation of rutile phase at a lower temperature. This also suggests that the anatase polymorph is more stable than the brookite phase during calcination or, in other words, the anatase → rutile process requires more energy than the brookite → rutile process. Another possible piece of evidence for supporting this claim is the crystalline compositions of H-T500 and H-T600. H-T500 and H-T600 are composed of 92% anatase and 8% brookite, and 93.2% anatase and 6.8% rutile, respectively. Since from 500 to 600 °C there is no reduction in the content of anatase, the brookite phase should have transformed to the rutile phase. After the formation of these preliminary rutile crystals, the anatase to rutile transformation happens very fast with calcination at 700 °C, at which point most of the anatase crystals (around 96.5%) have transformed to rutile.

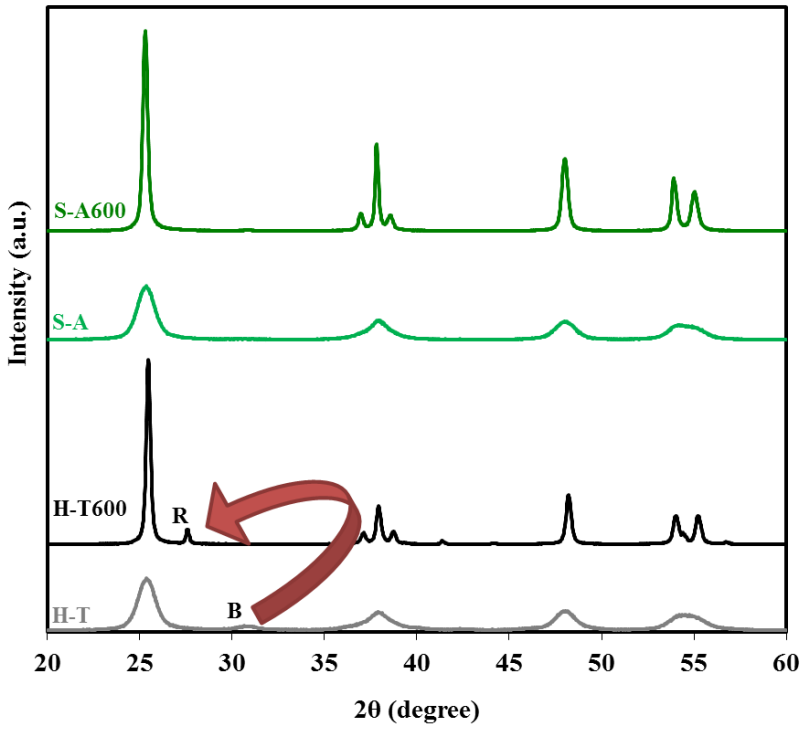

Figure 5.56 Impact of calcination at 600 °C on crystalline structure of H-T and S-A photocatalysts

5.4.2.2. Photocatalytic activity

The activity of photocatalysts calcined at various temperatures was assessed by degradation of toluene and MEK in air. Figure 5.57 displays the dependence of toluene and MEK removal efficiencies on calcination temperature. As could be expected from the results presented in Table 5.12, the photocatalytic activity of prepared TiO_2 samples considerably varies. The hydrothermally-prepared sample (H-T) exhibits high toluene and MEK removal efficiencies (48.7 and 46.0% respectively), mainly owed to its large surface area, hierarchically porous structure, and good crystallinity (more details in section 5.1). By calcination at 300 °C, the photocatalytic activity is enhanced and reaches its optimum values: 52.1% for toluene and 55.9% for MEK. This improvement mainly stems from the substantial increment in crystallinity without huge loss in the surface area or damage to the hierarchical structure. It can be deduced that at this point the best trade-off between the crystallinity and surface area could be achieved. Since gas–solid heterogeneous photocatalysis is a surface-based process, large surface area is certainly one of the key determining factors. Consequently, by increasing the calcination temperature to 500 °C, the photocatalytic activity sharply declines, suggesting that the enhancement in crystallinity (from 1.17 to 1.52) could not compensate for the reduction in surface area (from 138.0 to 59.5 m^2/g). For H-T600 and H-T700, toluene and MEK removal efficiencies are lower than 15%, which could have originated from the complete destruction of porous structure (loss of mesopores, Figure 5.51), dramatic crystal growth (Table 5.12), formation of rutile phase, and surface dehydroxylation (Figure 5.53b). Nevertheless, it is interesting to note that if we solely consider the influence of these factors on the overall performance of photocatalysts, greater performance drops should have been observed, suggesting that other parameters have contributed to the relatively good efficiency of H-T600 and H-T700. One justification could be the co-presence of anatase and rutile in the crystalline structure which leads to better charge carriers separation (Figure 5.54). On the other hand, given the smaller band gap of rutile compared with anatase and brookite, the rutile polymorph has a faster initial rate of photoactivation. In fact, it has been suggested that the antenna effect owed to the presence of rutile can increase the chance of electron excitation [256]. At 800 °C, no photocatalytic activity is seen for toluene or MEK, which is understandable considering the surface area and rutile crystal size of H-T800.

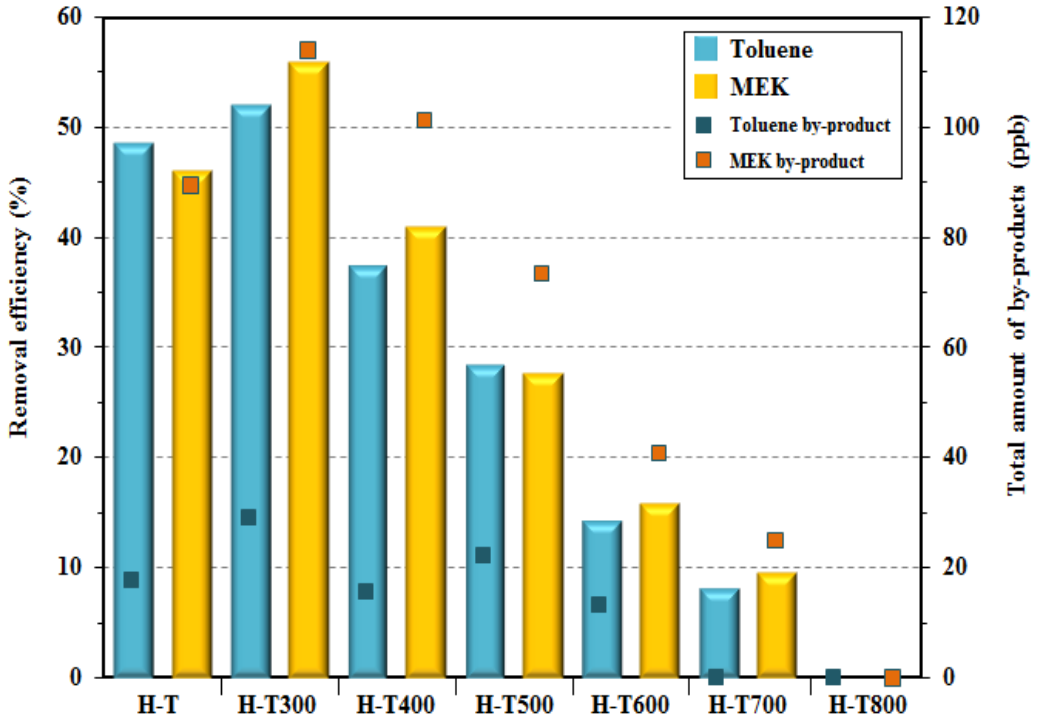

Figure 5.57 VOC removal efficiency and amount of generated by-products over various photocatalysts

5.5. Impact of titanium dioxide support material

In previous chapters, it has been demonstrated that photocatalytic oxidation can be regarded as a promising and efficient indoor air cleaning technology. Nevertheless, widespread application of UV-PCO technology in HVAC system of buildings is hampered by a number of practical and economic reasons caused by the following shortcomings. The removal efficiency of organic compounds (i.e. rate of photocatalytic reactions) is generally not satisfactorily high under actual operating conditions chiefly because of the low concentration of pollutants in air. The second critical issue is the formation of intermediates/by-products, which not only may result in photocatalyst deactivation, but also can pose serious health risks which are, in some cases, greater than the original pollutants. Last but not least, significant variations in the performance of PCO air purifiers with time and operating conditions (e.g. airflow rate, relative humidity, etc.) do not allow manufacturers and consumers to have realistic and reliable estimations of the performance to optimize the operation and plan regular regeneration/replacement. In this study, the first two above-mentioned challenges were attempted to be resolved by developing new TiO_2 materials with features specifically tailored for indoor air purification purposes (sections 5.1 through 5.4).

As briefly explained in section 1.2, as of now, activated carbon adsorption-based air cleaners are extensively implemented to capture indoor pollutants; however, once exhausted, the filter is either disposed of (harmful to the environment) or regenerated. Activated carbon regeneration is usually achieved via thermal reactivation which requires huge amount of energy (i.e. very costly) and brings undesirable textural changes in activated carbon (e.g. loss of microporosity).

In this section, we put forward a possible strategy to circumvent the current drawbacks associated with the oxidation-based and adsorption-based cleaning methods. The combination of titanium dioxide and activated carbon filter was investigated to concomitantly boost the efficiency of UV-PCO system and enable the in-situ regeneration of adsorbent.

5.5.1. Methodology

5.5.1.1. Photocatalyst coating on activated carbon filter

2.0 g of H-Base photocatalyst was added to 100 mL of deionized water and 100 mL of absolute ethanol and the resulting mixed suspension was stirred vigorously allowing the TiO_2 particles to

remain suspended in the solution. The activated carbon filter (Kynol®, BET surface area ~ 800 m^2/g) was immersed in the dispersing solution for 5 min and then dried at 110 °C for 2 h. This procedure was repeated several times depending on the desired TiO_2 surface loading. Finally, the titania coated filter was subjected to a thermal treatment at 150 °C for 24 h to completely remove the water from TiO_2/ACF and stabilize titania powder on the substrate. The advantages of this physical coating method are low-cost, simplicity and the possibility of using previously prepared photocatalyst with desired characteristics.

The experimental set-up design and operation are explained in details in sections 3.1.1 and 3.1.2. The PCO test conditions for this section are given in Table 5.14.

Table 5.14 PCO tests experimental conditions

Parameter	Value	Unit
Inlet concentration	1.93 ± 0.06, 4.85 ± 0.10	ppm
Relative humidity	17.6 ± 2.5	%
Volumetric flow rate	20	L/min
Residence time	0.03	s
Light intensity	5	mW/cm^2
Temperature	21.5 ± 2.2	°C
TiO_2 concentration	1± 0.05	mg/cm^2
TiO_2 support material	ACF or Nickel foam filter (NFF)	

5.5.2. Results and discussions

5.5.2.1. SEM characterization

Figure 5.58 illustrates the SEM images of H-Base/NFF and H-Base/ACF as well as their corresponding elemental mappings. The EDS elemental mapping was mainly carried out to study the distribution of Ti, O, and Ni/C and to confirm achievement of a homogeneous coating on the substrate. Considering the uniform distribution of red and green colors (represent Ti and O respectively), an acceptably good coating quality could be reached in both cases. It can be observed in Figure 5.58 that on the surface of support materials there are a lot of titania particles, dispersed throughout the surface, which will be beneficial for enhancing the activity.

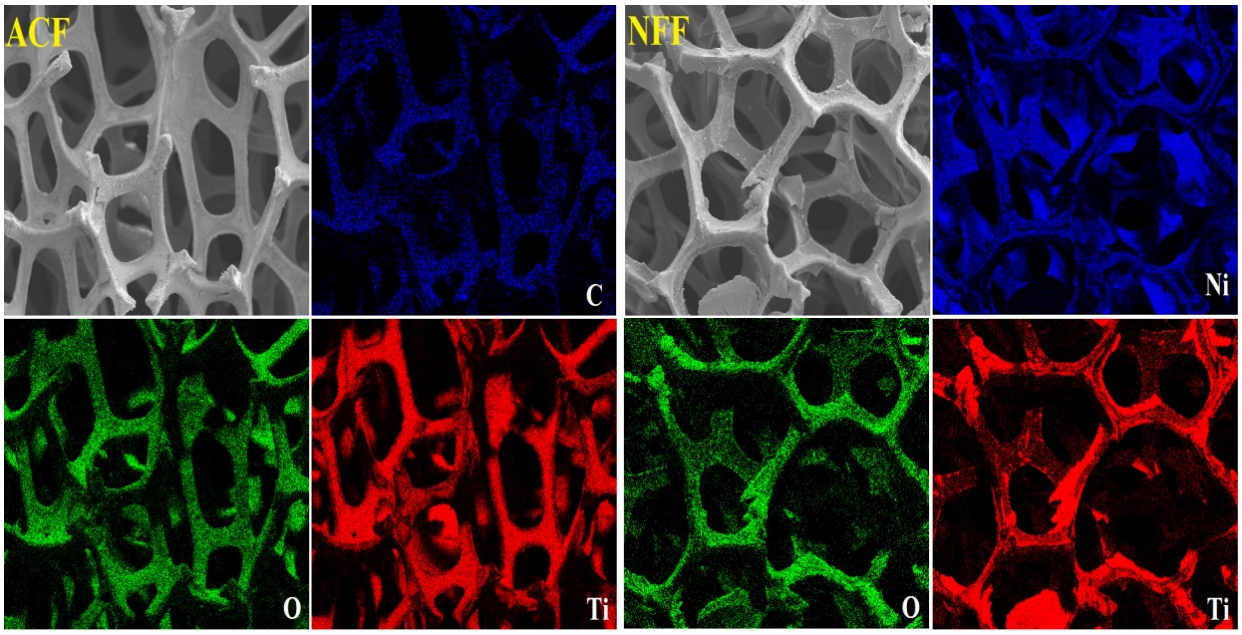

Figure 5.58 EDS elemental mappings of H-Base/ACF and H-Base/NFF

5.5.2.2. Adsorption and photocatalytic degradation of MEK

In order to have a better understanding of the role of ACF in PCO processes and distinguish mere adsorption from "adsorption + photocatalysis", the adsorption capacity and photocatalytic activity of the following systems were compared: uncoated ACF, P25/NFF, H-Base/NFF, P25/ACF, and H-Base/ACF. Figure 5.59 displays the adsorption performance of various systems under dark condition towards 2 ppm MEK at 20% RH. As could be expected from the adsorption study presented in section 4.1, P25/NFF shows insignificant adsorption capacity and complete saturation of the filter is noticed after only 98 min. Comparatively, H-Base/NFF exhibited a much higher capacity for MEK (breakthrough time = 242 min) mainly owed to its larger surface area with respect to P25 (155.5 vs 53.23 m^2/g) as well as its hierarchical porosity. With employing ACF as the support material for titania, the adsorption capacity for MEK is considerably augmented and 100% breakthrough is seen after ca. 15-19 h. ACF is a highly microporous carbon material with a very large pore volume and surface area, which enables huge pollutant uptake. The internal region of ACF consists of pores of varying widths: micropores (< 20 Å), mesopores (20-500 Å), and macropores (> 500 Å). The exact way that adsorption onto ACF surfaces occurs is still debated, with the main source of disagreement being the chemistry of the carbon surface. Knowing whether the process is based on van der Waals interactions (physisorption) with the carbon surface or on chemical reactions with the functional groups

(chemisorption) requires more in depth investigations. Nonetheless, the π-π interaction and donor-acceptor complex are among the most widely accepted theories for adsorption on activated carbon. The uncoated ACF shows the highest adsorption capacity for MEK, which suggests that the active surface area was diminished after titania coating. It is noteworthy that since ACF is a hydrophobic material, water does not interact strongly with the solid [257]. This can be particularly advantageous when dealing with air streams with high levels of humidity. However, even in the case of ACF, at high humidity, the moisture adsorption increases sharply due to capillary condensation and the adsorbed water fills the small pores in ACF, interfering with the adsorption of organic compounds. In our experiments, it can be assumed that the adsorption of MEK on P25/NFF or H-Base/NFF was more adversely affected by the presence of humidity with respect to that on P25/ACF or H-Base/ACF.

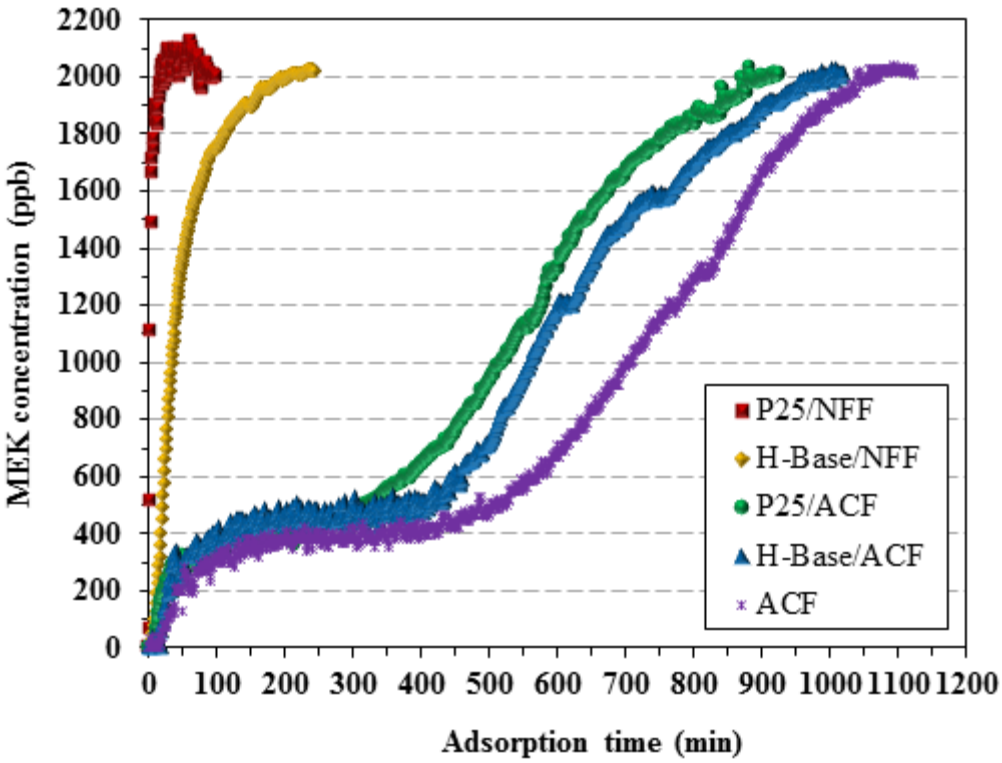

Figure 5.59 Dark adsorption of MEK on various photocatalytic air filters

During the first stage (Figure 5.59), the UV lamps are off and the MEK stream is passed through the photocatalytic bed until MEK concentration in the outlet stream equaled the inlet concentration (i.e. complete saturation). Once an equilibrium state between MEK adsorption and desorption was attained, the UV light was switched on and the trend in MEK concentration in the

outlet stream was followed with time [258, 259]. It should be mentioned that the concentration of MEK and by-products in this stage is determined (every 3 h) by HPLC analysis. Generally, two different behaviors are observed depending on whether the support material was NFF or ACF. For P25/NFF and H-Base/NFF, the outlet concentration of MEK gradually decreases due to the photocatalytic destruction of MEK until it reaches a quasi steady-state value. The steady-state MEK removal efficiency over P25/NFF is roughly 23.5%, while for H-Base/NFF it is 36.3%. This is simply attributable to the superior features of H-Base compared with P25 elaborated in section 5.1. Contrarily, for P25/ACF, H-Base/ACF, and ACF, an increase in the MEK outlet concentration is noted with respect to the inlet concentration when the UV-light is switched on. This is due to a complex trade-off between photocatalytic oxidation and desorption phenomena. Even though a portion of MEK participates in degradation reactions over TiO_2 when the UV-light is switched on, it is not possible for the photocatalyst to oxidize all pre-adsorbed MEK together with the incoming MEK. The magnitude of the initial peak in MEK concentration noticeably varies with the applied system. For uncoated ACF, no photocatalytic reaction can be envisaged; thus, a huge desorption peak (which is also exacerbated by the rise in temperature (around 4 °C) after the UV lamps are tuned on) is witnessed. The desorption of MEK from the uncoated ACF lasts for several hours until the outlet concentration equals the inlet one. At this point, MEK removal efficiency for uncoated ACF is literally zero and regeneration is necessary. For P25/ACF and H-Base/ACF after the initial peak, the concentration sharply drops and reaches a quasi steady-state condition after roughly 18 h of turning on the UV lamps. The steady-state MEK removal efficiency are 45.0 and 62.1% over P25/ACF and H-Base/ACF, respectively. For both P25 and H-Base photocatalysts, substitution of NFF with ACF leads to huge improvements in the removal ability of the filter (21.5-25.85 %). Figure 5.61 depicts the total amount of generated by-products during photo-oxidation of MEK on various air filters. Considering the absence of any catalytic reaction over uncoated ACF, no by-products was detected in the downstream of the filter. For all systems, the main by-products are acetone, acetaldehyde, and formaldehyde, while in the case of P25/NFF and H-Base/NFF very small quantities of propionaldehyde were also found. Three hours after the UV lamps were switched on, for all filters, large amounts of by-products are seen in the outlet stream (emphasized by the arrows).

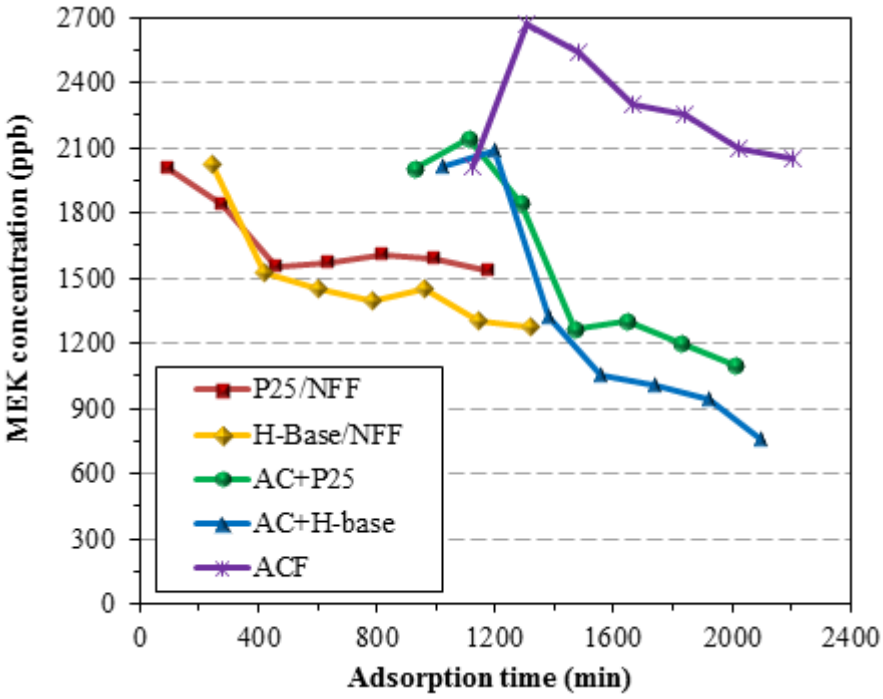

Figure 5.60 Photocatalytic degradation of MEK on various photocatalytic air filters

At this point, as could be inferred from Figure 5.60 as well, still there are plenty of pre-adsorbed MEK on the surface of the substrate and titania. This situation promotes two phenomena: (i) fast reaction rate because of the high concentration of MEK on titania and (ii) occupation of the majority of adsorption sites on activated carbon by MEK molecules. Both (i) and (ii) could reasonably explain the high concentration of by-products along with the high concentration of MEK (Figure 5.60). For the first six hours of operation under UV light, the amounts of by-products were higher for ACF supported titanias in comparison to NFF supported ones, which could be justified as follows. The amount of pre-adsorbed MEK on NFF supported titanias is much smaller than that on ACF supported ones; therefore, upon illumination, more MEK molecules go through oxidation reactions over P25/ACF and H-Base/ACF, leading to formation of more by-products. Additionally, despite the fact that ACF has a large surface area and can host the formed by-products, during the first few hours, most of the active sites are still occupied by MEK and unavailable to other molecules. Once the steady-state MEK removal is reached (roughly after 15 h), the amount of by-products in the gas-phase becomes much lower for the PCO systems with ACF support.

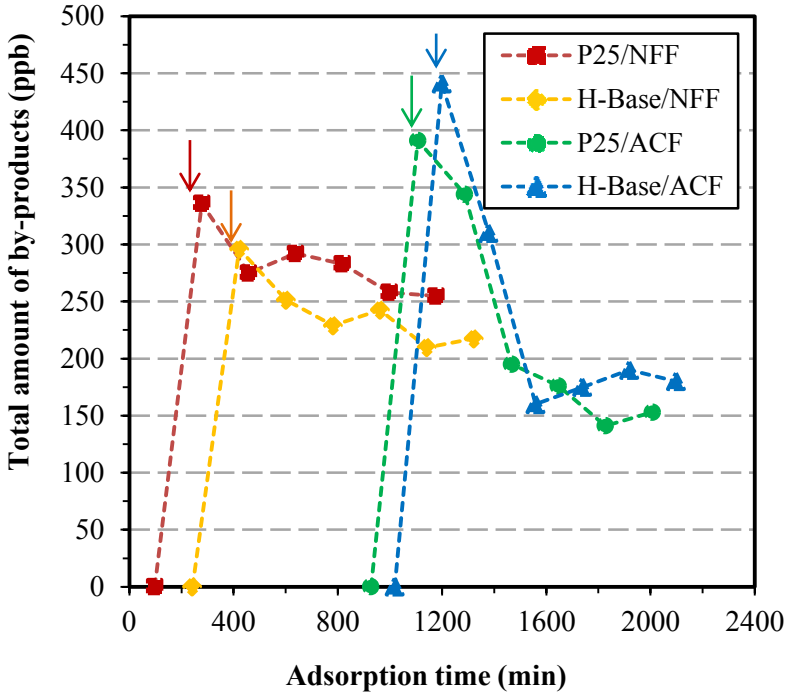

Figure 5.61 Total amount of generated by-products during MEK degradation on various filters

5.5.2.3. Mechanism for the enhanced activity of TiO_2/ACF

In buildings, concentration of VOCs is in the ppb or sub-ppb ranges and the contact time between the catalytic air filter and pollutants is extremely short. Under these circumstances, the overall performance of an air purifier is controlled by both the adsorption capacity and photoactivity of the catalyst. In this regard, it is believed that the combination of activated carbon filter (i.e. adsorption) and titanium dioxide (i.e. photocatalysis) can be beneficial in several ways which are elaborated below. The synergistic effect of absorption and photocatalytic degradation of MEK is shown in Figure 5.62.

1) Given the high affinity and capacity of activated carbon for air pollutants, via adsorption, a high concentration zone of reactants is built near TiO_2 particles. This followed by the transfer/diffusion of VOC molecules to photocatalytically active sites and/or hydroxyl radicals. In essence, ACF concentrates the VOC around (or continuously supplies VOC to) TiO_2 and enhances the reaction rate.
2) Considering the extremely fast recombination rate of charge carriers, adsorbed organic compounds can serve as traps for photogenerated holes and extend the electron-hole

lifetime. More electron-hole pairs means a greater population of hydroxyl radicals for oxidation of VOCs and by-products.

3) ACF adsorbs and increases the retention of intermediates through re-adsorption, thus allowing chain photocatalytic reactions to proceed more easily than over TiO_2/NFF. Consequently, a higher degree of mineralization to CO_2 and H_2O and a lower quantity of harmful by-products are achieved.
4) Photocatalytic degradation of MEK can extend the breakthrough time of ACF. MEK adsorbed on the external surface is first catalytically oxidized by TiO_2, resulting in a concentration difference between the exterior and interior of ACF. This difference acts as a driving force and initiates the migration of MEK from the internal micropores and mesopores of ACF to regions with TiO_2 particles. This pollutant transfer cycle continuously repeats and gives rise to an in-situ regeneration of ACF.
5) The adsorption competition among VOC, water vapor, and by-products molecules is greatly lessened by copious adsorption sites provided by ACF.

It is worth mentioning that the surface chemistry of activated carbon plays a critical role in having the suggested synergistic mechanism. The strength of interaction between the adsorbates and activated carbon should not limit the ability of organic molecules to maneuver within the pores of ACF. In other words, a carbonaceous material with the right adsorption strength will allow MEK molecules trapped within the porous matrix to transfer closer to the surface of TiO_2 where highly reactive species are produced.

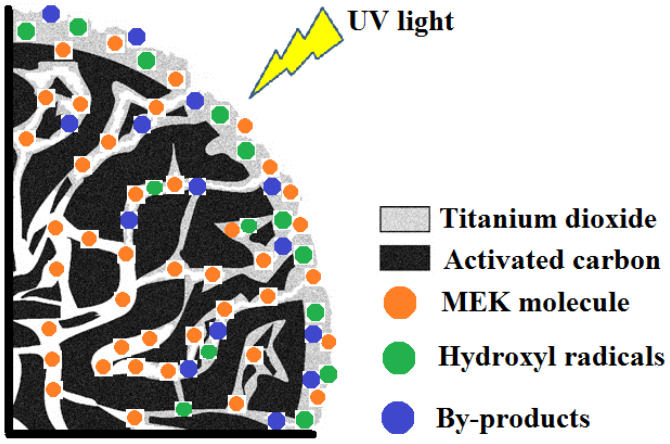

Figure 5.62 Schematic illustration of synergistic effect of adsorption-photocatalysis on TiO_2/ACF

5.5.2.4. Effect of TiO_2 loading on ACF

A series of TiO_2/ACF filters with different TiO_2 contents were prepared to study the influence of photocatalyst content on the removal efficiency and by-products generation (Figure 5.63). With increasing the amount of titania on activated carbon filter, MEK removal efficiency gradually increases and reaches its optimal value, 37.2%, at a loading density of 8 mg/cm^2. On the one hand, by increasing the amount of TiO_2, the adsorption capacity of ACF for MEK is reduced. The most likely reason for this behavior is the blockage of internal surfaces of ACF (surface of mesopores and micropores) by TiO_2 particles. Decrement in TiO_2-ACF composite surface area and pore volume with raising photocatalyst weight percent has been reported by several researchers [260, 261]. On the other hand, a larger titania loading provides more active sites for creation of oxidizing agents, which in turn advance the photocatalytic oxidation of MEK. Evidently in our experiments, the promoting effect of titania always overpowers the reduction in adsorption capacity, leading to a positive correlation between removal efficiency and loading. Additionally, considering the fact that activated carbon absorbs light both in visible and UV regions, the external surface of ACF should be entirely covered with titania particles, otherwise, the light utilization efficiency severely drops.

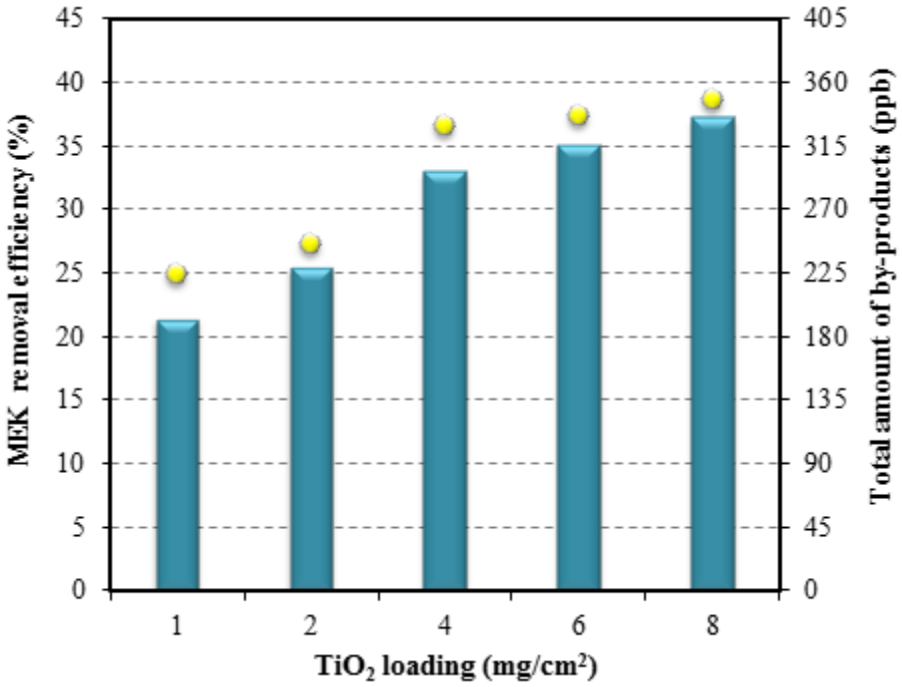

Figure 5.63 Influence of H-Base loading over ACF on MEK removal efficiency and by-products generation; MEK inlet concentration=5 ppm

It is also interesting to note that after the initial sharp increment in the removal efficiency with TiO_2 loading (from 1 to 4 mg/cm^2), increasing the amount of titania did not substantially affect the MEK degradation rate. It seems that at low loadings, the overall performance is controlled by the number of reactive species on titania, while at higher loadings, a combination of adsorption, mass transfer from ACF to TiO_2, and oxidation reactions governs the performance.

Chapter 6

6. Conclusions and recommendations

6.1. Summary and conclusion

The aim of this research was the development, characterization and evaluation of hierarchical TiO_2 photocatalysts with enhanced activity for photocatalytic oxidation in the gas phase for indoor air purification purposes. Toluene and MEK, two prevalent VOCs in residential and commercial buildings, were chosen as probe pollutants. For the photocatalysts preparation, various hydrothermal/solvothermal synthesis approaches were employed. The synthesis parameters including hydrothermal preparation time, temperature, pressure, pH, solvent, type of acid/base, titanium precursor, and calcination temperature were varied in order to study their impact on photocatalysts' properties and activity. TiO_2 properties including crystallinity, band gap, crystal phase, crystal size, surface area, porosity, surface chemistry, light-harvesting ability, exposed facet, and charge-separation efficiency were characterized by a wide range of analytical techniques such as X-ray diffraction, electron microscopy, N_2 adsorption, UV-vis spectroscopy, photoluminescence, thermo gravimetric analysis, hydroxyl radical analysis, Fourier transform infrared spectroscopy, and X-ray photoelectron spectroscopy. The photocatalytic performances were assessed in a single-pass small scale photoreactor with capability of operating in wide ranges of operating conditions such as relative humidity, airflow rate, light intensity, and pollutant concentration.

The following section summarizes the main findings and results of the work.

Major findings in Chapter 4 section 1:

- The adsorption capacity for MEK (a highly polar compound) was much higher than that of toluene (a non-polar compound) on all photocatalysts, regardless of the humidity content.
- Relative humidity negatively affects the adsorption capacity for both MEK and toluene, however to different extents due to the differences in water solubility and polarity.

- FTIR characterization of MEK/toluene saturated titania samples revealed that isolated OH groups (both terminal (Ti-OH) and bridged (Ti-OH-Ti)) serve as highly active adsorption sites for volatile organic compound molecules.
- In the case of MEK, high electron-donor ability of carbonyl group provides the possibility of H-bonding to the surface hydroxyl groups of titania. On the contrary, physisorption of toluene on TiO_2 surface takes place via weak Π-bonding to surface hydroxyls.
- FTIR characterization of samples after static adsorption of MEK or toluene showed that isolated hydroxyl groups red-shifted or completely/partially disappeared after VOC adsorption. These results reveled that there is a strong interaction between VOC molecules and isolated hydroxyls groups on titania surface.

Major findings in Chapter 4 section 2:

- Despite possessing lower crystalinity, PC500, UV100 and S5-300A outperformed P25 in toluene and MEK removal efficiency, primarily owed to their larger surface area, smaller crystal size, and higher concentration of surface hydroxyl groups.
- By increasing the RH from 0 to 20%, the pollutant removal efficiency improved mainly due to the formation of more hydroxyl radicals via reaction between adsorbed water with holes. At RH=50%, the removal efficiency declined due to the adsorption competition between VOC and water molecules over active sites on titania and also the presence of well-organized water film on TiO_2 which prevents effective contact between pollutants and catalyst surface.
- Micro/meso porous structures of UV100 and PC500 facilitated the adsorption of pollutants on TiO_2 coating, resulting in the higher activity for PC500 and UV100 compared to P25.
- Regardless of the catalyst type, VOC removal efficiency always decreased with increasing the airflow rate or inlet concentration. Parallel to that, almost always a larger quantity of by-products was detected in the gas phase as residence time or inlet concentration raised.

- As the light intensity decreased, the VOC removal efficiency sharply declined since at a lower light intensity, smaller number of photons is generated and consequently less e^--h^+ pairs are formed.
- Given the more efficient light utilization by P25, the decrement in light intensity less adversely affected the removal efficiency of P25 with respect to other samples.

Major findings in Chapter 5 section 1:

- All the hydrothermally-prepared samples using different hydrothermal times (1-48h), temperatures (100-220 °C), and filling ratios (20-90%) possessed good crystallinity (79.5-89 %), large surface area (134.9-237.2 m^2/g), small crystal size (5.9-10 nm), and mesoporous structure.
- SEM images revealed presence of macropores and marcochannels, and N_2 adsorption-desorption and TEM analyses indicated a significant amount of mesopores.
- The fluorescence intensity normalized by the sample surface area could be satisfactorily correlated with the relative anatase crystallinity, indicating that the level of crystallinity mainly governs the formation rate of $^{\bullet}OH$.
- The hydrothermal time and temperature had significant effects on the properties of yielded products and consequently the photoactivity, while comparatively autoclaving filling ratio was much less influential.
- With increasing the hydrothermal time or temperature, the relative anatase crystalinity, crystal size, and pore size increased, contrarily, specific surface area and porosity diminished.
- Photocatalyst prepared at 12 h, 200 ˚C, and 80% filling ratio exhibited the best toluene and MEK removal efficiencies, which surpassed those of P25 by factors of 2.08 and 1.85 times, respectively. The superior photocatalytic activity of developed TiO_2 catalysts might be attributed to high surface area and existence of meso-/macropores that provide a large number of active sites, and facilitate light penetration and pollutants diffusion.
- The activation energy for anatase-to-brookite transformation is smaller than that of brookite-to-rutile transformation. Therefore, the A→B transition can proceed at low temperatures (100-220 °C) and results in the appearance of brookite phase after hydrothermal synthesis.

- The increment in pore sizes and the reduction in surface area at more severe hydrothermal conditions can be attributed to the fact that smaller pores bear greater stress than the bigger ones; so, during hydrothermal synthesis smaller pores collapse sooner.

Major findings in Chapter 5 section 2:

- The key characteristics of photocatalysts including crystallinity, surface area, crystal size, OH population, morphology, and porosity could be tailored by varying the pH of hydrothermal solution or acid type.
- As general trends, crystallinity, crystal size, and e^--h^+ separation efficiency improved with the pH of aqueous solution while surface area, mesoporosity, surface OH density, and brookite content declined.
- XRD and HR-TEM confirmed that the yielded titania samples possess good crystallinity and mainly consist of anatase.
- Results of XPS analysis indicated that the population of hydroxyl groups on the surface of TiO_2 declines as the pH of preparation stage increases.
- Photoluminescence spectroscopy revealed that the enhancement in crystalinity has a huge impact on the separation of photo-induced charge carriers.
- Depending on the operating parameters, the highest photocatalytic activity was reached on different titania samples, meaning that the determining step varies with the characteristics of catalyst.
- Under the harshest operating condition (residence time=0.012 s, relative humidity=50%, concentration= 1000 ppb), the TiO_2 synthesized at pH of 4 using nitric acid achieved the highest MEK removal efficiency, 36.9%, which substantially surpassed that of P25, 14.5%.
- Degradation byproducts in the gas-phase were acetaldehyde, formaldehyde, acetone, and propionaldehyde, the last of which was newly identified in the current study.
- A tentative reaction pathway for MEK photodegradation was proposed, comprising H-abstraction, ß C-C scissions, surface reactions, radicals recombinations, and mineralization.

- Formation of anatase and brookite phases under mildly acidic and basic hydrothermal environments were discussed in the context of Ostwald step rule, arrangements of TiO_6 octahedra in different phases, and surface protonation.
- The ability of acids to form anatase phase followed the sequence of formic > sulfuric > acetic > nitric ~ chloric.
- Most of the developed photocatalysts reached HRIs below or close to one under actual operating conditions (i.e. low concentration), meaning we have a reliable and safe air purification system.

Major findings in Chapter 5 section 3:

- The formation mechanism of TSMS could be explained by Van der Waals forces. To lower the surface energy, nucleated particles form agglomerates and by forming spherical agglomerates the minimum surface-to-volume ratio and thus minimum surface free energy can be reached.
- The hierarchical structure of TMMS was inspected by SEM and TEM. The surface of TMMS is covered with numerous tiny square nanoplates. The spheres were composed of 1-D nanorods that are aligned radially from the center.
- Using sulfuric acid in the hydrothermal solution could slow down the hydrolysis and growth rates and, consequently, offered a better control over the morphology of TMMS.
- Porous hollow spheres (THS) could be fabricated by a single-step hydrothermal method in the presence of NH_4F.
- During THS synthesis, because of the higher solubility and surface energy of amorphous core compared to the outer surface, the dissolution (via F^- ions) and hollowing processes preferentially acted on the center of sphere.
- The high crystalline quality of THS and TNS originated mainly from in-situ dissolution–recrystallization in the presence of fluoride ions.
- TNS with high aspect ratio could be prepared via a solvothermal route at relatively low hydrothermal temperature. Instead of HF, TiF_4 was applied as the source of structure directing agent along with 2-propanol as the protective capping agent.
- TNS consisted of well-defined sheet-shaped structures with a rectangular outline with lateral dimensions of 50-70 nm and thickness of about 4.5-6.5 nm.

- For TNS, TEM analysis confirmed formation of truncated octahedra shape with [001] and [101] facets as the face and edge planes. The percentage of [001] facets of developed TNS was estimated to be around 83%.
- During preparation of titania nanotubes, the main experimental challenge was to retain the nanotubular structure during calcination since at high temperatures TNT tends to agglomerate and evolve into anatase nanoparticles.
- Sea urchin-like morphology was composed of numerous one dimensional rod-like (or spindle-like) structures along the radial direction starting from a common core.
- For TSU, initial reaction between TBOT and NaOH produced primary TiO_2 crystals which served as islands for growth of spindle-like structures after addition of EG.
- Despite the fact that crystal phase, crystallinity, and surface area were almost similar, different morphologies exhibited distinct photocatalytic activities.
- Except solid microspheres, all other morphologies exceeded commercial P25 in removal of MEK.
- TMMS good activity was ascribed to the hierarchical mesoporous structure composed of highly crystalline TiO_2 nanorods that facilitate the adsorption and desorption of reactants and products.
- THS high photoactivity was explained by: i. multireflections of UV light inside hollow spheres increased light harvesting ability; ii. porous shell and hollow structure provided efficient transport pathways for MEK molecules to the interior regions of THS.
- Titanium dioxide nanosheets by far were superior to all other morphologies in degradation of pollutants in air. TNS exhibited an excellent MEK removal efficiency, 71.3%, which was two times higher than the removal obtained by P25.
- The excellent activity of TNS was attributed to: i. existence of more reactive [001] facet; ii. higher density of uncoordinated titanium atoms on [001] facet which encouraged formation of terminal Ti-OH species; iii. surface fluorination which enhanced the charge carriers separation.

Major findings in Chapter 5 section 4:

- Surface area and amorphous content gradually declined with calcination temperature up to 400-500 °C, and then showed sudden drops for higher temperatures. Crystal size

showed small changes between 300-500 °C, and then experienced a drastic increase upon calcination at 600 and 700 °C.

- The first rutile crystals were formed after calcination at 600 °C. At 700 °C, the content of anatase TiO_2 was almost negligible and sample was 96% rutile. The complete anatase-to-rutile phase transformation was seen at 800 °C.
- Route I (hydrothermal treatment + calcination) could lead to titanium dioxides with better crystallinity and fewer surface defects with respect to Route II (direct calcination).
- Decrease in surface area of samples prepared via Route I after calcination was not as severe as that of samples of Route II, implying that the hydrothermal treatment improved the thermal stability of mesoporous framework.
- Increase in crystallinity during hydrothermal treatment would result in an elevation of the temperature for anatase-to-rutile transformation.
- Presence of a small amount of brookite contamination in the catalyst led to the formation of rutile phase at a lower temperature, suggesting that the anatase polymorph is more stable than the brookite phase during calcination.
- After hydrothermally-prepared sample calcined at 300 °C, the photocatalytic activity enhanced and reached its maximum among all samples calcined between 300 and 800 °C. This was attributed to the substantial increment in crystallinity without huge loss in the surface area or damage to the hierarchical structure.

Major findings in Chapter 5 section 5:

- The uncoated ACF showed the highest adsorption capacity for MEK, suggesting that the active surface area was diminished after titania coating.
- Combination of titanium dioxide and activated carbon filter exhibited better efficiency compared to TiO_2 coated on nickel foam as well as superior stability with respect to uncoated activated carbon filter.
- The steady-state MEK removal efficiency over P25/NFF, H-Base/NFF, P25/ACF and H-Base/ACF were 23.5, 36.3, 45.0, and 62.1% respectively.
- Thanks to ACF high adsorption affinity and capacity, ACF concentrated MEK molecules around (or continuously supplied VOC to) TiO_2 and enhanced the reaction rate.

- Photocatalytic degradation of MEK could effectively increase the breakthrough time of ACF. MEK adsorbed on ACF surface is continuously oxidized by TiO_2, giving rise to an in-situ regeneration of ACF.

6.2. Recommendations for further research

Based on the findings of this research, extensive literature review, and knowledge of the main shortcomings of current commercial indoor air purification units, in the following section, several possibilities for future work concerning the fabrication of new photocatalysts and assessment of the catalysts developed in this thesis for practical applications are put forward.

- Developing more advanced correlations between photocatalyst's properties and activity based on the experimental data presented in this study and in the literature by means of machine-learning based regression.
- Given the superior performance of titania hollow spheres and titania nanosheets, further investigation to optimize the key features of these promising morphologies for indoor air purification can be a very interesting field of research.
- Study the connections between other hydrothermal/solvothermal preparation variables (e.g. solvent characteristics) and the properties of yielded titania photocatalysts.
- This work was conducted in a small scale photoreactor for degradation of a single VOC (toluene or MEK). Evaluating the performance of photocatalysts in full scale and under more realistic operating conditions (mainly shorter residence time) is of great practical importance.
- In indoor environment a variety of VOCs exist, thus, the performance of photocatalysts need to be assessed towards a mixture of VOCs since the removal efficiency, degradation pathways, and generated by-products for toluene/MEK might be affected by the interference of other compounds.
- Photocatalytic air filter preparation cost and energy consumption associated with the UV-PCO system should be determined based on the operation protocols of air handling units of buildings. Subsequently, these values should be compared with those of conventional air cleaning technologies (e.g. adsorption) to estimate UV-PCO system competitiveness.
- More effective and reliable immobilization techniques must be established to coat the previously-prepared photocatalysts on various support materials.
- Long-term experiments of photocatalysts must be conducted in order to investigate the deactivation mechanism and magnitude.
- TiO_2 materials developed in this study might be applicable to other fields of catalysis such as water splitting, water treatment, hydrogen production, energy storage, and CO_2 reduction.

References

[1] T. Paul, D. Sree, H. Aglan, Effect of mechanically induced ventilation on the indoor air quality of building envelopes, Energy and Buildings, 42 (2010) 326-332.
[2] N.E. Klepeis, W.C. Nelson, W.R. Ott, J.P. Robinson, A.M. Tsang, P. Switzer, J.V. Behar, S.C. Hern, W.H. Engelmann, The National Human Activity Pattern Survey (NHAPS): a resource for assessing exposure to environmental pollutants, J Expo Anal Environ Epidemiol, 11 (2001) 231-252.
[3] L. Zhong, F. Haghighat, Photocatalytic air cleaners and materials technologies – Abilities and limitations, Building and Environment, 91 (2015) 191-203.
[4] S. Wang, H.M. Ang, M.O. Tade, Volatile organic compounds in indoor environment and photocatalytic oxidation: State of the art, Environment International, 33 (2007) 694-705.
[5] S.W. Verbruggen, TiO2 photocatalysis for the degradation of pollutants in gas phase: From morphological design to plasmonic enhancement, Journal of Photochemistry and Photobiology C: Photochemistry Reviews, 24 (2015) 64-82.
[6] EPA, https://www.epa.gov/indoor-air-quality-iaq/introduction-indoor-air-quality, in, 2018.
[7] T. Godish, Indoor Environmental Quality, CRC Press, 2016.
[8] G. Shaverdi, F. Haghighat, W. Ghaly, Development and systematic validation of an adsorption filter model, Building and Environment, 73 (2014) 64-74.
[9] A. Fujishima, X. Zhang, D.A. Tryk, TiO2 photocatalysis and related surface phenomena, Surface Science Reports, 63 (2008) 515-582.
[10] L. Zhong, F. Haghighat, P. Blondeau, J. Kozinski, Modeling and physical interpretation of photocatalytic oxidation efficiency in indoor air applications, Building and Environment, 45 (2010) 2689-2697.
[11] A. Aghighi, F. Haghighat, Using physical–chemical properties of reactants to estimate the performance of photocatalytic oxidation air cleaners, Building and Environment, 85 (2015) 114-122.
[12] J. Schneider, M. Matsuoka, M. Takeuchi, J. Zhang, Y. Horiuchi, M. Anpo, D.W. Bahnemann, Understanding TiO2 Photocatalysis: Mechanisms and Materials, Chemical Reviews, 114 (2014) 9919-9986.
[13] J. Mo, Y. Zhang, Q. Xu, Y. Zhu, J.J. Lamson, R. Zhao, Determination and risk assessment of by-products resulting from photocatalytic oxidation of toluene, Applied Catalysis B: Environmental, 89 (2009) 570-576.
[14] X. Li, J. Yu, M. Jaroniec, Hierarchical photocatalysts, Chemical Society Reviews, 45 (2016) 2603-2636.
[15] N.M. Kinsinger, A. Wong, D. Li, F. Villalobos, D. Kisailus, Nucleation and Crystal Growth of Nanocrystalline Anatase and Rutile Phase TiO2 from a Water-Soluble Precursor, Crystal Growth & Design, 10 (2010) 5254-5261.
[16] Y. Ma, X. Wang, Y. Jia, X. Chen, H. Han, C. Li, Titanium Dioxide-Based Nanomaterials for Photocatalytic Fuel Generations, Chemical Reviews, 114 (2014) 9987-10043.
[17] S.-D. Mo, W.Y. Ching, Electronic and optical properties of three phases of titanium dioxide: Rutile, anatase, and brookite, Physical Review B, 51 (1995) 13023-13032.
[18] A.T. Paxton, L. Thiên-Nga, Electronic structure of reduced titanium dioxide, Physical Review B, 57 (1998) 1579-1584.
[19] V. Puddu, H. Choi, D.D. Dionysiou, G.L. Puma, TiO2 photocatalyst for indoor air remediation: Influence of crystallinity, crystal phase, and UV radiation intensity on trichloroethylene degradation, Applied Catalysis B: Environmental, 94 (2010) 211-218.

[20] M. Hajaghazadeh, V. Vaiano, D. Sannino, H. Kakooei, R. Sotudeh-Gharebagh, P. Ciambelli, Heterogeneous photocatalytic oxidation of methyl ethyl ketone under UV-A light in an LED-fluidized bed reactor, Catalysis Today, 230 (2014) 79-84.
[21] S.T. Martin, H. Herrmann, W. Choi, M.R. Hoffmann, Time-resolved microwave conductivity. Part 1.-TiO2 photoreactivity and size quantization, Journal of the Chemical Society, Faraday Transactions, 90 (1994) 3315-3322.
[22] O. Tahiri Alaoui, A. Herissan, C. Le Quoc, M.e.M. Zekri, S. Sorgues, H. Remita, C. Colbeau-Justin, Elaboration, charge-carrier lifetimes and activity of Pd-TiO2 photocatalysts obtained by gamma radiolysis, Journal of Photochemistry and Photobiology A: Chemistry, 242 (2012) 34-43.
[23] F. Thevenet, O. Guaïtella, J.M. Herrmann, A. Rousseau, C. Guillard, Photocatalytic degradation of acetylene over various titanium dioxide-based photocatalysts, Applied Catalysis B: Environmental, 61 (2005) 58-68.
[24] J. Taranto, D. Frochot, P. Pichat, Photocatalytic Treatment of Air: Comparison of Various TiO2, Coating Methods, and Supports Using Methanol or n-Octane as Test Pollutant, Industrial & Engineering Chemistry Research, 48 (2009) 6229-6236.
[25] A. Alonso-Tellez, R. Masson, D. Robert, N. Keller, V. Keller, Comparison of Hombikat UV100 and P25 TiO2 performance in gas-phase photocatalytic oxidation reactions, Journal of Photochemistry and Photobiology A: Chemistry, 250 (2012) 58-65.
[26] Z. Zhang, C.-C. Wang, R. Zakaria, J.Y. Ying, Role of Particle Size in Nanocrystalline TiO2-Based Photocatalysts, The Journal of Physical Chemistry B, 102 (1998) 10871-10878.
[27] C.L. Bianchi, S. Gatto, C. Pirola, A. Naldoni, A. Di Michele, G. Cerrato, V. Crocellà, V. Capucci, Photocatalytic degradation of acetone, acetaldehyde and toluene in gas-phase: Comparison between nano and micro-sized TiO2, Applied Catalysis B: Environmental, 146 (2014) 123-130.
[28] A. Šuligoj, U.L. Štangar, A. Ristić, M. Mazaj, D. Verhovšek, N.N. Tušar, TiO2–SiO2 films from organic-free colloidal TiO2 anatase nanoparticles as photocatalyst for removal of volatile organic compounds from indoor air, Applied Catalysis B: Environmental, 184 (2016) 119-131.
[29] J. Araña, A.P. Alonso, J.M.D. Rodríguez, G. Colón, J.A. Navío, J.P. Peña, FTIR study of photocatalytic degradation of 2-propanol in gas phase with different TiO2 catalysts, Applied Catalysis B: Environmental, 89 (2009) 204-213.
[30] S.W. Verbruggen, K. Masschaele, E. Moortgat, T.E. Korany, B. Hauchecorne, J.A. Martens, S. Lenaerts, Factors driving the activity of commercial titanium dioxide powders towards gas phase photocatalytic oxidation of acetaldehyde, Catalysis Science & Technology, 2 (2012) 2311-2318.
[31] O. d'Hennezel, P. Pichat, D.F. Ollis, Benzene and toluene gas-phase photocatalytic degradation over H2O and HCL pretreated TiO2: by-products and mechanisms, Journal of Photochemistry and Photobiology A: Chemistry, 118 (1998) 197-204.
[32] M.R. Nimlos, E.J. Wolfrum, M.L. Brewer, J.A. Fennell, G. Bintner, Gas-Phase Heterogeneous Photocatalytic Oxidation of Ethanol: Pathways and Kinetic Modeling, Environmental Science & Technology, 30 (1996) 3102-3110.
[33] A.K. Boulamanti, C.J. Philippopoulos, Photocatalytic degradation of C5–C7 alkanes in the gas–phase, Atmospheric Environment, 43 (2009) 3168-3174.
[34] T.N. Obee, R.T. Brown, TiO2 Photocatalysis for Indoor Air Applications: Effects of Humidity and Trace Contaminant Levels on the Oxidation Rates of Formaldehyde, Toluene, and 1,3-Butadiene, Environmental Science & Technology, 29 (1995) 1223-1231.

[35] A.K. Boulamanti, C.A. Korologos, C.J. Philippopoulos, The rate of photocatalytic oxidation of aromatic volatile organic compounds in the gas-phase, Atmospheric Environment, 42 (2008) 7844-7850.
[36] G. Qijin, W. Qingming, Z. Bin, Adsorption and Photocatalytic Oxidation of Methanol–Benzene Binary Mixture in an Annular Fluidized Bed Photocatalytic Reactor, Industrial & Engineering Chemistry Research, 51 (2012) 15360-15373.
[37] R.M. Alberici, W.F. Jardim, Photocatalytic destruction of VOCs in the gas-phase using titanium dioxide, Applied Catalysis B: Environmental, 14 (1997) 55-68.
[38] K.-P. Yu, G.W.M. Lee, W.-M. Huang, C. Wu, S. Yang, The correlation between photocatalytic oxidation performance and chemical/physical properties of indoor volatile organic compounds, Atmospheric Environment, 40 (2006) 375-385.
[39] Q. Geng, Q. Guo, X. Yue, Adsorption and Photocatalytic Degradation Kinetics of Gaseous Cyclohexane in an Annular Fluidized Bed Photocatalytic Reactor, Industrial & Engineering Chemistry Research, 49 (2010) 4644-4652.
[40] L. Zhang, W.A. Anderson, S. Sawell, C. Moralejo, Mechanistic analysis on the influence of humidity on photocatalytic decomposition of gas-phase chlorobenzene, Chemosphere, 68 (2007) 546-553.
[41] D. Kibanova, M. Sleiman, J. Cervini-Silva, H. Destaillats, Adsorption and photocatalytic oxidation of formaldehyde on a clay-TiO2 composite, Journal of Hazardous Materials, 211–212 (2012) 233-239.
[42] X.-Y. Yang, A. Leonard, A. Lemaire, G. Tian, B.-L. Su, Self-formation phenomenon to hierarchically structured porous materials: design, synthesis, formation mechanism and applications, Chemical Communications, 47 (2011) 2763-2786.
[43] W. Schwieger, A.G. Machoke, T. Weissenberger, A. Inayat, T. Selvam, M. Klumpp, A. Inayat, Hierarchy concepts: classification and preparation strategies for zeolite containing materials with hierarchical porosity, Chemical Society Reviews, 45 (2016) 3353-3376.
[44] P. Yang, T. Deng, D. Zhao, P. Feng, D. Pine, B.F. Chmelka, G.M. Whitesides, G.D. Stucky, Hierarchically Ordered Oxides, Science, 282 (1998) 2244-2246.
[45] G.J.d.A.A. Soler-Illia, C. Sanchez, B. Lebeau, J. Patarin, Chemical Strategies To Design Textured Materials: from Microporous and Mesoporous Oxides to Nanonetworks and Hierarchical Structures, Chemical Reviews, 102 (2002) 4093-4138.
[46] X.-Y. Yang, Y. Li, A. Lemaire, J.-G. Yu, B.-L. Su, Hierarchically structured functional materials: Synthesis strategies for multimodal porous networks, in: Pure and Applied Chemistry, 2009, pp. 2265.
[47] M.-Q. Zhao, Q. Zhang, J.-Q. Huang, F. Wei, Hierarchical Nanocomposites Derived from Nanocarbons and Layered Double Hydroxides - Properties, Synthesis, and Applications, Advanced Functional Materials, 22 (2012) 675-694.
[48] D.R. Rolison, Catalytic Nanoarchitectures--the Importance of Nothing and the Unimportance of Periodicity, Science, 299 (2003) 1698-1701.
[49] J. Yu, H. Yu, H. Guo, M. Li, S. Mann, Spontaneous Formation of a Tungsten Trioxide Sphere-in-Shell Superstructure by Chemically Induced Self-Transformation, Small, 4 (2008) 87-91.
[50] H. Li, Z. Bian, J. Zhu, D. Zhang, G. Li, Y. Huo, H. Li, Y. Lu, Mesoporous Titania Spheres with Tunable Chamber Stucture and Enhanced Photocatalytic Activity, Journal of the American Chemical Society, 129 (2007) 8406-8407.

[51] X.W. Lou, Y. Wang, C. Yuan, J.Y. Lee, L.A. Archer, Template-Free Synthesis of SnO2 Hollow Nanostructures with High Lithium Storage Capacity, Advanced Materials, 18 (2006) 2325-2329.
[52] S.C. Yan, S.X. Ouyang, J. Gao, M. Yang, J.Y. Feng, X.X. Fan, L.J. Wan, Z.S. Li, J.H. Ye, Y. Zhou, Z.G. Zou, A Room-Temperature Reactive-Template Route to Mesoporous ZnGa2O4 with Improved Photocatalytic Activity in Reduction of CO2, Angewandte Chemie International Edition, 49 (2010) 6400-6404.
[53] Q. Zhang, W. Wang, J. Goebl, Y. Yin, Self-templated synthesis of hollow nanostructures, Nano Today, 4 (2009) 494-507.
[54] Q. Xiang, B. Cheng, J. Yu, Hierarchical porous CdS nanosheet-assembled flowers with enhanced visible-light photocatalytic H2-production performance, Applied Catalysis B: Environmental, 138 (2013) 299-303.
[55] H. Cheng, B. Huang, X. Qin, X. Zhang, Y. Dai, A controlled anion exchange strategy to synthesize Bi2S3 nanocrystals/BiOCl hybrid architectures with efficient visible light photoactivity, Chemical Communications, 48 (2012) 97-99.
[56] H. Cheng, B. Huang, P. Wang, Z. Wang, Z. Lou, J. Wang, X. Qin, X. Zhang, Y. Dai, In situ ion exchange synthesis of the novel Ag/AgBr/BiOBr hybrid with highly efficient decontamination of pollutants, Chemical Communications, 47 (2011) 7054-7056.
[57] Q.D. Truong, T.S. Le, H.T. Hoa, Fluoride-free self-templated synthesis of hollow TiO2 nanostructures for hydrogen evolution, CrystEngComm, 14 (2012) 4274-4278.
[58] J. Yu, G. Wang, B. Cheng, M. Zhou, Effects of hydrothermal temperature and time on the photocatalytic activity and microstructures of bimodal mesoporous TiO 2 powders, Applied Catalysis B: Environmental, 69 (2007) 171-180.
[59] Y. Shi, Y. Chen, G. Tian, H. Fu, K. Pan, J. Zhou, H. Yan, One-pot controlled synthesis of sea-urchin shaped Bi2S3/CdS hierarchical heterostructures with excellent visible light photocatalytic activity, Dalton Transactions, 43 (2014) 12396-12404.
[60] D. Zhang, G. Li, F. Wang, J.C. Yu, Green synthesis of a self-assembled rutile mesocrystalline photocatalyst, CrystEngComm, 12 (2010) 1759-1763.
[61] Y. Jiao, Y. Liu, F. Qu, X. Wu, Dendritic [small alpha]-Fe2O3 hierarchical architectures for visible light driven photocatalysts, CrystEngComm, 16 (2014) 575-580.
[62] J.G. Yu, H. Guo, S.A. Davis, S. Mann, Fabrication of Hollow Inorganic Microspheres by Chemically Induced Self-Transformation, Advanced Functional Materials, 16 (2006) 2035-2041.
[63] S. Liu, J. Yu, M. Jaroniec, Tunable Photocatalytic Selectivity of Hollow TiO2 Microspheres Composed of Anatase Polyhedra with Exposed {001} Facets, Journal of the American Chemical Society, 132 (2010) 11914-11916.
[64] L. Zhang, J.C. Yu, A sonochemical approach to hierarchical porous titania spheres with enhanced photocatalytic activity, Chemical Communications, (2003) 2078-2079.
[65] J. Yu, L. Zhang, B. Cheng, Y. Su, Hydrothermal Preparation and Photocatalytic Activity of Hierarchically Sponge-like Macro-/Mesoporous Titania, The Journal of Physical Chemistry C, 111 (2007) 10582-10589.
[66] Q. Xiang, J. Yu, Photocatalytic Activity of Hierarchical Flower-Like TiO2 Superstructures with Dominant {001} Facets, Chinese Journal of Catalysis, 32 (2011) 525-531.
[67] X. Wang, J.C. Yu, C. Ho, Y. Hou, X. Fu, Photocatalytic Activity of a Hierarchically Macro/Mesoporous Titania, Langmuir, 21 (2005) 2552-2559.

[68] X. Chen, X. Wang, X. Fu, Hierarchical macro/mesoporous TiO2/SiO2 and TiO2/ZrO2 nanocomposites for environmental photocatalysis, Energy & Environmental Science, 2 (2009) 872-877.
[69] K. Byrappa, M. Yoshimura, Handbook of hydrothermal technology, William Andrew, 2012.
[70] K. Yanagisawa, J. Ovenstone, Crystallization of anatase from amorphous titania using the hydrothermal technique: effects of starting material and temperature, The Journal of Physical Chemistry B, 103 (1999) 7781-7787.
[71] Y.V. Kolen'ko, A.A. Burukhin, B.R. Churagulov, N.N. Oleynikov, Synthesis of nanocrystalline TiO 2 powders from aqueous TiOSO 4 solutions under hydrothermal conditions, Materials Letters, 57 (2003) 1124-1129.
[72] S. Kim, M. Kim, S.-H. Hwang, S.K. Lim, Effects of hydrothermal temperature and acid concentration on the transition from titanate to titania, Journal of Industrial and Engineering Chemistry, 18 (2012) 1141-1148.
[73] H. Cheng, J. Ma, Z. Zhao, L. Qi, Hydrothermal Preparation of Uniform Nanosize Rutile and Anatase Particles, Chemistry of Materials, 7 (1995) 663-671.
[74] J. Yu, H. Yu, B. Cheng, X. Zhao, Q. Zhang, Preparation and photocatalytic activity of mesoporous anatase TiO 2 nanofibers by a hydrothermal method, Journal of Photochemistry and Photobiology A: Chemistry, 182 (2006) 121-127.
[75] M. Zhou, J. Xu, H. Yu, S. Liu, Low-temperature hydrothermal synthesis of highly photoactive mesoporous spherical TiO 2 nanocrystalline, Journal of Physics and Chemistry of Solids, 71 (2010) 507-510.
[76] C.-C. Wang, J.Y. Ying, Sol−Gel Synthesis and Hydrothermal Processing of Anatase and Rutile Titania Nanocrystals, Chemistry of Materials, 11 (1999) 3113-3120.
[77] S. Lei, W. Duan, Highly active mixed-phase TiO 2 photocatalysts fabricated at low temperatureand the correlation between phase compositionand photocatalytic activity, Journal of Environmental Sciences, 20 (2008) 1263-1267.
[78] K. Chen, L. Zhu, K. Yang, Tricrystalline TiO2 with enhanced photocatalytic activity and durability for removing volatile organic compounds from indoor air, Journal of Environmental Sciences, 32 (2015) 189-195.
[79] J.H. Kim, B.H. Noh, G.-D. Lee, S.-S. Hong, Hydrothermal synthesis of titanium dioxide using acidic peptizing agents and their photocatalytic activity, Korean Journal of Chemical Engineering, 22 (2005) 370-374.
[80] S. Liu, C. Liu, W. Wang, B. Cheng, J. Yu, Unique photocatalytic oxidation reactivity and selectivity of TiO2-graphene nanocomposites, Nanoscale, 4 (2012) 3193-3200.
[81] M.S. Akple, J. Low, Z. Qin, S. Wageh, A.A. Al-Ghamdi, J. Yu, S. Liu, Nitrogen-doped TiO2 microsheets with enhanced visible light photocatalytic activity for CO2 reduction, Chinese Journal of Catalysis, 36 (2015) 2127-2134.
[82] K. Chen, L. Zhu, K. Yang, Acid-assisted hydrothermal synthesis of nanocrystalline TiO2 from titanate nanotubes: Influence of acids on the photodegradation of gaseous toluene, Journal of Environmental Sciences, 27 (2015) 232-240.
[83] N.H. Nguyen, H. Bai, Photocatalytic removal of NO and NO2 using titania nanotubes synthesized by hydrothermal method, Journal of Environmental Sciences, 26 (2014) 1180-1187.
[84] J. Mo, Y. Zhang, Q. Xu, J.J. Lamson, R. Zhao, Photocatalytic purification of volatile organic compounds in indoor air: A literature review, Atmospheric Environment, 43 (2009) 2229-2246.

[85] J. Chen, H. Luo, H. Shi, G. Li, T. An, Anatase TiO2 nanoparticles–carbon nanotubes composite: Optimization synthesis and the relationship of photocatalytic degradation activity of acyclovir in water, Applied Catalysis A: General, 485 (2014) 188-195.
[86] H. Shi, J. Chen, G. Li, X. Nie, H. Zhao, P.K. Wong, T. An, Synthesis and characterization of novel plasmonic Ag/AgX-CNTs (X = Cl, Br, I) nanocomposite photocatalysts and synergetic degradation of organic pollutant under visible light, ACS Applied Materials and Interfaces, 5 (2013) 6959-6967.
[87] D. Eder, Carbon nanotube-inorganic hybrids, Chemical Reviews, 110 (2010) 1348-1385.
[88] Y. Zhang, Z.-R. Tang, X. Fu, Y.-J. Xu, TiO2−Graphene Nanocomposites for Gas-Phase Photocatalytic Degradation of Volatile Aromatic Pollutant: Is TiO2−Graphene Truly Different from Other TiO2−Carbon Composite Materials?, ACS Nano, 4 (2010) 7303-7314.
[89] M. Jafarikojour, M. Sohrabi, S.J. Royaee, A. Hassanvand, Evaluation and Optimization of a Novel Immobilized Photoreactor for the Degradation of Gaseous Toluene, CLEAN – Soil, Air, Water, 43 (2015) 662-670.
[90] R.A.R. Monteiro, A.M.T. Silva, J.R.M. Ângelo, G.V. Silva, A.M. Mendes, R.A.R. Boaventura, V.J.P. Vilar, Photocatalytic oxidation of gaseous perchloroethylene over TiO2 based paint, Journal of Photochemistry and Photobiology A: Chemistry, 311 (2015) 41-52.
[91] N. Quici, M.L. Vera, H. Choi, G.L. Puma, D.D. Dionysiou, M.I. Litter, H. Destaillats, Effect of key parameters on the photocatalytic oxidation of toluene at low concentrations in air under 254 + 185 nm UV irradiation, Applied Catalysis B: Environmental, 95 (2010) 312-319.
[92] J. Jeong, K. Sekiguchi, W. Lee, K. Sakamoto, Photodegradation of gaseous volatile organic compounds (VOCs) using TiO2 photoirradiated by an ozone-producing UV lamp: decomposition characteristics, identification of by-products and water-soluble organic intermediates, Journal of Photochemistry and Photobiology A: Chemistry, 169 (2005) 279-287.
[93] J. Jeong, K. Sekiguchi, K. Sakamoto, Photochemical and photocatalytic degradation of gaseous toluene using short-wavelength UV irradiation with TiO2 catalyst: comparison of three UV sources, Chemosphere, 57 (2004) 663-671.
[94] L. Cao, F.-J. Spiess, A. Huang, S.L. Suib, T.N. Obee, S.O. Hay, J.D. Freihaut, Heterogeneous Photocatalytic Oxidation of 1-Butene on SnO2 and TiO2 Films, The Journal of Physical Chemistry B, 103 (1999) 2912-2917.
[95] J. Mo, Y. Zhang, Q. Xu, R. Yang, Effect of TiO2/adsorbent hybrid photocatalysts for toluene decomposition in gas phase, Journal of Hazardous Materials, 168 (2009) 276-281.
[96] A. Bouzaza, C. Vallet, A. Laplanche, Photocatalytic degradation of some VOCs in the gas phase using an annular flow reactor: Determination of the contribution of mass transfer and chemical reaction steps in the photodegradation process, Journal of Photochemistry and Photobiology A: Chemistry, 177 (2006) 212-217.
[97] P.-A. Deveau, F. Arsac, P.-X. Thivel, C. Ferronato, F. Delpech, J.-M. Chovelon, P. Kaluzny, C. Monnet, Different methods in TiO2 photodegradation mechanism studies: Gaseous and TiO2-adsorbed phases, Journal of Hazardous Materials, 144 (2007) 692-697.
[98] F.V.S. Lopes, R.A.R. Monteiro, A.M.T. Silva, G.V. Silva, J.L. Faria, A.M. Mendes, V.J.P. Vilar, R.A.R. Boaventura, Insights into UV-TiO2 photocatalytic degradation of PCE for air decontamination systems, Chemical Engineering Journal, 204–206 (2012) 244-257.
[99] R.A.R. Monteiro, S.M. Miranda, C. Rodrigues-Silva, J.L. Faria, A.M.T. Silva, R.A.R. Boaventura, V.J.P. Vilar, Gas phase oxidation of n-decane and PCE by photocatalysis using an annular photoreactor packed with a monolithic catalytic bed coated with P25 and PC500, Applied Catalysis B: Environmental, 165 (2015) 306-315.

[100] P. Pichat, Some views about indoor air photocatalytic treatment using TiO2: Conceptualization of humidity effects, active oxygen species, problem of C1–C3 carbonyl pollutants, Applied Catalysis B: Environmental, 99 (2010) 428-434.
[101] H. Einaga, S. Futamura, T. Ibusuki, Heterogeneous photocatalytic oxidation of benzene, toluene, cyclohexene and cyclohexane in humidified air: comparison of decomposition behavior on photoirradiated TiO2 catalyst, Applied Catalysis B: Environmental, 38 (2002) 215-225.
[102] N. Bouazza, M.A. Lillo-Ródenas, A. Linares-Solano, Photocatalytic activity of TiO2-based materials for the oxidation of propene and benzene at low concentration in presence of humidity, Applied Catalysis B: Environmental, 84 (2008) 691-698.
[103] G. Vincent, P.M. Marquaire, O. Zahraa, Photocatalytic degradation of gaseous 1-propanol using an annular reactor: Kinetic modelling and pathways, Journal of Hazardous Materials, 161 (2009) 1173-1181.
[104] T. Guo, Z. Bai, C. Wu, T. Zhu, Influence of relative humidity on the photocatalytic oxidation (PCO) of toluene by TiO2 loaded on activated carbon fibers: PCO rate and intermediates accumulation, Applied Catalysis B: Environmental, 79 (2008) 171-178.
[105] T. Tytgat, B. Hauchecorne, A.M. Abakumov, M. Smits, S.W. Verbruggen, S. Lenaerts, Photocatalytic process optimisation for ethylene oxidation, Chemical Engineering Journal, 209 (2012) 494-500.
[106] W. Wang, Y. Ku, Photocatalytic degradation of gaseous benzene in air streams by using an optical fiber photoreactor, Journal of Photochemistry and Photobiology A: Chemistry, 159 (2003) 47-59.
[107] M. Sleiman, P. Conchon, C. Ferronato, J.-M. Chovelon, Photocatalytic oxidation of toluene at indoor air levels (ppbv): Towards a better assessment of conversion, reaction intermediates and mineralization, Applied Catalysis B: Environmental, 86 (2009) 159-165.
[108] E. Piera, J.A. Ayllón, X. Doménech, J. Peral, TiO2 deactivation during gas-phase photocatalytic oxidation of ethanol, Catalysis Today, 76 (2002) 259-270.
[109] M.-G. Jeong, E.J. Park, H.O. Seo, K.-D. Kim, Y.D. Kim, D.C. Lim, Humidity effect on photocatalytic activity of TiO2 and regeneration of deactivated photocatalysts, Applied Surface Science, 271 (2013) 164-170.
[110] J. Mo, Y. Zhang, Q. Xu, Effect of water vapor on the by-products and decomposition rate of ppb-level toluene by photocatalytic oxidation, Applied Catalysis B: Environmental, 132–133 (2013) 212-218.
[111] T.N. Obee, Photooxidation of Sub-Parts-per-Million Toluene and Formaldehyde Levels on Titania Using a Glass-Plate Reactor, Environmental Science & Technology, 30 (1996) 3578-3584.
[112] H. Einaga, T. Ibusuki, S. Futamura, Photocatalytic Oxidation of Benzene in Air, Journal of Solar Energy Engineering, 126 (2004) 789-793.
[113] T.N. Obee, S.O. Hay, Effects of moisture and temperature on the photooxidation of ethylene on titania, Environmental science & technology, 31 (1997) 2034-2038.
[114] D.H. Chen, X. Ye, K. Li, Oxidation of PCE with a UV LED Photocatalytic Reactor, Chemical Engineering & Technology, 28 (2005) 95-97.
[115] J.-M. Herrmann, Heterogeneous photocatalysis: fundamentals and applications to the removal of various types of aqueous pollutants, Catalysis Today, 53 (1999) 115-129.
[116] D. Kibanova, J. Cervini-Silva, H. Destaillats, Efficiency of clay - TiO 2 nanocomposites on the photocatalytic elimination of a model hydrophobic air pollutant, Environmental Science and Technology, 43 (2009) 1500-1506.

[117] Z. Pengyi, L. Fuyan, Y. Gang, C. Qing, Z. Wanpeng, A comparative study on decomposition of gaseous toluene by O3/UV, TiO2/UV and O3/TiO2/UV, Journal of Photochemistry and Photobiology A: Chemistry, 156 (2003) 189-194.
[118] S. Toby, L.J. Van de Burgt, F.S. Toby, Kinetics and chemiluminescence of ozone-aromatic reactions in the gas phase, The Journal of Physical Chemistry, 89 (1985) 1982-1986.
[119] D.S. Muggli, J.T. McCue, J.L. Falconer, Mechanism of the Photocatalytic Oxidation of Ethanol on TiO2, Journal of Catalysis, 173 (1998) 470-483.
[120] F. Benoit-Marquié, U. Wilkenhöner, V. Simon, A.M. Braun, E. Oliveros, M.-T. Maurette, VOC photodegradation at the gas–solid interface of a TiO2 photocatalyst: Part I: 1-butanol and 1-butylamine, Journal of Photochemistry and Photobiology A: Chemistry, 132 (2000) 225-232.
[121] J. Peral, D.F. Ollis, Heterogeneous photocatalytic oxidation of gas-phase organics for air purification: Acetone, 1-butanol, butyraldehyde, formaldehyde, and m-xylene oxidation, Journal of Catalysis, 136 (1992) 554-565.
[122] N.R. Blake, G.L. Griffin, Selectivity control during the photoassisted oxidation of 1-butanol on titanium dioxide, The Journal of Physical Chemistry, 92 (1988) 5697-5701.
[123] S.A. Larson, J.L. Falconer, Initial reaction steps in photocatalytic oxidation of aromatics, Catalysis Letters, 44 (1997) 57-65.
[124] T.J. Frankcombe, S.C. Smith, OH-Initiated Oxidation of Toluene. 1. Quantum Chemistry Investigation of the Reaction Path, The Journal of Physical Chemistry A, 111 (2007) 3686-3690.
[125] C.H. Ao, S.C. Lee, J.Z. Yu, J.H. Xu, Photodegradation of formaldehyde by photocatalyst TiO2: effects on the presences of NO, SO2 and VOCs, Applied Catalysis B: Environmental, 54 (2004) 41-50.
[126] X. Ye, D. Chen, J. Gossage, K. Li, Photocatalytic oxidation of aldehydes: Byproduct identification and reaction pathway, Journal of Photochemistry and Photobiology A: Chemistry, 183 (2006) 35-40.
[127] B. Hauchecorne, D. Terrens, S. Verbruggen, J.A. Martens, H. Van Langenhove, K. Demeestere, S. Lenaerts, Elucidating the photocatalytic degradation pathway of acetaldehyde: An FTIR in situ study under atmospheric conditions, Applied Catalysis B: Environmental, 106 (2011) 630-638.
[128] O. Debono, F. Thévenet, P. Gravejat, V. Héquet, C. Raillard, L. Le Coq, N. Locoge, Gas phase photocatalytic oxidation of decane at ppb levels: Removal kinetics, reaction intermediates and carbon mass balance, Journal of Photochemistry and Photobiology A: Chemistry, 258 (2013) 17-29.
[129] W. Choi, J.Y. Ko, H. Park, J.S. Chung, Investigation on TiO2-coated optical fibers for gas-phase photocatalytic oxidation of acetone, Applied Catalysis B: Environmental, 31 (2001) 209-220.
[130] G. Vincent, P.M. Marquaire, O. Zahraa, Abatement of volatile organic compounds using an annular photocatalytic reactor: Study of gaseous acetone, Journal of Photochemistry and Photobiology A: Chemistry, 197 (2008) 177-189.
[131] C. Raillard, V. Héquet, P. Le Cloirec, J. Legrand, Photocatalytic oxidation of methyl ethyl ketone over sol-gel and commercial TiO2 for the improvement of indoor air, Water Science and Technology, 53 (2006) 107-115.
[132] A.L. Attwood, J.L. Edwards, C.C. Rowlands, D.M. Murphy, Identification of a Surface Alkylperoxy Radical in the Photocatalytic Oxidation of Acetone/O2 over TiO2, The Journal of Physical Chemistry A, 107 (2003) 1779-1782.

[133] NIOSH, .S. National Institute for Occupational Safety and Health (NIOSH), http://www.cdc.gov/niosh/, (2018).
[134] H. Zhang, J.F. Banfield, Understanding Polymorphic Phase Transformation Behavior during Growth of Nanocrystalline Aggregates: Insights from TiO2, The Journal of Physical Chemistry B, 104 (2000) 3481-3487.
[135] A. Di Paola, M. Bellardita, L. Palmisano, Z. Barbieriková, V. Brezová, Influence of crystallinity and OH surface density on the photocatalytic activity of TiO2 powders, Journal of Photochemistry and Photobiology A: Chemistry, 273 (2014) 59-67.
[136] K.-i. Ishibashi, A. Fujishima, T. Watanabe, K. Hashimoto, Detection of active oxidative species in TiO2 photocatalysis using the fluorescence technique, Electrochemistry Communications, 2 (2000) 207-210.
[137] E. Jimenez-Relinque, M. Castellote, Quantification of hydroxyl radicals on cementitious materials by fluorescence spectrophotometry as a method to assess the photocatalytic activity, Cement and Concrete Research, 74 (2015) 108-115.
[138] A.H. Mamaghani, F. Haghighat, C.-S. Lee, Photocatalytic oxidation technology for indoor environment air purification: The state-of-the-art, Applied Catalysis B: Environmental, 203 (2017) 247-269.
[139] R. Portela, I. Jansson, S. Suárez, M. Villarroel, B. Sánchez, P. Avila, Natural silicate-TiO2 hybrids for photocatalytic oxidation of formaldehyde in gas phase, Chemical Engineering Journal, 310 (2017) 560-570.
[140] A. Alonso-Tellez, R. Masson, D. Robert, N. Keller, V. Keller, Comparison of Hombikat UV100 and P25 TiO2 performance in gas-phase photocatalytic oxidation reactions, Journal of Photochemistry and Photobiology A: Chemistry, 250 (2012) 58-65.
[141] A. Šuligoj, U.L. Štangar, A. Ristić, M. Mazaj, D. Verhovšek, N.N. Tušar, TiO2-SiO2 films from organic-free colloidal TiO2 anatase nanoparticles as photocatalyst for removal of volatile organic compounds from indoor air, Applied Catalysis B: Environmental, 184 (2016) 119-131.
[142] F. Haghighat, C.-S. Lee, B. Pant, G. Bolourani, N. Lakdawala, A. Bastani, Evaluation of various activated carbons for air cleaning – Towards design of immune and sustainable buildings, Atmospheric Environment, 42 (2008) 8176-8184.
[143] M.R. Nimlos, E.J. Wolfrum, M.L. Brewer, J.A. Fennell, G. Bintner, Gas-phase heterogeneous photocatalytic oxidation of ethanol: Pathways and kinetic modeling, Environmental Science and Technology, 30 (1996) 3102-3110.
[144] J. Araña, J.M. Doña-Rodríguez, O. González-Díaz, E. Tello Rendón, J.A. Herrera Melián, G. Colón, J.A. Navío, J. Pérez Peña, Gas-phase ethanol photocatalytic degradation study with TiO2 doped with Fe, Pd and Cu, Journal of Molecular Catalysis A: Chemical, 215 (2004) 153-160.
[145] S.W. Verbruggen, K. Masschaele, E. Moortgat, T.E. Korany, B. Hauchecorne, J.A. Martens, S. Lenaerts, Factors driving the activity of commercial titanium dioxide powders towards gas phase photocatalytic oxidation of acetaldehyde, Catalysis Science and Technology, 2 (2012) 2311-2318.
[146] M.F. Atitar, H. Belhadj, R. Dillert, D.W. Bahnemann, The relevance of ATR-FTIR spectroscopy in semiconductor photocatalysis, in: Emerging Pollutants in the Environment-Current and Further Implications, InTech, 2015.
[147] H. Lin, J. Long, Q. Gu, W. Zhang, R. Ruan, Z. Li, X. Wang, In situ IR study of surface hydroxyl species of dehydrated TiO2: towards understanding pivotal surface processes of TiO2 photocatalytic oxidation of toluene, Physical Chemistry Chemical Physics, 14 (2012) 9468-9474.

[148] M. Nagao, Y. Suda, Adsorption of benzene, toluene, and chlorobenzene on titanium dioxide, Langmuir, 5 (1989) 42-47.
[149] C. Deiana, E. Fois, S. Coluccia, G. Martra, Surface Structure of TiO2 P25 Nanoparticles: Infrared Study of Hydroxy Groups on Coordinative Defect Sites, The Journal of Physical Chemistry C, 114 (2010) 21531-21538.
[150] V. Augugliaro, S. Coluccia, V. Loddo, L. Marchese, G. Martra, L. Palmisano, M. Schiavello, Photocatalytic oxidation of gaseous toluene on anatase TiO2 catalyst: mechanistic aspects and FT-IR investigation, Applied Catalysis B: Environmental, 20 (1999) 15-27.
[151] J. Soria, J. Sanz, I. Sobrados, J.M. Coronado, A.J. Maira, M.D. Hernández-Alonso, F. Fresno, FTIR and NMR Study of the Adsorbed Water on Nanocrystalline Anatase, The Journal of Physical Chemistry C, 111 (2007) 10590-10596.
[152] H. Einaga, S. Futamura, T. Ibusuki, Photocatalytic decomposition of benzene over TiO2 in a humidified airstream, Physical Chemistry Chemical Physics, 1 (1999) 4903-4908.
[153] M.M. Ameen, G.B. Raupp, Reversible catalyst deactivation in the photocatalytic oxidation of diluteo-xylene in air, Journal of Catalysis, 184 (1999) 112-122.
[154] M. Minella, M.G. Faga, V. Maurino, C. Minero, E. Pelizzetti, S. Coluccia, G. Martra, Effect of fluorination on the surface properties of titania P25 powder: An FTIR study, Langmuir, 26 (2010) 2521-2527.
[155] L. Zhong, C.-S. Lee, F. Haghighat, Adsorption performance of titanium dioxide (TiO 2) coated air filters for volatile organic compounds, Journal of hazardous materials, 243 (2012) 340-349.
[156] K. Demeestere, J. Dewulf, H. Van Langenhove, B. Sercu, Gas-solid adsorption of selected volatile organic compounds on titanium dioxide Degussa P25, Chemical Engineering Science, 58 (2003) 2255-2267.
[157] A. Fujishima, T.N. Rao, D.A. Tryk, Titanium dioxide photocatalysis, Journal of Photochemistry and Photobiology C: Photochemistry Reviews, 1 (2000) 1-21.
[158] C. Hägglund, B. Kasemo, L. Österlund, In Situ Reactivity and FTIR Study of the Wet and Dry Photooxidation of Propane on Anatase TiO2, The Journal of Physical Chemistry B, 109 (2005) 10886-10895.
[159] A.L. Goodman, E.T. Bernard, V.H. Grassian, Spectroscopic Study of Nitric Acid and Water Adsorption on Oxide Particles: Enhanced Nitric Acid Uptake Kinetics in the Presence of Adsorbed Water, The Journal of Physical Chemistry A, 105 (2001) 6443-6457.
[160] A. Maudhuit, C. Raillard, V. Héquet, L. Le Coq, J. Sablayrolles, L. Molins, Adsorption phenomena in photocatalytic reactions: The case of toluene, acetone and heptane, Chemical Engineering Journal, 170 (2011) 464-470.
[161] J.N. Israelachvili, Intermolecular and Surface Forces, Elsevier Science, 2015.
[162] Q. Geng, Q. Guo, X. Yue, Adsorption and photocatalytic degradation kinetics of gaseous cyclohexane in an annular fluidized bed photocatalytic reactor, Industrial and Engineering Chemistry Research, 49 (2010) 4644-4652.
[163] T. Malaspina, K. Coutinho, S. Canuto, Ab initio calculation of hydrogen bonds in liquids: A sequential Monte Carlo quantum mechanics study of pyridine in water, Journal of Chemical Physics, 117 (2002) 1692-1699.
[164] S.C. Ringwald, J.E. Pemberton, Adsorption Interactions of Aromatics and Heteroaromatics with Hydrated and Dehydrated Silica Surfaces by Raman and FTIR Spectroscopies, Environmental Science & Technology, 34 (2000) 259-265.

[165] P.-A. Deveau, F. Arsac, P.-X. Thivel, C. Ferronato, F. Delpech, J.-M. Chovelon, P. Kaluzny, C. Monnet, Different methods in TiO 2 photodegradation mechanism studies: Gaseous and TiO 2-adsorbed phases, Journal of hazardous materials, 144 (2007) 692-697.
[166] K. Machowski, P. Kuśtrowski, B. Dudek, M. Michalik, Elimination of ketone vapors by adsorption on spherical MCM-41 and MCM-48 silicas decorated with thermally activated poly(furfuryl alcohol), Materials Chemistry and Physics, 165 (2015) 253-260.
[167] M.D. Hernández-Alonso, I. Tejedor-Tejedor, J.M. Coronado, M.A. Anderson, Operando FTIR study of the photocatalytic oxidation of methylcyclohexane and toluene in air over TiO2–ZrO2 thin films: Influence of the aromaticity of the target molecule on deactivation, Applied Catalysis B: Environmental, 101 (2011) 283-293.
[168] J. Ryczkowski, IR spectroscopy in catalysis, Catalysis Today, 68 (2001) 263-381.
[169] F. Shiraishi, T. Ishimatsu, Toluene removal from indoor air using a miniaturized photocatalytic air purifier including a preceding adsorption/desorption unit, Chemical Engineering Science, 64 (2009) 2466-2472.
[170] A.T. Hodgson, H. Destaillats, D.P. Sullivan, W.J. Fisk, Performance of ultraviolet photocatalytic oxidation for indoor air cleaning applications, Indoor Air, 17 (2007) 305-316.
[171] J.M. Coronado, M.E. Zorn, I. Tejedor-Tejedor, M.A. Anderson, Photocatalytic oxidation of ketones in the gas phase over TiO2 thin films: a kinetic study on the influence of water vapor, Applied Catalysis B: Environmental, 43 (2003) 329-344.
[172] R.M. Alberici, W.F. Jardim, Photocatalytic destruction of VOCS in the gas-phase using titanium dioxide, Applied Catalysis B: Environmental, 14 (1997) 55-68.
[173] J. Kirchnerova, M.L. Herrera Cohen, C. Guy, D. Klvana, Photocatalytic oxidation of n-butanol under fluorescent visible light lamp over commercial TiO2 (Hombicat UV100 and Degussa P25), Applied Catalysis A: General, 282 (2005) 321-332.
[174] V.S. Lusvardi, M.A. Barteau, W.E. Farneth, The Effects of Bulk Titania Crystal Structure on the Adsorption and Reaction of Aliphatic Alcohols, Journal of Catalysis, 153 (1995) 41-53.
[175] N. Quici, M.L. Vera, H. Choi, G.L. Puma, D.D. Dionysiou, M.I. Litter, H. Destaillats, Effect of key parameters on the photocatalytic oxidation of toluene at low concentrations in air under 254+185nm UV irradiation, Applied Catalysis B: Environmental, 95 (2010) 312-319.
[176] A.H. Mamaghani, F. Haghighat, C.-S. Lee, Gas phase adsorption of volatile organic compounds onto titanium dioxide photocatalysts, Chemical Engineering Journal, 337 (2018) 60-73.
[177] J.N. Israelachvili, Intermolecular and surface forces, Academic press, 2011.
[178] J. Mo, Y. Zhang, Q. Xu, Effect of water vapor on the by-products and decomposition rate of ppb-level toluene by photocatalytic oxidation, Applied Catalysis B: Environmental, 132-133 (2013) 212-218.
[179] C.L. Bianchi, S. Gatto, C. Pirola, A. Naldoni, A. Di Michele, G. Cerrato, V. Crocellà, V. Capucci, Photocatalytic degradation of acetone, acetaldehyde and toluene in gas-phase: Comparison between nano and micro-sized TiO2, Applied Catalysis B: Environmental, 146 (2014) 123-130.
[180] O. Debono, F. Thevenet, P. Gravejat, V. Hequet, C. Raillard, L. Lecoq, N. Locoge, Toluene photocatalytic oxidation at ppbv levels: Kinetic investigation and carbon balance determination, Applied Catalysis B: Environmental, 106 (2011) 600-608.
[181] L. Zhong, F. Haghighat, C.-S. Lee, N. Lakdawala, Performance of ultraviolet photocatalytic oxidation for indoor air applications: Systematic experimental evaluation, Journal of Hazardous Materials, 261 (2013) 130-138.

[182] D. Farhanian, F. Haghighat, Photocatalytic oxidation air cleaner: Identification and quantification of by-products, Building and Environment, 72 (2014) 34-43.
[183] D.A. Hansen, R. Atkinson, J.N. Pitts, Rate constants for the reaction of hydroxyl radicals with a series of aromatic hydrocarbons, The Journal of Physical Chemistry, 79 (1975) 1763-1766.
[184] M. Hajaghazadeh, V. Vaiano, D. Sannino, H. Kakooei, R. Sotudeh-Gharebagh, P. Ciambelli, Heterogeneous photocatalytic oxidation of methyl ethyl ketone under UV-A light in an LED-fluidized bed reactor, Catalysis Today, 230 (2014) 79-84.
[185] R.L. Penn, J.F. Banfield, Morphology development and crystal growth in nanocrystalline aggregates under hydrothermal conditions: insights from titania, Geochimica et Cosmochimica Acta, 63 (1999) 1549-1557.
[186] R.K. Wahi, Y. Liu, J.C. Falkner, V.L. Colvin, Solvothermal synthesis and characterization of anatase TiO2 nanocrystals with ultrahigh surface area, Journal of Colloid and Interface Science, 302 (2006) 530-536.
[187] P.-T. Hsiao, M.-D. Lu, Y.-L. Tung, H. Teng, Influence of Hydrothermal Pressure during Crystallization on the Structure and Electron-Conveying Ability of TiO2 Colloids for Dye-Sensitized Solar Cells, The Journal of Physical Chemistry C, 114 (2010) 15625-15632.
[188] J. Ovenstone, Preparation of novel titania photocatalysts with high activity, Journal of Materials Science, 36 (2001) 1325-1329.
[189] K. Yanagisawa, J. Ovenstone, Crystallization of Anatase from Amorphous Titania Using the Hydrothermal Technique: Effects of Starting Material and Temperature, The Journal of Physical Chemistry B, 103 (1999) 7781-7787.
[190] G. Li, S. Ciston, Z.V. Saponjic, L. Chen, N.M. Dimitrijevic, T. Rajh, K.A. Gray, Synthesizing mixed-phase TiO2 nanocomposites using a hydrothermal method for photo-oxidation and photoreduction applications, Journal of Catalysis, 253 (2008) 105-110.
[191] J. Yu, Y. Su, B. Cheng, M. Zhou, Effects of pH on the microstructures and photocatalytic activity of mesoporous nanocrystalline titania powders prepared via hydrothermal method, Journal of Molecular Catalysis A: Chemical, 258 (2006) 104-112.
[192] J.L. Blin, A. Léonard, Z.Y. Yuan, L. Gigot, A. Vantomme, A.K. Cheetham, B.L. Su, Hierarchically Mesoporous/Macroporous Metal Oxides Templated from Polyethylene Oxide Surfactant Assemblies, Angewandte Chemie International Edition, 42 (2003) 2872-2875.
[193] A. Vantomme, A. Léonard, Z.-Y. Yuan, B.-L. Su, Self-formation of hierarchical micro-meso-macroporous structures: Generation of the new concept “Hierarchical Catalysis”, Colloids and Surfaces A: Physicochemical and Engineering Aspects, 300 (2007) 70-78.
[194] Z. Wu, Z. Gu, W. Zhao, H. Wang, Photocatalytic oxidation of gaseous benzene over nanosized TiO2 prepared by solvothermal method, Chinese Science Bulletin, 52 (2007) 3061-3067.
[195] G. Bartosz, Use of spectroscopic probes for detection of reactive oxygen species, Clinica Chimica Acta, 368 (2006) 53-76.
[196] T. Hirakawa, Y. Nosaka, Properties of O2•- and OH• Formed in TiO2 Aqueous Suspensions by Photocatalytic Reaction and the Influence of H2O2 and Some Ions, Langmuir, 18 (2002) 3247-3254.
[197] W.-K. Jo, H.-J. Kang, (Ratios: 5, 10, 50, 100, and 200) Polyaniline–TiO2 composites under visible- or UV-light irradiation for decomposition of organic vapors, Materials Chemistry and Physics, 143 (2013) 247-255.

[198] K. Xia, D. Ferguson, Y. Djaoued, J. Robichaud, N. Tchoukanova, R. Brüning, E. McCalla, Template-free synthesis and photocatalytic activity of hierarchical porous titania with controlled texture and crystalline structure, Applied Catalysis A: General, 387 (2010) 231-241.
[199] X.-Y. Yang, A. Léonard, A. Lemaire, G. Tian, B.-L. Su, Self-formation phenomenon to hierarchically structured porous materials: design, synthesis, formation mechanism and applications, Chemical Communications, 47 (2011) 2763-2786.
[200] T.-D. Nguyen Phan, H.-D. Pham, T. Viet Cuong, E. Jung Kim, S. Kim, E. Woo Shin, A simple hydrothermal preparation of TiO2 nanomaterials using concentrated hydrochloric acid, Journal of Crystal Growth, 312 (2009) 79-85.
[201] D. Bahnemann, A. Henglein, L. Spanhel, Detection of the intermediates of colloidal TiO2-catalysed photoreactions, Faraday Discussions of the Chemical Society, 78 (1984) 151-163.
[202] H. Yin, Y. Wada, T. Kitamura, S. Kambe, S. Murasawa, H. Mori, T. Sakata, S. Yanagida, Hydrothermal synthesis of nanosized anatase and rutile TiO2 using amorphous phase TiO2, Journal of Materials Chemistry, 11 (2001) 1694-1703.
[203] W.S. Nam, G.Y. Han, A photocatalytic performance of TiO2 photocatalyst prepared by the hydrothermal method, Korean Journal of Chemical Engineering, 20 (2003) 180-184.
[204] Z. Wang, D. Xia, G. Chen, T. Yang, Y. Chen, The effects of different acids on the preparation of TiO2 nanostructure in liquid media at low temperature, Materials Chemistry and Physics, 111 (2008) 313-316.
[205] A. Pottier, S. Cassaignon, C. Chanéac, F. Villain, E. Tronc, J.-P. Jolivet, Size tailoring of TiO2 anatase nanoparticles in aqueous medium and synthesis of nanocomposites. Characterization by Raman spectroscopy, Journal of Materials Chemistry, 13 (2003) 877-882.
[206] W.F. Zhang, M.S. Zhang, Z. Yin, Q. Chen, Photoluminescence in anatase titanium dioxide nanocrystals, Applied Physics B, 70 (2000) 261-265.
[207] Q. Xiang, K. Lv, J. Yu, Pivotal role of fluorine in enhanced photocatalytic activity of anatase TiO2 nanosheets with dominant (001) facets for the photocatalytic degradation of acetone in air, Applied Catalysis B: Environmental, 96 (2010) 557-564.
[208] S.T. Nishanthi, S. Iyyapushpam, B. Sundarakannan, E. Subramanian, D. Pathinettam Padiyan, Inter-relationship between extent of anatase crystalline phase and photocatalytic activity of TiO2 nanotubes prepared by anodization and annealing method, Separation and Purification Technology, 131 (2014) 102-107.
[209] H. Tang, H. Berger, P.E. Schmid, F. Lévy, G. Burri, Photoluminescence in TiO2 anatase single crystals, Solid State Communications, 87 (1993) 847-850.
[210] J. Kaur, R. Singh, B. Pal, Influence of coinage and platinum group metal co-catalysis for the photocatalytic reduction of m-dinitrobenzene by P25 and rutile TiO2, Journal of Molecular Catalysis A: Chemical, 397 (2015) 99-105.
[211] Z. He, Z. Zhu, J. Li, J. Zhou, N. Wei, Characterization and activity of mesoporous titanium dioxide beads with high surface areas and controllable pore sizes, Journal of Hazardous Materials, 190 (2011) 133-139.
[212] Y. Qiu, X. Li, Synthesis of peroxo-titanium decorated H-titanate-nanotube-based hierarchical microspheres with enhanced visible-light photocatalytic activity in degradation of Rhodamine B, Dalton Transactions, 43 (2014) 14537-14541.
[213] B. Lindberg, R. Maripuu, K. Siegbahn, R. Larsson, C.G. Gölander, J.C. Eriksson, ESCA Studies of heparinized and related surfaces: 1. Model surfaces on steel substrates, Journal of Colloid and Interface Science, 95 (1983) 308-321.

[214] Y. Shuang, Y. Hou, B. Zhang, H.G. Yang, Impurity-Free Synthesis of Cube-Like Single-Crystal Anatase TiO2 for High Performance Dye-Sensitized Solar Cell, Industrial & Engineering Chemistry Research, 52 (2013) 4098-4102.
[215] M. Diak, M. Klein, T. Klimczuk, W. Lisowski, H. Remita, A. Zaleska-Medynska, E. Grabowska, Photoactivity of decahedral TiO2 loaded with bimetallic nanoparticles: Degradation pathway of phenol-1-13C and hydroxyl radical formation, Applied Catalysis B: Environmental, 200 (2017) 56-71.
[216] L. Wu, Y. Qiu, M. Xi, X. Li, C. Cen, Fabrication of TiO2 nanotubes-assembled hierarchical microspheres with enhanced photocatalytic degradation activity, New Journal of Chemistry, 39 (2015) 4766-4773.
[217] A.H. Mamaghani, F. Haghighat, C.-S. Lee, Photocatalytic degradation of VOCs on various commercial titanium dioxides: Impact of operating parameters on removal efficiency and by-products generation, Building and Environment, 138 (2018) 275-282.
[218] L. Zhong, F. Haghighat, C.-S. Lee, N. Lakdawala, Performance of ultraviolet photocatalytic oxidation for indoor air applications: Systematic experimental evaluation, Journal of Hazardous Materials, 261 (2013) 130-138.
[219] C. Raillard, V. Hequet, P. Le Cloirec, J. Legrand, Photocatalytic oxidation of methyl ethyl ketone over sol-gel and commercial TiO2 for the improvement of indoor air, 2006.
[220] T. Machold, W.Y. Suprun, H. Papp, Characterization of VOx-TiO2 catalysts and their activity in the partial oxidation of methyl ethyl ketone, Journal of Molecular Catalysis A: Chemical, 280 (2008) 122-130.
[221] G. Vincent, A. Queffeulou, P.M. Marquaire, O. Zahraa, Remediation of olfactory pollution by photocatalytic degradation process: Study of methyl ethyl ketone (MEK), Journal of Photochemistry and Photobiology A: Chemistry, 191 (2007) 42-50.
[222] K. Nakata, A. Fujishima, TiO2 photocatalysis: Design and applications, Journal of Photochemistry and Photobiology C: Photochemistry Reviews, 13 (2012) 169-189.
[223] S. Eiden-Assmann, J. Widoniak, G. Maret, Synthesis and Characterization of Porous and Nonporous Monodisperse Colloidal TiO2 Particles, Chemistry of Materials, 16 (2004) 6-11.
[224] Z. Liu, D.D. Sun, P. Guo, J.O. Leckie, One-Step Fabrication and High Photocatalytic Activity of Porous TiO2 Hollow Aggregates by Using a Low-Temperature Hydrothermal Method Without Templates, Chemistry – A European Journal, 13 (2007) 1851-1855.
[225] H.G. Yang, C.H. Sun, S.Z. Qiao, J. Zou, G. Liu, S.C. Smith, H.M. Cheng, G.Q. Lu, Anatase TiO2 single crystals with a large percentage of reactive facets, Nature, 453 (2008) 638.
[226] J. Zhu, S. Wang, Z. Bian, S. Xie, C. Cai, J. Wang, H. Yang, H. Li, Solvothermally controllable synthesis of anatase TiO2 nanocrystals with dominant {001} facets and enhanced photocatalytic activity, CrystEngComm, 12 (2010) 2219-2224.
[227] D.L. Morgan, H.-W. Liu, R.L. Frost, E.R. Waclawik, Implications of Precursor Chemistry on the Alkaline Hydrothermal Synthesis of Titania/Titanate Nanostructures, The Journal of Physical Chemistry C, 114 (2010) 101-110.
[228] C.-C. Tsai, H. Teng, Regulation of the Physical Characteristics of Titania Nanotube Aggregates Synthesized from Hydrothermal Treatment, Chemistry of Materials, 16 (2004) 4352-4358.
[229] K.P. Cabral, W. Kurniawan, H. Hinode, Three-dimensional sea urchin-like TiO2 synthesized via facile hydrothermal method: Its properties and solar photocatalytic activity, Journal of Environmental Chemical Engineering, 3 (2015) 2786-2796.

[230] J. Li, J. Xu, W.-L. Dai, H. Li, K. Fan, Direct hydro-alcohol thermal synthesis of special core–shell structured Fe-doped titania microspheres with extended visible light response and enhanced photoactivity, Applied Catalysis B: Environmental, 85 (2009) 162-170.
[231] C.-R. Ke, L.-C. Chen, J.-M. Ting, Photoanodes Consisting of Mesoporous Anatase TiO2 Beads with Various Sizes for High-Efficiency Flexible Dye-Sensitized Solar Cells, The Journal of Physical Chemistry C, 116 (2012) 2600-2607.
[232] H.G. Yang, G. Liu, S.Z. Qiao, C.H. Sun, Y.G. Jin, S.C. Smith, J. Zou, H.M. Cheng, G.Q. Lu, Solvothermal Synthesis and Photoreactivity of Anatase TiO2 Nanosheets with Dominant {001} Facets, Journal of the American Chemical Society, 131 (2009) 4078-4083.
[233] T. Kasuga, M. Hiramatsu, A. Hoson, T. Sekino, K. Niihara, Formation of Titanium Oxide Nanotube, Langmuir, 14 (1998) 3160-3163.
[234] Q. Chen, W. Zhou, G.H. Du, L.M. Peng, Trititanate nanotubes made via a single alkali treatment, Advanced Materials, 14 (2002) 1208-1211+1178.
[235] G.H. Du, Q. Chen, P.D. Han, Y. Yu, L.M. Peng, Potassium titanate nanowires: Structure, growth, and optical properties, Physical Review B - Condensed Matter and Materials Physics, 67 (2003) 353231-353237.
[236] Z.Y. Yuan, X.B. Zhang, B.L. Su, Moderate hydrothermal synthesis of potassium titanate nanowires, Applied Physics A: Materials Science and Processing, 78 (2004) 1063-1066.
[237] T. Shibata, N. Sakai, K. Fukuda, Y. Ebina, T. Sasaki, Photocatalytic properties of titania nanostructured films fabricated from titania nanosheets, Physical Chemistry Chemical Physics, 9 (2007) 2413-2420.
[238] M.D. Hernández-Alonso, S. García-Rodríguez, S. Suárez, R. Portela, B. Sánchez, J.M. Coronado, Highly selective one-dimensional TiO2-based nanostructures for air treatment applications, Applied Catalysis B: Environmental, 110 (2011) 251-259.
[239] H. Yu, J. Yu, B. Cheng, Photocatalytic activity of the calcined H-titanate nanowires for photocatalytic oxidation of acetone in air, Chemosphere, 66 (2007) 2050-2057.
[240] T. Kasuga, M. Hiramatsu, A. Hoson, T. Sekino, K. Niihara, Titania nanotubes prepared by chemical processing, Advanced Materials, 11 (1999) 1307-1311.
[241] D.V. Bavykin, V.N. Parmon, A.A. Lapkin, F.C. Walsh, The effect of hydrothermal conditions on the mesoporous structure of TiO2 nanotubes, Journal of Materials Chemistry, 14 (2004) 3370-3377.
[242] G.H. Du, Q. Chen, R.C. Che, Z.Y. Yuan, L.-M. Peng, Preparation and structure analysis of titanium oxide nanotubes, Applied Physics Letters, 79 (2001) 3702-3704.
[243] A.G. West, C. Barner-Kowollik, S. Perrier, Poly(ethylene glycol) as a ‘green solvent’ for the RAFT polymerization of methyl methacrylate, Polymer, 51 (2010) 3836-3842.
[244] X. Jiang, Y. Wang, T. Herricks, Y. Xia, Ethylene glycol-mediated synthesis of metal oxide nanowires, Journal of Materials Chemistry, 14 (2004) 695-703.
[245] J. Yu, W. Wang, B. Cheng, B.-L. Su, Enhancement of Photocatalytic Activity of Mesporous TiO2 Powders by Hydrothermal Surface Fluorination Treatment, The Journal of Physical Chemistry C, 113 (2009) 6743-6750.
[246] C. Minero, G. Mariella, V. Maurino, E. Pelizzetti, Photocatalytic Transformation of Organic Compounds in the Presence of Inorganic Anions. 1. Hydroxyl-Mediated and Direct Electron-Transfer Reactions of Phenol on a Titanium Dioxide−Fluoride System, Langmuir, 16 (2000) 2632-2641.

[247] C. Minero, G. Mariella, V. Maurino, D. Vione, E. Pelizzetti, Photocatalytic Transformation of Organic Compounds in the Presence of Inorganic Ions. 2. Competitive Reactions of Phenol and Alcohols on a Titanium Dioxide−Fluoride System, Langmuir, 16 (2000) 8964-8972.
[248] J.H. Pan, X. Zhang, A.J. Du, D.D. Sun, J.O. Leckie, Self-Etching Reconstruction of Hierarchically Mesoporous F-TiO2 Hollow Microspherical Photocatalyst for Concurrent Membrane Water Purifications, Journal of the American Chemical Society, 130 (2008) 11256-11257.
[249] M. Liu, L. Piao, L. Zhao, S. Ju, Z. Yan, T. He, C. Zhou, W. Wang, Anatase TiO2 single crystals with exposed {001} and {110} facets: facile synthesis and enhanced photocatalysis, Chemical Communications, 46 (2010) 1664-1666.
[250] M. Lazzeri, A. Vittadini, A. Selloni, Structure and energetics of stoichiometric ${\mathrm{TiO}}_{2}$ anatase surfaces, Physical Review B, 63 (2001) 155409.
[251] N. Roy, Y. Sohn, D. Pradhan, Synergy of Low-Energy {101} and High-Energy {001} TiO2 Crystal Facets for Enhanced Photocatalysis, ACS Nano, 7 (2013) 2532-2540.
[252] T. Tachikawa, S. Yamashita, T. Majima, Evidence for Crystal-Face-Dependent TiO2 Photocatalysis from Single-Molecule Imaging and Kinetic Analysis, Journal of the American Chemical Society, 133 (2011) 7197-7204.
[253] M. Wang, F. Zhang, X. Zhu, Z. Qi, B. Hong, J. Ding, J. Bao, S. Sun, C. Gao, DRIFTS Evidence for Facet-Dependent Adsorption of Gaseous Toluene on TiO2 with Relative Photocatalytic Properties, Langmuir, 31 (2015) 1730-1736.
[254] D.S. Kim, S.-Y. Kwak, The hydrothermal synthesis of mesoporous TiO2 with high crystallinity, thermal stability, large surface area, and enhanced photocatalytic activity, Applied Catalysis A: General, 323 (2007) 110-118.
[255] J.G. Yu, Y.R. Su, B. Cheng, Template-Free Fabrication and Enhanced Photocatalytic Activity of Hierarchical Macro-/Mesoporous Titania, Advanced Functional Materials, 17 (2007) 1984-1990.
[256] T. Tong, J. Zhang, B. Tian, F. Chen, D. He, Preparation of Fe(3+)-doped TiO(2) catalysts by controlled hydrolysis of titanium alkoxide and study on their photocatalytic activity for methyl orange degradation, 2008.
[257] Y. Tao, C.-Y. Wu, D.W. Mazyck, Removal of methanol from pulp and paper mills using combined activated carbon adsorption and photocatalytic regeneration, Chemosphere, 65 (2006) 35-42.
[258] A.H. Mamaghani, F. Haghighat, C.-S. Lee, Performance of various commercial TiO2 in photocatalytic degradation of a mixture of indoor air pollutants: Effect of photocatalyst and operating parameters, Science and Technology for the Built Environment 28 (2018) 234-246.
[259] A.H. Mamaghani, F. Haghighat, C.-S. Lee, Hydrothermal/Solvothermal synthesis and treatment of TiO_2 for photocatalytic degradation of air pollutants: Preparation, characterization, properties, and performances, Chemosphere 219 (2018) 804-825.
[260] H.P. Kuo, C.T. Wu, R.C. Hsu, Continuous reduction of toluene vapours from the contaminated gas stream in a fluidised bed photoreactor, Powder Technology, 195 (2009) 50-56.
[261] G. Xue, H. Liu, Q. Chen, C. Hills, M. Tyrer, F. Innocent, Synergy between surface adsorption and photocatalysis during degradation of humic acid on TiO2/activated carbon composites, Journal of Hazardous Materials, 186 (2011) 765-772.